Universität Zürich[UZH]

Physik-Institut

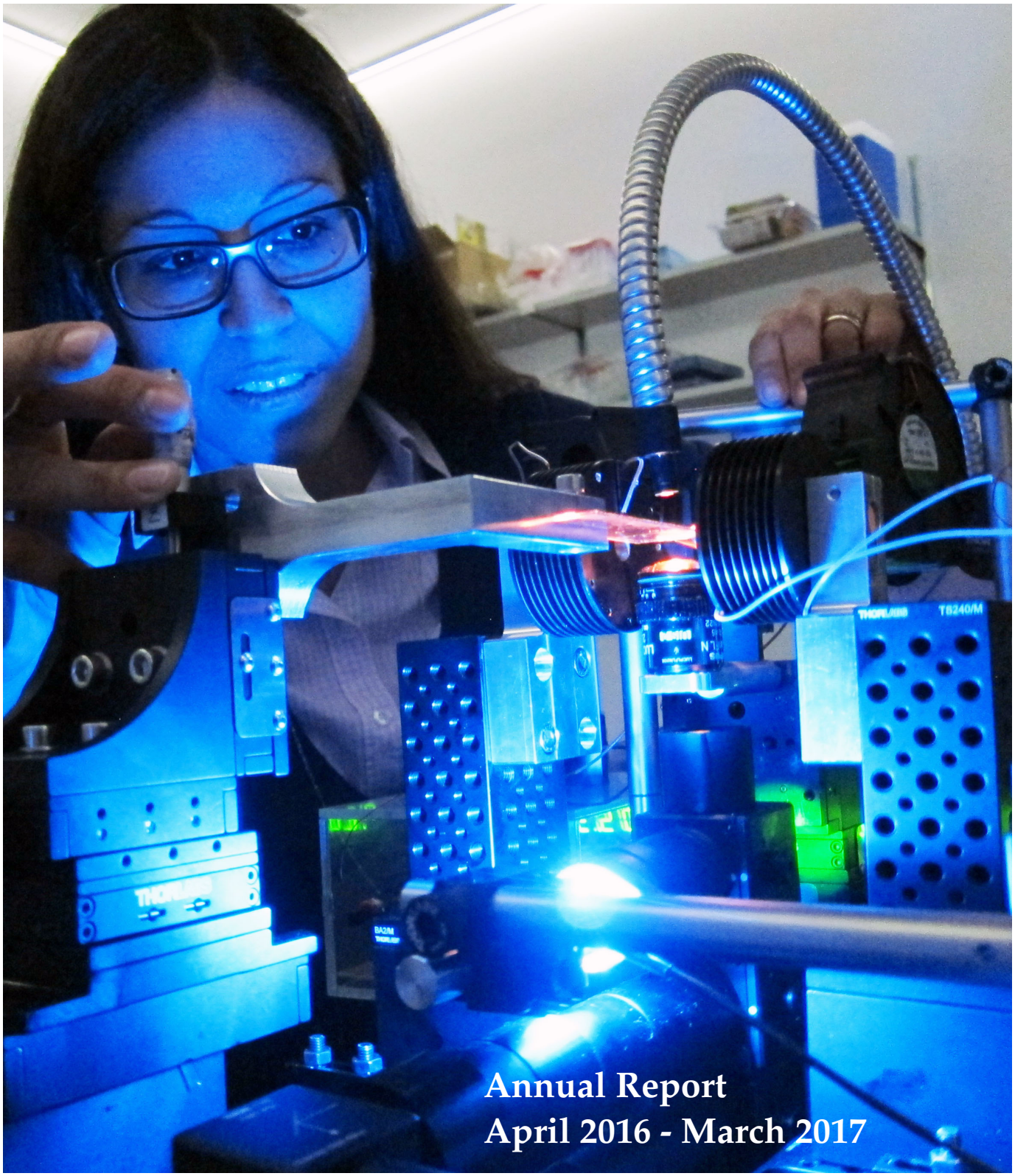

Annual Report
April 2016 - March 2017

Universität Zürich[UZH]

Physik-Institut

Annual Report
April 2016 - March 2017

Winterthurerstrasse 190, CH-8057 Zürich/Schweiz

Front picture: Lara Selvaggi at work adjusting her magnetic tweezer on a custom built fluorescence microscope (Sec. 16).

Picture on the back: Optical setup for imaging behind turbid layers (Sec. 16).

Secretariat	044 635 5721	sekretariat@physik.uzh.ch
Prof. C. Aegerter	044 635 5813	christof.aegerer@physik.uzh.ch
Prof. L. Baudis	044 635 5777	laura.baudis@physik.uzh.ch
Prof. F. Canelli	044 635 5784	florencia.canelli@physik.uzh.ch
Prof. J. Chang	044 635 5748	johan.chang@physik.uzh.ch
Prof. H.-W. Fink	044 635 5801	hwfink@physik.uzh.ch
Prof. T. Gehrmann	044 635 5818	thomas.gehrmann@physik.uzh.ch
Prof. M. Grazzini	044 635 5806	grazzini@physik.uzh.ch
Prof. M. Greber	044 635 5744	greber@physik.uzh.ch
Prof. G. Isidori	044 635 5751	gino.isidori@physik.uzh.ch
Prof. P. Jetzer	044 635 5819	jetzer@physik.uzh.ch
Prof. B. Kilminster	044 635 5802	ben.kilminster@physik.uzh.ch
Prof. T. Neupert	044 635 4800	titus.neupert@physik.uzh.ch
Prof. J. Osterwalder	044 635 5827	osterwal@physik.uzh.ch
Prof. S. Pozzorini	044 635 6014	pozzorin@physik.uzh.ch
Prof. A. Schilling	044 635 5791	schilling@physik.uzh.ch
Prof. N. Serra	044 635 5725	nicola.serra@physik.uzh.ch
Prof. A. Signer	056 310 3661	adrian.signer@psi.ch
Prof. U.D. Straumann	044 635 5768	ulrich.straumann@physik.uzh.ch

---

The annual reports are available on the internet: http://www.physik.uzh.ch/reports.shtml.

Preface

In this report the interested reader will find a broad overview of the various research activities of the members of the Physik-Institut, including highlights of the last year and progress reports of ongoing projects. The experimental research spans a wide range from particle and astroparticle physics, hard and soft condensed matter physics, surface physics and nanoscience, to the physics of biological systems. Theoretical activities include precision calculations of processes in quantum chromodynamics and new theories beyond the standard model of particle physics, astrophysics and general relativity, and since 2016 also theoretical condensed matter physics as Prof. Titus Neupert joined our department. His work on topological phenomena in electronic systems is introduced in Section 11.

The physics department employs about 150 scientific, technical and administrative staff, originating from 28 countries. As a small- to medium-size physics department, we have chosen to define priority areas, with several groups working for instance in particle and in condensed matter physics. To increase the diversity of research topics, which is important in particular for the students, other physics-related research groups from within the Faculty of Science and beyond are affiliated to our department. Presently, ten working groups, covering fields such as soft condensed matter at the nanoscale, computational science, medical physics, bio-imaging, astrophysics and cosmology and biophysics (see: `www.physik.uzh.ch/en/research.html`) are affiliated and are open to offer Bachelor or Master projects for our students. An example is the affiliation of the group of Prof. Jan Unkelbach, a recently appointed medical physicist in the department of radiation oncology of the University Hospital.

An important asset to the research environment in the Physik-Institut are the excellent mechanical and electronics workshops, as well as the efficient IT and administrative support. Thanks to this strong infrastructure department, our research groups have been able to make important contributions to large international projects, like for the XENON1T project (Baudis group), the Cherenkov Telescope Array (CTA, Straumann group), or the CMS detector upgrade for the Large Hadron Collider at CERN (Kilminster and Canelli groups).

Also in this year, our groups were very active in organizing conferences, for example the International LISA Symposium (Prof. Philippe Jetzer) or the well attended Workshop on Topological Quantum Phenomena (Profs. Titus Neupert and Johan Chang). A particularly noteworthy success is the ERC Advanced Grant awarded to Prof. Laura Baudis. The professors of the department take part in many scientific organizations, including the national research council, research committees of the Paul Scherrer Institut and advisory boards and panels of numerous international research institutions. Our former director, Prof. Ulrich Straumann, for instance took over the managing directorship of the CTA Organization gGmbH. The professors also contribute to the academic self administration of the university and are members of many national and international search committees for new professors.

As more than 1100 students are taught physics at our university all physicists of the institute are involved in teaching. We run courses for students in the medical faculty and those in our own faculty studying biology, chemistry, geography, earth system sciences, mathematics and the new course of studies in biomedicine. For the latter an additional service lecture in basic physics was introduced. Already in the first year the enrollement was high with about 150 students.

In the period of 11-17 July 2016 our department hosted the 47th International Physics Olympiad. A total of 398 high school students from 84 countries participated in this competition and were accompanied by 256 supervisors and functionaries. This big event, which was organised by Prof. Andreas Schilling and Andrea Schneider, required all personnel resources of the department for several days. Some of our scientific and technical people were busy for several months with designing the experimental and theoretical problems that the students had to solve. The whole event was a big success that attracted the attention of the local, national and international media.

The editorial responsibility of the annual report has been handed over to Dr. Katharina Müller. She follows the footsteps of Dr. Andries van der Schaaf, who has shaped its format for the last 17 years.

Zürich, May 2017

Prof. Dr. Jürg Osterwalder

Prof. Dr. Detlef Brinkmann

October 3, 1931 (Esens/D) - February 20, 2017 (Uster/CH)

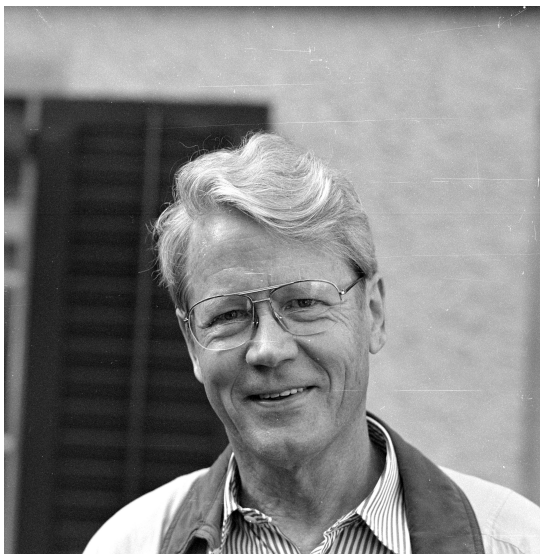

Detlef Brinkmann attended schools in Northern Germany and enrolled afterwards in 1952 at the University of Göttingen. There he passed the 'Vordiplom (BSc) in 1954 and then transferred to the University of Zürich, where he obtained his 'Diplom' (MSc) in experimental physics in 1958. *'Nuclear magnetic resonance in gaseous Xenon'*[1] was the title of his thesis carried out under the guidance of Prof. Dr. Hans Staub, which led to a PhD in 1961. Besides low energy nuclear physics at a Van-de-Graaff accelerator nuclear magnetic resonance (NMR) was the primary research subject, which Hans Staub pioneered in Switzerland after he returned from Stanford in 1949. Detlef Brinkmann continued to apply NMR techniques during his postdoctoral research at Rutgers University in New Brunswick, New Jersey (USA), and further after his return to our institute in 1965. After submission of a 'Habilitationsschrift' on the *'Displacement of the Local Magnetic Field in the Nuclear Resonance of Noble Gases'*[2] in 1968 he served as Lecturer, became Assistant Professor in 1972, was promoted to Associate Professor in 1976 and finally to Full Professor in 1983. In 1999 he retired as Professor Emeritus.

During his many years as a professor at our institute Detlef Brinkmann led a dedicated research group, which made significant contributions to the physics of condensed matter using NMR and NQR (Nuclear Quadrupole Resonance) techniques. The wide field of his scientific work ranged from noble gases and natural minerals to synthetic substances, such as quasi-one-dimensional and super-ion conductors. Since the 1980s his research has focused on the investigation of high-temperature superconductors, especially their behavior under pressure. In this area he collaborated with the IBM Rüschlikon research laboratory and Prof. Dr. Karl Alex Müller.

In addition to his successful research, Detlef Brinkmann was also a popular academic teacher, he enthusiastically taught the introductory physics courses and engaged in didactics discussions within the European Physical Society. Since his initial course in the 1980s on the fundamentals of solid state physics at our institute it is an integral part of the physics curriculum here.

Detlef Brinkmann had an excellent and fruitful scientific network inside Switzerland (e.g. ETHZ, ABB) and outside in Europe (including MPI Stuttgart, University of Grenoble or the Kazan Federal University in the Russian Republic Tatarstan), as well as in America (Argonne National Lab, General Electric, University of Washington and the State University of New York at Albany) and Asia. Here, Detlef Brinkmann had very active research connections to Japan, Singapore and India, where he was appointed Pandit Jawaharlal Nehru Professor at the University of Hyderabad in 1999. Numerous researchers from the corresponding institutes used the good contacts to our institute for a research stay of a few months at UZH. Detlef Brinkmann served as President of the International Committee on Nuclear Quadrupole Interactions (NQI) for many years and was responsible for a series of symposia and conferences held in this field. In 2001 he received the NQI Award.

[1] Translated from the German title *'Kernresonanz im gasförmigen Xenon'*

[2] Translated from the German title *'Verschiebung des lokalen magnetischen Feldes in der Kernresonanz von Edelgasen'*

Personnel

Scientific personnel

Thea Klæboe	Årrestad	Sec. 10
Mirco	Ackermann	Sec. 16
PD Dr. Christof	Aegerter	Sec. 16
Michele	Atzeni	Sec. 9
Simone	Balmelli	Sec. 2
Peter	Barrow	Sec. 4
Prof. Laura	Baudis	Sec. 3, 4
Carlo	Bernard	Sec. 14
Dr. Roland	Bernet	Sec. 9
Dr. Christopher	Betancourt	Sec 9, 8
Iaroslava	Bezshyiko	Sec 9, 8
Dr. Ruxandra	Bondarescu	Sec. 2
Marzia	Bordone	Sec. 1
Dr. Sophia	Borowka	Sec. 1
Yannik	Bötzel	Sec. 2
Espen	Bowen	Sec. 9
Adam	Brown	Sec. 4
Federico	Buccioni	Sec 1
Dr. Dario	Buttazzo	Sec 1
Dr. Lea	Caminada	Sec. 10
Prof. Florencia	Canelli	Sec. 6, 10
Chiara	Capelli	Sec. 4
Dr. Luca	Castiglioni	Sec. 14
Prof. Johan	Chang	Sec. 12
Dr. Marcin	Chrząszcz	Sec. 9
Dr. Leandro	Cieri	Sec 1
Dr. Ashley	Cook	Sec 11
Paule	Dagenais	Sec 16
Dr. Annapaola	de Cosa	Sec. 10
Riccardo	del Burgo	Sec. 10
Dr. Luis	de Lima	Sec. 14
Philippe	Denzel	Sec. 2
Daniel	Destraz	Sec. 12
Simone	Devoto	Sec. 12
Lorenzo	de Vittori	Sec. 2
Dr. Silvio	Donato	Sec. 10
David	Dreher	Sec. 16
Jonas	Eschle	Sec. 9
Dr. Conrad	Escher	Sec. 15
Prof. Hans-Werner	Fink	Sec. 15
Dr. Stefan	Förster	Sec. 14
Dr. Arno	Gadola	Sec. 6
Camilla	Galloni	Sec. 10
Dr. Michelle	Galloway	Sec. 4
Alsu	Gazizulina	Sec. 13
Prof. Thomas	Gehrmann	Sec. 1
Elena	Graverini	Sec. 8, 9
PD Dr. Massimiliano	Grazzini	Sec. 1
Prof. Thomas	Greber	Sec. 14
Roman	Gredig	Mu3e
Dr. Nicolas	Greiner	Sec. 1
Dr. Admir	Greljo	Sec. 1
Dr. Henrik	Grundmann	Sec. 13
Dr. Maria	Haney	Sec. 2
Catalin	Hanga	Sec. 1
Dr. Adrian	Hemmi	Sec. 14
Dr. Matthias	Hengsberger	Sec. 14
Dr. Roman	Hiller	Sec. 3
Dr. Andreas	Hinzmann	Sec. 10
Marius	Höfer	Sec. 1
Dr. Tomas	Hreus	Sec. 10
Shang-Xiong	Huang-fu	Sec. 13
Daniel	Hulme	Sec. 1
Agnieszka	Ilnicka	Sec. 1
Prof. Gino	Isidori	Sec. 1
Dr. Dimitri	Ivanov	Sec. 1
Oleh	Ivashko	Sec. 12
Prof. Philippe	Jetzer	Sec. 2
Dr. Tomas	Ježo	Sec. 1
Dominik	Kara	Sec. 1
Dr. Alexander	Karlberg	Sec. 1
Dr. Shingo	Kazama	Sec. 4
Prof. Benjamin	Kilminster	Sec. 10, 8, 5
Dr. Alexander	Kish	Sec. 3, 4
Pavlo	Kliuiev	Sec. 14
Aram	Kostanyan	Sec. 14
Rafael	Küng	Sec. 2
Davide	Lancierini	Sec. 9
Flavio	Lanfranconi	Sec. 16
Dr. Clemens	Lange	Sec. 10
Dr. Dominik	Leuenberger	Sec. 14
Junhui	Liao	Sec. 5
Dr. Jonas	Lindert	Sec. 1
Federica	Lionetto	Sec. 9
Dr. Jean-Nicolas	Longchamp	Sec. 15
Dr. Adriano	Lopresti	Sec. 1
Marianna	Lorenzo	Sec. 15
Peter	Lowdon	Sec. 1
Archana	Mallavalli	Sec. 16
Dr. David	Marzocca	Sec. 1
Dr. Christian	Matt	Sec. 12
Andrea	Mauri	Sec. 9
Daniel	Mayani Paras	Sec. 4
Dr. Javier	Mazzitelli	Sec. 1
Michael	Miloradovic	Sec. 4
Rizalina	Mingazheva	Sec. 4
Dr. Elisa	Miniussi	Sec. 14
Dr. Claude	Monney	Sec. 14

Niccolo	Moretti	Sec. 1
Dr. Katharina	Müller	Sec. 9
Prof. Titus	Neupert	Sec. 11
Jennifer	Ngadiuba	Sec. 10
Jan	Niehues	Sec. 1
Dr. Zbynek	Novotny	Sec. 14
Seulghi	Ok	Sec. 11
Deniz Gizem	Oeztürk	Sec. 1
Prof. Jürg	Osterwalder	Sec. 14
Dr. Patrick	Owen	Sec. 9
Payam	Pakarha	Sec. 4
Andrea	Pattori	Sec. 1
Lionel	Philippoz	Sec. 2
Francesco	Piastra	Sec. 4
Deborah	Pinna	Sec. 10
Prof. Stefano	Pozzorini	Sec. 1
Dr. Albert	Puig	Sec. 9
Sahil	Puri	Sec. 16
Chloe	Ransom	Sec. 3
Giorgia	Rauco	Sec. 10
Dr. Peter	Robmann	Sec. 5, 7, 10
PD Dr. Prasenjit	Saha	Sec. 2
Daniel	Salerno	Sec. 10
Hayk	Sargsyan	Sec. 1
Andreas	Schärer	Sec. 2
Dr. Lukas	Schertel	Sec. 16
Prof. Andreas	Schilling	Sec. 13
Frank	Schindler	Sec. 11
Dr. Jale	Schneider	Sec. 16
Dr. Marek	Schönherr	Sec. 1
Adrian	Schuler	Sec. 14
Korbinian	Schweiger	Sec. 10
Dr. Claudia	Seitz	Sec. 10
Dr. Lara	Selvaggi	Sec. 16
Prof. Nicola	Serra	Sec. 8, 9
Dr. Andrey	Sidorenko	Sec. 12
Prof. Adrian	Signer	Sec. 1
Dr. Rafael	Silva Coutinho	Sec. 9
Roland	Stania	Sec. 14
PD Dr. Olaf	Steinkamp	Sec. 9
Dr. Barbara	Storaci	Sec. 8, 9
Prof. Ulrich	Straumann	Sec. 6, 9
Denys	Sutter	Sec. 12
Dr. Yuta	Takahashi	Sec. 10
Lakshmi Das	Thazhe Veettil	Sec. 12
Marco	Tresch	Sec. 9
Sokratis	Trifinopoulos	Sec. 1
Dr. Severine	Urdy	Sec. 16
Dr. Andries	van der Schaaf	Sec. 7
Dr. Denys	van Dyk	Sec. 1
Dr. Achim	Vollhardt	Sec. 6, 9, 18
Kay	Waltar	Sec. 14
Qiang	Wang	Sec. 13
Dr. Yuehuan	Wei	Sec. 4
Andreas	Weiden	Sec. 9
Flavio	Wicki	Sec. 15
Dr. Marius	Wiesemann	Sec. 1
Julien	Wulf	Sec. 4
Wolf-Dietrich	Zabka	Sec. 14
Xiaofu	Zhang	Sec. 13
Max	Zoller	Sec. 1
Dr. Alberto	Zucchetta	Sec. 10

Technical and adminstrative personnel

Dr. Carlos	Abellan Beteta	Sec. 9
Chris	Albrecht	Sec. 17
Kurt	Bösiger	Sec. 17
Tiziano	Crudeli	Technical support
Patrick	Donà	Sec. 14
Daniel	Florin	Sec. 18, 6
Brigitte	Freund	Secretariat
Carmelina	Genovese	Secretariat
Ruth	Halter	Secretariat
Andreas	James	Sec. 3,4
Thomas	Kälin	Sec. 14
Simon	Karrer	Sec. 18
Gian	Knüsel	Sec. 17
Bruno	Lussi	Sec. 17
Reto	Maier	Sec. 17
Brandon	Markwalder	Sec. 17
Lucien	Pauli	Lecture demonstrations
Jan Ten	Pierick	Sec. 2
Monika	Röllin	Secretariat
Marcel	Schaffner	Sec. 17
Silvio	Scherr	Sec. 17
Regina	Schmid	Secretariat
Andrea	Schneider	IPhO
Karen	Schraader Frigg	Admistration
Stefan	Siegrist	Sec. 13
Stefan	Steiner	Sec. 6, 9
Kim Jennifer	Studenski	Administration
Marc	Türler	Administration
Jonas	Vergés	Sec. 15
Pascal	Weyeneth	Sec. 17
David	Wolf	Sec. 18

Contents

1 Theory of Elementary Particles

M. Bordone, S. Borowka, F. Buccioni, D. Buttazzo, L. Cieri, S. Devoto, T. Gehrmann, M. Grazzini, N. Greiner, A. Greljio, C. Hanga, D. Hulme, A. Ilnicka, G. Isidori, T. Jezo, D. Kara, A. Karlberg, J. Lindert, A. Lopresti, P. Lowdon, D. Marzocca, J. Mazzitelli, N. Moretti, D. Müller, J. Niehues, G. Oeztürk, A. Pattori, S. Pozzorini, H. Sargsyan, M. Schönherr, A. Signer, S. Trifinopoulos, Y. Ulrich, D. van Dyk, A. Visconti, M. Wiesemann, D. Wyler, M. Zoller

in collaboration with: RWTH Aachen, CERN, IMSc Chennai, TU Dresden, Durham University, INFN Firenze, Freiburg University, INFN and University of Genova, DESY Hamburgh, University of Lyon, Stephan Insistue Ljubljana, Mainz University, Michigan State University, University of Milano Bicocca, MPI Munich, LPT Orsay, INFN and University of Padova, Peking University, University of San Martin, Siegen University, SLAC Stanford, IFIC Valencia, ETH Zürich.

The particle theory group at the Physik-Institut works on a broad spectrum of research projects related to the interpretation of data from high energy particle colliders. These cover precision calculations of benchmark observables, simulation of full collider events, identification of optimal observables for searches and measurements, physics beyond the Standard Model, as well as developments of calculational techniques. We summarize some highlights of last year's research below.

1.1 Next-to-leading order QCD predictions for top-quark pair production with up to three jets

The top quark as the heaviest known elementary particle plays a fundamental role, both in the Standard Model and in new physics scenarios. Experimental analyses of Large Hadron Collider (LHC) data collected during run II will provide unprecedented reach at high energy and in exclusive phase space regions with associated production of jets and vector bosons or Higgs bosons. The production of a $t\bar{t}$ system in association with multiple jets plays an especially important role as a background to new physics searches and to various Higgs and Standard Model analyses. In particular, the precise theoretical control of $t\bar{t}$+multijet backgrounds is one of the most important prerequisites for the observation of top-quark production in association with a Higgs boson, which would give direct access to the top-quark Yukawa coupling.

In this context, it is crucial to dispose of next-to-leading order (NLO) QCD predictions for $t\bar{t}$ production in association with the highest possible number of extra jets. However, the technical complexity of such calculations grows extremely fast with the number N_{jets} of extra jets. This is illustrated in Table 1.1, which lists the number of one-loop Feynman diagrams that contribute to a few representative partonic channels as a function of N_{jets}. At $N_{\text{jets}} > 1$ the level of complexity starts to be very high, and the first NLO calculations for $pp \to t\bar{t} + 2\,\text{jets}$ [1–3] belong to the breakthroughs of the so-called NLO revolution. Very recently we have present the first NLO results for $t\bar{t} + 3\,\text{jets}$. At present only few scattering processes with more than four final-state particles are known at NLO, and the calculation at hand is the first one that deals with a $2 \to 5$ process with seven colored external particles including also heavy quarks. These results could be achieved thanks to OpenLoops [4, 5], an automated generator of one-loop matrix elements that was developed in the recent years at our institute. It allows to perform multi-particle NLO calculations with remarkably high efficiency.

In [6] we have presented a series of NLO calculations for $pp \to t\bar{t} + 0, 1, 2, 3\,\text{jets}$ at the 13 TeV LHC. Exploiting the unprecedented reach in jet multiplicity, we have studied the scaling behavior in N_{jets}, and we have shed new light on the general issue of scale setting and theoretical scale uncertainties in the context of multi-scale processes.

Tab. 1.1 – Number of one-loop Feynman diagrams in representative partonic channels in $pp \to t\bar{t} + N\,\text{jets}$ for $N = 0, 1, 2, 3$.

partonic channel \ N	0	1	2	3
$gg \to t\bar{t} + N\,g$	47	630	9'438	152'070
$u\bar{u} \to t\bar{t} + N\,g$	12	122	1'608	23'835
$u\bar{u} \to t\bar{t}u\bar{u} + (N-2)\,g$	–	–	506	6'642
$u\bar{u} \to t\bar{t}d\bar{d} + (N-2)\,g$	–	–	252	3'321

The multiple scales that enter $t\bar{t}+$ multijet cross sections and distributions can be distributed over more than two orders of magnitude. In this situation, finding renormalization (μ_R) and factorization (μ_F) scales that ensure a decent convergence of perturbative QCD for the widest possible range of observables is not trivial. Moreover, in the presence of a wide spectrum of scales, the standard approach of using factor-two scale variations for the estimation of theoretical uncertainties due to missing higher-order effects becomes questionable. Motivated by these observations, to gain more insights into the scale dependence of $t\bar{t}+$ multijet production and related uncertainties we have compared the standard approach of using a hard scale choice ($\mu = H_T/2$), against the MiNLO method [7]. The latter can be regarded as an optimal scale-setting approach for multi-scale processes, as it resums soft and collinear logarithms that emerge in the presence of large ratios of scales. Our study provides the first systematic comparison of these two approaches.

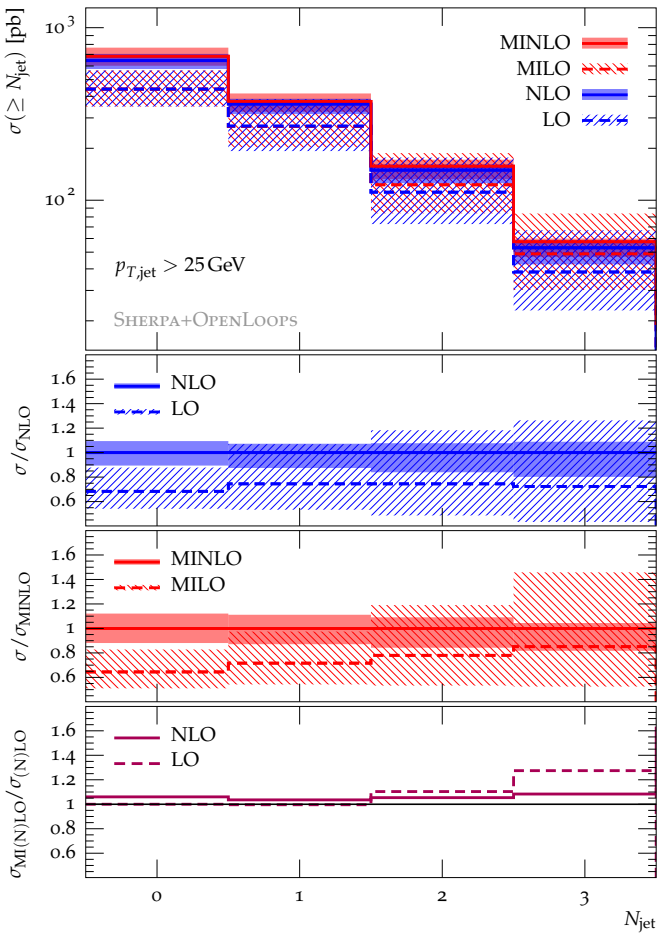

FIG. 1.1 – Inclusive $t\bar{t}+$ multijet cross sections at the 13 TeV LHC with a minimum number $N = 0, 1, 2, 3$ of jets at $p_{T,\text{jet}} \geq 25$ GeV.

As an illustration of our results, we show in Fig. 1.1 the jet multiplicity distribution for $t\bar{t} + 0, 1, 2, 3$ jets. The top panel displays four predictions, stemming from fixed-order LO and NLO calculations, and from MiNLO computations at LO and NLO (labeled 'MiLO' and 'MiNLO'). The second panel shows the ratio between LO and NLO predictions at fixed order, while the third panel shows the ratio between MiLO and MiNLO predictions. The last panel shows the ratio between MiNLO and NLO. The bands illustrate scale uncertainties estimated through independent factor-two rescaling of μ_R and μ_F. Fixed-order predictions feature rather large NLO corrections of about +50% for all jet multiplicities, while MiNLO results feature steadily decreasing corrections for increasing N_{jets}. In both cases, LO scale uncertainties tend to grow by more than 10% at each extra jet emission, while (MI)NLO scale uncertainties are significantly reduced, and the total width of the (MI)NLO variation bands is about 20–25% for all considered N_{jets} values. Comparing fixed-order NLO and MiNLO predictions we observe a remarkable agreement at the level of 4–8%. This supports NLO and MiNLO scale-uncertainty estimates based on factor-two variations.

In general, for a wide wide range of observables at the 13 TeV LHC, we found remarkably good agreement between the predictions generated at fixed order and with the MiNLO method [6]. More precisely, MiNLO cross sections tend to feature a better perturbative convergence and to lie systematically above NLO ones. But the differences turn out to be well consistent with factor-two scale variations of the respective predictions. These findings significantly extend and consolidate the conventional picture of theoretical uncertainties that results from standard scale choices and scale variations. The anticipated level of theoretical precision for $t\bar{t}+$ multijet production is at the level of ten percent or better.

[1] A. Bredenstein, A. Denner, S. Dittmaier, and S. Pozzorini, Phys. Rev. Lett. **103** (2009) 012002.

[2] F. Cascioli, P. Maierhöfer, N. Moretti, S. Pozzorini, and F. Siegert, Phys. Lett. **B734** (2014) 210-214.

[3] S. Höche, F. Krauss, P. Maierhöfer, S. Pozzorini, M. Schönherr, and F. Siegert, Phys. Lett. **B748** (2015) 74-78.

[4] F. Cascioli, P. Maierhöfer, and S. Pozzorini, Phys. Rev. Lett. **108** (2012) 111601.

[5] F. Cascioli, J. Lindert, P. Maierhöfer, and S. Pozzorini, *The OpenLoops one-loop generator*, publicly available at http://openloops.hepforge.org.

[6] S. Höche, P. Maierhöfer, N. Moretti, S. Pozzorini, and F. Siegert, Eur. Phys. J. **C77** (2017), no. 3 145

[7] K. Hamilton, P. Nason, and G. Zanderighi, JHEP **1210** (2012) 155.

1.2 $W^{\pm}Z$ production at NNLO

The production of a pair of vector bosons is among the most relevant physics processes at LHC. Besides playing a central role in precision tests of the gauge structure of electroweak (EW) interactions and in studies of the mechanism of EW symmetry breaking, vector-boson pair production constitutes an irreducible background in most of the Higgs-boson measurements and in many searches for physics beyond the Standard Model (SM). The Tevatron collaborations have measured cross sections for vector-boson pair production at invariant masses larger than those probed at LEP2, setting limits on the corresponding anomalous couplings, and the LHC experiments are now continuing this research program and delivering results with increasing accuracy.

In the following we focus on $W^{\pm}Z$ production, which offers a valuable test of the triple gauge-boson couplings, and is an important SM background in many searches. We present next-to-next-to-leading order (NNLO) theoretical predictions [8] for this process at the LHC and compare them with the ATLAS and CMS data. The required tree-level and one-loop amplitudes were obtained with the OpenLoops [9] generator, which employs the Denner-Dittmaier algorithm for the numerical evaluation of one-loop integrals and implements a fast numerical recursion for the calculation of NLO scattering amplitudes within the SM. The two-loop amplitudes are taken from [10]. The required amplitudes are infrared divergent and are combined by using the q_T subtraction method [11] as implemented in the numerical program MATRIX.

In the following we present predictions for proton–proton collisions with $\sqrt{s} = 7, 8, 13$ and 14 TeV, setting the central scales μ_R and μ_F to $\mu_R = \mu_F = \mu_0 \equiv \frac{1}{2}(m_Z + m_W) = 85.7863\,\text{GeV}$. Scale uncertainties are obtained by independently varying μ_R and μ_F in the range $0.5\mu_0 \leq \mu_R, \mu_F \leq 2\mu_0$ with the constraint $0.5 \leq \mu_R/\mu_F \leq 2$. The cross section results are always summed over the electrical charges of the final-state W bosons.

We first present results for the ATLAS definition of the $W^{\pm}Z$ cross sections, reported in Tab. 1.2, where we compare with the 7 and 8 TeV ATLAS measurements of Ref. [12] and Ref. [13], respectively. The relative impact of radiative corrections ranges between 63% and 83% at NLO and between 8% and 11% at NNLO for the collider energies under consideration.

In contrast to ZZ and WW production, in the case of $W^{\pm}Z$ the $\mathcal{O}(\alpha_S^2)$ corrections are genuine NNLO corrections to the $q\bar{q}$ channel. Since the $W^{\pm}Z$ final state is electrically charged, the production process does not receive contributions from a loop-induced gluon-fusion channel. The rather large impact of radiative corrections is due to the existence of a *radiation zero* in the Born scattering amplitudes. More precisely, the partonic on-shell Born $W^{\pm}Z$ amplitude exhibits an *approximate* radiation zero, which is broken by real corrections starting from NLO, thereby leading to a large impact of radiative corrections.

The perturbative uncertainties, estimated via scale variations, drop from about $\pm 5\%$ at NLO to about $\pm 2\%$ at NNLO. In particular, the impact of NNLO corrections is larger than anticipated from NLO scale variations. The large size of QCD radiative corrections is due to an approximate radiation zero which is present in the on-shell amplitude at LO. Since all partonic channels are included at NNLO, and the NNLO corrections, although significant, are still much smaller than the NLO effects, we expect that scale variations should provide the correct order of magnitude of the uncertainty from yet uncalculated higher-order contributions beyond NNLO.

Comparing with the experimentally measured cross sections [12, 13], we find that the inclusion of NNLO corrections clearly improves the agreement between data and theory, in particular at 8 TeV, where the measurement is most precise. While the central NLO prediction is roughly 2σ away from the measured cross section at 8 TeV, the NNLO prediction is right on top of the data with fully overlapping uncertainty bands.

Next, we provide theory predictions for the $W^{\pm}Z$ cross sections as defined by CMS in Tab. 1.3, where

Tab. 1.2 – Total cross sections with ATLAS mass window $66\,\text{GeV} < m(Z) < 116\,\text{GeV}$ at LO, NLO and NNLO. The available ATLAS data from Refs. [12, 13] are also shown.

$\sqrt{s}$ [TeV]	σ_{LO} [pb]	σ_{NLO} [pb]	σ_{NNLO} [pb]	σ_{ATLAS} [pb]
7	$11.028(8)^{+0.5\%}_{-1.2\%}$	$17.93(1)^{+5.3\%}_{-4.1\%}$	$19.34(3)^{+1.6\%}_{-1.8\%}$	$19.0\,^{+1.4}_{-1.3}(\text{stat})^{+0.9}_{-0.9}(\text{syst})^{+0.4}_{-0.4}(\text{lumi})$
8	$13.261(9)^{+1.3\%}_{-2.1\%}$	$22.03(2)^{+5.1\%}_{-3.9\%}$	$23.92(3)^{+1.7\%}_{-1.8\%}$	$24.3\,^{+0.6}_{-0.6}(\text{stat})^{+0.6}_{-0.6}(\text{syst})^{+0.5}_{-0.5}(\text{lumi})^{+0.4}_{-0.4}(\text{theo})$
13	$24.79(2)\ ^{+4.2\%}_{-5.2\%}$	$44.67(3)^{+4.9\%}_{-3.9\%}$	$49.62(6)^{+2.2\%}_{-2.0\%}$	
14	$27.14(2)\ ^{+4.7\%}_{-5.7\%}$	$49.50(3)^{+4.9\%}_{-4.0\%}$	$55.10(7)^{+2.3\%}_{-2.0\%}$	

TAB. 1.3 – Total cross sections with CMS mass windows of $71\,\text{GeV} < m(Z) < 111\,\text{GeV}$ for 7 and 8 TeV, and $60\,\text{GeV} < m(Z) < 120\,\text{GeV}$ for 13 and 14 TeV, at LO, NLO and NNLO. The available CMS data from Refs. [14, 15] are also shown.

$\sqrt{s}$ [TeV]	σ_{LO} [pb]	σ_{NLO} [pb]	σ_{NNLO} [pb]	σ_{CMS} [pb]
7	$10.902(7)^{+0.5\%}_{-1.2\%}$	$17.72(1)^{+5.3\%}_{-4.1\%}$	$19.18(3)^{+1.7\%}_{-1.8\%}$	$20.76\,^{+1.32}_{-1.32}(\text{stat})^{+1.13}_{-1.13}(\text{syst})^{+0.46}_{-0.46}(\text{lumi})$
8	$13.115(9)^{+1.3\%}_{-2.1\%}$	$21.80(2)^{+5.1\%}_{-3.9\%}$	$23.68(3)^{+1.8\%}_{-1.8\%}$	$24.61\,^{+0.76}_{-0.76}(\text{stat})^{+1.13}_{-1.13}(\text{syst})^{+1.08}_{-1.08}(\text{lumi})$
13	$25.04(2)\ ^{+4.3\%}_{-5.3\%}$	$45.09(3)^{+4.9\%}_{-3.9\%}$	$49.98(6)^{+2.2\%}_{-2.0\%}$	$40.9\ ^{+3.4}_{-3.4}(\text{stat})^{+3.1}_{-3.3}(\text{syst})^{+1.3}_{-1.3}(\text{lumi})^{+0.4}_{-0.4}(\text{theo})$
14	$27.39(2)\ ^{+4.7\%}_{-5.7\%}$	$49.91(4)^{+4.9\%}_{-4.0\%}$	$55.60(7)^{+2.3\%}_{-2.0\%}$	

we also quote the results of the CMS measurements performed at 7 [14] and 8 [15] TeV . The slightly different definition of the Z-mass window as compared to ATLAS has only a very mild impact on the cross section. In particular, both the relative size of higher-order corrections and the bands obtained by scale variation are almost identical to the ones obtained with the ATLAS definition. Comparing with the measured cross sections, we again find excellent agreement between our NNLO predictions and the cross sections reported by CMS for $\sqrt{s} = 7$ and 8 TeV, where the inclusion of NNLO corrections clearly improves the agreement, in particular at 8 TeV. The measurement at 13 TeV undershoots the NNLO prediction, being consistent with it only at the level of about 2σ. However, at this early stage of LHC Run 2, the measurement still comes with quite large experimental uncertainties of both systematical and statistical nature, and the measured cross section might still be subject to a significant shift with respect to its central value, once statistics increases. Fig. 1.2 shows a summary plot where we compare NLO and NNLO predictions to all available LHC measurements of the total $W^{\pm}Z$ cross section.

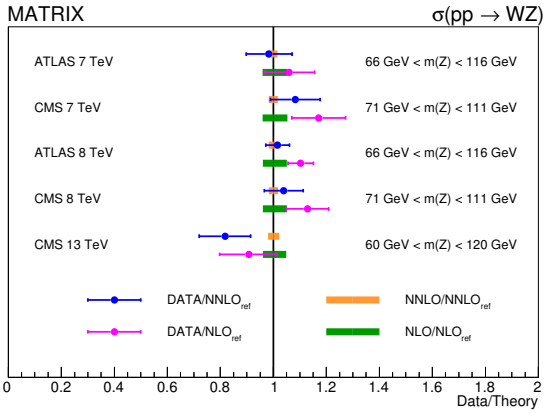

FIG. 1.2 – Summary plot for comparison of NLO and NNLO predictions with the available LHC measurements of the total $W^{\pm}Z$ cross section. Theory uncertainties are obtained through scale variations as described in the text.

[8] M. Grazzini, S. Kallweit, D. Rathlev, and M. Wiesemann, Phys. Lett. **B761** (2016) 179-183.

[9] F. Cascioli, P. Maierhofer, and S. Pozzorini, Phys. Rev. Lett. **108** (2012) 111601.

[10] T. Gehrmann and L. Tancredi, JHEP **02** (2012) 004.

[11] S. Catani and M. Grazzini, Phys. Rev. Lett. **98** (2007) 222002.

[12] G. Aad et al. [ATLAS collaboration], Eur. Phys. J. **C72** (2012) 2173.

[13] G. Aad et al. [ATLAS collaboration], Phys. Rev. **D93** (2016), no. 9 092004.

[14] CMS Collaboration, CMS-PAS-SMP-12-006.

[15] CMS Collaboration, CMS-PAS-SMP-16-002.

1.3 NNLO QCD corrections to jet production in deep inelastic scattering

Hadronic jets in deeply inelastic electron-proton collisions are produced by the scattering of a parton from the proton with the virtual gauge boson mediating the interaction. The HERA experiments have performed precision measurements of inclusive single jet production and di-jet production in the Breit frame, which provide important constraints on the strong coupling constant and on parton distributions in the proton. We recently completed the calculation of the NNLO QCD corrections to these processes [16].

The QCD corrections at this order involve three types of scattering amplitudes: the two-loop amplitudes for two-parton final states, the one-loop amplitudes for three-parton final states and the tree-level amplitudes for four-parton final states. The contribution from each partonic final state multiplicity contains infrared divergences from soft and collinear real radiation and from virtual particle loops; these infrared singularities cancel only once the different multiplicities are summed together for any infrared-safe final state definition. To implement the

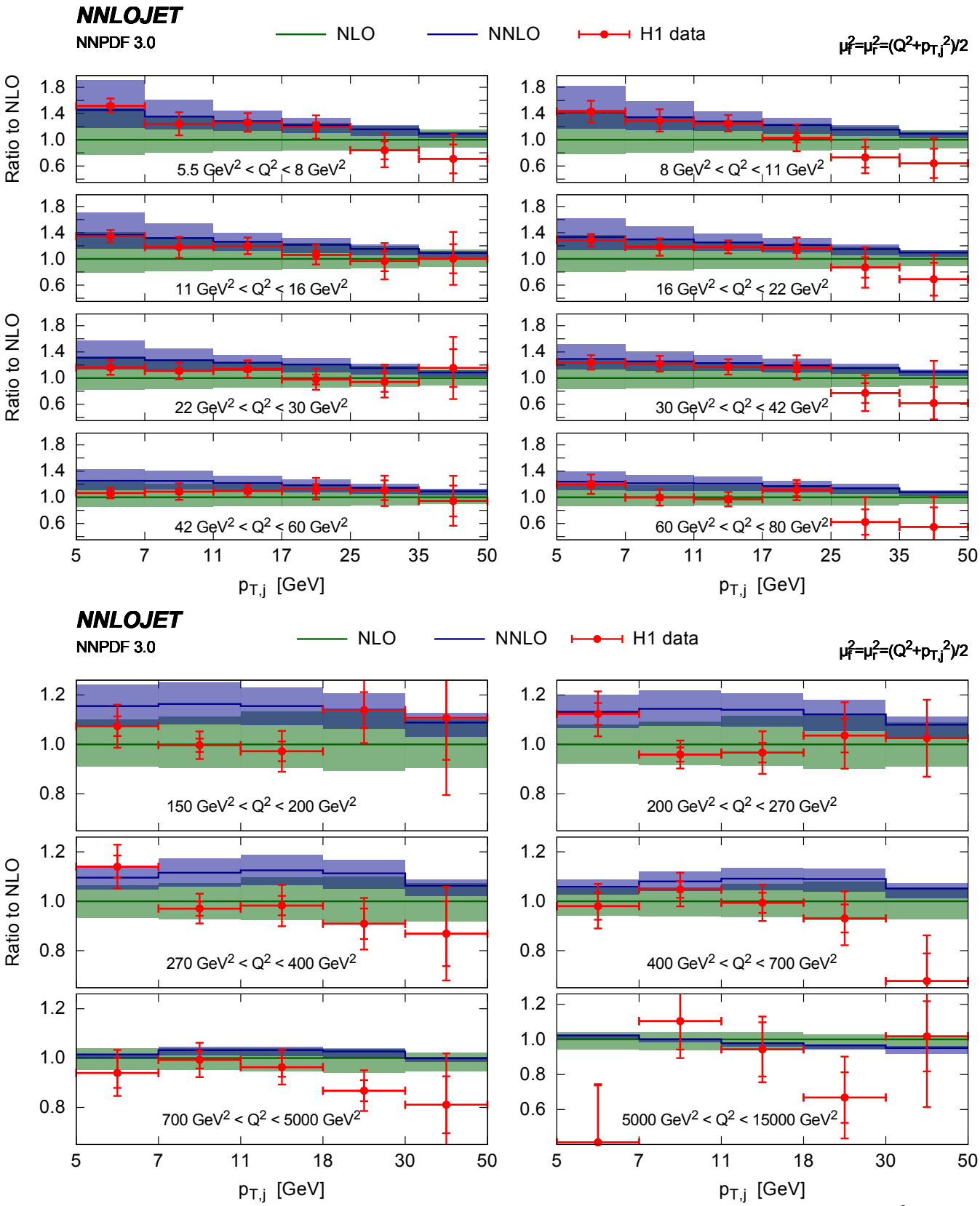

FIG. 1.3 – Inclusive jet production cross section as a function of the jet transverse momentum $p_{T,B}$ in bins of Q^2, compared to H1 data [22].

different contributions into a numerical program, a procedure for the extraction of all infrared singular configurations from each partonic multiplicity is needed. Our calculation is based on the antenna subtraction method [17], which constructs the subtraction terms for the real radiation processes out of antenna functions that encapsulate all color-ordered unresolved parton emission in between a pair of hard radiator partons, multiplied with reduced matrix elements of lower partonic multiplicity. By factorizing the final state phase space accordingly, it is possible to analytically integrate the antenna functions to make their infrared pole structure explicit, such that the integrated subtraction terms can be combined with the virtual corrections to yield a finite result. The combination of real radiation contributions and unintegrated antenna subtraction terms is numerically finite in all infrared limits, such that all parton-level contributions to two-jet final states at NNLO can be implemented into a numerical program (parton-level event generator). This program can then incorporate the jet algorithm used in the experimental measurement as well as any type of event selection cuts. A substantial part of the infrastructure of our program is common to other NNLO calculations of jet production observables within the antenna subtraction method [18–21], which are all part of a newly developed code named NNLOJET.

Inclusive jet production in deep inelastic scattering has been widely studied by the H1 and ZEUS experiments at DESY HERA. The jet measurements are performed in the Breit frame, where the transverse momentum requirement on the jet ensures the existence of a partonic recoil, even if only a single jet is reconstructed in the kinematical acceptance.

Figure 1.3 compares our NNLO predictions to the H1 data. We observe that the NNLO corrections are very substantial at low-Q^2 and low-p_T^B, with an up to 60% enhancement with respect to NLO. These large corrections are within the NLO uncertainty band (close to the upper edge), and result in a residual theory uncertainty of 20% even at NNLO. Especially at low Q^2, the shape and normalization of the theory prediction changes significantly going from NLO to NNLO, and results in a considerably improved theoretical description of the data, as statistically quantified in the experimental H1 study [22]. With increasing Q^2, the size of the NNLO corrections decreases, accompanied with very small residual theoretical uncertainties (decreasing from 10% at $Q^2 = 150$ GeV^2 to 2% at 5000 GeV^2). In this region, the combination of precision data with the newly derived NNLO corrections has clearly the potential to provide important new constraints for precision QCD studies.

[16] J. Currie, T. Gehrmann, and J. Niehues, Phys. Rev. Lett. **117** (2016), no. 4 042001.

[17] A. Gehrmann-De Ridder, T. Gehrmann, and E. W. N. Glover, JHEP **09** (2005) 056.

[18] A. Gehrmann-De Ridder, T. Gehrmann, E. W. N. Glover, A. Huss, and T. A. Morgan, Phys. Rev. Lett. **117** (2016), no. 2 022001.

[19] A. Gehrmann-De Ridder, T. Gehrmann, E. W. N. Glover, A. Huss, and T. A. Morgan, JHEP **07** (2016) 133.

[20] X. Chen, J. Cruz-Martinez, T. Gehrmann, E. W. N. Glover, and M. Jaquier, JHEP **10** (2016) 066.

[21] A. Gehrmann-De Ridder, T. Gehrmann, E. W. N. Glover, A. Huss, and T. A. Morgan, JHEP **11** (2016) 094.

[22] V. Andreev *et al.* [H1 collab.], Eur. Phys. J. **C77** (2017), no. 4 215.

1.4 Charged Lepton-Flavor Violation

While it is by now well established that lepton flavor is not conserved in the neutral sector (neutrinos), so far there is no experimental evidence for lepton-flavor violation in the charged sector. Within the SM such processes have a branching ratio $\mathcal{B}$ that is much too small to be detected in any foreseeable experiment. Hence, any experimental signature of charged lepton-flavor violation (cLFV) is a clear signal for physics beyond the SM.

At the Paul Scherrer Institute (PSI) there are experiments ongoing and planned to improve the sensitivity in cLFV searches in two golden channels, namely $\mu \to e\gamma$ by MEG [23] and $\mu \to 3e$ by Mu3e [24]. One of the many issues that these experiments are faced with is the irreducible background of SM processes with very low-energy neutrinos. In the case of Mu3e, the SM process $\mu^+ \to e^+(e^+e^-)\nu_e\bar{\nu}_\mu$ cannot be distinguished from the signal if the invisible energy $\not{E} \equiv E(\nu_e) + E(\bar{\nu}_\mu)$ tends to zero. Hence it is important to have reliable predictions of this SM process. In Ref. [25] we have presented a fully differential computation at next-to-leading order in the electromagnetic coupling α. As an illustration, in the left panel of Fig. 1.4 we show the $\not{E}$ spectrum, taking into account cuts on the final state electrons that mimic the Mu3e detector. The corrections turn out to be negative and amount to about -15% for $\not{E} \lesssim 3$ MeV. Thus, there are considerably fewer background events than anticipated from a leading-order computation.

Apart from studying background events for the cLFV experiments at PSI, we have also analyzed [26] the complementarity of these experiments, using an effective-theory approach with dimension 6 operators to describe physics beyond the SM. As an example, in the right panel of Figure 1.4 we compare the constraining power of MEG, Mu3e and future electron conversion experiments (e.g. COMET) on C_L^D and C_{ee}^{VRR}, the Wilson coefficients of the

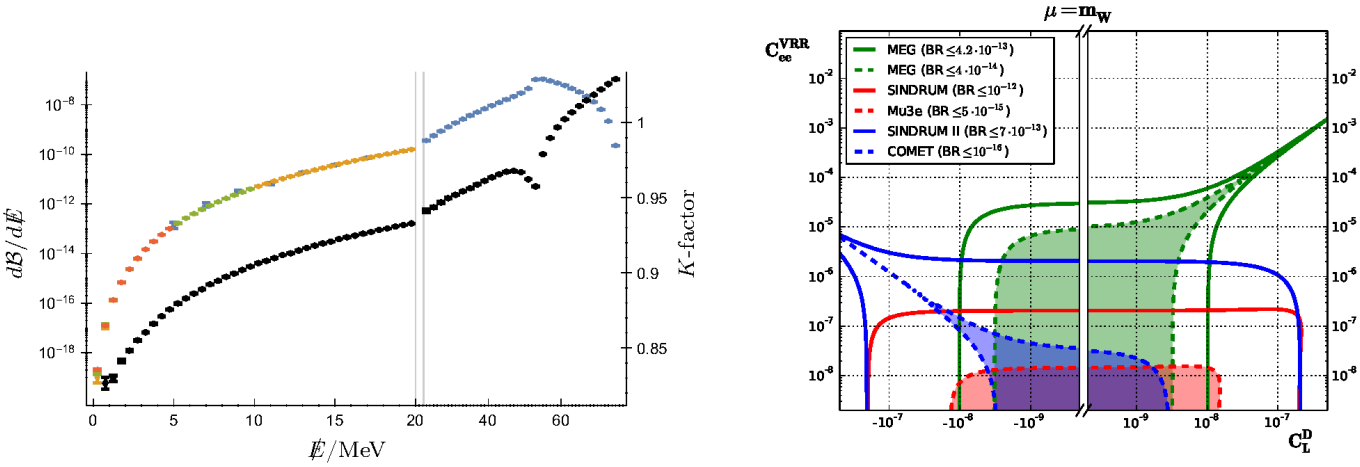

FIG. 1.4 – Left panel: invisible energy spectrum of the process $\mu^+ \to e^+(e^+e^-)\nu_e\bar{\nu}_\mu$ at NLO, taking into account the geometry of the future Mu3e detector. Right panel: Comparison of sensitivity on the Wilson coefficients C_L^D and C_{ee}^{VRR} from various cLFV experiments.

dipole operator and a four-fermion operator, respectively. The main feature of this example extends to many other Wilson coefficients: the various cLFV experiments complement each other in that they are most sensitive to different scenarios of beyond the SM physics.

[23] A. M. Baldini *et al.* [MEG Collaboration], Eur. Phys. J. **C76** (2016), no. 8 434

[24] A. Blondel *et al.*, arXiv:1301.6113.

[25] G. M. Pruna, A. Signer, and Y. Ulrich, Phys. Lett. **B765** (2017) 280-284.

[26] A. Crivellin, S. Davidson, G. M. Pruna, and A. Signer, arXiv:1702.0302.

1.5 Flavor physics within and beyond the SM

In the last few years the indirect search for physics beyond the Standard Model (SM) in the flavor sector has become particularly interesting in view of a series of experimental "anomalies" in B decays. Although their statistical significance is still limited, these anomalies indicate possible violations of Lepton Flavor Universality (LFU) both in charged- and in neutral-current semi-leptonic B decays. Motivated by these observations, we have analyzed various aspects of LFU, both from a pure phenomenological perspective and in the context of motivated extensions of the SM. Our research has been articulated along three main directions.

- *SM predictions for LFU tests.*
  In Ref. [27] we have have presented the first reliable SM predictions of two of the key observables used to test LFU in neutral-current B decays, namely the ratios $R_K = \Gamma[B \to K\mu^+\mu^-]/\Gamma[B \to Ke^+e^-]$ and $R_{K^*} = \Gamma[B \to K^*\mu^+\mu^-]/\Gamma[B \to K^*e^+e^-]$. We have shown that, within the SM, these ratios differ by 1 by at most $\pm 1\%$ (for $m_{\ell\ell} > 1$ GeV), offering a very clean probe of physics beyond the Standard Model.

- *New physics analyses based on Effective Theory approaches and simplified models.*
  In 2015 our group has demonstrated, for the first time, the possibility of a coherent explanation of both charged- and neutral-current LFU anomalies, namely i) the breaking of τ–μ universality in $B \to D^{(*)}\ell\nu$ decays; ii) the breaking of μ–e universality in $B \to K\ell^+\ell^-$ decays. Such combination is highly non-trivial due to severe constraints from other observables, both at low- and high-energies. Continuing along this research direction, we have further investigated such bounds [28–31] using both Effective Field Theory (EFT) approaches and simplified dynamical models. The result of our analysis is that a combined explanation of these effects require some moderate tuning (in the EFT parameter space) but is still possible. A general prediction resulting from a combined explanation of these anomalies is the expectation of sizeable deviations from the SM in $pp \to X + \tau^+\tau^-$ (for large $m_{\tau\tau}$) within the reach of future ATLAS and CMS searches.

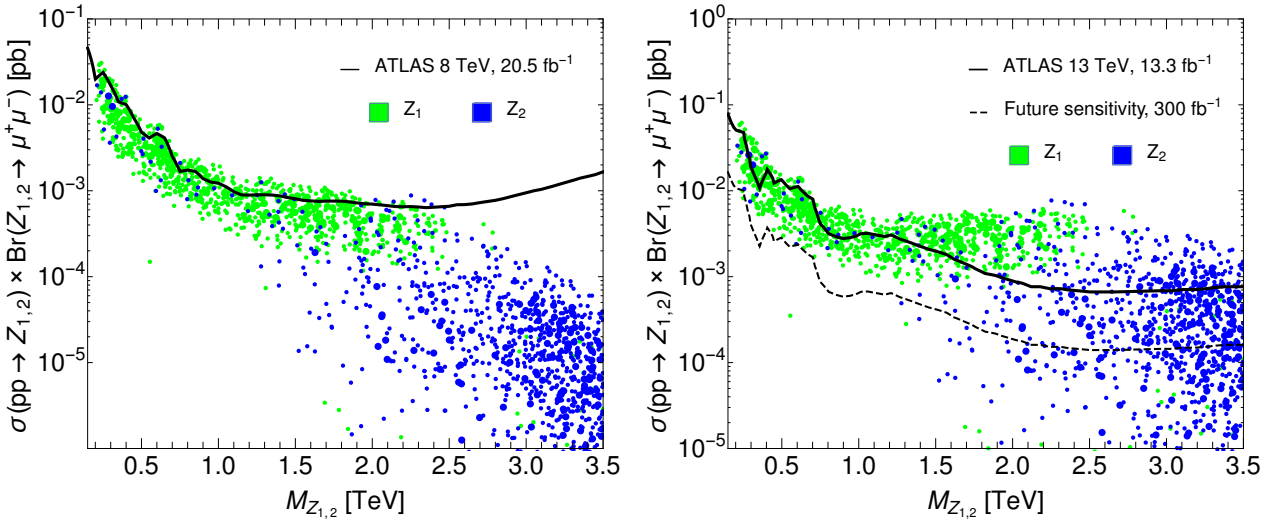

FIG. 1.5 – Predictions for the LHC signals ($\sigma \times \mathcal{B}$) at 8 TeV (left) and 13 TeV (right) for $\mu^+\mu^-$ resonance searches for the leptophilic Z_1 (green) and the leptophobic Z_2 (blue) states predicted in the model of Ref. [32], based on dynamical Yukawa couplings and addressing B-physics anomalies. Present limits are shown with black line, and future-projected with dashed line.

- *UV completions.*
  The last research line is the attempt to find motivated UV completions for the simplified models addressing these anomalies. In 2016 we identified two interesting examples of UV completions: i) a model based on a gauged non-Abelian flavor symmetry (motivated by a dynamical explanation of quark and lepton Yukawa couplings) [32]; ii) a class of models based on vector-like confinement (motivated by a solution to the hierarchy problem) [33]. In both cases we have exploited the signatures of such models at high-p_T, in view of future searches by ATLAS and CMS (see e.g. Fig. 1.5).

[27] M. Bordone, G. Isidori, and A. Pattori, Eur. Phys. J. **C76** (2016), no. 8 440.

[28] F. Feruglio, P. Paradisi, and A. Pattori, Phys. Rev. Lett. **118** (2017), no. 1 011801.

[29]] D. A. Faroughy, A. Greljo, and J. F. Kamenik, Phys. Lett. **B764** (2017) 126-134.

[30] C. Biggio, M. Bordone, L. Di Luzio, and G. Ridolfi, JHEP **10** (2016) 002.

[31] M. Bordone, G. Isidori, and S. Trifinopoulos, arXiv:1702.0723.

[32] A. Crivellin, J. Fuentes-Martin, A. Greljo, and G. Isidori, Phys. Lett. B766 (2017) 77-85.

[33] D. Buttazzo, A. Greljo, G. Isidori, and D. Marzocca, JHEP 08 (2016) 035.

2 Astrophysics and General Relativity

Y. Boetzel, R. Bondarescu, P. Denzel, M. Haney, Ph. Jetzer, R. Küng, L. Philippoz, P. Saha, A. Schärer

For describing most of astrophysical phenomena, Newtonian gravity is adequate, but for situations involving very strong gravitational fields, or cosmological distances, or the effect of gravity on light, or just extremely precise measurements, relativistic gravity is needed. After more than hundred years, Einsteinian gravity continues to pass all tests thrown at it, and meanwhile reveals new manifestations such as gravitational waves (GW), whose detection has been announced on 11 February 2016 [1]. Indeed, on 14 September 2015 the two LIGO detectors simultaneously observed a transient gravitational wave signal, which has been interpreted as due to the merger of two black holes with masses of about 36 $M_\odot$ and 29 $M_\odot$, respectively. A further event has been detected on 26 December 2015 and announced on 15 June 2016 [2]. Exploring various aspects of general relativity is the area of our research.

[1] B.P. Abbott *et al.*, LIGO and Virgo Collaborations, Phys. Rev. Lett. 116, 061102, 2016.

[2] B.P. Abbott *et al.*, LIGO and Virgo Collaborations, Phys. Rev. Lett. 116, 061102241103, 2016.

2.1 Gravitational Waves

2.1.1 LISA Pathfinder

Ph. Jetzer is member of the LISA Pathfinder (LPF) science working team and of the LISA consortium board. LISA Pathfinder is a European Space Agency (ESA) mission launched on 3 December 2015 from the European Spaceport in Kourou, French Guiana with a Vega rocket. Following six apogee-raising manoeuvres, the spacecraft reached its final science orbit around the first Sun-Earth Lagrange point L1, 1.5 million kilometers from Earth, on 22 January 2016.

The goal of LPF is to place two test masses in a nearly perfect gravitational free-fall, and control and measure their relative motion with unprecedented accuracy, at the level required for a future space-based gravitational wave (GW) observatory, such as LISA. This requirement is achieved through innovative technologies comprising inertial sensors, an optical metrology system, a drag-free control system and a micro-Newton thruster system.

The LISA Technology Package (LTP) is the main payload on board of LPF, which was developed jointly by several European institutes and industries including ones from Switzerland. It contains two identical cubic test masses of 1.9 kg and 46 mm in size made of gold-platinum. Each is suspended in its own vacuum vessel with capacitive sensors to monitor the relative position of the test masses with respect to the satellite, laser interferometry to determine the relative positions and attitudes of the two test masses, and the drag-free control system to adjust the relative alignment of the satellite and test masses through a mixture of micro-Newton (cold gas) thrusters and capacitive actuation. The cubes serve both as mirrors for the laser interferometer and as inertial references for the drag-free control system of the spacecraft, exactly as will be used for LISA.

On 22 February 2016 the two cubes housed in the LTP of LPF were left to move under the effect of gravity alone, and one day later the spacecraft's main operating mode was switched on for the first time. The LPF scientific mission started officially on 1 March. Based on only 55 days of science operations LPF could already demonstrate that the key technologies needed to build a space-based GW observatory are properly working. It turned out that the two test masses are freely falling under the influence of gravity alone, unperturbed by other external forces, to a precision more than five times better than originally required. The two cubes are almost motionless with respect to each other, with a relative residual acceleration lower than 10^{-14} g, with g being Earth's gravitational acceleration. For the remaining forces acting on the test masses, three main sources of noise, depending on the frequency, were identified (see Fig. 2.1).

At the lowest frequencies accessible to the experiment, below 1 mHz (on the left of the figure), one measures a small centrifugal force acting on the cubes, which is caused by a combination of the shape of LPF's orbit and the effect of the noise in the signal of the startrackers used to orient it. The contribution of the centrifugal force to the relative acceleration of the two test masses has been subtracted. Further investigations are under way to better identify the source of the residual noise after subtraction.

At frequencies in the range 1-60 mHz (at the centre of the figure),the control over the test masses is limited by gas molecules bouncing off the cubes: a small number of them remain in the surrounding vacuum. This effect was seen to be reducing as more molecules were vented into space, and it is expected to lower further in time.

At higher frequencies, between 60 mHz and 1 Hz (on the right of the figure),LPF's precision is limited only by the sensing noise of the optical metrology system used to monitor the position and orientation of the test masses. Nicely, the performance of this system has already surpassed the level of precision required by a future gravitational-wave observatory

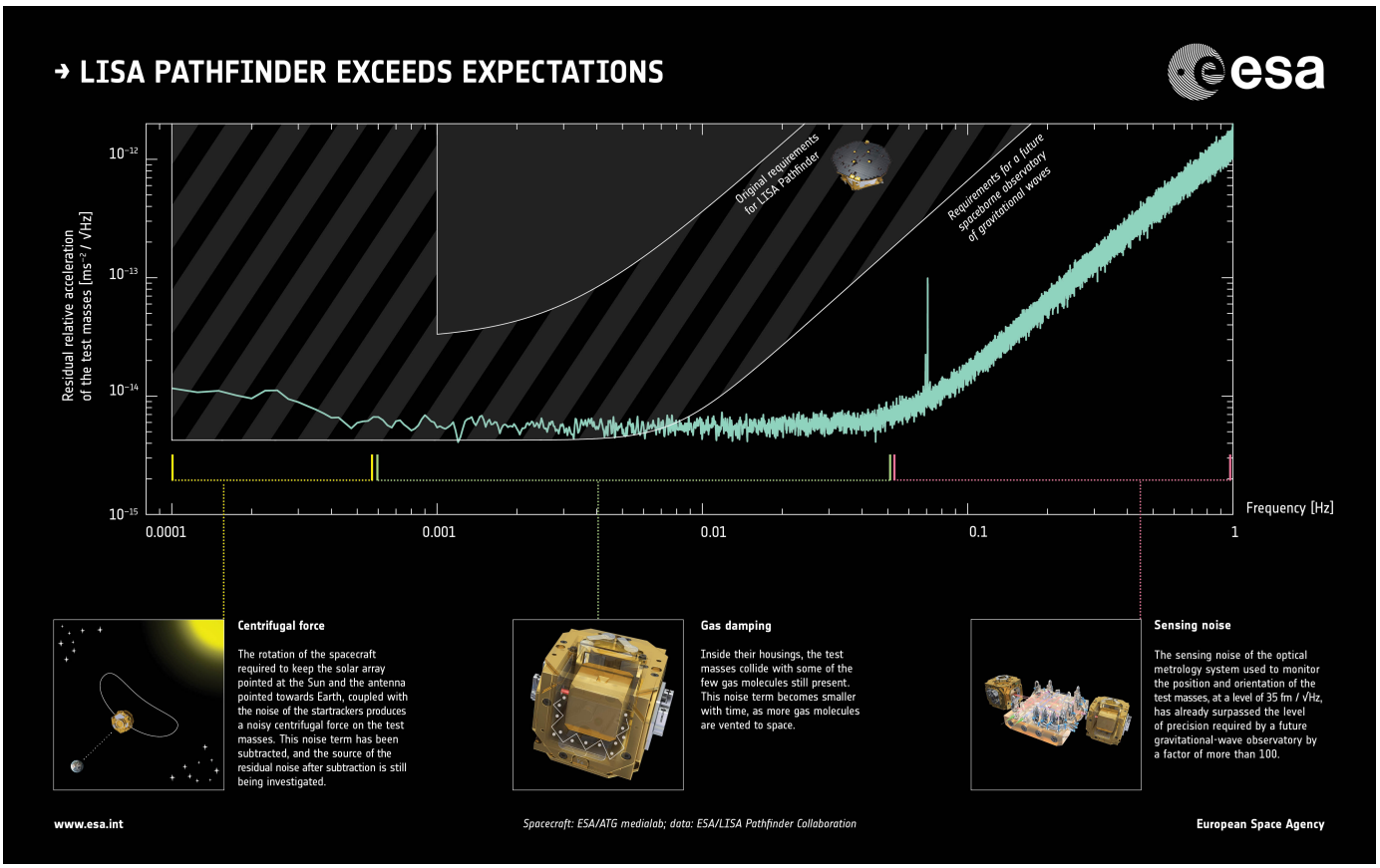

FIG. 2.1 – ESA/ATG medialab; data: ESA/LISA Pathfinder collaboration

by a factor of more than 100. These findings were announced on 7 June 2016 in a press conference by ESA. In the meantime the LPF performances improved further.

The demonstration of the LPF's key technologies opens the door to the development of LISA, which will be capable of detecting gravitational waves emanating from a wide range of objects in the Universe.

In November 2013 ESA has selected *The Gravitational Universe* as the science theme to be explored by ESA's Large class mission L3. Following the success of LPF, the LISA consortium had to submit to ESA a mission proposal by mid January 2017.

2.1.2 Gravitational waves and LISA

The scope of LISA is to detect and study low-frequency GW from about 0.1 mHz to 1 Hz, and thus to complement ground-based gravitational observatories. LISA opens new possibilities for astrophysical studies by allowing, for instance, to detect supermassive black holes (typically of $10^6 - 10^7\ M_\odot$) merging at cosmological distances. Mergers of a supermassive black hole with another compact object (such as another black hole or a neutron star) produce a very clean GW signal which LISA will be able to measure with high precision. Alternative gravity theories influence the dynamics of such mergers and hence LISA is expected either to directly see the imprints of certain alternative theories or to put severe constraints on them. Another class of objects, which will be observed by LISA, are ultra-compact binaries, in particular of white dwarfs in our Galaxy. They are important sources of gravitational waves in the mHz frequency range. Moreover, it will be possible to detect or put strong constraints on the primordial GW background, which is just, as the cosmic microwave background, a leftover from the Big Bang.

Yannick Bötzel is studying gravitational waves from compact binaries in eccentric inspiralling orbits. In particular he could already provide an elegant analytic solution to the 3PN-accurate Kepler equation, associated with the 3PN-accurate generalized quasi-Keplerian parameterization for compact binaries in eccentric orbits. This is an important step for getting accurate GW templates from compact binaries in inspiralling eccentric orbits.

The detection of gravitational waves and the corresponding determination of polarization modes is a powerful tool to discriminate between general relativity and alternative theories of gravity such as $f(R)$ theories. Besides the usual two transverse-traceless tensor modes present in general relativity, there are indeed up to two

additional scalar ones: a massive longitudinal mode and a massless transverse mode (the so-called breathing mode), as well as two vector modes. Lionel Philippoz is addressing the question of whether a given LISA configuration can provide a sufficient sensitivity to those additional polarization modes, and how to extract this information from a signal produced by a stochastic GW background.

Maria Haney joined our group as a post-doc in January 2017. As a member of the LIGO Scientific Collaboration (LSC) since 2014, she is directly involved in the development of tools and pipelines for the analysis of LIGO data.

In March 2017, Philippe Jetzer, Maria Haney and Yannick Bötzel joined the GEO600 collaboration and were subsequently approved for LSC membership, establishing the first LSC group in Switzerland. Our proposed contribution to LSC research includes template waveform development for the gravitational-wave search and parameter estimation efforts, as well as tests of general relativity with gravitational-wave data from binary black hole mergers.

2.1.3 XI International LISA Symposium

The XI International LISA Symposium took place at the University of Zürich (Irchel Campus) from 5 to 9 September 2016 [3]. Given these spectacular developments in the field of GW, it came as no surprise that the interest in the community for the LISA Symposium increased and indeed about 250 participants attended the meeting, which was in all aspects very successful. The format was such as to have only plenary talks, in total some 68 talks. Almost 100 posters were presented. The main topics of the talks covered the first results from LISA Pathfinder, the further development of LISA and an overview of the results obtained so far by the ground based gravitational wave detectors (LIGO and VIRGO) as well as Pulsar Timing Arrays. Several talks covered different aspects of astrophysics and cosmology related to gravitational waves. One talk was devoted on the preliminary results of the satellite Microscope, whose aim is to test the equivalence principle in general relativity. On one afternoon there was a joint eLISA and L3ST (a NASA committee) consortium meeting. There were also programmatic talks given by Prof. A. Gimenez (Science Director of ESA) and by Dr. Paul Hertz (Astrophysics Division director of NASA). It is planned to publish the proceedings soon.

[3] http://www.physik.uzh.ch/events/lisa2016/

2.2 Gravitational Lensing

That gravitational lensing — specifically that light is affected by both space and time parts of the metric, unlike Newtonian bodies, which are affected only by the time part — is too well known to need elaborating here. Nowadays, however, gravitational lensing is valued, more than as a test of general relativity, as a way of detecting matter that would be otherwise invisible.

On the scale of galaxies and clusters of galaxies, gravitational lensing is very important as a probe of dark matter. Extracting the information on mass distributions, however, requires solving a non-trivial inverse problem. R. Küng, P. Denzel and P. Saha, together with external collaborators, have worked on the problem of mapping a mass distribution from lensing observables. One part of this work is the development of an improved method for modelling galaxy lenses and furthermore, a theoretical formulation and computational interface to enable modelling in a citizen-science context. The other aspect is mapping and interpreting dark-matter structure in strong-lensing galaxy-clusters

2.3 Space clocks and relativity

Together with S. Lecomte from CSEM in Neuchâtel, M. Rothacher from ETH Zürich, Q. Wang and P. Rochat from Spectratime in Neuchâtel and some of their collaborators, we conducted a study on behalf of the Swiss Space Office (SSO) for a satellite mission called E-GRIP (Einstein Gravitational Red-shIft Probe) to test general relativity using an on board hydrogen maser. The clock would be sensitive to Earth's gravitational redshift to the level of 2×10^{-6}, as well as to the space-curvature around Earth and the frame-dragging by Earth's spin. In addition, E-GRIP would provide a wealth of science for time and frequency metrology- and geodesy. After delivering a first report in December 2015, we were requested to study the proposal further. The final report (Phase 0 Study Report) was then presented on 20 June 2016 at SSO.

Andreas Schärer worked on how one could measure planetary spin with satellites and to estimate the frame-dragging in spacecraft timing signals. As examples he analysed the Juno mission, a satellite in a highly eccentric orbit around Jupiter, and the Cassini mission around Saturn.

2.4 Scalar-Tensor Theories

Scalar-tensor theories are a promising class of alternative theories of gravitation. They contain, in addition to the metric tensor of GR, a scalar degree of freedom. Upcoming precision experiments might detect violations of general relativity, which could be explained by such theories. Together with Manuel Hohmann from the University of Tartu, Estonia, Andreas Schärer studies multi-scalar-tensor theories. These theories are a further generalization which contain multiple such scalar fields.

3 GERDA: Neutrinoless Double Beta Decay in ^{76}Ge

Laura Baudis, Andreas James, Roman Hiller, Alexander Kish,
Michael Miloradovic, Rizalina Mingazheva, Chloe Ransom

in collaboration with: INFN Laboratori Nazionali del Gran Sasso LNGS, Jagellonian University Cracow, Institut für Kern- und Teilchenphysik Technische Universität Dresden, Joint Institute for Nuclear Research Dubna, Institute for Reference Materials and Measurements Geel, Max Planck Institut für Kernphysik Heidelberg, Universitá di Milano Bicocca e INFN Milano, Institute for Nuclear Research of the Russian Academy of Sciences, Institute for Theoretical and Experimental Physics Moscow, Russian Research Center Kurchatov Institute, Max-Planck-Institut für Physik München, Dipartimento di Fisica dell Universitá di Padova e INFN, Physikalisches Institut Eberhard Karls Universität Tübingen.

(GERDA Collaboration)

All results from neutrino oscillation experiments indicate that neutrinos are massive [1]. Such experiments are insensitive to the absolute mass scale of neutrinos, but this can instead be extracted from kinematic studies of beta decays, and from the neutrinoless double beta ($0\nu\beta\beta$) decay. Moreover, the observation of this decay would prove that the neutrino is a Majorana fermion and that lepton number is violated in nature.

12 The most stringent upper limit on the half-life of this decay for ^{76}Ge comes from the Germanium Detector Array (GERDA) [2], as detailed below. Existing and future neutrinoless double beta decay experiments should be able to probe the so-called degenerate and inverted mass hierarchy regions, testing the effective Majorana neutrino mass down to ∼10-50 meV (see [3] for a recent review, including future projects).

[1] M. Gonzalez-Garcia, Phys. Dark Univ **4** (2014) 1-5.

[2] M. Agostini *et al.*,Nature **544** (2017) 47-52.

[3] R. Henning, Rev. Phys. **1** (2016) 29-35.

3.1 The GERDA Experiment

The GERDA experiment aims to detect $0\nu\beta\beta$ decay of ^{76}Ge, and is currently acquiring science data at Laboratori Nazionali del Gran Sasso (LNGS). GERDA uses high-purity germanium diodes, enriched in ^{76}Ge. The diodes, arranged in seven strings, act simultaneously as the detector and source material and are submerged in liquid argon (LAr). A water Cherenkov veto surrounds the LAr cryostat, to reject interactions from cosmic muons. Filled with ultra-pure water, the water tank also provides shielding against external radiation.

In the first stage of the experiment (Phase I), which lasted from 2011 to 2013, ten detectors with an active mass of 15 kg were used, resulting in a total exposure of 21.6 kg·y. A tenfold lower background than in previous experiments was obtained, with 1×10^{-2} events/(keV·kg·y) at the Q-value of the decay ($Q_{\beta\beta}$). No $0\nu\beta\beta$-decay signal was observed in Phase I, and a lower limit of $T_{1/2}^{0\nu\beta\beta} > 2.1 \times 10^{25}$ y at 90% C.L. for the half-life of the decay was derived [4].

During the experiment's upgrade (Phase II) in the spring of 2015, new, enriched Broad Energy Germanium (BEGe) detectors were built, extensively tested and mounted into the LAr cryostat [5], and an active LAr veto system was installed at LNGS. The aim of this stage is to reach a sensitivity of $T_{1/2}^{0\nu\beta\beta} = O(10^{26})$y with a background index of 10^{-3} events/(keV·kg·y) after an exposure of ∼100 kg·y. By December 2015, all 40 detectors were installed and characterised, and the Phase II data taking of GERDA started. Our group has contributed to the tests of the BEGe detectors, to the liquid argon veto [6], to the upgraded calibration system hardware and software and to new, low-neutron-emission ^{228}Th sources.

The LAr veto, shown in Fig. 3.1, left, is equipped with photomultiplier tubes and silicon photomultipliers (SiPMs) to detect the scintillation light induced by interactions in the argon, triggered by an event in a germanium detector. All channels are working and the LAr veto's performance is stable in time. Figure 3.1, right, shows the acquired background energy spectrum, including the effect of the argon veto.

The first five months of GERDA Phase II data were unblinded in June 2016. In the analysis, the Phase I data were considered as well, including a data period that was not used in the first publication. Hence the total exposure is 34.4 kg·y. The background level in the BeGe detectors in Phase II is $0.7^{+1.1}_{-0.5} \times 10^{-3}$ events/(keV·kg·y), meaning that the background goal of Phase II has been reached. There was no signal for $0\nu\beta\beta$ decay in the combined data set, and we thus place an improved lower limit on the half-life of $T_{1/2}^{0\nu\beta\beta} > 5.2 \times 10^{25}$ y (90% C.L.) [7].

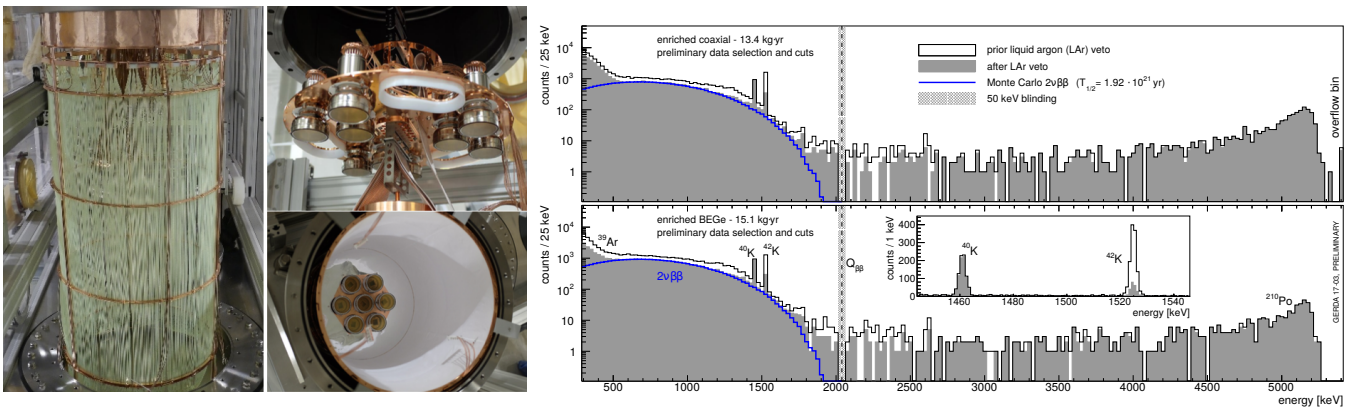

FIG. 3.1 – (Left): Picture of the liquid argon veto system: fibre curtain with SiPM readout at the top, and top and bottom arrangement of PMTs with the coated, wavelength shifting reflector foil. (Right): Energy spectra of Phase II data sets before (open histogram) and after the argon veto (filled histogram). The expected $2\nu\beta\beta$ spectrum (blue line) is also shown, as well as the sum spectrum around the two potassium lines (^{40}K peak at 1461 keV, and the ^{42}K peak at 1525 keV) in the insert.

GERDA-Upgrade is a step towards a 200 kg stage, to be constructed at LNGS by the new collaboration, LEGEND, (recently formed by GERDA, MAJORANA and other groups), which itself is the precursor of a future, ton-scale ^{76}Ge experiment. The aimed sensitivities are $T_{1/2}^{0\nu\beta\beta} > 10^{26}$ y and $T_{1/2}^{0\nu\beta\beta} > 10^{27}$ y for GERDA-Upgrade and the 200 kg stage, respectively.

In the following we detail our recent contributions to GERDA.

[4] Gerda Collaboration, M. Agostini *et al.*, Phys. Rev. Lett. **111** (2013) 122503.

[5] M. Agostini *et al.*, Eur. Phys. J. C75 **2** (2015) 39.

[6] L. Baudis, G. Benato, R. Dressler, F. Piastra, I. Usoltsev, M. Walter, JINST **10.09** (2015) P09009.

[7] M. Agostini *et al.*, Nature **544** (2017) 47-52.

3.2 Energy calibration

The GERDA experiment is calibrated by temporarily exposing the germanium detectors to ^{228}Th sources and evaluating the position of known emission lines in the recorded energy spectrum. Our group is part of the calibration team which performs the weekly calibrations, and we are responsible for analysing and evaluating the calibration data.

For the main result of GERDA Phase II, the $0\nu\beta\beta$-search, we determined the energy resolution for BEGe-type detectors and coaxial-type detectors to be 3.0±0.2 keV and 4.0±0.2 keV, respectively, with an estimated systematic uncertainty on the energy scale of 0.2 keV [8]. The combined data for evaluating the resolution is shown in Fig. 3.2. The evaluation of the full systematic uncertainties is an ongoing effort.

Furthermore, we maintain and develop the analysis framework used for calibration. Currently, we are optimising and parallelising it to meet the rising performance demands of the ever increasing amount of data and detector channels. In addition, we aim to improve the user interface and algorithm to more easily distribute calibration analysis work and monitoring, especially with regard to the upcoming, larger LEGEND experiment. We maintain the hardware of the existing calibration systems, and we produced the currently employed calibration sources [9]. For the upgraded phase of GERDA, we will produce another batch of 3-4 ^{228}Th sources with a low neutron-emission rate as a replacement for the existing ones, given the short ^{228}Th half-life of 1.9 yr.

[8] M. Agostini *et al.*, Nature **544** (2017) 47-52.

[9] L. Baudis, G. Benato, P. Carconi, C. M. Cattadori, P. De Felice, K. Eberhardt, R. Eichler, A. Petrucci, M. Tarka, M. Walter, JINST **10.12** (2015) P12005.

3.3 Pulse shape simulations and background model

Understanding and modelling the background of GERDA is key to the interpretion of physics data. We participate in the background modelling effort, based on Monte Carlo simulations of decays of radioactive isotopes in detector materials, using the measured activity levels [10]. Currently, these simulations are limited to the energy deposition inside the germanium detectors, and do not include the signal generation in the Ge diodes. Consequently, the impact of the detector response and signal processing, as well as the pulse shape properties required for pulse shape discrimination (PSD), cannot be accurately accounted for. We are implementing a code for pulse shape simulation, based on the ADL libraries [11], into the common simulation framework of the GERDA and MAJORANA collaborations, MaGe [12]. We have performed

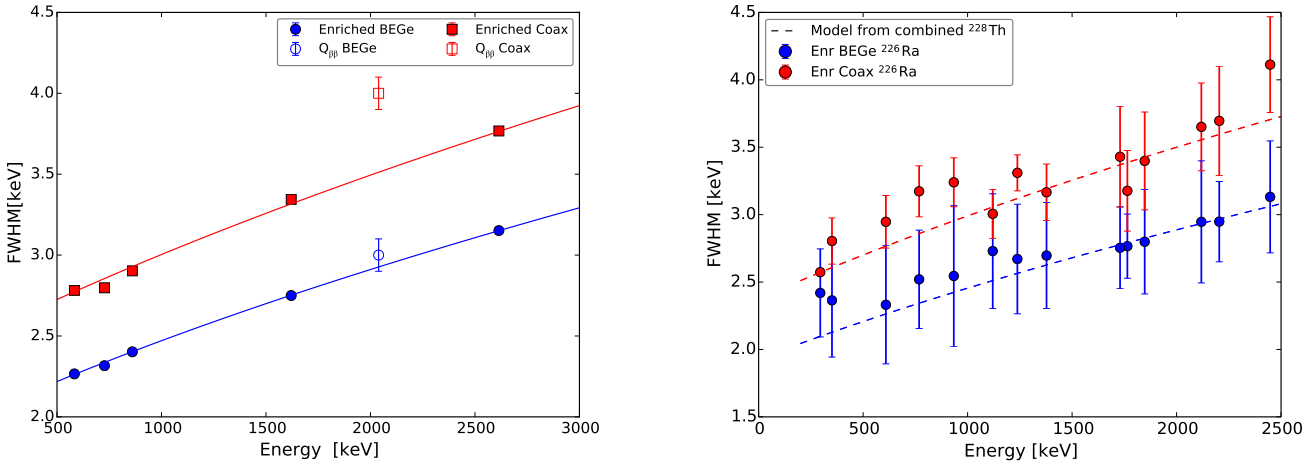

FIG. 3.2 – (Left): The energy resolution, determined from the combined calibration data set with ^{228}Th sources, for BEGe (blue) and coaxial (red) type detectors, respectively, as a function of energy. To explain the energy resolution of the physics data (hollow markers) at $Q_{\beta\beta}$, additional, systematic effects have to be taken into account. (Right): The resolution for BEGe (blue) and coaxial (red) detectors, obtained from calibration data with a ^{226}Ra source. The aim was to cross check the ^{228}Th calibration results, and extend the range to lower energies. The dashed lines represent the model obtained from ^{228}Th calibration data. Here the error bars reflect the spread in resolution over individual detectors.

simulations of the electric field and weighting potential, required for calculating the induced charge on the read-out electrode for BEGe detectors (examples are shown in Fig. 3.3, left and centre). Together with our interface to extract the detector geometry of individual germanium detectors and energy deposits directly from MaGe, pulse shape simulations can now be performed from individually simulated energy deposits. An example of a simulated signal in a BEGe type detector is shown in Fig. 3.3, right. Our immediate plan is to include static and dynamic noise components, and ultimately perform realistic end-to-end simulations of interactions in the BEGe detectors. After the development of the simulation software is completed, it will be validated by comparing it to calibration and science data.

With accurate pulse shape simulations, we can treat our Monte Carlo simulations of the various background components in the same way as our physics data. By using the identical data analysis chain we can thus create a complete background model that includes PSD. Since PSD strongly affects the spectral shape of our remaining background, this variation must be reproduced by the background model, possibly leading to the identification of new components. We will also increase the accuracy of the model by re-simulating components strongly affected by the active volume size of the Ge diodes with improved knowledge of the dead-layer extent.

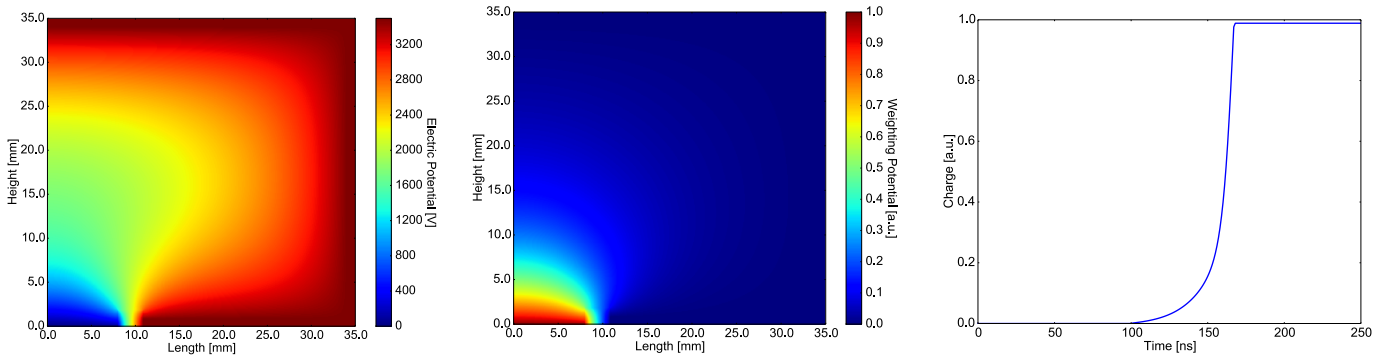

FIG. 3.3 – (Left, centre): Simulation of the electric field and weighting potential in a BEGe type detector. These potentials are used to calculated the drift paths of charge carriers and the induced charge on the electrodes for pulse shape simulations. (Right): Simulated charge signal on the read-out electrode of a detector.

[10] M. Agostini, *et al.*, Eur. Phys. J. C **74.4** (2014) 2764.

[11] B. Bruyneel, B. Birkenbach, P. Reiter, Eur. Phys. J. A **52.3** (2016) 70.

[12] M. Boswell, *et al.*, IEEE Trans. Nucl. Sci. **58** (2011) 1212-1220.

3.4 PMTs for direct detection of scintillation light in liquid argon

One of the distinctive features of GERDA is the liquid argon veto. It enables detection and rejection of background events with an energy deposit in the liquid argon. Liquid argon scintillation light has a wavelength of 128 nm and cannot easily be detected, as there are very few materials transparent to this light, including the quartz windows of the PMTs used in the experiment. Instead, we wavelength shift the light to optical wavelengths using foils surrounding each detector string and a curtain of fibres, coated with a wavelength shifting material. The downsides of this technique are the limited geometrical coverage, and the introduction of additional materials into the LAr cryostat.

One material transparent to liquid argon scintillation light is MgF_2. We tested one 3-inch R11065 PMT from Hamamatsu with a MgF_2 window during operation at room temperature, and in cryogenic nitrogen and liquid argon environments using our PMT testing facilities. (LArS and Sandbox), measuring the PMT's characteristic properties: gain, dark count rate and after-pulse rate. We obtained a gain of 6.5×10^6 at a nominal operating voltage of 1500 V, similar to values for the regular version of this PMT. To confirm the detection of liquid argon scintillation light, measurements with an alpha-emitting ^{241}Am source inside LArS were taken. The mean recorded waveform is shown in Fig. 3.4. It displays the intensity of light after the first detected photon. Its form is characteristic for the liquid argon scintillation light, as the intensity follows the exponential de-excitation rates of the short (here ∼7.8 ns) and long (here ∼1.4 µs) lived excited states responsible for the scintillation.

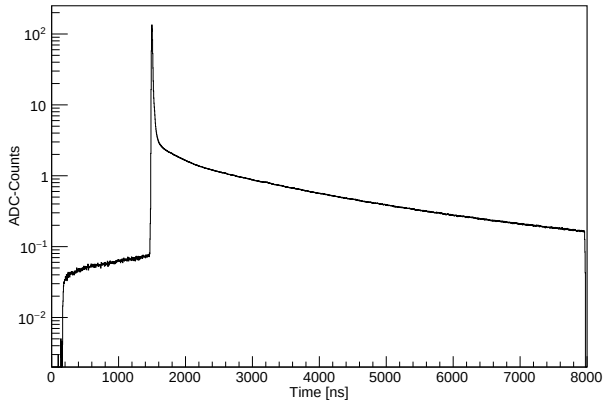

FIG. 3.4 – Average waveform, recorded with the PMT with MgF_2 window in liquid argon with an alpha-emitting source.

We also tested the leak tightness of the tube, by observing the rate of after-pulses and in particular ion-initiated after-pulses in several measurements in nitrogen and argon over the course of about a year. Ion-initiated after-pulses were identified by their characteristic delay relative to the trigger pulse. The after-pulse rate was acceptable, even after several cool-down/warm-up stress cycles, and did not degrade over time: as an example, the relative rate (per triggered photoelectron) in the nitrogen peak was 7.2×10^{-4}% and 8.8×10^{-4}% a year ago and in a recent measurement, respectively, while the total relative after-pulse rates were 0.37% and 0.34%.

We aim to confirm these results, and test for micro-light emission (observed in some of the R11410 PMTs) by operating at least two units face-to-face, over a longer period of time to prove their applicability in liquid argon cryostats. This is of interest to several planned experiments in the low-background community, including LEGEND. If successful, we plan to investigate the possibility to realise a liquid argon veto, where the standard PMTs are replaced by those with MgF_2 windows.

3.5 Super-WIMP search

With its unprecedented low background, GERDA may be sensitive to bosonic super-WIMPs [13] with masses up to 1 MeV in the low energy region of the energy spectrum. Bosonic super-WIMPs can be completely absorbed by a germanium atom via the axio-electric effect and result in a peak in the energy spectrum, centred around their rest mass. Existing limits, obtained by other germanium- and xenon-based experiments, reach up to 145 keV [14, 15]. With this analysis, we aim to extend the direct search range for bosonic super-WIMPs to 1 MeV. In Fig. 3.5 examples of expected event rates for various couplings in the pseudo-scalar particle case, and of the corresponding signatures in the GERDA energy spectrum are shown.

For this analysis, the performance of the Ge detectors, currently optimised on the high-energy range around 2039 keV, has to be evaluated at low energies. We performed a special calibration with a ^{226}Ra source to determine the quality of the energy reconstruction and resolution down to the low energy threshold around 175 keV. No hints of a significant degradation of the energy reconstruction were found towards low energies and the resolution (at FWHM), shown in Fig. 3.2, right, is in the range 2-3 keV. Furthermore we plan to extend the background model, currently limited to an energy threshold of 600 keV, to low energies and investigate the possibility to reduce the background in this region by means

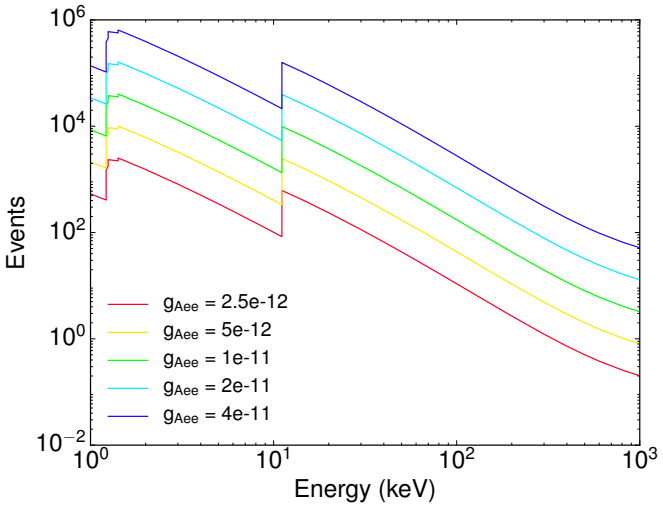

FIG. 3.5 – Expected total number of events from pseudoscalar super-WIMPs of various coupling strengths to electrons, with a GERDA exposure of 5.8 kg·yr.

of PSD. While above 1 MeV the background rejection by PSD is well established [16], it was suggested that its performance breaks down below these energies, due to the higher impact of noise. By adding measured noise traces to signal traces and analysing the impact on the PSD, we found the background rejection, for example for multi-site events, degrades due to noise from 80-90% at high energies to around 50% at the low energy threshold. This must be cross-checked by detailed pulse shape simulations, as mentioned above. We thus plan to adapt and use the PSD methods developed for high energies at the lower end of the energy spectrum.

[13] M. Pospelov, A. Ritz, M. B. Voloshin, Phys. Rev D **78** (2008) 115012.

[14] K. Abe, *et al.*, Nucl. Instrum. Meth. A **716** (2013) 78-85.

[15] N. Abgrall, *et al.*, arXiv[nucl-ex] (2016) 1612.00886.

[16] M. Agostini, *et al.*, Eur. Phys. J. C **73.10** (2013) 2583.

3.6 The GERDA Upgrade

Considering the initial results from Phase II, only a fraction of a background event is expected in the region of interest in the entire exposure of this phase. Thus, GERDA is the first "background-free" experiment in the field, and sensitivity grows linearly with time. It will reach $T_{1/2}^{0\nu\beta\beta} \sim 10^{26}$ y in three years of continuous operation. GERDA has validated the concept of background suppression by the use of a liquid argon veto and pulse shape analysis, and shown that it is suitable to reach an extremely low background level with a high discovery potential.

The background at the Q-value of the $0\nu\beta\beta$-decay is world-best: it is lower by a factor of ten compared to experiments using other isotopes, after normalisation by the energy resolution and the total efficiency. Hereby, the GERDA half-life sensitivity is similar to that of KAMLAND-ZEN for ^{136}Xe, despite KAMLAND-ZEN experiment's 10-fold larger exposure. Thus, it is well-motivated to increase the overall GERDA detector mass, in order to increase sensitivity, and reach the 10^{26} y half-life goal on a faster timescale. A discovery of $0\nu\beta\beta$ decay would have far-reaching implications for cosmology and particle physics. To make a convincing case for such a discovery, an ultra-low background level, an excellent energy resolution as well as the possibility to distinguish a signal-like event from an unknown gamma-line from a nuclear transition is mandatory. The latter is achieved in GERDA by pulse shape analysis and a potential signature in the liquid argon.

The cryostat used by GERDA can house up to 200 kg of detectors, and such an arrangement would be background-free up to an exposure of 1000 kg·y. The first step (GERDA-Upgrade) is to replace the inner detector string made of detectors with natural Ge composition with 7–8 new, enriched Ge detectors. The subsequent step, in the framework of the new collaboration LEGEND, is to operate a total of 200 kg of Ge diodes in an upgraded infrastructure at LNGS. This would be a first step towards a ton-scale ^{76}Ge experiment, to be constructed within a larger international collaboration. GERDA-Upgrade would demonstrate another milestone in background reduction, since a level of $\sim 10^{-4}$ events/(keV·kg·y) is required for the 200 kg stage. This is to be achieved by replacing the cables with existing, lower-radioactivity versions, and by improving the light yield of the liquid argon veto.

4 Dark Matter Detection with XENON and DARWIN

Peter Barrow, Laura Baudis, Yanina Biondi, Adam Brown, Chiara Capelli, Michelle Galloway, Andreas James, Shingo Kazama, Gaudenz Kessler, Alexander Kish, Chris Marentini, Daniel Mayani, Francesco Piastra, Yuehuan Wei, Julien Wulf

in collaboration with: Albert Einstein Center for Fundamental Physics Bern, Columbia University, UCLA, UCSD, INFN, University of Münster, Coimbra University, Subatech, The Weizmann Institute of Science, University of Mainz, SJTU, MPIK Heidelberg, Stockholm University, Rice University, University of Chicago, University of Bologna, Nikhef and Amsterdam University, Purdue University, NYU of Abu Dhabi

(XENON Collaboration)

Astronomical and cosmological observations reveal that the vast majority of the matter and energy content of our universe is invisible – or dark – and interacts neither strongly nor electromagnetically with ordinary matter. Results from the Planck satellite [1] show that about 68% of the overall budget is dark energy, leading to the observed accelerated expansion of the cosmos. Another 27% is composed of dark matter, a yet-undetected form of matter whose presence is needed to explain the observed large-scale structures and galaxies. While dark matter interacts gravitationally with baryonic matter, any additional interactions, if existing, must be very weak with extremely small cross sections [2]. Because the Standard Model of particle physics does not accommodate dark matter, the observationally-driven need for its existence is one of the strongest indications for physics beyond the standard model. The direct detection and subsequent characterisation of dark matter particles is, therefore, one of the major experimental challenges of modern particle and astroparticle physics [3,4]. Many theories beyond the Standard Model predict viable candidates; one particular class are Weakly Interacting Massive Particles (WIMPs) [3,5].

One concept to detect dark matter is based on dual-phase noble gas time projection chambers (TPCs), where the prompt scintillation light (S1) and the delayed proportional scintillation light signal from the charge (S2) are measured. Both signals are employed for a precise reconstruction of the event vertex and to suppress backgrounds by rejection of multiple-scatter interactions, as dark matter particles are expected to interact only once. The charge-to-light ratio S1/S2 is exploited to separate the expected signal, namely nuclear recoils (NR), from the dominant electronic recoil (ER) background.

The XENON100 experiment [6, 7], a liquid xenon (LXe) TPC with a 62 kg active target, has reached its sensitivity goal and excluded spin-independent WIMP-nucleon cross sections above $1 \times 10^{-45}\,\mathrm{cm}^2$ at a WIMP mass of $55\,\mathrm{GeV}/c^2$ [8]. These constraints are superseded by the results from the LUX [9] and PANDAX [10] collaborations. While LUX operated a 250 kg TPC at SURF, PANDAX operates a 500 kg detector at the JinPing laboratory. They exclude spin-independent WIMP-nucleon scattering cross sections above $1.1 \times 10^{-46}\,\mathrm{cm}^2$ at $50\,\mathrm{GeV}/c^2$.

The next increase in sensitivity will come from XENON1T, which operates a total of 3.2 t of liquid xenon inside a cryostat surrounded by a large water Cherenkov shield. We successfully commissioned the XENON1T detector at the Laboratori Nazionali del Gran Sasso (LNGS) and started the first science run in November 2016. In the following, we will present our latest XENON100 results and the status of the XENON1T experiment. We will then describe the progress on the next-generation of dark matter detectors XENONNT and DARWIN and conclude with current R&D activities of our group.

[1] P. A. R. Ade *et al.* [Planck Collaboration], Astron. Astrophys. **571** (2014) A16.

[2] M. W. Goodman and E. Witten, Phys. Rev. D **31** (1985) 3059.

[3] G. Bertone, D. Hooper and J. Silk, Phys. Rept. **405** (2005) 279.

[4] L. Baudis, Phys. Rev. G **43** (2016) no.4, 044001.

[5] G. Jungman, M. Kamionkowski and K. Griest, Phys. Rept. **267** (1996) 195.

[6] E. Aprile *et al.* [XENON Collaboration], Phys. Rev. Lett. **107** (2011) 131302.

[7] E. Aprile *et al.* [XENON Collaboration], Astropart. Phys. **35** (2012) 573.

[8] E. Aprile *et al.* [XENON Collaboration], Phys. Rev. D **94** (2016) no.12, 122001.

[9] D. S. Akerib *et al.* [LUX Collaboration], Phys. Rev. Lett. **118** (2017) no.2, 021303.

[10] C. Fu *et al.* [PandaX Collaboration], Phys. Rev. Lett. **118** (2017) no.7, 071301.

4.1 Inelastic WIMP-nucleus interaction and search of bosonic super-WIMPs with XENON100

XENON100 is a 161 kg double-phase xenon TPC, which employs two arrays of low-radioactivity, VUV-sensitive photomultipliers (PMTs) to detect the prompt (S1) and charge-induced proportional (S2) scintillation light signals induced by particles interacting in the target volume, containing 62 kg of ultra-pure liquid xenon (LXe). The remaining 99 kg of LXe act as an active veto shield against background radiation. The XENON100 detector concluded acquisition of science data in 2016 and we are completing analyses for several physics channels. In the end of 2016, after a combined run analysis and an integrated period of 477 live days, the experiment has reached a sensitivity of 1.1×10^{-45} cm^2 at 50 GeV/c^2 and 90% confidence level on the spin-independent elastic WIMP-nucleon scattering cross section [11].

Apart from the standard WIMP analyses, at UZH we have focussed on the study of inelastic WIMP-nucleus interactions and on a search for bosonic super-WIMPs. Both manuscripts are under review by the collaboration. The first study is on the spin-dependent, inelastic scattering of WIMPs on nuclei, which induces a transition of ^{129}Xe to a low-lying excited nuclear state (the $3/2^+$ state, 39.6 keV above the $1/2^+$ ground state) [12]. The experimental signature is a NR detected simultaneously with the prompt de-excitation photon [13]. The region of interest (ROI) is based on ^{241}AmBe calibration data, as shown in Fig. 4.1, left, and extends from 60 pe to 210 pe for the prompt, and from 4×10^3 pe to 16×10^3 pe for the proportional scintillation, respectively. The ROI is divided into nine sub-regions, which contain a similar number of expected background events. The control regions are used for cross-checks of the background shape distribution and are selected to be as close as possible to the ROI. The distribution of events in the ROI is shown in Fig. 4.1, centre: a total of 764 events are observed, with an expected background of 756 $\pm$5 (stat) $\pm$55 (sys) events. This result is interpreted via a binned profile likelihood approach, and a 90% CL$_s$ confidence level limit [14] is set on the spin-dependent WIMP-nucleon cross section as a function of the WIMP mass (shown in Fig. 4.1, right). With a minimum of 3.3×10^{-38} cm^2 at 100 GeV/c^2, it is the most stringent result in this interaction channel.

At UZH we also searched for bosonic super-WIMPs [15], which are warm dark matter candidates with masses at the keV-scale that could couple electromagnetically to Standard Model particles via the axio-electric effect. The expected signature is a mono-energetic peak at the super-WIMP's rest mass. Compared to an analogous search for axion-like particles in [16], we extended the mass range to 125 keV and employed both scintillation and ionisation signals to determine the energy scale, thus improving the energy resolution from 14%, based on S1-only, to 5.7% at 100 keV. The distribution of events in the ROI is shown in Fig. 4.2, left, together with the expected signal for different pseudo-scalar bosonic super-WIMP masses, an axio-electric coupling $g_{Aee} = 5\times10^{-12}$, and a local density of 0.3 GeV/cm^3. The profile likelihood analysis showed that our data is compatible with the background model. We set competitive limits in the 8-50 keV/c^2 mass range (see Fig. 4.2, centre and right), excluding couplings to electrons $g_{Aee} > 3\times10^{-13}$ and $\alpha/\alpha' > 2\times10^{-28}$ at 90% C.L. for pseudo-scalar and vector super-WIMPs.

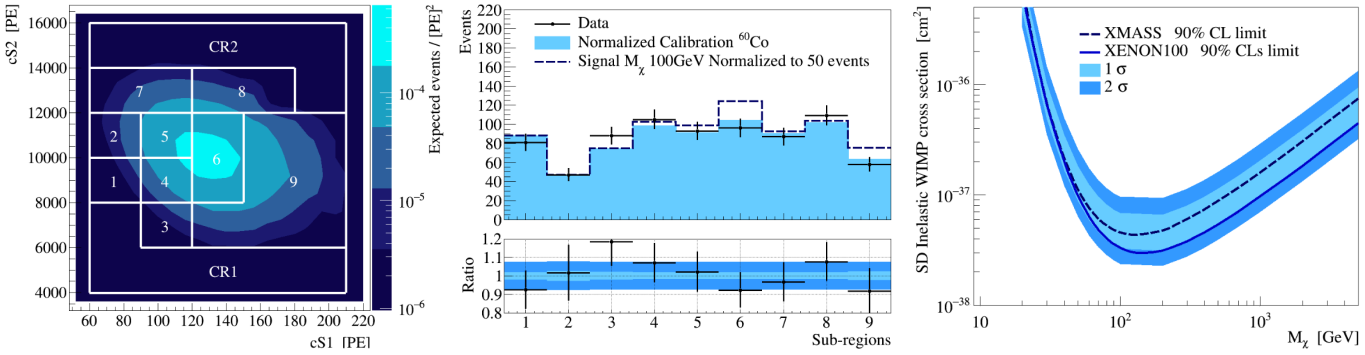

FIG. 4.1 – (Left): Signal distribution for inelastic WIMP-^{129}Xe interactions obtained from a Monte Carlo simulation of a 100 GeV/c^2 WIMP, normalised to 50 events. The signal (1-9) and control (CR1, CR2) regions are indicated. (Centre): Distribution of observed events in the region of interest (data points), along with the normalised distribution from calibration data (filled histogram), and expected signal (blue dashed). The bottom panel displays the ratio between data and expected background, where the light and dark blue shaded areas represent the statistical and systematic uncertainties on the background expectation, respectively. (Right): Upper limit (blue curve) on the WIMP-nucleon cross section in a function of the WIMP mass, together with result from the XMASS experiment (dashed) [17].

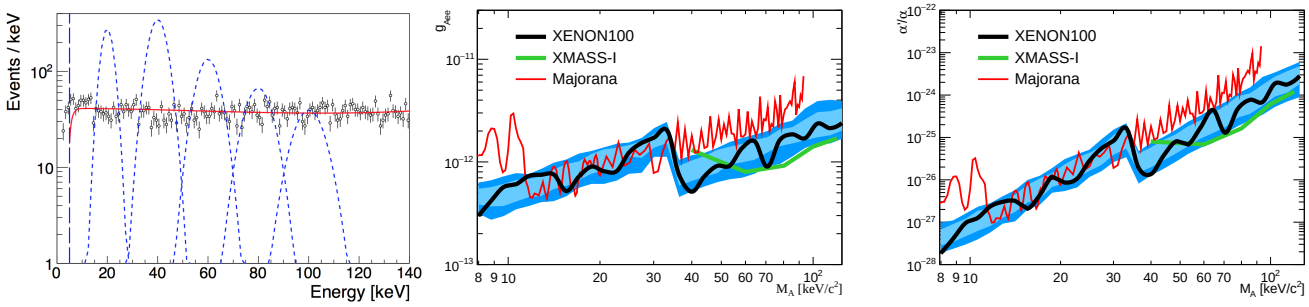

FIG. 4.2 – (Left): Distribution of events (data points) in the super-WIMP search region, between 5 and 140 keV. Also shown is the background model (red curve) along with the expected signal for super-WIMPs with various pseudo-scalar masses, and an axio-electric coupling $g_{Aee} = 5\times10^{-12}$ (blue dashed peaks). (Centre and right): The 90% C.L. upper limits on the coupling of the pseudo-scalar and vector super-WIMPs, respectively, in a function of particle mass, together with the results from XMASS-I [18] and Majorana [19].

[11] E. Aprile *et al.* [XENON Collaboration], Phys. Rev. D **94** (2016) no.12, 122001.

[12] J. R. Ellis, R. A. Flores and J. D. Lewin, Phys. Lett. B **212** (1988) 375.

[13] L. Baudis, G. Kessler, P. Klos, R. F. Lang, J. Menèndez, S. Reichard and A. Schwenk, Phys. Rev. D **88** (2013) no.11, 115014.

[14] A. L. Read, In *Geneva 2000, Confidence limits* 81-101.

[15] M. Pospelov, A. Ritz and M. B. Voloshin, Phys. Rev. D **78** (2008) 115012.

[16] E. Aprile *et al.* [XENON Collaboration], Phys. Rev. D **90** (2014) no.6, 062009, Erratum: [Phys. Rev. D **95** (2017) no.2, 029904].

[17] H. Uchida *et al.* [XMASS-I Collaboration], PTEP **2014** (2014) no.6, 063C01.

[18] K. Abe *et al.* [XMASS Collaboration], Phys. Rev. Lett. **113** (2014) 121301.

[19] N. Abgrall *et al.* [Majorana Collaboration], arXiv:1612.00886 [nucl-ex].

4.2 The first science run with XENON1T

The design of the XENON1T experiment started in 2010, while the underground construction work in LNGS Hall B started in fall 2013. The combined cryostat, cryogenic and storage system (ReStoX) were successfully commissioned in summer of 2015. In November 2015 the TPC was attached to the inner cryostat inside the water shield. Afterwards, the commissioning work started, followed by the detector characterisation and calibration campaign. The detector was filled with 3.2 t of liquid xenon from ReStoX in mid-April 2016. The operation lasted about two weeks, reaching a filling speed of 650 kg/day after the initial cool-down period. The core xenon handling systems performance met or exceeded the design specifications and the filling operation was completed. With the cryostat filled, the cryogenic system has been in continuous operation for the last months, maintaining the liquid xenon at constant temperature and pressure (temperature rms $<$0.04 C, pressure rms $\sim$ 1 mbar). The first science run started in November 2016. The TPC is thus filled with liquid xenon since April 2016, and the primary scintillation (S1) as well as the delayed proportional signal from the charge (S2) are recorded by the two arrays of 248 PMTs, where 127 are placed above, and 121 below the LXe target. For each interaction, the PMTs observe a certain number of photoelectrons (pe). For the initial science run, the drift field is similar to the one in LUX (0.16 kV/cm), after which the field will be increased. The electron extraction field is around 10 kV/cm, and ensures 100% electron extraction efficiency. The electron lifetime is around 600 µs, and linearly increasing due to the online purification of the liquid. Figure 4.3, shows the science data acquisition period, interspersed by various calibration runs with external and internal sources. Due to several earthquakes on January 18, after which the detector required a few days to recover (trip of the TPC high voltages, LXe level oscillations), we decided to analyse the first $\sim$34 live days and release initial results in early sum-

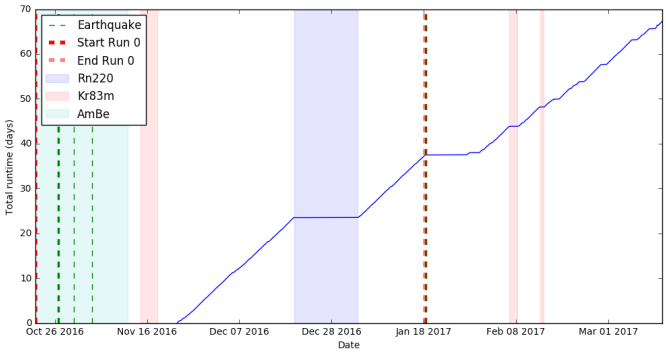

FIG. 4.3 – The science data taking period (runtime in days, shown as blue curve), interspersed by calibration runs with external and internal sources such as AmBe (NR band), ^{83m}Kr (energy scale) and ^{220}Rn (ER band).

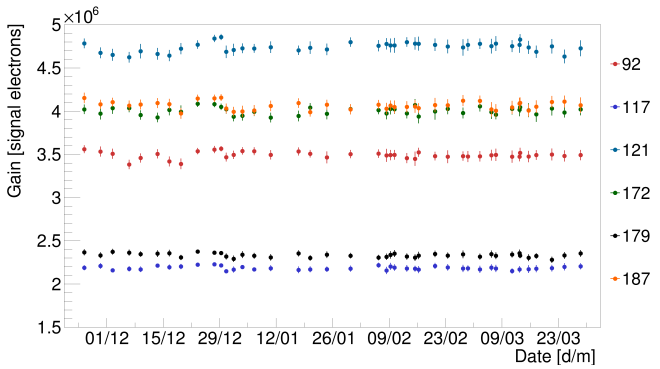

FIG. 4.4 – An example of the gain evolution during several months for 6 PMTs in XENON1T.

mer 2017. A combination of this data with the new science data (>45 days as of now) will follow.

We are responsible for the in-situ calibration of the photomultiplier tubes and monitor their stability in time, including the after-pulse rates. Three independent gain measurement methods were developed in our group and implemented for the routine calibration of the PMTs. These are based on external LEDs and low-intensity (single photon) scintillation pulses from particle interactions, and yield consistent results within the systematic uncertainties of each method. An example of long-term stability for 6 PMTs is shown in Fig. 4.4. We have developed a database (DB) based on an open-source MySQL management system, to store and monitor various operational parameters of the PMTs, such as gain, single photoelectron resolution, after-pulse and dark count rates, and track their long-term stability. Other information, e.g. radioactivity values and laboratory tests for each phototube, is also stored in the same DB, allowing us to study correlations between various parameters.

We substantially contribute to the analysis of the calibration and science data of the XENON1T experiment, from the development and validation of the data quality selection criteria to the final physics analyses. We contributed to the first XENON1T science run (end Nov 2016 - January 18, 2017) with algorithms for event selection, event vertex reconstruction, signal corrections and energy calibrations. We are continuing our work on data from this run, as well as from the second run (that started in February 2017) and will focus on various physics analyses of the first science as well.

4.3 The XENONnT and DARWIN project

In parallel to the ongoing XENON1T analysis work, we are working on a new TPC design for the planned upgrade, XENONnT. Many of the major components in XENON1T are constructed such that an upgrade to a detector housing more than twice the amount of LXe will become feasible once the science goals of XENON1T are achieved. However it requires the construction of a new inner cryostat and a new TPC. We are co-responsible for the design, fabrication, assembly, and testing of the new TPC. The design will be largely based on the configuration which we have developed for XENON1T, with confirmed stability in liquid xenon as well as sufficiently low radioactivity levels but with a 40% increase in linear dimensions. The increased size of the TPC, accommodating a liquid-xenon total (active target) mass of 7.5 t (6.0 t), will improve the sensitivity by a factor of ten.

As polytetrafluorethylen (PTFE) efficiently reflects the scintillation light from liquid xenon, the internal surfaces of the field cage will consist of interlocking side panels of polished PTFE and self-centring PTFE disks to surround the PMTs on the top and bottom of the field cage. This design accommodates for PTFE shrinkage at cryogenic temperatures. Because the fluorine in PTFE has a very high cross section for (α,n) reactions, an effort was made to replace the PTFE in areas where it is not essential. Therefore the support structures will be made of Torlon, for it has good structural properties, a high dielectric constant, and a much lower expected contribution to the neutron background. The first samples for the main XENONnT TPC materials have been procured and their screening is underway.

We are responsible for the production of the voltage-divider circuits for the XENONnT PMTs, which will provide good linearity in the full DAQ range while maintaining high single-photon sensitivity at a gain of 2×10^6, with a power distribution below 0.25 W/channel. The design will be largely based on the configuration which we have developed for XENON1T. We initiated a study of the outgassing properties of various substrates (e.g. Cirlex and CuFlon) for the printed circuits with a dedicated facility at UZH [20], and the design will be optimised based on the obtained results, together with the information from the radioactive screening campaign with γ- and mass-spectrometry.

We have to guarantee that all of the XENONnT PMTs will not fail during the lifetime of the XENONnT detector. For this purpose the PMT testing facility for the XENON1T PMTs at UZH has been upgraded. The upgrade, shown in Fig. 4.5, can house 10 PMTs simultaneously, allowing for more efficient PMT qualification measurements.

To amplify the PMT signals induced by low-energy interactions in the target, and thus improve the single photon detection efficiency, in XENON1T we use commercial linear amplifiers (Phillips 776). Since XENONnT and DARWIN will start to have a competitive sensitivity to the neutrinoless double-beta decay [21,22], where the energy region of interest is around 2.5 MeV, we are working on the design and optimisation of an amplifier circuit to increase the dynamic range. Several prototypes have been developed and characterised, and the current configuration is based on an asymmetrically polarised operational amplifier LMH6629, and an additional wide-band, low-distortion OPA842 from Texas Instruments. It features a low input voltage noise of 0.69 nV/$\sqrt{\text{Hz}}$, input current noise of 2.6 pA/$\sqrt{\text{Hz}}$, and a high bandwidth of

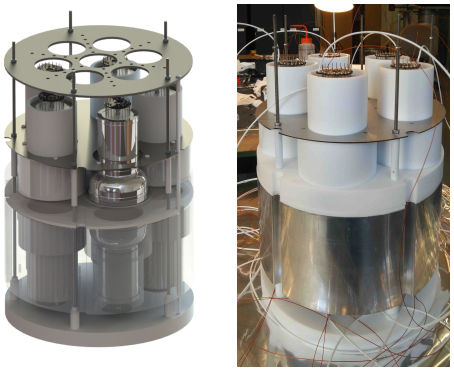

FIG. 4.5 – The inner part of the MarmotXL photosensor test facility at the UZH (drawing, left and a picture, right). The aluminium filler reduces the amount of xenon required to cover the phototubes, while the PTFE jackets insulate the metal bodies. A larger cryostat vessel, not shown here, provides the vacuum insulation during cryogenic operation. The previous version of the facility is also described in [23].

900 MHz. The output signal is split into two channels, hence one is attenuated by a factor of two, while the other is amplified by a factor of ten. A 8-channel NIM board is under construction and will be tested in-situ with the XENON1T data acquisition system.

[20] Walter, M., Ph.D. Thesis, University of Zurich, 2015.

[21] E. Aprile *et al.* [XENON Collaboration], JCAP **1604** (2016) no.04, 027.

[22] L. Baudis, A. Ferella, A. Kish, A. Manalaysay, T. Marrodan Undagoitia and M. Schumann, JCAP **1401** (2014) 044.

[23] P. Barrow *et al.*, JINST **12** (2017) no.01, P01024.

4.4 R&D for XENON and DARWIN

The Xurich II detector has been designed to measure the scintillation and ionisation yields of LXe from low-energy nuclear recoils. The measured volume-averaged light yield at 9.4 keV is 15.0 pe/keV at zero field, and 10.8 pe/keV at a drift and extraction field of $\sim$1 kV/cm and $\sim$10 kV/cm, respectively. Together with a high yield S2 signal of $\approx 2\times10^3$ pe/keV, this allows us to reach a sub-keV energy threshold. The energy resolution from the combined S1 and S2 signals is (5.8$\pm$0.3)% at 32 keV, comparable to state-of-the-art $xy-$position sensitive LXe detectors [24].

The z-coordinate of an interaction in a dual-phase TPC is linearly related to the measured delay time between the S1 and S2 signals. This dependence, together with the precise knowledge of the physical dimension of the TPC, allowed us to measure the drift velocity of electrons (at 184 K) for electric fields from $\sim$0.2 to $\sim$1.3 kV/cm, relevant for current and future large-scale dual-phase xenon TPCs. As shown in Fig. 4.6, the measured electron drift velocity ranges from

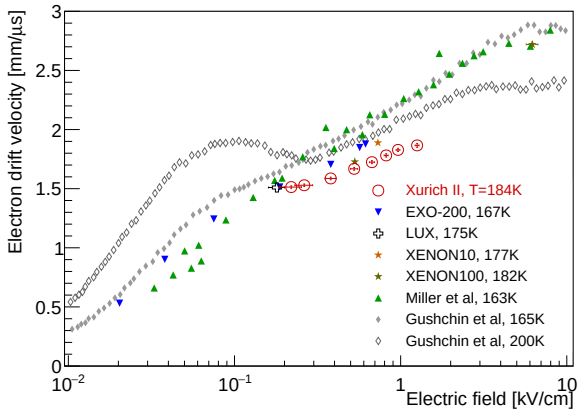

FIG. 4.6 – Electron drift velocity as a function of electric field measured with Xurich II (open red circles), together with literature values [25–30].

1.63 to 2.00 mm/μs, and we observe good agreement with other measurements performed at similar temperatures. A manuscript detailing these results, along with the description of the detector and its commissioning data, is under preparation. The detector is currently acquiring data at the D-D fusion neutron generator facility at UZH. We use Compton scatters of 662 keV γ-rays from a ^{137}Cs source to characterise the TPC response to electromagnetic interactions, and elastic neutron scatters at all angles to study the nuclear recoils at low energies.

To calibrate the Xurich II detector down to energies of $\sim$1 keV, we are developing a method for the injection of ^{37}Ar gas into the active volume of the detector. This isotope can be produced by neutron irradiation of natural argon gas at the neutron activation station of the SINQ facility at the Paul Scherrer Institute, similar to the method in [31]. The ^{37}Ar decay will provides two low-energy lines, at 2.82 keV and 0.27 keV, following the K- and L-shell electron capture. Such a calibration will not only provide relevant information for our study of low-energy xenon response with Xurich II, but will also be used to develop a new low-energy calibration standard for large-scale detectors such as XENON and DARWIN.

[24] S. Stephenson *et al.*, JINST **10** (2015) no.10, P10040.

[25] E. Aprile *et al.* [XENON Collaboration], Astropart. Phys. **54** (2014) 11.

[26] E. Aprile *et al.* [XENON Collaboration], J. Phys. G **41** (2014) 035201.

[27] L. S. Miller, S. Howe and W. E. Spear, Phys. Rev. **166** (1968) 871.

[28] P. F. Sorensen, Ph.D. Thesis, Brown University, 2008.

[29] D. S. Akerib *et al.* [LUX Collaboration], Phys. Rev. Lett. **112** (2014) 091303.

[30] J. B. Albert *et al.*, Phys. Rev. C **95** (2017) no.2, 025502.

[31] S. Sangiorgio *et al.* [EXO-200 Collaboration], Nucl. Instrum. Meth. A **728** (2013) 69.

5 Searching for Dark Matter and Neutrinos with CCD Detectors

J. Liao, B. Kilminster, and P. Robmann

in collaboration with: Fermi National Accelerator Laboratory, University of Chicago, University of Michigan, Universidad Nacional Autónoma de México, Universidad Nacional de Asunción de Paraguay

(DAMIC Collaboration)

Using thick, fully-depleted, low-noise CCDs, we are able to search for low-energy nuclear recoils which produce a small number of ionization electrons. The DAMIC (Dark Matter in CCDs) experiment uses this technology to provide high sensitivity for directly detecting weakly interacting dark matter (DM) particles (WIMPs) with mass below 5 GeV. The CONNIE (Coherent Neutrino Nucleus Interaction) experiment uses the same type of detector to search for the process of neutrinos scattering coherently off nuclei, a process which is predicted by the standard model, but has currently never been experimentally observed.

5.1 DAMIC

DAMIC searches for low-mass DM which is motivated by the similar abundances of baryons and DM, and the disparity of the matter-antimatter densities [1–3]. First results for DAMIC were obtained from data collected in 2011 [4]. At that time, these DAMIC results constituted the best limits for DM mass below 4 GeV, but have been superseded since. The main challenge in searching for low mass DM is measuring the low energy deposit of the associated nuclear recoils in the detection material. DAMIC uses CCDs with an electronics noise of σ=7.2 eV corresponding to a 5σ=36 eV threshold, which is the lowest of any current DM detector. CCD detectors are silicon pixel detectors that shift charge from the capacitor of one pixel to the next by generating potential wells until reaching a charge amplifier which converts the charge to voltage (Fig. 5.1). The DAMIC CCD detectors were fabricated by Lawrence Berkeley National Laboratory [5] originally for the Dark Energy Camera (DECam) [6, 7]. DECam CCDs [8] are 30 times thicker (500 - 650 µm) than commercial CCDs, leading to correspondingly higher detection efficiencies. Each CCD has up to 16 million 15 µm x 15 µm pixels and is read out by two amplifiers in parallel. The electronic gain is $\sim$ 2.5 µV/e. The signal is digitized after correlated double sampling and the noise performance improves by reducing the readout speed. The lowest noise, $\sigma < 2e^-$ (R.M.S.) per pixel, was achieved with readout times of 50 µs per pixel [9].

In 2015, the upgraded DAMIC experiment collected data in SNOLab, which boasts 6000 meter-water-equivalent of overburden that provides shielding from backgrounds induced by cosmic ray muons. This new DAMIC experiment took 0.6 kg·days of data using four 5.5-gram CCDs, each 5 times the mass of those used in the previous experiment. The CCDs are installed inside a copper box cooled to -150°C to reduce dark current. The cold copper also shields the detectors against infrared radiation. A closed cycle helium gas refrigerator is used to maintain the low temperature. Lead and polyethylene shield against γ-rays and neutrons. The detector is connected through a readout cable to the preamplifiers located outside the lead shield. The detector package is housed in a cylindrical vacuum vessel fabricated with oxygen-free copper, and maintained at 10^{-7} Torr with a turbo molecular pump. Results of this data run were published in 2016 [10], showing that DAMIC is competitive with other low-mass DM searches.

Given the low energy threshold and excellent energy resolution to resolve low energy signals, DAMIC has discovered a niche for searching for different types of DM candidates. One such candidate is known as the hidden photon [11]. Like an ordinary photon, a hidden photon can be absorbed by an electron in a detector material. However, the hidden photon would have a mass and be non-relativistic, allowing it to clump in DM halos in the manner of weakly interacting massive particles. One interesting difference of hidden photons with respect to

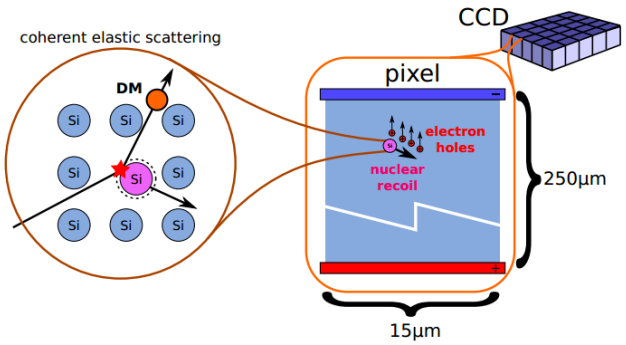

FIG. 5.1 – DAMIC detection principle: hypothetical DM particles scatter coherently off silicon nuclei, producing a nuclear recoil that is recorded as charge on pixels in the CCD. A prototype setup with a CCD thickness of 250 µm is shown.

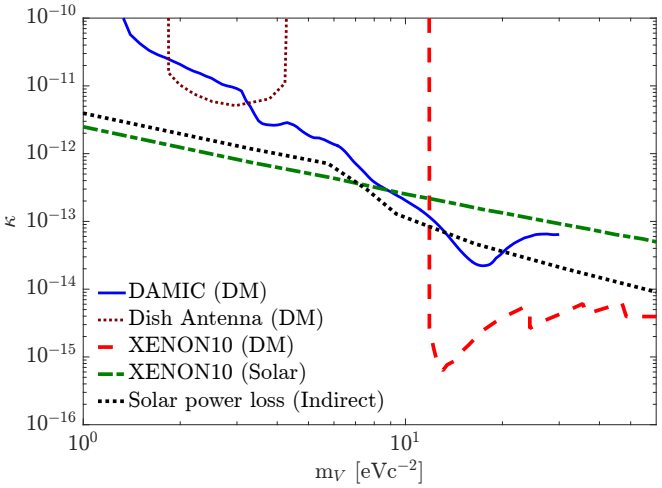

FIG. 5.2 – DAMIC exclusion plot (90% C.L.) for the hidden-photon kinetic mixing κ as a function of the hidden-photon mass m_V.

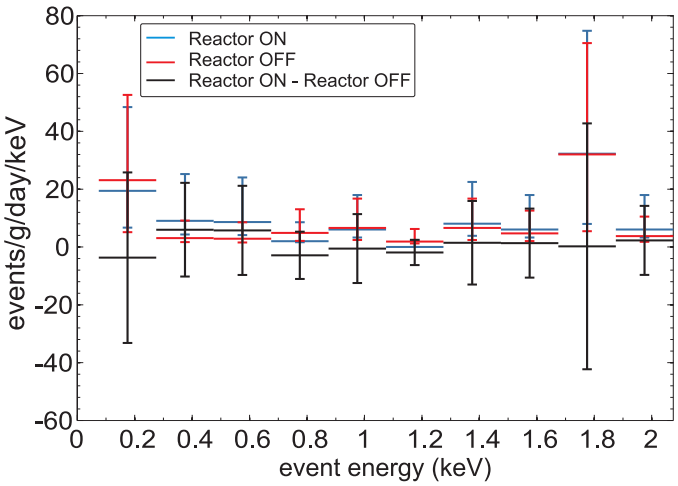

FIG. 5.3 – A comparison of CONNIE data, collected with the reactor on and off, demonstrates that there are no additional backgrounds present during reactor operation.

WIMPs is that the interaction does not depend on the velocity distribution of the particles. Using 6.25 days of data acquired in 2016, DAMIC was able to set the best direct limits on hidden photons within the mass range of 3 - 12 eV/c^2 as in Fig. 5.2 [12]. DAMIC is currently collecting data with an even-lower background rate, and will publish these new results in the next year.

[1] D.B. Kaplan, Phys. Rev. Lett. **68**, 741 (1992).

[2] D.E. Kaplan, M.A. Luty and K.M. Zurek, Phys. Rev. D **79**, 115016 (2009).

[3] D. Hooper and W. Xue, Phys. Rev. Lett., 110, 041302 (2013).

[4] J. Barreto *et al.* (DAMIC Collaboration), Phys. Lett. B **711**, 264 (2012).

[5] S.E. Holland *et al.*, IEEE Trans. Electron Dev., **50** 225 (2003).

[6] B. Flaugher, *Ground-based and Airborne Instrumentation for Astronomy*, Ian S. McLean editor; Iye, Masanori, Proceedings of the SPIE, Volume 6269, (2006).

[7] Dark Energy Survey Collaboration, astro-ph/0510346.

[8] J. Estrada and R. Schmidt, *Scientific Detectors for Astronomy 2005*, J.E. Beletic, J.W. Beletic and P. Amico editors, Springer (2006).

[9] Estrada *et al.*, Proceedings of SPIE 2010.

[10] A. Aguilar-Arevalo *et al.* [DAMIC Collaboration], Phys. Rev. D **94**, no. 8, 082006 (2016).

[11] M. Pospelov, A. Ritz, and M. B. Voloshin, Phys. Rev. D**78**, 115012 (2008); J. Redondo and M. Postma, JCAP 0902, 005 (2009); A. E. Nelson and J. Scholtz, Phys. Rev. D**84**, 103501 (2011); P. Arias *et al.*, JCAP 1206, 013 (2012).

[12] A. Aguilar-Arevalo *et al.* (DAMIC Collaboration), Phys. Rev. Lett. **118**, no. 14, 141803 (2017).

5.2 CONNIE

Although coherent neutrino-nucleus scattering (CNNS) is the neutrino process with the largest standard-model cross-section and already predicted in 1974 [13] it has not yet been observed yet due to the difficulty in its detection. The process is an important input to supernova simulations, and a deviation from the expectation could indicate new physics [14]. Neutrino-nucleus scattering would be observed by neutrinos in the MeV-range scattering off nuclei and providing them with keV-range energy recoils, resulting in an ionization signal of less than 100 eV. The CCDs used in the DAMIC experiment are well-suited for identifying this process due to their low energy threshold, and we have designed a new experiment using many of the same technologies as in DAMIC to search for CNNS.

An ongoing experimental effort called CONNIE, which consists of an array of CCD detectors located 30 m outside a 3.8 GW_{th} nuclear reactor in Brazil, is currently collecting data in order to measure the coherent neutron scattering process. The detection of the coherent scattering of neutrinos is done by comparing data collected with the reactor on (RON) and the reactor off (ROFF). The radiation background is the ultimate limit for the sensitivity of the experiment. The backgrounds include cosmic-ray muons, which typically deposit 80 keV of minimum ionizing energy in a 250 µm-thick CCD. They are easily identified as straight tracks and removed from data providing they do not produce secondary particles by interacting with the shielding. A comparison of ROFF and RON data show that there is no significant extra background component from the reactor (Fig. 5.3). The cur-

rent radiation background observed in the engineering array is ∼3000 events/kg/day/keV (d.r.u.) at 0.5 keV. Preliminary results from an engineering run in 2015 using two CCDs, with an active mass of 4 grams of silicon and 19 days of RON and 15 days of ROFF data, indicate that backgrounds from fission products of the nuclear reactor are manageable, and provide first estimates of the sensitivity to coherent neutrino scattering using this detection technology of two orders of magnitude above standard model predictions [15]. These results indicate that the CONNIE experiment can feasibly yield a first observation of the CNNS process.

In July of 2016, the CONNIE experiment was upgraded to contain fourteen 6-gram CCDs, yielding a total mass of 83.6 grams. The CCDs have less defects than in the previous run, and some charge-injection problems that led to higher electronics noise during readout were solved. The noise is now verified to be 50% lower, allowing the experimental energy threshold to decrease by 50%. A further improvement has been the reduction of radio-impurities in the CCD packaging. The combined improvements in terms of mass, energy threshold, and lower background rates mean that the signal yield expected by the upgraded CONNIE experiment is 130 times greater. This greatly improves the expected signal significance, such that evidence for CNNS could be achieved within two years.

[13] D. Z. Freedman, Phys. Rev. D 9, 1389 (1974).

[14] R. Essig, R. Harnik, J. Kaplan and N. Toro, Phys. Rev. D **82**, 113008 (2010).

[15] A. Aguilar-Arevalo, *et al.*, Journal of Instrumentation 11, 7, P07024 (2016).

5.2.1 Calibration and testing

Of vital importance to both DAMIC and CONNIE is a correct energy calibration of nuclear recoils. This calibration for DM or neutrinos in the detector is factorized into the ionization energy calibration as determined from direct and fluorescent X-rays, and the signal quenching observed for ionizing nuclear recoils. The quenching factor has been measured in Si for recoil energies above 4 keV [16], showing good agreement with the Lindhard model [17, 18].

We have performed an experiment at the Tandem Van der Graaf of the University of Notre Dame in which monochromatic neutrons are scattered off a silicon detector target. The scattering angle and neutron time-of-flight are used to determine the nuclear recoil energy, and the ionization energy is measured in the silicon detector. The scattered neutrons are detected with a set of ∼20 scintillating bar counters placed at variant angles (from 20 to 70 degree) that correspond to the low recoil energies of interest (1 - 30 keV).

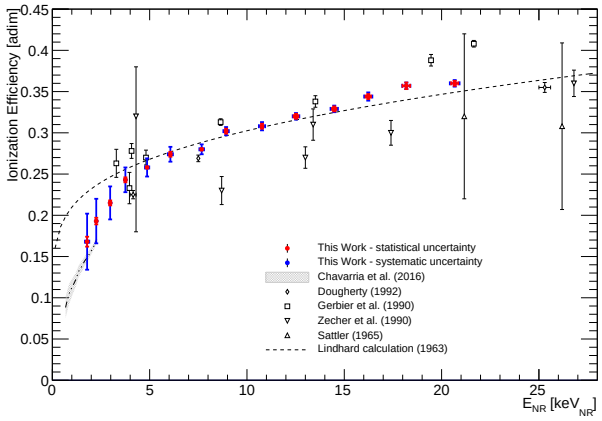

FIG. 5.4 – Results from Antonella data compared to the Lindhard model [17, 18] and testing the consistency with [21].

Besides designing and testing the detector for this calibration experiment, our group developed a GEANT [19] simulation of the detector setup to confirm the neutron beam flux, to model resonances of neutrons on silicon, and to determine the energy using the timing. The experiment was performed in 2015, and the results have been submitted for publication in 2017 [20]. Some of our collaborators have measured the quenching factor in the range from 680 eV to 2.3 keV using an independent technique [21], and have observed a deviation from the Lindhard model. Our result measures the quenching factor in the 1.8 to 20 keV range, showing agreement with this new calibration in the lower energy range, but also showing consistency with previous measurements in the upper energy range. The implication is that experiments using the Lindhard model at low energies could be overestimating the energy deposited in their detector, thereby overestimating their sensitivity to nuclear recoils from dark matter or neutrino scattering.

[16] J.D. Lewin and P.F. Smith, Astropart. Phys. 6, 87 (1996).

[17] J. Lindhard, V. Nielsen, M. Scharff, and P.V. Thomsen, Mat. Fys. Medd. Dan. Selsk **33**, 10 (1963).

[18] H. Chagani *et al.*, JINST 3 (2008) P06003.

[19] http://geant4.cern.ch.

[20] F. Izraelevitch *et al.*, arXiv:1702.00873 [physics.ins-det].

[21] A. E. Chavarria *et al.*, Phys. Rev. D **94**, no. 8, 082007 (2016).

6 Very High Energy Gamma Ray Astronomy with CTA

F. Canelli, D. Florin, A. Gadola, S. Steiner, U. Straumann, A. Vollhardt, D. Wolf

in collaboration with: MPI für Kernphysik Heidelberg, Universität Erlangen, Universität Innsbruck, Universität Tübingen and over 210 institutes from 32 countries

(CTA)

The next generation of Imaging Atmospheric Cherenkov Telescopes (IACT) for the detection of very high energy (VHE) gamma rays is on its way with the Cherenkov Telescope Array (CTA) project (www.cta-observatory.org). CTA aims to broaden the detectable energy range of VHE gamma rays and to improve on the precision of locating their origin compared to existing IACTs. This will be realized with two arrays, one on the southern hemisphere with about 100 and one on the northern hemisphere with about 20 IACTs. Three sizes of telescopes are foreseen to cover the full energy range of tens of GeV up to hundreds of TeV.

In the past year several major steps brought the CTA project closer to its realization. The first step was the foundation of the CTA Observatory (CTAO), a limited liability company (gGmbH), as an interim entity. Another step was the final site selection for the two telescope arrays. La Palma (Canary Islands) has been chosen to host the northern array at the same location as the already existing MAGIC [2] Cherenkov telescopes. The southern array will be located on the European Southern Observatory (ESO) area in Chile and should be operated by ESO. While the final agreement has already been signed for La Palma, CTAO is expected to finalize the contract with ESO in early 2017. In early March 2016 UZH group leader Prof. Ulrich Straumann was elected as Managing Director (MD) of the CTAO for one year (see e.g. [1]). Prof. Straumann has already been confirmed by the CTA council for a second period as MD beginning of 2017.

Since the UZH CTA group is involved in several major projects of CTA, i.e. camera mechanical body with safety and power for FlashCam, mirror actuators, interface control documents as well as the master clock for the whole telescope array, time management among the sub-projects is essential. A large part of the time is also invested into paperwork for different reviews, project planning and documentation.

6.1 FlashCam camera body

The FlashCam camera [3] is the first fully digital Cherenkov telescope camera and will suit the mid-size telescope of CTA. One major contribution of our group towards the camera has been the development and production of prototype series of photon-detector units. However, for a future mass-production of the units the responsibility was handed over to the University of Erlangen. The second large contribution is the design and production of the whole camera body mechanics including the camera safety control, the power control and distribution, as well as the cooling. After the first prototype body was tested on its mechanical compatibility with the mid-size telescope structure prototype in Adlershof, Berlin, the majority of the time was devoted to the integration of the lessons learned into the mechanical and electrical designs and the ordering of material for two additional prototype cameras. The redesign of the camera body is now finished, material ordered and already in-house and assembly of the body mechanics has started beginning of this year. Figure 6.1 shows the current state of one of the two camera bodies in our assembly hall. The two bodies should be ready

FIG. 6.1 – Assembly work of two prototype camera bodies has started with the aim of shipping the bodies to the integration lab in Heidelberg for the installation of the electronics in summer 2017. Shown is the rear view of one of the prototypes with open doors, installed racks, safety and power cabinet in the left lower corner, as well as the heat exchangers and fan trays.

FIG. 6.2 – Two safety and power cabinets under 24/7 testing before installation into the camera.

for shipment to the integration lab in Heidelberg in the course of this summer.

The safety and power cabinet of the camera has also been redesigned slightly to accommodate a more up-to-date control unit with a dedicated safety matrix and to make the cabinet even easier to maintain. Two prototypes have been assembled in-house and completed last year and have since been put to several functionality tests and long-term operation (over 4'000 hours of continuous operation accomplished). Figure 6.2 shows the two cabinets before being installed in the camera bodies.

6.2 Mirror actuator

The 220 actuator sets (figure 6.3), each consisting of two actuators and a fix point, produced in 2015 have meanwhile been tested by our Japanese collaborators and it was found that the mechanical tolerance was too large for some devices. This triggered an internal process of localizing the problematic production step and improving on the reliability of the production of the pieces. After fixing the few outliers and increasing the mechanical tolerance specifications from 20 up to 30 µm such to avoid an increased price due to hand-selection of good parts, all devices were accepted. It is expected that the actuators can be sent to the site for final installation on the first large-size telescope prototype on La Palma by the end of the year.

FIG. 6.3 – Latest version of the Zurich actuator as produced for the large-size prototype telescope.

The consolidation of devices which could be used across the different telescope types and hence reduce costs and improve maintainability has already started a long time ago in CTA. In this process the Zurich actuators have been chosen as standard actuators for the whole CTA. This means that a production batch of roughly 12'000 single actuators over the period of the next few years needs to be planned and organized. This step needs to be evaluated very carefully and will make an extension of the existing team a necessity.

[1] SBFI Newsletter, April 2016

[2] J. A. Coarasa *et al.*, (MAGIC collaboration), J. Phys. Soc. Jap. Suppl. 77B (2008) 49.

[3] G. Pühlhofer *et al.*, (FlashCam Collaboration), arXiv 1211.3684 [astro-ph.IM] (2012).

7 The $\pi^+ \to e^+\nu_e$ / $\pi^+ \to \mu^+\nu_\mu$ branching ratio

P. Robmann, A. van der Schaaf and P. Truöl

in collaboration with: University of Virginia, Charlottesville, USA; Institute for Nuclear Studies, Swierk, Poland; JINR, Dubna, Russia; PSI, Villigen, Switzerland and Rudjer Bošković Institute, Zagreb, Croatia

(PEN Collaboration)

The branching ratio $B \equiv \Gamma_{\pi^+\to e^+\nu_e}/\Gamma_{\pi^+\to\mu^+\nu_\mu}$ in lowest order is given by the product of a phase-space factor and a helicity factor:

$$B \simeq \left(\frac{m_\pi^2 - m_e^2}{m_\pi^2 - m_\mu^2}\right)^2 \times \frac{m_e^2}{m_\mu^2}$$
$$= 5.4869 \times 2.3390 \times 10^{-5} = 1.2834 \times 10^{-4}.$$

Uncertainties associated with the hadronic corrections cancel and radiative corrections slightly lower this value to 1.2353×10^{-4} [1]. Allowing for flavour dependence of g_ℓ (see graph below) B must be multiplied by g_e^2/g_μ^2.

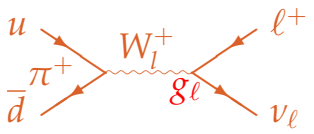

A measurement of B allows sensitive tests of both the $V-A$ structure and the lepton universality of the weak interaction. Until recently the experimental result $1.2312(37)\times10^{-4}$ dated back over thirty years [2] and two new experiments [3] aim at a reduction of the error by almost an order of magnitude. A first result of our PIENU friends, $1.2344\pm0.0023(\text{stat})\pm0.0019(\text{syst})\times10^{-4}$ based on 10% of their data set, was published two years ago [4].

Lepton universality can be tested in other systems too. Results are shown in Tab. 7.1 and 7.2.

TAB. 7.1 – SM and observed values for B_π and B_K

	$\Gamma_{\pi^+\to e^+\nu}/\Gamma_{\pi^+\to\mu^+\nu}$	$\Gamma_{K^+\to e^+\nu}/\Gamma_{K^+\to\mu^+\nu}$
theory	$1.2353(1)\times10^{-4}$	$2.477(1)\times10^{-5}$
experiment	$1.2312(37)\times10^{-4}$	$2.488(12)\times10^{-5}$

TAB. 7.2 – lepton universality tests (τ is the lepton or a lifetime)

decay	g_e/g_μ	g_τ/g_μ	g_τ/g_e
$\pi^+ \to \bar{l}\nu_l$	0.9985(16)		
$K^+ \to \bar{l}\nu_l$	1.0018(26)		
$K^+ \to \pi\bar{l}\nu_l$	0.998(2)		
$\tau^+ \to \bar{l}\nu\bar{\nu}$	0.9998(20)		
$W^+ \to \bar{l}\nu_l$	0.997(10)	1.039(13)	1.036(14)
$\tau \to \pi$ / $\pi \to \mu$		0.996(5)	
$\tau \to K$ / $K \to \mu$		0.979(17)	
$\tau \to e \times \tau_\mu/\tau_\tau$		1.0006(22)	
$\tau \to \mu \times \tau_\mu/\tau_\tau$			1.0005(23)

7.1 The PEN setup

The most expensive component by far is a 3π Sr spherical pure-CsI calorimeter (see Figs. 7.1, 7.2) used to measure positron and photon energies. Pure CsI has its main scintillation decay-time component around 28 ns, much shorter than most other inorganic scintillators.

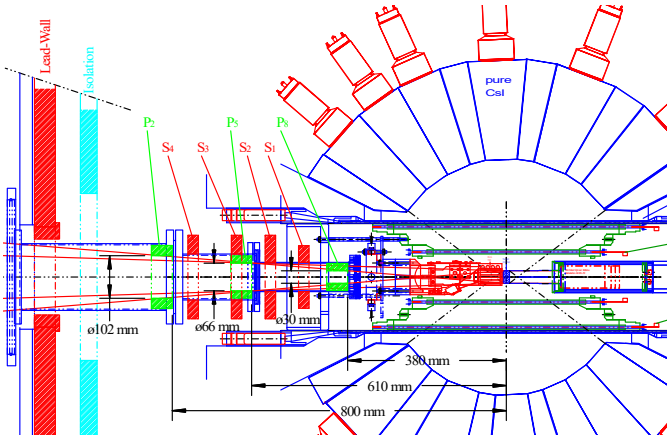

FIG. 7.1 – the PEN setup, $z-y$ cross section.

[1] V. Cirigliano and I. Rosell, JHEP **10** (2007) 5; Phys. Rev. Lett. **99** (2007) 231801.

[2] G. Czapek *et al.*, Phys. Rev. Lett. **70** (1993) 17; D. I. Britton *et al.*, Phys. Rev. Lett. **68** (1992) 3000.

[3] PEN Collaboration, PSI experiment R-05-01 (2005), D. Počanić and A. van der Schaaf, spokespersons; PIENU Collaboration, TRIUMF proposal 1072 (2006), D. Bryman and T. Numao, spokespersons.

[4] A. Aguilar-Arevalo *et al.*, [PIENU Collaboration], Phys. Rev. Lett. **115** (2015) 071801.

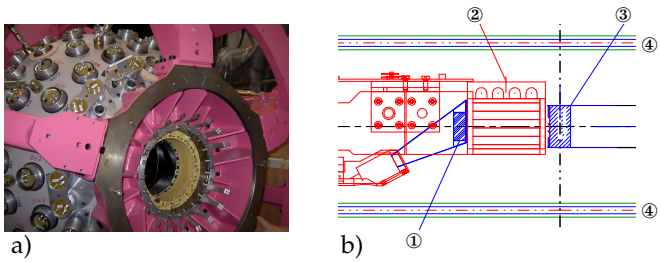

FIG. 7.2 – a) the PEN CsI calorimeter before cabling.
b) target region.
① degrader scintillator, ② mini TPC,
③ target scintillator, and ④ inner MWPC.

PEN took data at PSI during the years 2008 - 2010. Pions from the πE1 beam line stop in a plastic scintillator after having crossed a thin scintillator in an intermediate focus 4 m upstream, a small time-projection chamber (mini TPC) for accurate tracking (see Fig. 7.3) and a degrader scintillator, situated close to the target scintillator. Figure 7.4 shows a distribution of beam counter energy versus time of flight. Time of flight is not only used for particle identification but also for an accurate pion energy determination, event by event, used as input in the target waveform analysis.

Decay positrons from $\pi \to e\nu$ and the sequence $\pi \to \mu\nu$, $\mu \to e\nu\bar{\nu}$, are tracked in two cylindrical MWPCs with analogue cathode strip readout.

The positron energy is determined primarily with the CsI calorimeter. A cylindrical plastic scintillator hodoscope in front of the calorimeter is used both for timing and for particle identification (in particular to separate decay positrons and protons from pion reactions) through $\Delta E - E$.

Whereas the $\pi^+ \to e^+\nu(\gamma)$ decay was recorded with almost 100% efficiency for e^+ emitted in the calorimeter acceptance, the $\pi - \mu$ branch was recorded only for $\Delta t_{\pi e} < 220$ ns. Events with e^+ energies below ≈ 48 MeV were pre-scaled by typically a factor 20.

7.2 Data analysis

The recorded data have been studied in great detail. Calibrations are done and most features observed are reproduced by simulation (see previous annual reports for details).

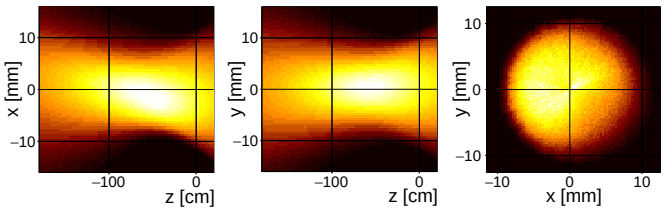

FIG. 7.3 – Mini TPC trajectories. The beam spot, limited by a $\varnothing = 20$ mm collimator, is shifted in x for best suppression of beam e^+ situated further to the left.

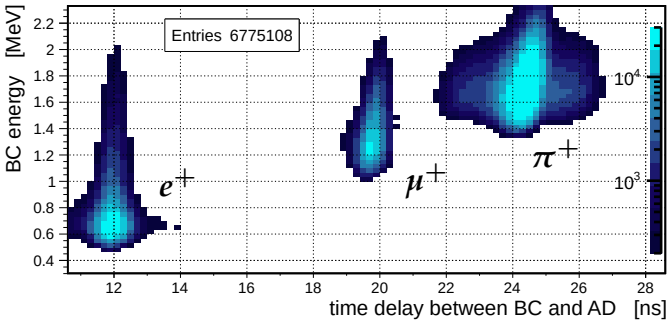

FIG. 7.4 – Beam counter (BC) energy versus time of flight between BC and active degrader (AD) at 75 MeV/c beam momentum. Beam particles (e^+, μ^+ and π^+) are well separated.

Key observables are the $e^+(\gamma)$ invariant mass (μ) and $\Delta t_{\pi e}$. The invariant mass is calculated as the sum of the observed total energy (so e^+ plus γ energies) and observed total momentum (e^+ plus γ momenta, which equals the ν momentum). These observables are reconstructed without individual particle identification, so even for small $e\gamma$ opening angle. The decay sequence $\pi^+ \to \mu^+\nu$ followed by $\mu^+ \to e^+\nu\bar{\nu}(\gamma)$ is characterized by a continuous invariant mass distribution with endpoint m_μ and time delay first rising with τ_π and then falling with τ_μ=2.197 μs.

7.2.1 Target waveform analysis

An important ingredient in the event reconstruction is the (non)observation of a muon signal in the target waveform. The target waveform has contributions from the stopping pion and the decay positron. In most cases there is also the signal from a 4.1 MeV intermediate muon. Figure 7.5 shows target energy distributions for clean $\pi \to \mu \to e$ sequences. Whereas π's and μ's stop in the target (so the distributions represent their kinetic energies) the e^+ energy is the energy loss only which scales with path length and is smeared by Landau fluctuations. Figure 7.6 illustrates for millions of events how π and μ signals merge when the pion decay-time approaches zero.

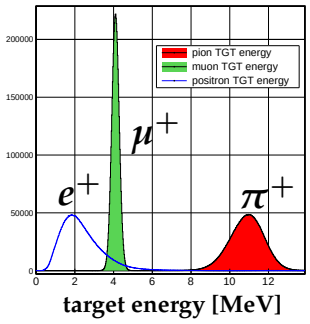

FIG. 7.5 – Target energy distributions for well-separated $\pi \to \mu \to e$ sequences. Secondary μ^+ and e^+ should not be confused with the beam particles in Fig.7.4! Energy quenching has been corrected for. In pion decay at rest muons are monoenergetic with T=4.1 [MeV].

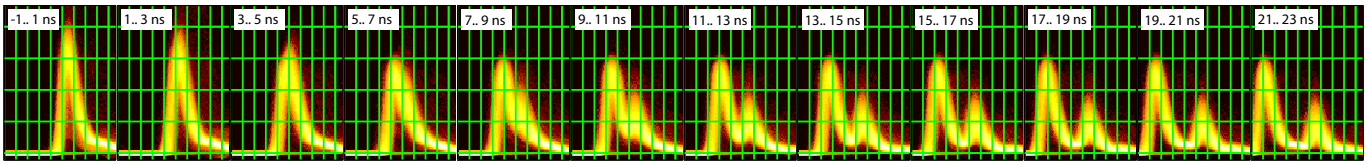

FIG. 7.6 – Filtered $\pi \to \mu$ target signals for windows on the pion decay time (increasing from -1.1 ns to 23 ns) as indicated for events with late positrons.

Figure 7.7 illustrates how the occurrence of an intermediate muon is tested. First the waveform is filtered by multiplication with a vector optimized for optimal almost symmetric output shape. The numerical procedure removes signal tails beyond the scintillator's intrinsic decay-time and reflections caused by imperfect transmission lines. The π^+ and e^+ signals are predicted, based on the full event information. The only free parameter is the location of the 4.1 MeV muon signal. The algorithm gives as output the difference in χ^2 between the hypotheses of a muon or not (see Fig. 7.8). Note that the two event classes can be separated by a factor thousand at least, ten times better than by invariant mass.

7.2.2 Full kinematic reconstruction of $\pi \to e\nu\gamma$

Since the trigger of the experiment, based on the total CsI energy, also selected radiative decays $\pi \to e\nu\gamma$ in the geometric acceptance defined by the CsI calorimeter, the PEN data allow for the first time the analysis of this decay mode in almost the full phase space. The decay $\pi \to e\nu\gamma$ is of interest since, contrary to the inner Bremsstrahlung contribution, the structure-dependent contributions are not helicity suppressed [5].

During 2016 the data analysis was re-organized such that $\pi \to e\nu\gamma$ events can be reconstructed independent of $e\gamma$ opening angle and γ energy. The new approach is based on total energy and total momentum, observed in the full 3π Sr acceptance of PEN which immediately gives the invariant mass (see Fig. 7.9). Combined with the e^+ tracking information a complete kinematic reconstruction is made in the full phase space of the decay, including the region with potential muon decay background which could not be accessed before. Presently the attempt is made to improve the theoretical prediction[3] and to get rid of the stratified sampling.

By the time of writing a full reconstruction of the measurements is in place. What remains to be done is a thorough analysis of the systematic error in B. It is dominated by uncertainties in the low-energy tail of the invariant-

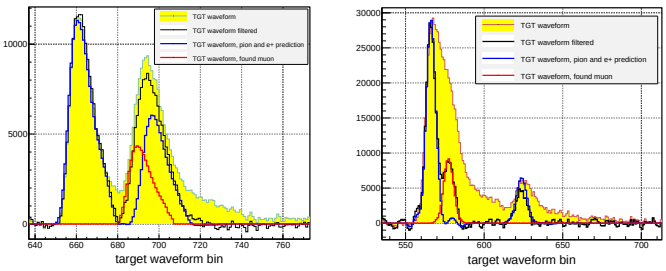

FIG. 7.7 – Two examples of target waveforms and their reconstruction (see text).

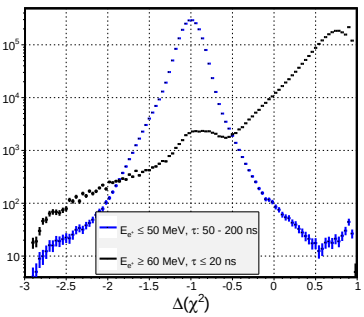

FIG. 7.8 – $\Delta(\chi^2)$ of the target waveform analysis. Events with a muon peak at -1, those without at +1.

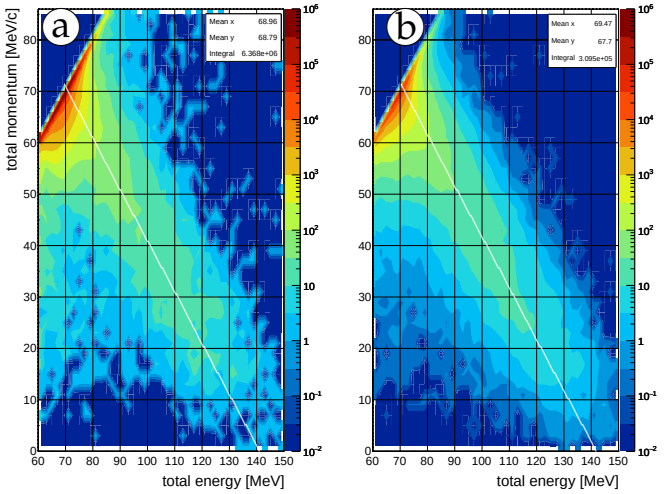

FIG. 7.9 – Distributions of total observed momentum versus total observed energy for events without μ in the target waveform; a) measurement, b) $\pi \to e\nu\gamma$ simulation. In the decay $\pi \to e\nu\gamma$ at rest the total momentum is equal to the ν momentum, so $E + pc = m_\pi c^2$ (white lines). In the present simulation events with $E \approx pc$ (low γ energy and small $e\gamma$ opening angle) have been suppressed.

[3] We acknowledge advice by Gino Isidori in these matters.

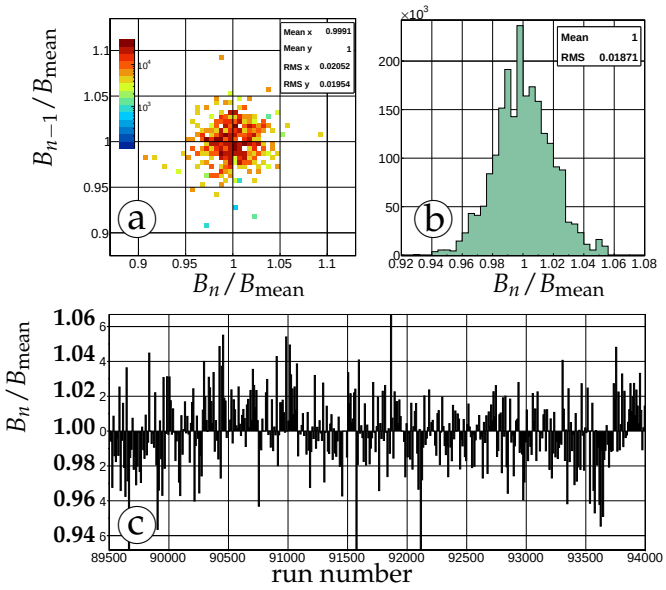

FIG. 7.10 – B, normalized to its mean value, during 2009 for six hour beam periods. a) correlation between consecutive measurements of B_n/B_{mean}. b) distribution of B_n/B_{mean} weighted with $N_{\pi\to e\nu}$ observed during the measuring period. c) B_n/B_{mean} versus run number.

mass distribution which ultimately relies on simulation. The uncertainty in the fraction of $\pi^+ \to \mu^+\nu(\gamma)$ decays within the chosen $\Delta t_{\pi e}$ window is minimized by choosing a window corresponding to the situation in which the event rate is equal at both ends. For a 100 ns wide window this happens for 81.4 - 181.4 ns.

Figure 7.10 gives a feeling of the PEN data quality. Shown are simple determinations of B during the first year of data-taking, corresponding to roughly one third of the full data set. For beam periods of ≈ 6 hours B is determined in a simple cut analysis of invariant mass, $\Delta t_{\pi e}$ and $\Delta(\chi^2)$ of the target waveform. The statistical error of the full data set as deduced from Fig. 7.10 b) is below 0.05%.

FIG. 7.11 – PEN crew solving problems in a bar in Charlottesville. Left to right: Charlie Glaser, Anthony Palladino, Andries van der Schaaf, Mike Vitz, and Martin Lehman.

The final results of PEN are in Virginia hands after the old man on Fig. 7.11 retired on April 1st 2017.

[5] For details see the 2013 PEN report http://www.physik.uzh.ch/reports.shtml.

8 Particle Physics with SHiP

C. Betancourt, I. Bezshyiko, E. Graverini, P. Owen, N. Serra, B. Storaci

The full SHiP collaboration consists of 45 institutes from Bulgaria, Chile, Denmark, France, Germany, Italy, Japan, Russia, Sweden, Switzerland, Turkey, Ukraine, the United Kingdom and the United States of America.

(SHiP Collaboration)

SHiP is a newly proposed general purpose fixed target facility at the CERN SPS accelerator. A 400 GeV proton beam will be dumped on a heavy target in order to produce 2×10^{20} proton-target interactions in five years. A dedicated detector downstream of the target will probe a variety of models with light long-lived exotic particles with masses below $\mathcal{O}(10\,\mathrm{GeV/c^2})$. Active neutrino cross-sections and angular distributions will also be studied, thanks to a dedicated detector placed between the target and the hidden sector detector [1].

SHiP's flagship goal is to use decays of charm and beauty mesons to search for Heavy Neutral Leptons (HNLs), which are right-handed partners of the Standard Model (SM) neutrinos. The existence of such particles is strongly motivated by theory, as they can simultaneously solve multiple problems left open by the SM. In the Neutrino Minimal Standard Model (νMSM), HNLs allow to explain the baryon asymmetry of the Universe, account for the pattern of neutrino masses and oscillations and provide a dark matter candidate [2].

Our group was one of the founding groups since the Expression of Interest submitted in 2013 [1]. We continue to play a leading role by taking charge of the physics programme (Nicola Serra is convener for the SHiP physics performance) and of part of the detector design and R&D (Barbara Storaci is convener for the upstream veto and timing detectors).

The experiment has recently been positively reviewed by the relevant scientific committee at CERN (SPSC), who requested the preparation of a Comprehensive Design Report (CDR). The CDR will be incorporated into the European Strategy Document of CERN which will be prepared by the year 2019.

[1] W. Bonivento *et al.*, arXiv:1310.1762, SPSC-EOI-010.

[2] A. Takehiko, S. Blanchet and M. Shaposhnikov, Phys. Lett. B631 151-156 (2005)

8.1 SHiP detector

A dedicated beam line extracted from the SPS will convey a 400 GeV/c proton beam at the SHiP facility [3, 4]. The beam will be stopped in a Molybdenum and Tungsten target, at a center-of-mass energy of about 27 GeV. Approximately 2×10^{20} proton-target collisions (PoT) are foreseen in five years of operation. The target will be followed by a hadron stopper and a system of shielding magnets to sweep muons away from the fiducial decay volume. A neutrino detector consisting of OPERA-like bricks of laminated lead and emulsions, followed by a tracker and a muon spectrometer, will allow for measurement and identification of charged particles produced in charged current neutrino interactions. An upstream tagger will help detect and veto charged particles produced in front of the main decay volume, contained in a 50 m long cylindrical vacuum vessel with elliptical section. A straw tagger is placed in vacuum 5 m downstream of the entrance lid of the vessel. An additional background tagger surrounds the fiducial decay volume. Its walls enclose 30 cm of liquid scintillator. The Hidden Sector (HS) detector will comprise: a tracking system placed in vacuum at the end of the vessel, made of 5 m long straw tubes organized in four stations in a 1 Tm magnetic field; a high-accuracy timing detector; and a particle identification system featuring electromagnetic and hadronic calorimeters followed by a muon system made of four active layers interlaced with iron.

Recently, we played a leading role in studying the reoptimization of the SHiP detector. In order to get closer to the target, thereby increasing the acceptance, the vacuum vessel was redesigned with a conical shape. In addition, the sweeping magnet was also reoptimized. The layout of the SHiP experiment after the reoptimization is shown in Fig. 8.1.

[3] W. Bonivento *et al.*, arXiv:1310.1762, SPSC-EOI-010.

[4] M. Anelli *et al.*, [SHiP Collab.], arXiv:1504.04956.

8.2 SHiP studies

8.2.1 SHiP magnet studies

I. Bezshyiko

A muon flux of 10^{11}/spill is expected in SHiP. These muons could incur background, and hence their flux has to be reduced by several orders of magnitude over the shortest possible distance to achieve the largest possible acceptance for HNLs. SHiP adopted the use of a series of magnets to deflect the muons out of the acceptance of the spectrometer. The muon shield had the strict requirement to sweep muons out of the (x,y)=(5,10) m area at the

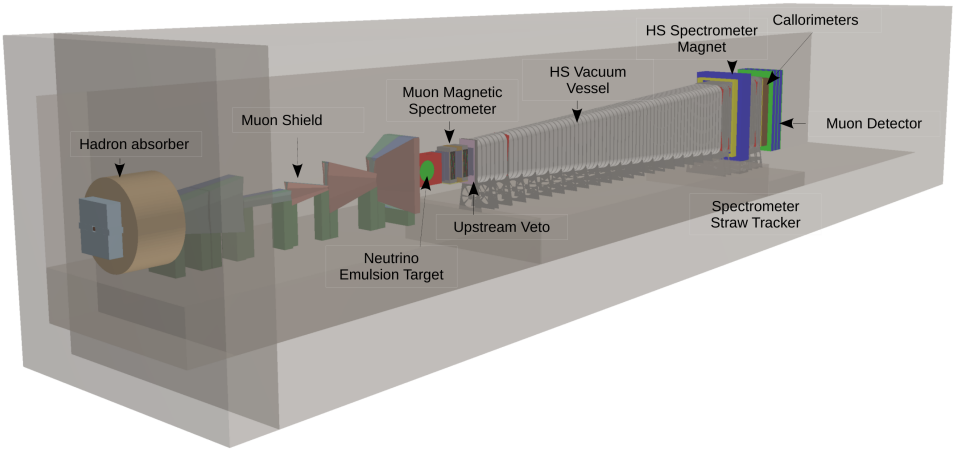

FIG. 8.1 – Overview of the SHiP detector. From left to right we have: the target, followed by the hadron stopper, the muon shield, the neutrino and Light-Dark-Matter detector (emulsion detector and muon magnetic spectrometer), the Hidden Sector vacuum vessel and the Hidden Sector spectrometer. The latter consists of straw tube tracking stations, a dipole magnet, a veto-timing detector, a calorimeter system and a muon system.

beginning of the decay vessel in the configuration of the technical proposal. SHIP now moved to a conical vessel design, which relaxes the requirement of the shield, having to clear only 5x10 m at the position of the last tracking station.

Our group took a major role in the optimization of the active muon shield for the new SHiP geometry configuration. The optimization had the goal to reduce the amount of used iron, but maintain a decent muon reduction. New procedures were developed for simulation and optimization of the shield magnets taking into account the total mass of the magnets and the background level from muons in the spectrometer. A special function was written in the FAIRROOT framework to configure the magnets taking into account the necessary space for their coils and shaping their armature to reduce their magnetic reluctance. The total mass of iron for the muon shield was reduced from 2896 to 1845 tons while keeping the background level from muons at an acceptable level [5].

[5] I. Bezshyiko, H. Dijkstra, "The Active Muon Shield", CERN-SHiP-NOTE-2016-005.

8.2.2 Timing detector

C. Betencourt, R. Brüngler, N. Serra and B. Storaci

Background muons, mostly backscattered from the surrounding walls, can enter the decay vessel and can be reconstructed as fake signals. This combinatorial di-muon background is randomly distributed in time along the whole length of a spill, so an effective rejection of these events would be a coincidence timing requirement. In order to reduce this background to an acceptable level, a dedicated timing detector located between the spectrometer and the calorimeters with a timing resolution of 100 ps or less is required [6].

Our group is studying one option for such a detector consisting of rows of plastic scintillating bars, readout on either end by Silicon Photomultipliers. Such a technology has already been shown to resolve signals on the sub 100 ps range [7]. Effort is ongoing to optimize the geometry and electronic readout of such a set-up as would be appropriate for SHiP. Initial studies indicate that a resolution down to 50 ps is possible [8].

[6] M. Anelli *et al.*, [SHiP Collab.], arXiv:1504.04956.

[7] P. Cattaneo *et al.*, IEEE Trans. Nucl. Sci. 61, 2657, (2014).

[8] C. Betancourt *et al.*, JINST 12, (2017).

8.2.3 Background studies

I. Bezshyiko, and N. Serra

The flux of neutrinos is estimated to be 10^{11} neutrinos per spill, with an energy spectrum ranging from 2 GeV to about 350 GeV. A large statistic sample of neutrino interactions with the detector material was simulated, corresponding to the amount of neutrino interactions expected in five years of SHiP operation. Neutrino interactions were found to mainly take place in the muon magnetic spectrometer of the tau neutrino detector, in the entrance window of the vacuum vessel and in its surrounding walls. The probability that neutrinos interact with the residual gas inside the decay volume is negligible if the vacuum pressure is 10^{-6} bar. A more detailed analysis showed that many of these background events can be rejected by using the veto tagger and requiring that the reconstructed candidate points back to the primary target [9]. This would allow to relax the requirements on the vacuum pressure.

The topology of the products of the neutrino interactions is such that relatively loose selection cuts allow efficient rejection. Table 8.1 shows that no HNL candidates were found which satisfy all the selection cuts. Less than 0.1 background events were found for non-pointing events without using the information from the surround veto tagger. Detailed investigation

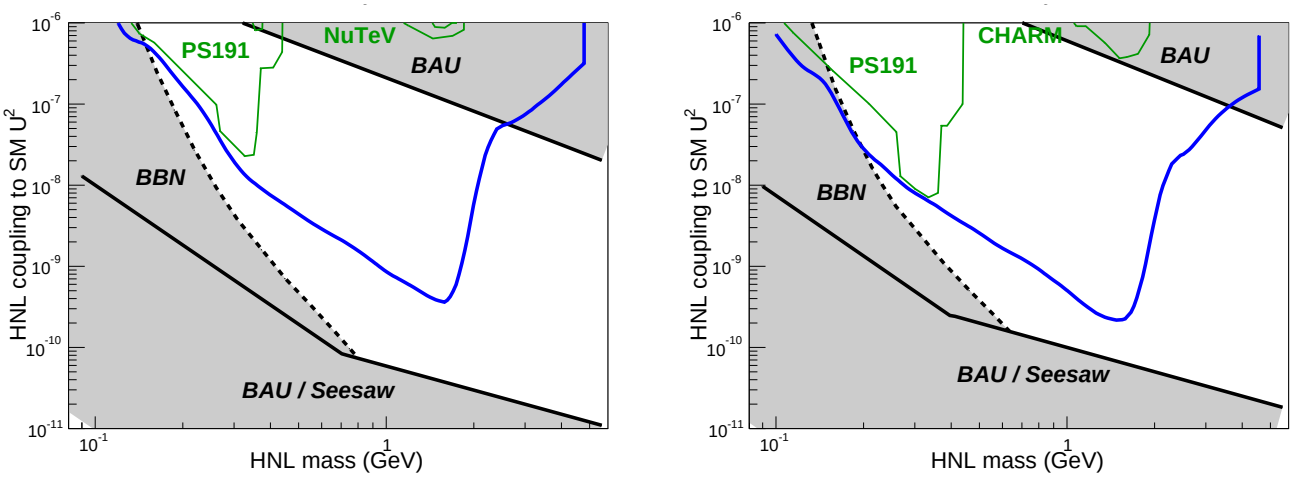

FIG. 8.2 – SHiP's sensitivity to HNLs assuming normal (left) or inverted (right) hierarchy of the SM neutrino masses. The parameter space of the νMSM is superimposed.

of these events revealed a strong correlation between the reconstructed vertex and the geometrical position of the closest hit in the vacuum tagger, which allows to make the selection based on only part of the tagger. In general the interaction products do not point to the target, do not have a reconstructed vertex inside the decay volume, and have very poor track quality.

TAB. 8.1 – Expected neutrino background in 5 years

Selection type	HNL cand.
Pointed events, with veto system	0
Pointed events, no veto system	0
Non-pointed events, with veto system	0
Non-pointed events, no veto system	<0.1

[9] M. Anelli *et al.*, [SHiP Collab.], arXiv:1504.04956.

8.2.4 SHiP sensitivity

E. Graverini, N. Serra and P. Owen

Our group has provided the official SHiP sensitivity estimates for the νMSM, the SHiP flagship theory, and for dark photons, the gauge bosons of a minimalistic theory based on the breaking of a $U(1)$ symmetry in the HS.

The SHiP physics sensitivities are evaluated on the basis of the official simulation and reconstruction package, called FAIRSHIP, the development of which our group contributed substantially, and of a fast Monte Carlo simulation developed in order to determine both the rate of HNLs produced at the target and the acceptance of the HNL decay products. From these estimates, the expected number of events in five years of SHiP operation is calculated. SHiP's sensitivity to HNLs assuming normal or inverted hierarchy of the SM neutrino masses is shown in Fig. 8.2.

The official software and the fast simulation were compared and validated against each other. The official software, that contains a full GEANT4 description of the material and detector geometry, was used to devise offline selections able to suppress the background while maintaining a large signal acceptance. To assess the impact of the reconstruction and selection on the signal, a correction to the fast simulation is applied as a function of the mass of the HNL, based on the outcome of the full simulation, separately for two body and three body decays.

A very similar method, analogous the one used by the authors of [10], was used to estimate SHiP's sensitivity to dark photons. SHiP's sensitivity is shown in Fig. 8.3. Several other models with hidden particles can be studied at SHiP and are described in Ref. [11].

[10] J. Blümlein and J. Brunner, Phys. Lett. B731 (2014).

[11] S. Alekhin et al., arXiv:1504.04855, CERN-SPSC-2015-017.

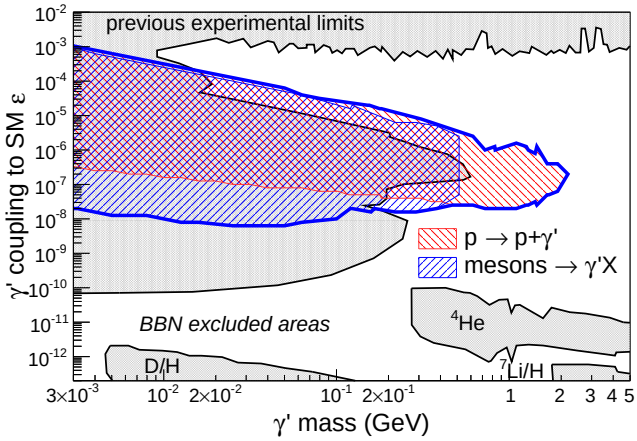

FIG. 8.3 – SHiP's sensitivity to dark photons. Previous searches, as well as limits from cosmological observations, are superimposed.

9 Particle Physics with LHCb

C. Abellan, M. Atzeni (since January 2017), R. Bernet, Ch. Betancourt, I. Bezshyiko, E. Bowen (until February 2016), M. Chrząszcz[1], E. Graverini, F. Lionetto, A. Mauri, K. Müller, P. Owen (since May 2016), A. Puig Navarro (since September 2016), N. Serra, R. Silva Coutinho, St. Steiner, O. Steinkamp, B. Storaci, U. Straumann, M. Tresch (until March 2017), A. Vollhardt, and A. Weiden

[1] also at Henryk Niewodniczanski Institute of Nuclear Physics, Polish Academy of Sciences, Kraków, Poland

The full LHCb collaboration consists of 71 institutes from Brazil, China, Colombia, France, Germany, Ireland, Italy, Poland, Romania, Russia, Spain, Switzerland, the Netherlands, Ukraine, the United Kingdom and the United States of America.

(LHCb Collaboration)

LHCb is a dedicated heavy flavour physics experiment at the CERN Large Hadron Collider (LHC) [1] optimised for precision tests of the Standard Model (SM) and for indirect searches for physics beyond the SM (BSM) through precision measurements of *CP* violating phases and rare heavy-quark decays. The detector is designed as a forward spectrometer, fully instrumented in the pseudorapidity range $2 < \eta < 5$. This forward acceptance and the ability to trigger on particles with relatively low transverse momentum allow to probe particle production in a unique kinematic range.

The Zurich group is responsible for the operation and maintenance of silicon detectors in the tracking system and contribute to the R&D for the upgraded LHCb detector. Furthermore, our group makes significant contributions to measurements of rare B-meson and τ lepton decays as well as measurements involving electroweak gauge bosons. Members of our group play important coordination roles within the collaboration: N. Serra is member of the editorial board, B. Storaci operations coordinator, K. Müller deputy chair of the speakers bureau and O. Steinkamp deputy project leader of the silicon tracker.

[1] LHCb Collab., JINST 3 S08005 (2008).

9.1 LHCb detector

The LHCb detector was successfully operated in Run I (2009-2013), where data corresponding to an integrated luminosity of 3 fb^{-1} was collected at centre of mass energies ($\sqrt{s}$) of 7 and 8 TeV. In Run II, which started in May 2015, the centre of mass energy increased to 13 TeV. In 2016 LHCb collected about 1.7 fb^{-1} of good quality data in pp collisions. In addition, data samples were collected in pPb collisions and pHe fixed target collisions using the internal gas target. This sample with an integrated luminosity of 0.4 nb^{-1} was used for the first measurement of antiproton production outside of the Earth's atmosphere [2].

[2] LHCb Collab., LHCb-CONF-2017-002.

9.1.1 TT Detector performance

E. Graverini, A. Mauri, O. Steinkamp, B. Storaci

The Tracker Turicensis (TT) detector continued to perform excellently in 2016. At the end of the year, more than 99.5% of its 143'360 readout channels were fully operational. Towards the end of the year, a small number of detector modules began to suffer from the breaking of wire bonds in between silicon sensors and front-end readout chips. This phenomenon had already been observed during the first months of operation in 2010, but the cause for these failures have never been fully understood. The newly affected modules were repaired in January 2016. We acknowledge the excellent work of Stefan Steiner and our former colleague Tariel Sakhelashvili, now at Dectris Ltd., Baden-Daettwil, for their invaluable contribution to this effort. The single-hit detection efficiency remained very close to 100%; the observed position resolution is 53 µm, compared to 48 µm expected from simulation. Studies of the spatial alignment of the detector elements are still ongoing and a further improvement in position resolution can be expected.

The radiation damage of the silicon detectors was monitored regularly by measuring leakage currents and by performing charge-collection efficiency scans (details have been reported in previous annual reports). The results of our studies agree well with expectations and no degradation of the detector performance is expected until its foreseen replacement during the LHCb upgrade in the next long LHC shutdown in 2019.

9.2 LHCb upgrade

C. Abellan, Ch. Betancourt, I. Bezshyiko, F. Lionetto, O. Steinkamp

The LHCb collaboration prepares for a comprehensive upgrade during the second long shutdown of the LHC in 2019/2020 [3]. The upgraded detector is going to be able to operate at a five times higher instantaneous luminosity, permitting to collect interesting events at increased rate. Moreover, the detector will be fully read out at the LHC bunch-crossing frequency of 40 MHz, eliminating the need for a hardware-based low-level trigger and thereby significantly increasing selection efficiencies for many final states of interest.

The current TT detector will have to be replaced as part of this upgrade, since its front-end readout electronics is not compatible with the new readout scheme. The replacement for the TT, dubbed Upstream Tracker (UT), is being developed by a collaboration including our group as well as CERN and six institutions from Italy, Poland and the US [4]. To best exploit our experience in operating the existing detector, we have taken the responsibility for the development of detector control software, power distribution, the monitoring of operational and environmental parameters, and detector safety. Moreover, we play a prominent role in the testing of the newly developed front-end readout chip (SALT) and have contributed in test beam efforts to qualify radiation-hard silicon sensors for the UT. Due to recent funding cuts, our future involvement in the upgrade project is currently unclear.

[3] LHCb Collab., CERN-LHCC-2012-007.

[4] LHCb Collab., CERN-LHCC-2014-001.

9.3 Track reconstruction at software trigger level

E. Bowen, E. Graverini, B. Storaci, M. Tresch

Fast and efficient track reconstruction algorithms are crucial for the successful operation of the all-software trigger of the upgraded LHCb detector. We developed a novel algorithm connecting track segments in the vertex detector to hits in the UT, which allowed to speed up the track reconstruction to the required level, with no loss in reconstruction efficiency [5]. We back-ported this algorithm for use with the current detector. This back-ported algorithm was introduced in the software trigger during 2015 and was used also throughout 2016. The faster track reconstruction allowed to apply less stringent trigger requirements, increasing data collection rates for various analyses and reducing systematic uncertainties due to selection biases in others. Moreover, the successful operation of the algorithm in actual data taking provided an important proof-of-principle for the upgrade. We remain responsible for the maintenance of the code.

[5] E. Bowen and B. Storaci, CERN-LHCb-PUB-2013-023.

9.4 Physics results

The LHCb collaboration published about 60 physics papers during the past year [6], covering a wide range of topics. Some of the main results are highlighted below, while analyses with direct contributions from our group will be discussed in more detail in the next sections.

The study of the very rare decays $B^0_{(s)} \to \mu\mu$ is one of the key analyses of LHCb. Since New Physics (NP) may contribute at the same order of magnitude as the SM, the measurements of the branching fractions strongly constrain the allowed parameter space for NP models. LHCb published the first observation by a single experiment of the decay $B^0_s \to \mu\mu$, with a statistical significance of 7.8 standard deviations [7]. The measured branching fraction $(3.0 \pm 0.6 + 0.3 - 0.2) \cdot 10^{-9}$ is in agreement with the SM prediction and is the most precise measurement of this quantity to date. The effective lifetime of B^0_s lifetime was measured to be $2.04 \pm 0.44 \pm 0.05$ ps in agreement with the SM prediction.

A combination of measurements sensitive to the CKM angle γ, which is a measure of the amount of *CP* violation in the SM, was performed [8]. The combination yields $\gamma = (72.2^{+6.8}_{-7.3})^\circ$ corresponding to the most precise determination of γ from a single experiment to date.

The parameter A^Δ, which is related to the photon polarisation in $b \to s\gamma$ transitions, was determined from a time-dependent analysis of the $B^0_s \to \Phi\gamma$ decay rate. The measured value of $A^\Delta = 0.98^{+0.46}_{-0.52}{}^{+0.23}_{-0.20}$ is consistent with the SM prediction [9].

The hadronic B^0 decay into a K^+K^- pair was observed for the first time and the branching fractions for $B^0 \to K^+K^-$ and $B^0 \to \pi^+\pi^-$ measured with unprecedent precision [10]. The decay into a kaon pair is the rarest fully hadronic B decay mode ever observed. Precise knowledge of the branching fractions of these decays is needed to improve the understanding of QCD dynamics in the more general sector of two-body B-hadron decays. The invariant mass distribution of the K^+K^- is shown in Fig. 9.1.

The phenomenon of *CP* violation has been observed so far in the K and B-meson systems. LHCb published first evidence of *CP* violation in baryons using the decays $\Lambda^0_b \to p\pi^-\pi^+\pi^-$ and $\Lambda^0_b \to p\pi^-K^+K^-$ [11] with a statistical significance corresponding to 3.3 standard deviations. *CP* violation was also searched for in charm decays where mixing induced and direct *CP* asymmetries are expected to be small, but can be highly enhanced by NP contributions. The LHCb measurements of asymmetries in the time-dependent rates of $D^0 \to K^+K$ and $D^0 \to \pi^+\pi$ decays show no evidence for *CP* violation and improve on the precision of the previous best measurements by nearly a factor of two [12].

Besides many significant contributions in studies of b-hadrons, results from spectroscopy and production measurements at LHCb have caught considerable attention. LHCb

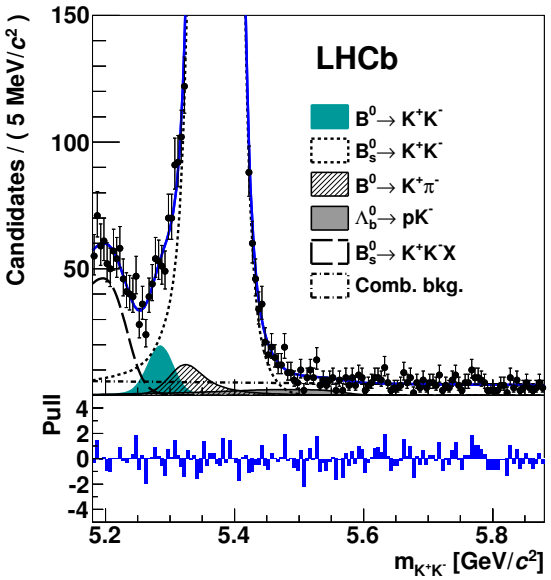

FIG. 9.1 – Invariant mass $m_{K^+K^-}$ distribution. The fitted contribution for $B^0 \to K^+K^-$ is shown as full area.

reported the observation of four exotic particles decaying into a J/ψ and a Φ meson in $B^+ \to J/\psi\Phi K^+$ decays [13]. Their properties are consistent with their interpretation as four-quark particles (tetraquarks or strange charm charged meson pairs). Evidence for exotic hadron production consistent with the previously observed states $P_c^+(4450)$, $P_c(4380)$ and $Z_c(4200)$ was also found in the decay $\Lambda_b^0 \to J/\psi p\pi^-$ [14].

[6] http://lhcb.web.cern.ch/lhcb/

[7] LHCb Collab., arXiv:1703.05747 [hep-ex].

[8] LHCb Collab., JHEP **12** (2016) 087.

[9] LHCb Collab., Phys. Rev. Lett. **118** 021801.

[10] LHCb Collab., Phys. Rev. Lett. **118** (2017) 081801.

[11] LHCb Collab., Nature Phys. (2017).

[12] LHCb Collab., arXiv:1702.06490 [hep-ex].

[13] LHCb Collab., Phys. Rev. Lett. **118** (2017) 022003.

[14] LHCb Collab., Phys. Rev. Lett. **117** (2016) 082003.

9.4.1 Angular analysis of the decay $B^0 \to K^*\mu^+\mu^-$

E. Bowen, M. Chrząszcz, N. Serra, R. Coutinho, A. Mauri

The decay $B^0 \to K^*\mu^+\mu^-$ is a flavour changing neutral current with a branching ratio of about 10^{-6}. Since new particles may enter in loops with competitive amplitudes angular observables are sensitive probes of NP. Measurements of this decay performed by our group with an integrated luminosity corresponding to 1 fb^{-1} [15] have shown significant tensions with respect to SM predictions, corresponding to about 3.7 standard deviations. These measurements are widely discussed in the literature. Several authors have interpreted these measurements as a possible sign of physics beyond the SM [16],while others have pointed out to possible underestimated QCD uncertainties [17].Our group has been leading the measurement of angular observables with 3 fb^{-1} [18]. We have contributed to various aspects of the analysis including the signal selection, the correction of detector acceptance and the determination of angular observables. In particular, we proposed a novel method based on the moments of the angular distribution [19]. This method allows to measure the angular observables in small bins of dimuon invariant mass. In addition, we have shown that the method of moments is more robust against mis-modelling of the angular distribution. Figure 9.2 shows the comparison between the SM predictions from [20] (yellow bands) and the measurement of P_5' with a likelihood (black points) and the method of moments (red points).Good agreement is observed with the different methods. The new measurement exhibit a deviation with respect to the theory predictions of about 3 standard deviations for each of the two bins in the region $4.0 < q^2 < 8.0\,\text{GeV}^2/c^4$, where q^2 is the invariant mass squared of the two muons.

The $B \to K\pi\mu^+\mu^-$ system above the $K^*(892)$ resonance has so far received little attention. We have pioneered the measurement of angular observables for this decay, in the region dominated by the resonances $K^{*0,2}(1430)$. This measurement is challenging, since several different K^* resonances contribute to this $K\pi$ invariant mass. Considering $S-$, $P-$ and $D-$ waves there are in total 41 independent moments, which give access to the full angular distribution. This analysis led to the world's first measurement of this decay. In addition to the 41 independent angular moments (20 are shown in Fig. 9.3), we measured the differential branching ratio as a function of q^2 and the fraction of $D-$wave (f_D). While it was naively expected to observe a dominant $D-$wave contribution, we have no evidence of such a contribution and we set an upper limit $f_D < 0.29$ at 95% CL. This result is unexpected since the $B^0 \to J/\psi K\pi$ decay has a dominant $D-$wave contribution in this region (around 70%) of the $K\pi$ invariant mass. This effect could be due to a large breaking of QCD factorisation.

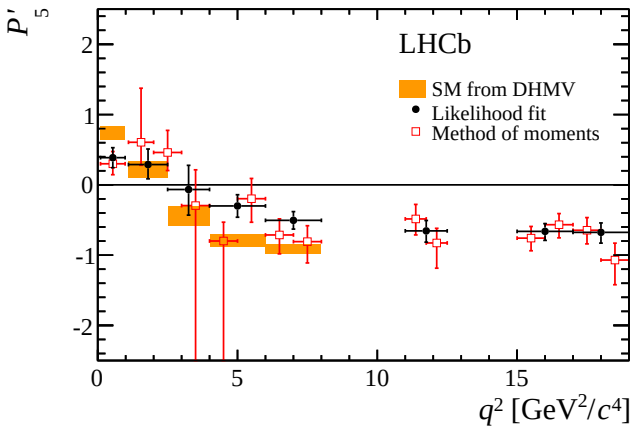

FIG. 9.2 – The angular observable P_5' in the decay $B^0 \to K^{*0}\mu^+\mu^-$ measured by LHCb with a data set corresponding to 3 fb^{-1} compared to the SM predictions from Ref. [20].

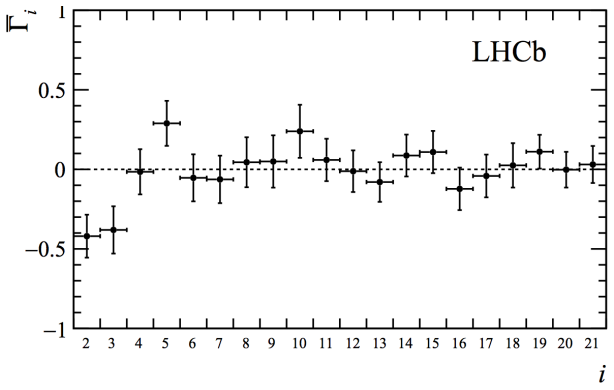

FIG. 9.3 – Measurement of the 20 out of 41 moments in the decay $B^0 \to K^{*0}\mu\mu$.

[15] LHCb Collab., Phys.Rev.Lett. 111 (2013) 191801.

[16] A. Karan et al., arXiv:1603.04355;
S. Descotes-Genon, J. Matias and J. Virto,
Phys. Rev. D 88, 074002 (2013);
R. Gauld, F. Goertz and U. Haisch,
JHEP 1401 (2014) 069;
A. J. Buras and J. Girrbach, JHEP 1312 (2013) 009;
W. Altmannshofer and D. M. Straub,
Eur. Phys. J. C73 (2013) 2646;
D. Ghosh, M. Nardecchia and S. A. Renner,
arXiv:1408.4097.

[17] F. Beaujean, C. Bobeth, D. van Dyk,
Eur. Phys. J. C 74 (2014) 2897;
J. Lyon, R. Zwicky, arXiv:1406.0566;
M. Ciuchini et al., JHEP 1305 (2013) 043.

[18] LHCb Collab., JHEP 02 (2016) 104.

[19] F. Beaujean, M. Chrzaszcz, N. Serra and D. van Dyk,
Phys. Rev. D 91, 114012 (2015).

[20] S. Descotes-Genon *et al.*, JHEP 01 (2013) 048.

9.4.2 Study of $b \to se^+e^-$ transitions

R. Coutinho, F. Lionetto, A. Puig, N. Serra

The measurement of the ratio of branching fractions $R_K = \mathcal{B}(B^+ \to K^+\mu^+\mu^-)/\mathcal{B}(B^+ \to K^+e^+e^-)$ was found to be 2.6 standard deviations in tension with respect to SM predictions [21]. Several authors have argued that this deviation is consistent with the deviations observed in $b \to s\mu\mu$ decays, which could be an indication of NP that breaks the lepton universality of the SM. The recent LHCb result on the ratio of branching fractions $R_{K^*} = \mathcal{B}(B^+ \to K^*\mu^+\mu^-)/\mathcal{B}(B^+ \to K^*e^+e^-)$ [22], also showing deviations above two sigma with respect to the SM, has added even more interest to these tantalising hints of NP. Our group is involved in several tests of lepton universality in $b \to se^+e^-$ transitions. The main goal will be to measure the asymmetry $A(P_5') = (P_5^{ee\prime} - P_5^{\mu\mu\prime})/(P_5^{ee\prime} + P_5^{\mu\mu\prime})$ using $B^0 \to K^{*0}\mu^+\mu^-$ and $B^0 \to K^{*0}e^+e^-$ decays; this analysis is of key importance to reinforce the R_X measurements, as its dependency on experimental effects is very different. To provide a quick and robust check to the R_X anomalies, we also plan to study these angular asymmetries using a simplified counting experiment. In addition, the measurements of the ratio of branching ratios $R_{K\pi} = \mathcal{B}(B^0 \to K\pi\mu^+\mu^-)\mathcal{B}(B^0 \to K\pi e^+e^-)$ and $R_{K\pi\pi} = \mathcal{B}(B^+ \to K\pi\pi\mu^+\mu^-)\mathcal{B}(B^+ \to K\pi\pi e^+e^-)$ in a wide range of $K\pi$ and $K\pi\pi$ masses, which our group is leading, have the potential to confirm or disprove lepton universality hints in rare decays. In both cases, the di-electron mode has never been observed, so a first observation will also need to be performed.

[21] LHCb Collab., Phys. Rev. Lett. **113** (2014), 151601.

[22] LHCb Collab., arXiv:1705.05802.

9.4.3 Measuring the Breaking of Lepton Flavour Universality in $B \to K^*\ell^+\ell^-$

R. Coutinho, N. Serra in collaboration with D. van Dyk

Inspired by the recent measurements of $b \to s\ell^+\ell^-$ transitions we proposed a new set of observables D_i ($i = 4, 5, 6s$), sensitive to LFU-breaking effects in the decays $B \to K^*\ell^+\ell^-$ ($\ell = e, \mu$) [23]. These observables are branching-ratio-weighted averages of differences (with respect to the final-state lepton flavour) of the angular observables $S_{4,5,6s}$. In the presence of LFU-breaking NP effects in $\mathcal{C}_9^{(\ell)}$ their theoretical uncertainties due to charm-induced hadronic contributions are kinematically suppressed to $< 7\%$ in the region of $1 \leq q^2 \leq 6\,\text{GeV}^2$. This allows predictions in the NP scenarios that can be systematically improved as our knowledge of the $B \to K^*$ form factors and CKM Wolfenstein parameters improves.

The D_i observables can be measured at the LHCb or at the Belle II experiments, either by performing likelihood fits of the angular distribution of the decays $B \to K^*\ell^+\ell^-$ or by using the method of moments. We found that in order to obtain 3σ evidence for NP in only these observables and using the method of moments, roughly 1500 $B \to K^*e^+e^-$ signal events are necessary in either experiment (Figure 9.4).

[23] N. Serra, R. Silva Coutinho and D. van Dyk,
Phys. Rev. D 95, 035029 (2017).

9.4.4 Search for new scalar particles in B decays

M. Chrząszcz, A. Mauri, N. Serra

At LHCb the light inflaton, or more in general any other light scalar from the hidden sector mixing with the Higgs, can be searched for by analysing the decay $B^+ \to K^+\chi$, where the light scalar χ subsequently decays into a pair of muons. We have carried out this analysis setting the world's best limits as a function of the mass and lifetime of the χ scalar particle [24]. Our analysis sets severe limits on the inflaton

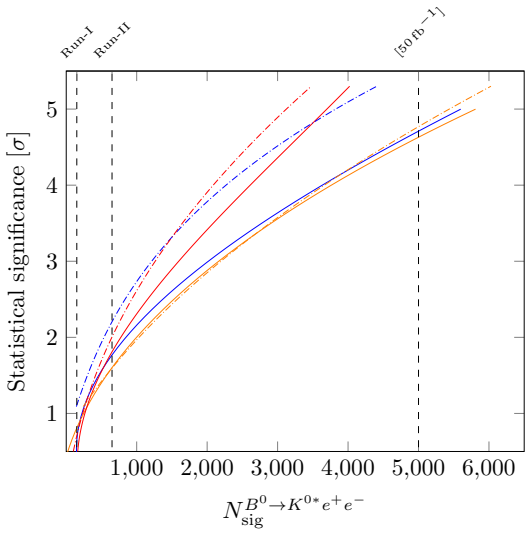

FIG. 9.4 – Projected statistical-only significance as a function of the extrapolated yields in LHCb for the (blue) $\langle D_5\rangle_{1,6}$ and (orange) $\langle D_{6s}\rangle_{1,6}$ observables, obtained from the (solid line) method-of-moments and (dash-dotted line) likelihood fit. The red lines indicate the combined significance.

model (Fig. 9.5) and now only corners of the phase-space are allowed, making the model highly unlikely.

[24] LHCb Collab., Phys. Rev. D **95**, 071101 (2017).

9.4.5 Semileptonic decays

M. Chrząszcz, E. Graverini, P. Owen, N. Serra

The strongest evidence for a violation of lepton universality is seen in the branching fraction of semileptonic decays involving a τ lepton. In particular, the measurement of the observables $R(D)$ [25, 26] and $R(D^*)$ [25–27]. This enhancement can be explained in many extensions to the SM which preferentially couple to third generation leptons, such as an additional charged Higgs boson.

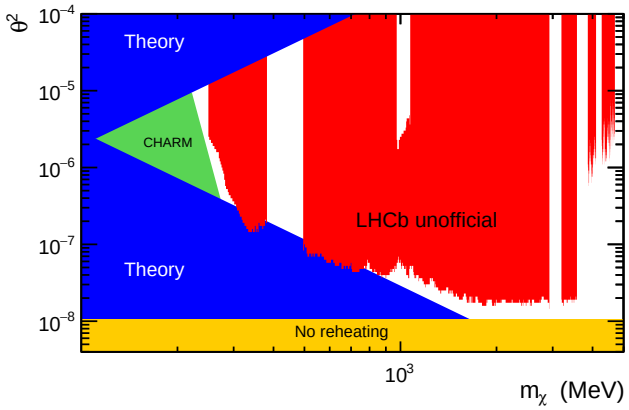

FIG. 9.5 – Interpretation of the limits of the $B^+ \to K^+\chi$ analysis in the context of the inflaton model. The phase space of allowed regions (white) is severely reduced, leaving only corners.

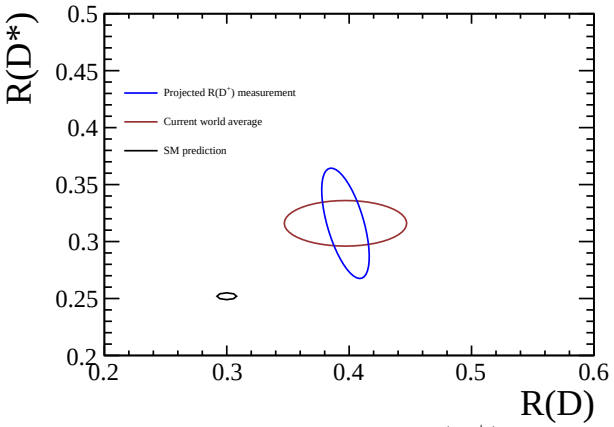

FIG. 9.6 – Projection for the observable $R(D^+)$ for Run II of LHCb, compared with the current world average [28] of the observable $R(D^{(*)})$. This measurement has the potential to break the correlation between $R(D)$ and $R(D^*)$.

Our group is presently involved in supplementing this information with the measurement of $R(D^+)$, which has the potential to disentangle enhancements to the observables $R(D)$ and $R(D^*)$. We are also involved in a new test of lepton universality, measuring the ratio $R(\Lambda_c^*) = \mathcal{B}(\Lambda_b^0 \to \Lambda_c^*\tau\nu)\mathcal{B}(\Lambda_b^0 \to \Lambda_c^*\mu\nu)$. This measurement is important to confirm present tensions and also to provide complementary information as this is a measurement of a fermion decay, which behaves differently under the laws of angular momentum conservation. An illustration of the sensitivity for $R(D^+)$ can be seen in Fig. 9.6.

[25] J. P. Lees *et al.* [BaBar Collab.], Phys.Rev.D 88, 072012 (2013).

[26] M. Huschle *et al.* [Belle Collab.], Phys. Rev. D 92, 072014 (2015).

[27] LHCb Collab., Phys. Rev. Lett. 115 (2015) 111803.

[28] HFAC Collaboration http://www.slac/stanford.edu/xorg/hfag

9.4.6 Charmless

R. Coutinho

The study of charmless three-body decays of neutral B mesons and beauty baryons to final states containing K_S^0 mesons is of great interest for improving the understanding of hadronic interactions and in the search for CP violation effects. Searches for the remaining unobserved mesonic channel $B_s^0 \to K_S^0 K^+ K^-$ has been performed using a sample of pp collision data. An indication for this decay is obtained and its branching fraction, relative to the $B^0 \to K_S^0\pi^+\pi^-$ decay, is determined. Updated branching fraction measurements of the other $B_{(s)}^0 \to K_S^0 h^+ h'^-$ decay modes (where $h^{(\prime)} = \pi, K$), are also presented prior to the forthcoming Dalitz plot analyses with the Run I data sample. The paper draft of this result is

under final collaboration circulation and will be submitted to JHEP soon.

Dalitz-plot analyses of the most prominent modes, *i.e.* $B^0 \to K^0_S\pi^+\pi^-$ and $B^0_s \to K^0_S K^+\pi^-$, have been performed and are close to completion. The first observation of a non-vanishing *CP* asymmetry in the decay $B^0 \to K^*(892)^+\pi^-$ is obtained, with a significance of 6 standard deviations. Moreover, the results from the first untagged decay-time-integrated amplitude analysis in the B^0_s mode are either first to date or in good agreement with, and more precise than, the previous measurements.

As-yet no confirmation of *CP* violation has been found in *b*-hadron decays, further studies are rather compelling. An interesting channel to investigate is the $\Lambda^0_b \to K^0_S p\pi^-$, which has been previously studied with $1.0\,\text{fb}^{-1}$ [29]. Although the *CP* asymmetry observed shows no significant deviation from zero, this measurement is statistically dominated. Therefore, an update of this analysis with full Run I and a subset of Run II dataset is of great interest and it is being performed by our group. Moreover, inspired by the methodology implemented in $B^\pm \to h^\pm h^\mp h^\pm$ decays that recently revealed large anisotropies in the phase-space distribution [30], we are extending this treatment for this baryonic mode, that significantly enhances the discovery potential of *CP* violation. In particular, this approach is able to measure asymmetries in the decay $\Lambda^0_b \to pK^{*-}$, which is predicted to have a large *CP* violation effect.

[29] LHCb Collab., J. High Energy Phys. **04** (2014) 087

[30] LHCb Collab., Phys. Rev. D **90** (2014) 112004

9.4.7 Measurements with electroweak bosons

M. Chrząszcz, K. Müller, M. Tresch, A. Weiden

Our group has been constantly contributing to the LHCb measurements involving electroweak bosons in the past years. A measurement of Z production at $\sqrt{s} = 13\,\text{TeV}$ has been published recently [31]. These measurements are of general interest as they are sensitive to the momentum distribution of the partons in the proton (PDFs) in a kinematic region not accessible to other experiments. The description of the PDFs is important for all production measurements at LHC and their uncertainty limits the reach of direct searches for rare or new processes. Besides the inclusive production of electroweak bosons new measurements have been performed by LHCb of exclusive final states such as electroweak bosons with jets [32] or W plus $b\bar{b}$ or $c\bar{c}$ production [33].

In the past year work in our group concentrated on the measurement of Z bosons with the associated production of a long lived particle (K^0_S or Λ^0). This probes the soft part of the interaction (hadronisation, fragmentation and multiple interactions) which cannot be calculated perturbatively but is modelled in Monte Carlo programs which need to be tuned to data. As the LHC is a hadron collider, the understanding

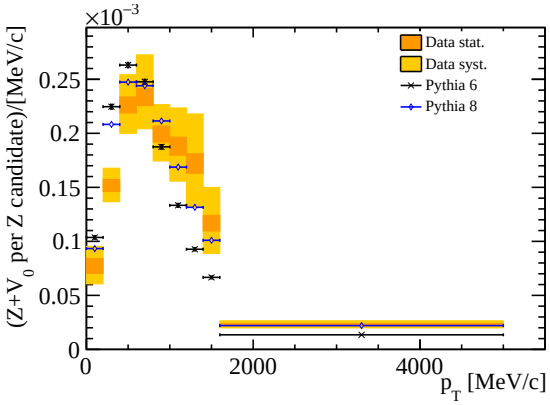

FIG. 9.7 – Number of K^0_S per Z boson as a function of p_T for data and predictions by PYTHIA.

of the soft part of QCD plays a crucial role also for measurements at ATLAS and CMS, such as searches for new particles or precision measurements of the Higgs boson. For a full picture the soft contribution should be measured in as many different processes as possible. The analysis of Z boson production in association with strange hadrons was the topic of the thesis of Marco Tresch, where a first measurement of the number of K^0_S or $\Lambda/\overline{\Lambda}$ in events with a Z boson decaying into two muons was performed as function of the opening angle between the Z boson and the strange composite particle or the transverse momentum of the latter.

As an example Fig. 9.7 shows the p_T distribution of the K^0_s in comparison to predictions from PYTHIA 6 and PYTHIA 8. For ZK^0_S production PYTHIA 8 better describes the distribution at high p_T, being a reflection of the hard diffractive processes which are included in the latter. For $Z\Lambda$ production both predictions significantly underestimate the data in agreement with observations by LHCb at lower scales [34]. The measurements however suffer from large uncertainties mainly due to limited statistics in the simulation samples needed for the efficiency correction.

[31] LHCb Collab., JHEP **09** (2016) 136.

[32] LHCb Collab., JHEP **05** (2016) 131.

[33] LHCb Collab., Phys. Lett. **B767** (2017) 110.

[34] LHCb Collab., JHEP **08** (2011) 034.

9.5 Summary and Outlook

The LHCb experiment has performed very well throughout the 2016 LHC run with a very high data taking efficency and stable running even with heavy ion collisions. The LHCb collaboration continued to produce high quality results, which resulted in more than 40 publications and many conference contributions, many of these already based on the new data collected at a centre of mass energy of 13 TeV. The Zurich group made important contributions to the operation of the experiment, physics analyses and preparation for the upgrade.

10 Particle physics with the CMS experiment at CERN

T. Årrestad, L. Caminada, F. Canelli, A. de Cosa, R. del Burgo, S. Donato, C. Galloni, G. Giannini, A. Hinzmann, T. Hreus, B. Kilminster, C. Lange, I. Neutelings, J. Ngadiuba, D. Pinna, G. Rauco, P. Robmann, D. Salerno, K. Schweiger, C. Seitz, Y. Takahashi, A. Zucchetta

in collaboration with:

CMS - Collaboration

The CMS experiment acquired a record year of data in 2016, collecting over 40 fb^{-1} of 13 TeV center of mass proton-proton collisions, more than all previous years combined. During an extended year-end shutdown between 2016 and 2017 data taking, a new 4-layer pixel detector was installed in the center of CMS, set to provide the experiment with improved triggering, tracking, and vertexing capabilities.

Here we present an overview of our CMS activities. Our major activity in 2016 was completing and commissioning the new 4-layer Phase 1 pixel detector system. We have also maintained and operated the present pixel detector which has taken data from 2010 to 2016, and are beginning with simulation studies and the design of a future Phase 2 pixel upgrade, envisioned to be ready in 2023. Besides our work on the original and upgraded pixel detectors, we are also involved in trigger development and monitoring as well as physics data analysis on a number of different topics.

Our physics analysis program addresses fundamental questions in particle physics. After the discovery of a Higgs particle at the LHC [1], studying its properties is among the primary goals. We are testing the fermionic couplings of the Higgs boson, with several analyses geared towards its couplings to tau leptons, top quarks, and bottom quarks. We are testing several theoretical models which could extend the Standard Model (SM), with new particle states at a few TeV. These generate loop corrections with the necessary cancellations to stabilize the Higgs boson mass. Models such as supersymmetry, extra dimensions, and vector-like quarks justify the mysteriously low Higgs boson mass, and predict a wide range of new particles, which we are sifting through CMS data to observe.

Members of our group play important coordination roles. In the period covered by this report, S. Donato acted as co-convener of the Software Tools, Online Releases and Menus subgroup under Trigger Coordination. A. de Cosa was subgroup convener within the Beyond 2 Generations (B2G) physics group, A. Hinzmann acted as convener of the JetMET algorithms and reconstruction group, and C. Seitz as subgroup convener within the inclusive Supersymmetry (SUSY) physics group. Y. Takahashi was main editor of the Higgs Tau observation group. S. Donato and L. Caminada are members of the Swiss Tier 3 computing steering committee. F. Canelli is on the CMS Management Board, and B. Kilminster is on the Management Board for the phase 1 upgrade and the Tracker group.

[1] ATLAS collaboration, Phys. Lett. B **716** (2012) 29; CMS collaboration, Phys. Lett. B **716** (2012) 30.

10.1 The CMS experiment

CMS [2] is one of the multipurpose detectors at the LHC. It consists of different layers of detectors optimized for position and energy measurements of particles produced in collisions. An all-silicon tracker, an electromagnetic calorimeter, and a hadronic sampling calorimeter are all contained within a large-bore 3.8 T superconducting solenoid. Beyond the solenoid there are four layers of muon detectors. The CMS tracker is composed of the inner pixel detector and the outer silicon strip detector. Up until the end of 2016, the pixel detector has consisted of three barrel layers (BPIX) at 4.4, 7.3, and 10.2 cm, and two forward/backward disks (FPIX) at longitudinal positions of $\pm$34.5 cm and $\pm$46.5 cm and extending in radius from about 6 to 15 cm. The high segmentation of the pixel detector allows for high-precision tracking in the region closest to the interaction point. The pixel detector information is crucial for primary vertex and pile-up vertex reconstruction, and identification of long-lived τ-leptons and B-hadrons. The performance of the current pixel detector has been excellent. It is noteworthy that the BPIX was built by the Swiss Consortium, PSI, ETH and the University of Zurich.

[2] CMS collaboration, JINST **3** (2008) S08004.

10.2 Detector maintenance and operation

The CMS pixel detector is a central component in the reconstruction of high-quality data used in Physics analysis. It performed very reliably during the whole period of data taking at the LHC at a very high efficiency and with more than 98% of its 66 million channels working. Our group made

significant contributions to the operation of the pixel detector as well as the re-calibration during technical stops of the accelerator. Our group is responsible for the monitoring of detector performance and operational parameters, which is crucial in order to respond with preventive actions that ensure high-quality physics data. In particular, we keep track of the evolution of the radiation damage to the silicon sensors with increasing luminosity, measure threshold and noise distributions, as well as pixel hit resolutions, and determine the impact of pixel dynamic inefficiencies.

The pixel detector hit efficiency as a function of instantaneous luminosity is shown in Fig. 10.1. The efficiency is well above 99% for the outer two layers of the BPIX detector and forward disks, while limitations in the readout speed at higher luminosities degrade the efficiency for the innermost layer. In order to maintain the excellent performance of the pixel detector at the higher luminosities foreseen in the coming years, the pixel detector has been exchanged with an upgraded system as described in section 10.3.

To be well-prepared for a short commissioning period and to gain experience with the upgraded system, a pilot pixel system was installed into CMS and has been operating since 2014. The pilot system suffered from read-out problems that prevented it from data-taking within the CMS data acquisition system. Our group scrutinized and determined the nature of these erroneous events, leading to new firmware, which reduces the error rate by 3 to 4 orders of magnitude, eventually allowing the pilot system to successfully join the CMS data-taking.

Our group is also involved in another key part of the CMS detector, the trigger system. We took care of development and maintenance of the High Level Trigger (HLT) code, along with preparation and testing of trigger menus in the different 2016 data taking scenarios, including the special proton-lead collision data taking. We contributed in the monitoring of HLT trigger rates by producing dedicated MC samples. We also worked in the online b-tagging development with both 2016 and 2017 pixel geometry [3].

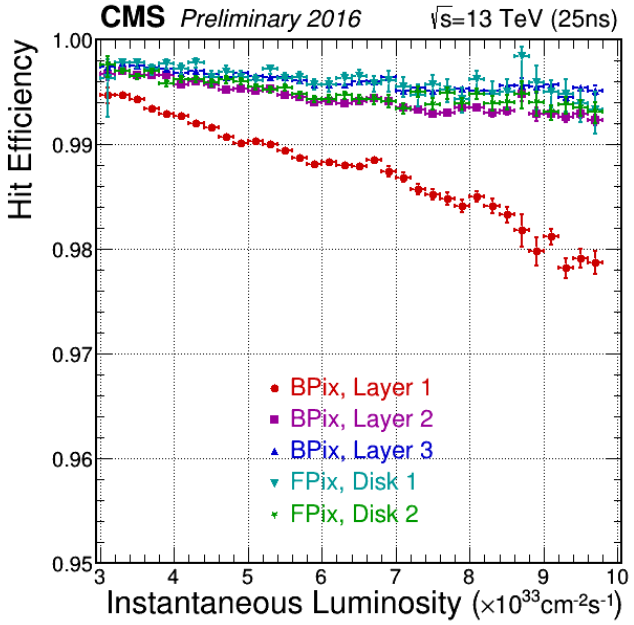

FIG. 10.1 – The pixel detector hit efficiency as a function of instantaneous luminosity for the three barrel layers and the two forward disks as measured during data-taking in 2016.

[3] CMS collaboration, CMS-DP-2017/011.

10.3 Upgrades

Our group, together with ETH Zürich and PSI, led the development and construction of a new and improved pixel system, the so-called Phase 1 pixel upgrade. The CMS Phase 1 pixel upgrade combines a new pixel readout chip, which minimizes detection inefficiencies, with several other design improvements. The current 3-layer BPIX, 2-disk FPIX detector was replaced with a 4-layer BPIX, 3-disk FPIX detector. The upgraded BPIX detector consists of four 57 cm long layers of silicon pixel modules serviced by 2.2 m of supply tubes which transport cooling tubes, electrical power, and optical signals to and from the pixel detector. The addition of an extra layer, closer to the beam pipe, demands a complete redesign of the power, cooling, and electronics.

Together with the UZH workshop we built the supply tube mechanical structure and designed and fabricated the new lightweight, thin-walled CO_2 cooling system. The supply tube multi-layer carbonized foam structure houses the electronics, cooling, power distribution, module control boards, and DC-DC converters. The cooling system is constructed in a complicated looping structure in order to cool the individual detector components including pixel modules, DC-DC converters and opto hybrids. In order to protect against possible corrosion, we use a special-quality steel alloy for all parts, and implement computerized, machine-automated laser welding. The production of the supply tube mechanics and the cooling system has been completed and passed highest quality assurance standards.

The assembly of the readout electronics, the power lines and the cooling loops on the supply tube structure took place at the end of 2016 at UZH. The dense arrangement of the many individual components in the constrained radial envelope make the assembly procedure very challenging. During and after the assembly all the components need to be tested and validated before merging the supply tubes and the pixel detector modules. More than 2000 single optical fibers and 1000 low-voltage and high-voltage power-lines had to be connected and tested as shown in Fig 10.2.

The fully tested supply tubes were then merged with the BPIX detector at PSI in January 2017 before transporting the completed detector system to CERN. Our group made significant contributions during an intense period of detector

FIG. 10.2 – Shown are the four CMS pixel supply tubes half-shells in various stages of completion, with control and readout electronics, power, fibers, and cooling.

checkout and testing in view of the installation in CMS only one month later. This allowed us to transport the detector in a fully functional state to CERN and to successfully install it into CMS within the tight schedule. Our efforts now focus on commissioning and calibration to prepare the detector for stable and efficient operation during the next run.

The upgraded pixel detector is designed to provide optimal performance for the whole Phase 1 operation, until the third long shutdown of the accelerator (2023-2025) when a new pixel detector for the High Luminosity (HL) LHC will be installed (Phase 2). To meet the challenges arising from the increased luminosity of the machine, we are already now performing R&D for the next generation of pixel systems. In particular efforts are ramping up to evaluate the performance of different designs concerning the number and positioning of the pixel layers, the optimal pixel size as well as the overall mechanical design and technical implementation.

10.4 Analysis algorithms

Our group regularly contributes to measuring and improving the CMS performance in terms of physics objects (such as particles and jets) and algorithms. The group helped producing the jet energy scale and resolution measurement [4], as well as validating a likelihood-based tagger capable of discriminating jets initiated by quarks from those initiated by gluons [5]. We introduced machine learning techniques to improve the performance of the quark-gluon tagger, increasing the probability of correct assignment of quark initiated jets with up to 10% compared to the previous likelihood-based tagger at the same mis-tag rate.

We have extended efforts in the identification of τ objects, especially in the development of a *boosted tau* algorithm [6] capable of identifying two τ-leptons produced in close proximity to one another, as would be the case in the decay of a heavy particle. This can be used to identify boosted Higgs and Z bosons decaying to τ-leptons. Together with our major contribution to the development of algorithms used to identify boosted W and Z bosons decaying into quarks, we have a comprehensive search program for new physics in the boosted boson topology. In parallel, we are working on tackling one of the main challenges of LHC Run-2, namely the mitigation of effects related to multiple interactions in the same bunch crossing ("pileup"). One approach is to use local shape information, event pileup properties and tracking information together to mitigate the effect of pileup on jet observables. This technique was validated in data for the first time and was found to maintain W-tagging performance up to at least 40 simultaneous interactions [5].

[4] CMS collaboration, JINST **12** P02014.

[5] CMS collaboration, CMS-PAS-JME-16-003.

[6] CMS collaboration, CMS-DP-2016-038.

10.5 Higgs Properties

10.5.1 Higgs boson couplings to top quarks

The search for the Higgs boson produced in association with a top-quark pair (ttH) is the only way to directly probe the order-one Higgs-top coupling and, among ttH channels, the search for the Higgs boson decaying into b quarks probes only third-generation Higgs-fermion couplings, with the largest Higgs branching ratio of $H \to bb$ ($\sim 58\%$).

An excess of 4.4 standard deviations over SM backgrounds was observed in the search for ttH after Run-1, combining ATLAS and CMS results, while an excess of 2.0 standard deviation was expected [7]. This corresponds to a Higgs boson cross section of $\mu = 2.3^{+0.7}_{-0.6}$ times the SM prediction and might be a hint of New Physics.

We have searched for $t\bar{t}H(\to b\bar{b})$ with 12.9 fb^{-1} of Run-2 data both in the single and double lepton final states [9]. The analysis exploited the Matrix Element Method (MEM) we developed in the last years [8] combined with a machine learning discriminant. The MEM distribution of an analysis category is shown in Fig. 10.3. A background under fluctuation has been reported ($\mu = -0.19^{+0.80}_{-0.81}$) while an excess of 1.5 standard deviations was expected. This analysis will be updated with the whole 2016 dataset (~ 38 fb^{-1}).

We are looking to include the fully hadronic final state which has a branching ratio as large as 46% in the $t\bar{t}H(\to b\bar{b})$ analysis. Challenges are the multijet QCD background and its estimate from data, along with the application of the MEM in an environment with significant combinatorial background given the large number of jets in the final states. Meanwhile, we are developing a trigger with online b-tagging for the 2017 data taking, exploiting the new pixel detector.

[7] CMS and ATLAS collaborations, JHEP **08** (2016) 045.

[8] CMS collaboration, EPJ C **75** (2015) 251.

[9] CMS collaboration, CMS-PAS-HIG-16-038.

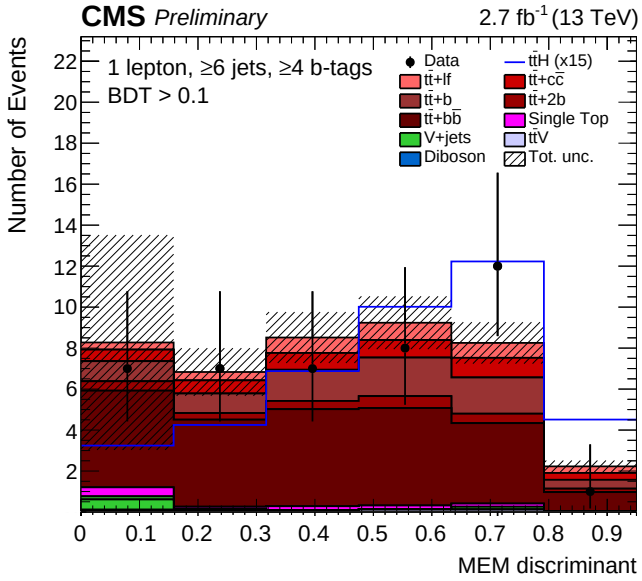

FIG. 10.3 – The MEM discriminant for one category of ttH candidate events before the final fit.

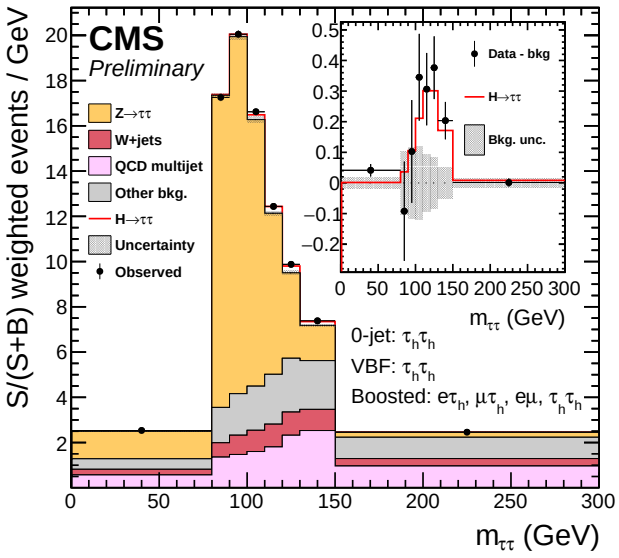

FIG. 10.4 – New CMS observation of H $\rightarrow \tau\tau$, produced by combining several final states.

10.5.2 Higgs coupling to τ leptons

Discovering the fermionic final states of the Higgs boson and measuring its coupling strength are imperative to verify or detect possible deviations from the Standard Model. The $\tau\tau$ final state of the Higgs boson is the most promising channel due to its large SM-expected event rate in conjunction with its manageable backgrounds. In LHC Run-1, there was an excess of events corresponding to 3.2 standard deviations over the predicted backgrounds. Our group pushed forward this measurement using 2016 data, mainly contributing to the most sensitive $\tau_\mu\tau_\mathrm{h}$ and $\tau_e\tau_\mathrm{h}$ final states, with τ_μ and τ_e a leptonic (electron or muon) decay of the tau-lepton, and τ_h a hadronic decay. The results are extracted via two-dimensional maximum likelihood fits in the planes defined by the full or visible $\tau\tau$ mass, and the event kinematics. We observed an excess of events with 4.9 standard deviations for a mass of 125 GeV. The observed signal rate is in good agreement with the SM expectation. Figure 10.4 shows the observed signal. This is a good starting point to further investigate Higgs boson properties, especially the Charge-Parity ($\mathcal{CP}$) nature of the Higgs boson in fermionic Higgs boson decays.

Related to this, we are extending our analysis to search for low mass $\tau\tau$ resonances, predicted by many new physics models. In some scenarios, taus from the new resonance would possess non-trivial polarizations. Our experience of measuring τ polarization in $Z \rightarrow \tau\tau$ will be exploited in the next year.

10.6 Searches for new phenomena

10.6.1 Search for vector-like quarks

Many extensions of the SM, such as composite Higgs, extra dimensions, and little Higgs, predict the existence of a new class of heavy quarks, named vector-like quarks (VLQ) [10–14]. The existence of such particles would represent a solution to the hierarchy problem. Single electroweak production of VLQs has not yet been well-explored, despite the production being dominant above masses of 700 GeV. Our group has made a significant impact in the search for singly produced VLQs, carrying out two different searches, looking for massive B and T VLQs. Our focus is on two specific final states: $T \rightarrow tZ \rightarrow bq\bar{q}\,\nu\nu$ and $B \rightarrow bH \rightarrow b\,b\bar{b}$.

The new heavy resonances decay into highly boosted quarks and bosons, whose decay products are merged into a unique "fat" jet, for which we use special techniques for identification. The two searches are performed with the entire dataset collected at 13 TeV in 2016 and are currently ongoing. The results are expected to be published soon.

[10] S. Fajfer, A. Greljo, J. F. Kamenik and I. Mustac, JHEP **1307** (2013) 155.

[11] P. W. Graham, A. Ismail, S. Rajendran and P. Saraswat, Phys. Rev. D **81** (2010) 055016.

[12] M. Schmaltz and D. Tucker-Smith, Ann. Rev. Nucl. Part. Sci. **55**, 229 (2005).

[13] N. Arkani-Hamed, A. G. Cohen and H. Georgi, Phys. Lett. B **513** (2001) 232.

[14] L. Wang and X. F. Han, Phys. Rev. D **86** (2012) 095007.

10.6.2 Search for heavy resonances in di-boson events

The UZH group plays a leading role in searches for heavy resonances, with masses larger than 1 TeV, decaying into a pair of standard model bosons (W, Z, or the Higgs boson). These heavy resonances are predicted by a large number of theoretical models that extend the SM and provide an explanation for the hierarchy problem. The most credited theories include extra dimensions, composite Higgs, heavy vector-triplets, and additional $U(1)$ gauge groups [15]. These models predict the presence of massive spin-0 Radions, spin-2 Gravitons, or spin-1 heavy W' or Z' bosons which may decay with a significant branching fraction into SM bosons.

As a consequence of the heavy mass of the new particles, and the large Lorentz boost of the decay products, the pair of particles originating from the decay of the SM bosons usually have a small angular separation and special identification and reconstruction techniques must be employed. In 2016, the new generation PUPPI [16] and Soft Drop [17] algorithms have been commissioned by the Zurich group, ensuring an optimal reconstruction of the boson mass and the jet substructure even in the harsher data-taking conditions encountered in 2016. A novel reconstruction algorithm for identifying boosted $H \to \tau\tau$ decay was developed and commissioned within our group (Fig. 10.5) [18]. This technique is currently being used in the $X \to HH \to b\bar{b}\tau\tau$ and $X \to VH \to q\bar{q}\tau\tau$ analysis ($V = W, Z$), produced also by the Zurich group.

These advanced techniques are applied to searches for diboson resonances. In the first months of 2016, we completed the searches for the processes $X \to VV \to q\bar{q}q\bar{q}$, $X \to WV \to \ell\nu q\bar{q}$ [19], and $X \to VH \to (\nu\nu, \ell\nu, \ell\ell)b\bar{b}$ [20] based on the 2015 data set, accounting for 2.3 fb^{-1}. The latter represented a novelty for CMS, and both of them have been accepted for publication by refereed journals. The sensitivity of the individual searches is boosted by combining all $\sqrt{s} = 8$ and 13 TeV searches with boosted W, Z, and Higgs bosons in 12 final states, setting the most stringent limits on new models at the time [21]. As their combination is found to yield a large gain in sensitivity (Fig. 10.6), this work represents a powerful tool for future resonance searches with the large expected diboson event data sample at the LHC.

In 2016, the LHC has provided an integrated luminosity of 36 fb^{-1}, and searches for heavy particles are among the most benefited by the larger dataset. The UZH group completed two high-profile searches in hadronic final states, $X \to VV \to q\bar{q}q\bar{q}$ [22, 23] and $X \to VH \to q\bar{q}b\bar{b}$ (Fig. 10.7) [24]. These two searches exploit synergy by using common identification techniques for boosted W and Z bosons. The VH analysis, performed for the first time in Run II, represents one of the first applications of an algorithm designed to recognize the presence of two b quarks in the same hadronic jet. Although no significant excess over the estimated background has been observed, these searches put the most stringent limits on the parameters of the models

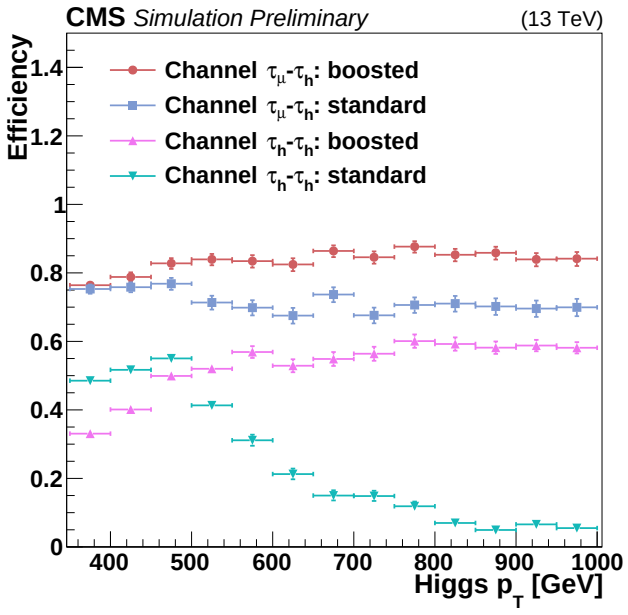

FIG. 10.5 – Reconstruction efficiency for $H \to \tau\tau$ decays with large Higgs boson Lorentz boost, as a function of the Higgs boson transverse momentum, for the CMS standard τ and the dedicated "boosted" reconstruction [18].

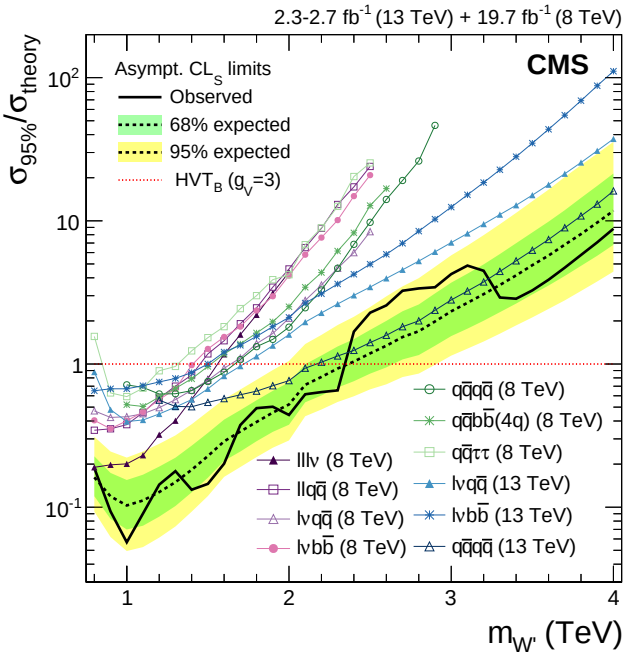

FIG. 10.6 – Expected and observed upper limits at 95% C.L. on σ/σ_{theory}, where σ_{theory} is the cross section predicted by a heavy vector triplet model, as a function of the mass of a heavy W' resonance $m_{W'}$. Different markers indicate the expected limits of the various analyses used in the combination [21].

to date (Fig. 10.6). These new results are expected to be published soon, and the combination of the searches performed with the 2016 data promises to further increase the exclusion limit on the mass of the resonances.

[15] K. Agashe *et al.*, Phys. Rev. D **76** (2007) 036006; L. Randall, R. Sundrum, Phys. Rev. Lett. **83** (1999) 3370; D. Marzocca *et al.*, JHEP **08** (2012) 013; R. Rattazzi *et al.*, JHEP, 2011(10), 2011; D. Pappadopulo *et al.*, arXiv:1402.4431.

[16] D. Bertolini *et al.*, JHEP **2014** (2014) 59.

[17] A. J. Larkoski *et al.*, JHEP **05** (2014) 146.

[18] CMS Collaboration, CERN-CMS-DP-2016-038.

[19] CMS collaboration, CMS-PAS-B2G-16-004, submitted to JHEP.

[20] CMS collaboration, CMS-PAS-B2G-16-003, submitted to PLB.

[21] CMS collaboration, CMS-PAS-B2G-16-007.

[22] CMS collaboration, CMS-PAS-B2G-16-021.

[23] CMS collaboration, CMS-PAS-B2G-17-001.

[24] CMS collaboration, CMS-PAS-B2G-17-002.

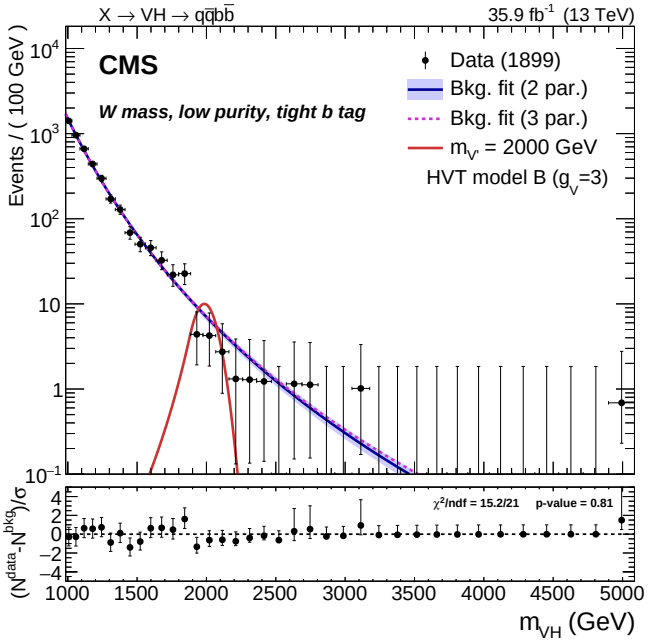

FIG. 10.7 – Spectrum of the reconstructed $V \to q\bar{q}$ and $H \to b\bar{b}$ invariant mass in the category of the $X \to VH \to q\bar{q}b\bar{b}$ analysis where the highest-mass event has been observed [24].

10.6.3 Supersymmetry

One of the favored extensions of the SM is supersymmetry (SUSY), predicting a variety of new particles at the TeV scale, that differ in spin from their SM counterparts. SUSY provides an elegant solution to some of the shortcomings of the SM, including the hierarchy problem and the nature of dark matter.

One SUSY model describes pair production of gluinos ($\tilde{g}$), the superpartner of the SM gluons, where each gluino decays into two top quarks and the lightest supersymmetric particle (LSP), $\tilde{\chi}_1^0$. These events would provide a striking signature with many jets, leptons, and missing energy in the final state. Our group has been part of one of the efforts to search for this type of decay in the exclusive single lepton final state, which has the advantage of a large branching ratio and a fairly clean SM background mainly originating from top quark pair production with additional jets. Figure 10.8 shows the interpretation of the results in terms of the gluino simplified model, where gluinos up to a mass of 1800 GeV are excluded. This result is based on the full dataset of 35.9 fb^{-1} collected during 2016 and was made public in March 2017 [25], with a journal publication currently in preparation.

[25] CMS collaboration, CMS-PAS-16-042.

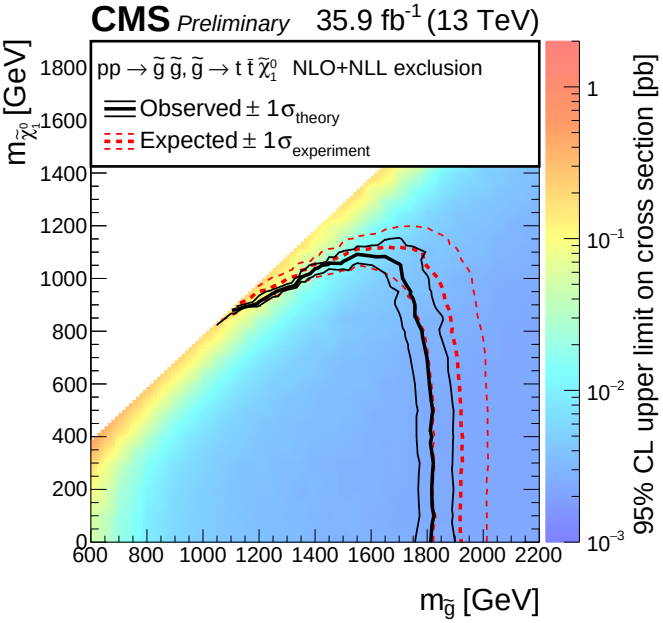

FIG. 10.8 – Cross section limits at a 95% CL for the $\tilde{g} \to t\bar{t}\tilde{\chi}_1^0$ simplified model, as a function of the gluino and LSP masses. The solid black (dashed red) lines correspond to the observed (expected) mass limits, with the thicker lines representing the central values and the thinner lines representing the $\pm 1\sigma$ uncertainty bands related to the theoretical (experimental) uncertainties.

10.6.4 Search for dark matter particles with top quarks

In several new physics models a weakly interacting massive particle arises naturally as a dark matter (DM) candidate. So far, however, there is no established knowledge about its properties and interactions with ordinary matter. DM may couple to matter in proportion to mass, leading to DM being produced with top quarks at the LHC [26].

The DM particle would escape detection, therefore the signature of this type of event is large missing energy recoiling against the top quarks. Our group has made a significant impact on this search with 8 TeV [28] and the 13 TeV data collected in 2015 [29]. Compared to our Run 1 results important improvements were achieved, such as an acceptance increase by including the hadronic final state, the use of simplified models with an explicit definition of the mediator for the interpretation of the results [27], and a shape-based fit for the signal extraction. Fig. 10.9 shows new exclusion limits expected to be published soon. In addition to top quark pairs, DM can also be produced in association with a single top quark [30]. This new process is expected to increase the sensitivity of the $t\bar{t}$+DM channel up to a factor of two. The search for this new type of processes is currently ongoing in our group.

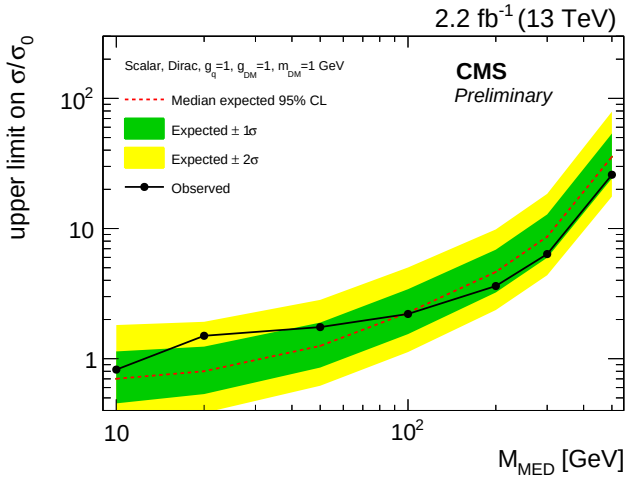

FIG. 10.9 – Expected and observed 95% CL upper limit on the ratio of the DM production cross section to the model expectation as a function of the scalar mediator mass (m_{MED}) with the single-lepton and hadronic channels combined. A DM mass of 1 GeV is assumed [29].

[26] J. M. Beltran *et al.*, HEP pp. 1 17, 2010;
T. Lin *et al.*, Phys. Rev. D, 88, (2013) 063510.

[27] D. Abercrombie *et al.*, arXiv:1507.00966.

[28] CMS collaboration, JHEP **06** (2015) 121.

[29] CMS collaboration, CMS-EXO-16-005.

[30] D. Pinna *et al.*, arXiv:1701.05195.

11 Condensed matter theory group

Titus Neupert, Ashley Cook, Seulgi Ok, and Frank Schindler

The condensed matter theory group studies topological phenomena in electronic systems. Numerical and analytical tools are used to model phases of matter and understand their unique physical properties. The term topology refers to a field of mathematics that is concerned with the relations of objects to each other if one allows for smooth deformations of these objects. Objects that can be transformed into each other by smooth deformations are said to be topologically equivalent. For example, one can smoothly deform a donut into a coffeecup but not a donut into a muffin. Thus a donut and a muffin are topologically different. Applying the same concepts to phases of quantum matter yields phenomena that are universal and surprisingly robust to perturbations. They are often related to measurable observables which are universally quantized, such as the Hall conductivity in the integer quantum Hall effect.

Topological systems can be strongly interacting, in which case we are often interested in phenomena related to so-called topological orders. Topologically ordered phases of matter are best understood in quasi two-dimensional systems with an energy gap at zero temperature, and are characterized by emergent fractionalized excitations. These so-called anyons could be used in future quantum computing devices. Our research group is mostly interested in a conceptual understanding of topological order and its generalization, for example to three dimensions. One of the projects completed this year [1] is concerned with possible phase transitions in topologically ordered states with anyonic excitations. In particular we showed that in many cases anyons with bosonic self-statistics cannot undergo a Bose-Einstein condensation transition. This results hints at a certain phase stability of states with uncondensable bosons.

We also study weakly or non-interacting systems, in which case interesting topological phenomena result from the band theory of solids. Such topological band characterizations were first discovered for insulating systems. The classic example in this category is the integer quantum Hall effect with its quantized topological Hall conductivity. It was recently joined by time-reversal symmetric insulators with topological properties. All of these systems are defined by the existence of boundary modes which cannot be removed by boundary perturbations that respect the symmetries protecting the topological character, such as time-reversal symmetry. Time-reversal symmetric topological insulators exist in two and three spatial dimensions and are characterized by a single Kramers pair of edge modes and a single, non-degenerate Dirac surface state, respectively.

More recently, the notion of topological band structures was extended from insulators to metals and semimetals. This direction of research characterizes symmetry-protected degeneracies in momentum space by topological numbers, showing that they are generic and can be robust against a large class of perturbations. The degeneracies can be point-like, giving rise to so-called Weyl or Dirac semimetals, or line-like, resulting in so-called nodal-line semimetals. Below we discuss in more detail a project [2] which defined a new class of such topological semimetals.

We have also entertained a series of experimental collaborations over the last year [3], [4], [5], of which the study of spin-polarized channels on the surface step edges of a so-called crystalline topological insulator stands out [5]. These one-dimensional edge channels are well localized, extremely robust against disorder, elevated temperatures, and magnetic fields.

[1] T. Neupert *et al.*, *No-Go Theorem for Boson Condensation in Topologically Ordered Quantum Liquids*, New Journal of Physics **18**, 123009 (2016).

[2] L. Muechler, A. Alexandradinata, T. Neupert, R. Car, *Topological Nonsymmorphic Metals from Band Inversion*, Phys. Rev. X **6**, 041069 (2016).

[3] D. Sutter *et al.*, *Hallmarks of Hund's coupling in the Mott insulator Ca_2RuO_4*, Nature Comm. (2017).

[4] P. K. Biswas *et al.*, *Suppression of magnetic excitations near the surface of the topological Kondo insulator SmB_6*, Phys. Rev. B **95**, 020410(R) (2016).

[5] P. Sessi *et al.*, *Robust spin-polarized midgap states at step edges of topological crystalline insulators*, Science **354**, 1269-1273 (2016).

[6] M. Laubach *et al.*, *Density wave instabilities and surface state evolution in interacting Weyl semimetals*, Phys. Rev. B **94**, 241102(R) (2016).

11.1 Nonsymmorphic topological metals

A large part of the activities in the condensed matter theory group was concerned with the exploration of new types of topological metals and semimetals over the past year. Topological metals display various intriguing physical properties, such as protected modes on the surface of the crystal and record-high changes in the resistivity when a magnetic field is applied ("titanic magnetoresistance") [7].

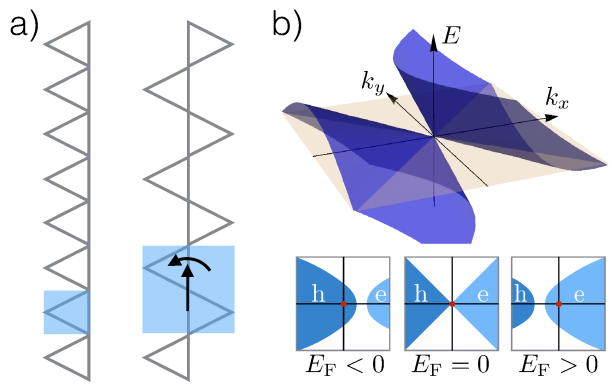

FIG. 11.1 – Nonsymmorphic semimetals. a) One-dimensional lattice with symmorphic (left) and nonsymmorphic (right) symmetry. The nonsymmorphic symmetry is a combination of translation and mirror reflection. b) Energy dispersion of a strongly Lorentz-violating Dirac fermion for which the velocity of both branches of the dispersion have the same sign for some direction of propagation. As a consequence, the Dirac point is a symmetry-protected touching point of a electron and a hole pocket (lower panels).

In a collaboration with researchers from Yale and Princeton, we proposed a new class of topological metals with a type of symmetry that is abundantly found in crystals, namely a nonsymmorphic symmetry [8]. This class of metals is topological in the sense of being robust to both deformations by the external environment, as well as to more microscopic deformations within the crystal itself.

A close look at the symmetries of a crystal, such as rotations, reflections, and translations, shows that crystals divide in two classes, called symmorphic and nonsymmorphic. Symmorphic crystals transform into themselves under discrete translations by the lattice period, rotations and reflections. Just as abundant in nature are nonsymmorphic crystals, which transform into themselves under symmetry operations that combine a rotation or a reflection with a translation by a fraction of the lattice period. As illustrated in Fig. 11.1 a), the left image has symmorphic symmetry, while the right image is nonsymmorphic, that is, under a reflection with respect to the horizontal bisecting line, combined with a translation by half the lattice period, the image returns to itself.

Nonsymmorphic symmetries lead to fundamentally different arrangements of the atoms in a crystal, which in turn have a profound influence on their electronic properties. Indeed, crystals with the nonsymmorphic symmetry of Fig. 11.1 a), and having an odd number of electrons per lattice period, are guaranteed to be metals [9]. For an even number of electrons, we find distinct phases of matter that exhibit either metallic or insulating behavior; a transition between an insulator and a metal is accompanied by a change in the symmetry properties. Such changes are discrete, in the sense of changing from one integer to another. In analogy to how there is no continuous way to change from integer into another, the metallic states of matter are profoundly robust and cannot easily be transformed into a different state of matter. Practically, these crystals are not as susceptible to impurities and defects as regular crystals, making them attractive candidates for electronic devices.

Using the language of topology, this new state is different from other electronic states that can exist in a nonsymmorphic crystal. In the present case it is the topology of the quantum-mechanical wavefunctions that distinguishes the electronic states. Electrons having the nonsymmorphic symmetry of Fig. 11.1 a) behave as if they had an additional degree of freedom that can only take two discrete values, analogous to the half-integer-spin degree of freedom in electrons. A unique property of spin, which has an analogy in the nonsymmorphic case, is that it does not return back to itself after a rotation of 360 degrees but only after a rotation of 720 degrees. This resembles walking around a Moebius strip, where one only returns to the starting point after going around the strip twice.

The theory was applied to the material WTe_2 which has garnered attention for its highly unusual resistivity under the effect of a magnetic field. Recent photoemission experiments have also shown that the electrons in WTe_2 absorb right-handed photons differently than they would left-handed photons. The theory that was formulated showed that these experiments on WTe_2 can be understood based on the topological properties of this new class of metals. The topologically protected band crossing in these nonsymmorphic semimetals is of the form of a Dirac cone, i.e., resembling that of massless relativistic electrons. Such an electronic structure is already known from atomically thin carbon layers, i.e., graphene. However, our study uncovered that the monolayer of WTe_2 realizes an interesting twist to this electronic structure, in that the velocity of the Dirac electrons becomes very anisotropic. This anisotropy is so strong that the velocities of the two branches of the Dirac cone have the same sign in one direction of space, while they have opposite signs in another as seen in Fig. 11.1 b). This forces the Dirac cone to 'tilt over' and can be seen as a strong breaking of Lorentz symmetry [10] – a situation distinct from the Lorentz symmetric Dirac cones in graphene, for example.

[7] A. N. Mazhar *et al.*, *Large, non-saturating magnetoresistance in WTe_2*, Nature **514** 205 (2014).

[8] L. Muechler, A. Alexandradinata, T. Neupert, R. Car, *Topological Nonsymmorphic Metals from Band Inversion*, Phys. Rev. X **6**, 041069 (2016).

[9] H. Watanabe *et al.*, *Filling-Enforced Gaplessness in Band Structures of the 230 Space Groups*, Phys. Rev. Lett. **117**, 096404.

[10] H. Watanabe *et al.*, *Type-II Weyl semimetals*, Nature **527** 495 (2015).

11.2 No go theorem for Bose-Einstein condensation of anyons

Topologically ordered states of matter are realized in quasi two-dimensional systems, such as the fractional quantum Hall effect. The zero-temperature ground state of such a system is a gapped quantum liquid, i.e., it is a completely featureless state. What is most interesting are the elementary excitations above this liquid ground state. One can construct localized excitations that have particle-like character and striking universal properties and can move freely in the liquid (one says they are deconfined). The excitations have fractionalized quantum numbers with respect to those of the constituent particles out of which the quantum liquid is made (electrons), for example by carrying a sharply defined fraction of the elementary charge. More important, however, are the fractionalized quantum-statistical properties of these excitations. Free particles in nature come only in two species, fermions and bosons, depending on whether the quantum mechanical wave function acquires a minus sign when two of these particles are interchanged. The fractionalized particles in topologically ordered systems can change the phase of the quantum mechanical wave function by any (rational) amount when transported around one another (Fig. 11.2 a). They are thus called anyons. Even more strikingly, such anyons can entirely change the quantum mechanical state of the system when transported around one another. If this is the case, they are called non-Abelian anyons. Physicists have envisioned building a particularly robust quantum computer based on these exotic properties of non-Abelian anyons [11].

Of all these quantum mechanical particles, bosons stand out by their ability to undergo a Bose-Einstein condensation: They can coherently appear in large numbers in a quantum system, driving it into a new phase [12, 13]. This effect has been shown in cold atomic gases, for example, and is closely related to the phenomenon of superconductivity.

Our study shows that not all bosons can undergo a Bose-Einstein condensation transition [14]. We proved a no-go theorem by which the condensation of classes of non-Abelian *bosons*, which appear as excitations in topologically ordered quantum liquids, is forbidden. This is relevant because Bose condensation is a common mechanism by which phase transitions between topologically ordered phases are driven (Fig. 11.2 b). Roughly speaking, the theorem states that if the amount of quantum information carried by the non-Abelian boson is smaller than the quantum information carried by the particles it can branch into after the condensation transition, there is an obstruction against its condensation.

An interesting application of our theorem applies to bosons that appear in so-called Fibonacci topological order, which is of particular interest to the aim of building a topological quantum computer. We show that Fibonacci topological order cannot undergo any type of condensation transition.

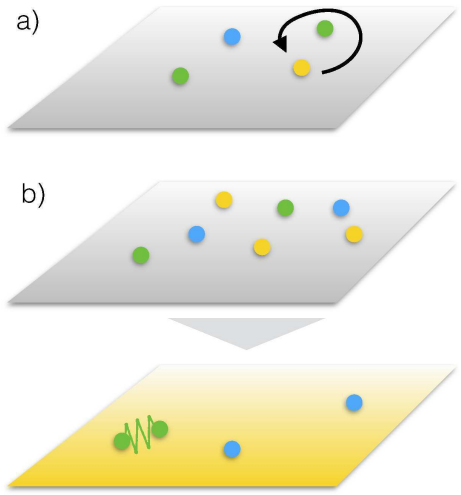

FIG. 11.2 – Two-dimensional topologically ordered states are characterized by several types of anyon quasiparticle excitations (colored dots). a) A key property of topologically ordered phases is that when anyons are adiabatically braided around one another, the quantum state of the entire system can change. b) A class of transitions between anyon theories can be described by the condensation of a bosonic anyon (here in yellow). The condensation changes the type of topological order, for instance by confining part of the anyons that are then not part of the low-energy excitations anymore, as depicted for the green anyon here.

This may point to a certain robustness of this topological order. More broadly, our results shed light on the rich mathematical structure behind topologically ordered states with anyons.

[11] C. Chamon, *et al. Topological Aspects of Condensed Matter Physics, Chapter 2*, Lecture Notes of the Les Houches Summer School: Volume 103, August 2014.

[12] F. A. Bais and J. K. Slingerland, *Condensate-induced transitions between topologically ordered phases*, Phys. Rev. B **79**, 045316 (2009).

[13] T. Neupert *et al. Boson condensation in topologically ordered quantum liquids*, Phys. Rev. B **93**, 115103 (2016).

[14] T. Neupert *et al. No-Go Theorem for Boson Condensation in Topologically Ordered Quantum Liquids*, New Journal of Physics **18**, 123009 (2016).

11.3 Spin-polarized step-edge states on the surface of topological crystalline insulators

Of the various collaborations that we have entertained with experimental groups, we want to highlight one that discovered a new type of one-dimensional conducting states on the surface of a very special crystal, as so-called topological crystalline insulator [15].

A topological crystalline insulator is an insulating three-dimensional crystal with gapless, i.e., conducting, electronic states on its surface. These surface states behave like relativistic Dirac electrons, just as in graphene, with the difference that they have a well-defined spin direction that is tied to their propagation direction (Fig. 11.3 b). The surface cannot be made insulating unless one breaks symmetries of the crystal such as certain mirror symmetries. In practice, these surface Dirac electrons are found to be a robust property of topological crystalline insulators, that is largely insensitive to imperfections of the surface [16].

Our experimental collaborators from the University of Wuerzburg, Germany, carefully examined the surface of the topological crystalline insulator (Pb,Sn)Se with a scanning-tunneling microscope and spectroscope. This device can resolve the topography and electronic structure of surfaces with atomic scale resolution and precision. Besides the expected surface states, they found one-dimensional conducting channels exactly at places of the surface where a step-edge is located. A step edge is the termination of extra layer(s) of atoms on the surface. Even more strikingly, these one-dimensional channels were only present if the step edge was an odd number of atomic layers thick (like one and three layers), while no extra states where found if the step was a even number of atomic layers high.

This systematic observation can be explained by the topological electronic structure of the surface, which can be seen as an exotic form of a Dirac semimetal [17]. In the rock salt lattice structure of (Pb,Sn)Se (the same structure as regular salt, NaCl, see Fig. 11.3 a), even and odd step edges can, when viewed from above, be distinguished as follows (see Fig. 11.3 c): For even steps, the lattice structure on either side looks exactly the same. For odd steps, the lattice structure on one side is translated by a fractional (half) lattice vector with respect to the other side. This fractional translation has nontrivial implications for the surface electronic states: The quantum mechanical wave functions acquire a nontrivial phase, so-called Berry phase, under such a translation. As a result the surface state Dirac electron wave functions cannot be phase-matched between both sides of the step edge everywhere. This interference or phase frustration results in the presence of extra electronic states which are bound to the step edge as observed in the experiment (Fig. 11.3 e).

The one dimensional channels bound to the odd step edges have remarkable properties. First, they seem to travel along the step edge almost unperturbed, i.e., with very little back scattering from impurities. Second, they are nearly dispersionless, meaning that they are found at the same energy independent of the momentum along the edge. Third, they were still observed at temperatures as high as 80 K and in magnetic fields of up to 11 T (the highest field accessible by the apparatus). Fourth, they are confined to a very narrow region of only about 10 nm. Together, these characteristics make them a promising platform to build electronics and quantum devices on the smallest scales.

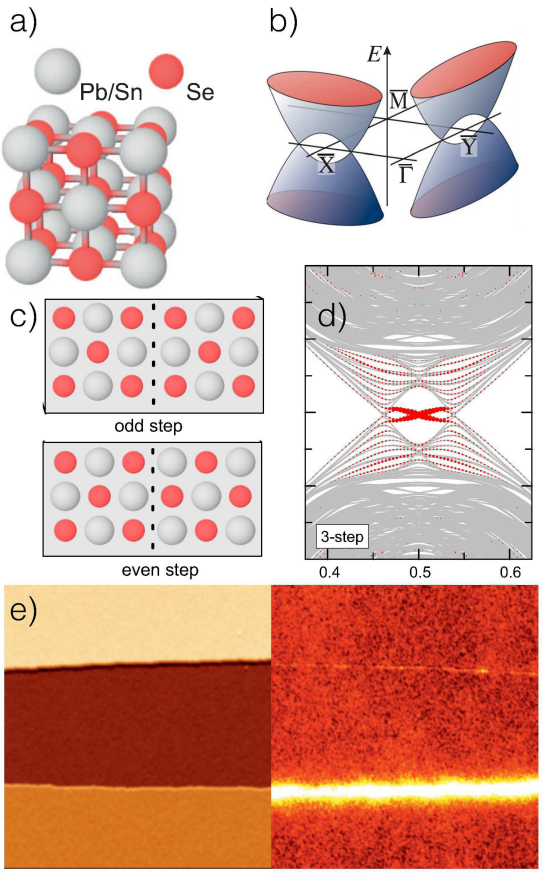

FIG. 11.3 – One-dimensional step-edge states on the surface of three-dimensional topological crystalline insulators. a) Rocksalt lattice structure of (Pb,Sn)Se. b) Four topologically protected non-spin-degenerate Dirac cones in the surface Brillouin zone of (Pb,Sn)Se. c) Difference between odd and even step edge when viewed from above. The lattice structure on the left and right of the odd step edge is related by a fractional lattice translation. d) Numerical simulation of the electronic structure of a three atoms high step edge (energy vs. momentum along the edge). Highlighted in red are the states localized along the step edge. e) Scanning tunneling microscope image of an even step edge (above) and an odd step edge (below). Left is the topography and right is the spectroscopy image, which clearly shows the one-dimensional channel bound to the odd step edge.

[15] P. Sessi *et al.*, *Robust spin-polarized midgap states at step edges of topological crystalline insulators*, Science **354**, 1269-1273 (2016).

[16] L. Fu, *Topological Crystalline Insulators*, Phys. Rev. B **106**, 106802 (2011).

[17] T. Hsieh *et al.*, *Topological crystalline insulators in the SnTe material class*, Nature Communications **3**, 982 (2012).

12 Superconductivity and Magnetism

L. Das, D. Sutter, O. Ivashko, D. Destraz, C. Matt, A. Sidorenko, J. Chang
Associated PhD student - SINERGIA Network: C. Fatuzzo (EPFL)

in collaboration with: Paul Scherrer Institute (M. Dantz, X. Lu, D. E. McNally, N. Plumb, M. Shi, & T. Schmitt), EPFL Lausanne (G. Gatti, N. E. Shaik, H. M. Rønnow & M. Grioni), University of Zurich (C. Monney, A. Schilling & Neupert), University of Central Lancashire, UK (P. G. Freeman), Technical University of Denmark, Denmark (N. B. Christensen), Dipartimento di Fisica 'E. R. Caianiello', Salerno-Italy (V. Granata, R. Fittipaldi & A. Vecchione), Hokkaido University, Japan (T. Kurosawa, M. Oda, & N. Momono), Karlsruher Institut für Technologie, Germany (Konstantin Ilin & Michael Siegel), National Tsing Hua University, Taiwan (T.-R. Chang, H.-T. Jeng), College de France, France (M. Kim & A. Georges), Advanced Light Source, USA (S. Moser, C. Jozwiak, A. Bostwick, E. Rotenberg), Diamond Light Source, UK (T. K. Kim & M. Hoesch)

We present three research projects on strongly correlated electron system studies by complementary techniques such as Resonant Inelastic X-ray Scattering (RIXS), Angle Resolved Photo-Electron Spectroscopy (ARPES) and magnetotransport experiments. Our work covers different electron correlated phenomena. One study provides the electronic structure of the paramagnetic Mott insulating phase of Ca_2RuO_4. Another study is focused on the superconducting fluctuations in the normal state of dirty NbN films. Finally, we have studied the antiferromagnetic spin excitations in the high-temperature superconductor $La_{2-x}Sr_xCuO_4$.

12.1 Nature of the Mott-insulating state of Ca_2RuO_4

A rich variety of electronic instabilities of the Fermi sea emerge as a result of manybody interactions. This leads to fascinating phenomena such as superconductivity, electron- and spin-density wave orders or Mott metal-insulator transitions (MIT). Understanding these different ground states is important in order to gather a full picture of a particular problem. In the case of $Ca_{2-x}Sr_xRuO_4$ ($x = 0, .., 2$), the two end members form diametrically opposed ground states, where Sr_2RuO_4 is a potential chiral $p-$wave superconductor [1] and Ca_2RuO_4 a Mott-insulator [2]. Typically, the Mott-insulating state emerges in systems with a half-filled band and a high ratio of Coulomb interaction U to the bandwidth W. In Ca_2RuO_4, the t_{2g}-manifold is occupied by four electrons, producing a 2/3 filled band, which inhibits a simple explanation of the ground state [3].

Experimentally, it has been found that in the intermediate composition $Ca_{1.5}Sr_{0.5}RuO_4$, metallic transport properties coexist with a Curie-Weiss behaviour of the magnetic susceptibility with $S = 1/2$ per Ru-ion. This may be a possible realisation of a so-called orbital-selective Mott phase (OSMP), where a Mott gap opens for a subset of bands while the others remains metallic [4].

Angle resolved photoemission spectroscopy (ARPES) experiments on $Ca_{1.8}Sr_{0.2}RuO_4$ – the critical composition triggering the MIT – lead to contradicting interpretations of the ground state, favouring [6] or disfavouring [5] the orbital selective Mott scenario.

Extending this idea to Ca_2RuO_4 implies orbital dependent Mott gaps. Another explanation is the crystal field stabilisation of the d_{xy} orbitals due to the c-axis compression of the RuO-octahedra. As a result, the d_{xy} orbitals are completely filled, and thus band insulating while the half-filled d_{yz}/d_{xz} orbitals are Mott localized. Relatively little is known about the low-energy electronic structure of Ca_2RuO_4 and thus impeding a resolution of the effective ground state.

We have conducted ARPES experiments on Ca_2RuO_4 in the paramagnetic Mott-insulating phase at $T = 150\,K$, revealing its band structure. Near the Fermi level, three bands are observed [Fig. 12.1 a), b)]. (*i*) A broadened flat band, extending throughout the whole Brillouin zone ($\mathcal{C}$-band). (*ii*) A fast dispersing band ($\mathcal{B}$-band) evolving around the zone centers and merging with the flat band. (*iii*) Structure in the spectral weight distribution closest to the Fermi level ($\mathcal{A}$-band).

In conjunction with first-principle calculations performed with Density Functional Theory (DFT) including spin-orbit coupling, the observed spectral features can be explained by introducing a phenomenological self-energy $\hat{\Sigma}(\omega)$ in the Green's function $\hat{\mathcal{G}}(\mathbf{k}, \omega) = [\omega - \hat{\mathcal{H}}_{\mathbf{k}} - \hat{\Sigma}(\omega)]^{-1}$ [Fig. 12.1 c)]. In this fashion, we incorporate an enhanced crystal field splitting (Δ_{CF}) of the d_{xy} states and a spectral gap ($\Delta_{xz/yz}$) acting on the d_{yz}/d_{xz} states. Furthermore, we performed Dynamical Mean Field Theory (DMFT) calculations to gain deeper insight [Fig. 12.1 d)]. There the Hund's coupling J and Coulomb interaction U enter as crucial parameters, shaping the spin- and orbital degrees of freedom of the t_{2g}-multiplet. We used $U = 2.3\,eV$ and $J = 0.4\,eV$ which successfully explain correlated phenomena of other ruthen-

ate compounds [7]. The fast dispersing $\mathcal{C}$-band and flat $\mathcal{B}$-band are reproduced and assigned to a d_{xy} and a d_{yz}/d_{xz} orbital character, respectively. Although not smoothly connected to the $\mathcal{C}$-band, the $\mathcal{A}$ close to the Fermi level also carries d_{xy} character. It is found that the d_{xy} orbital driven bands are completely filled and the d_{yz}/d_{xz} bands are Mott-insulating with a band splitting across the Fermi level of order $U + J$. Ca_2RuO_4 is thus a paradigmatic example of a combined band- and Mott-insulator. These results are published in Nature Communications [8].

[1] A. Damascelli *et al.*, Phys. Rev. Lett. **85**, 5194-5197 (2000).

[2] A. V. Puchkov *et al.*, Phys. Rev. Lett. **81**, 2747-2750 (1998).

[3] H. Watanabe *et al.*, PNAS **112**, 14551-14556 (2015).

[4] V. Anisimov *et al.*, Eur. Phys. J. B **25**, 191 (2002).

[5] A. Shimoyamada *et al.*, Phys. Rev. Lett. **102**, 086401 (2009).

[6] M. Neupane *et al.*, Phys. Rev. Lett. **103**, 097001 (2009).

[7] J. Mravlje *et al.*, Phys. Rev. Lett. **106**, 096401 (2011).

[8] D. Sutter *et al.*, Nat. Comm. **8**, 15176 (2017).

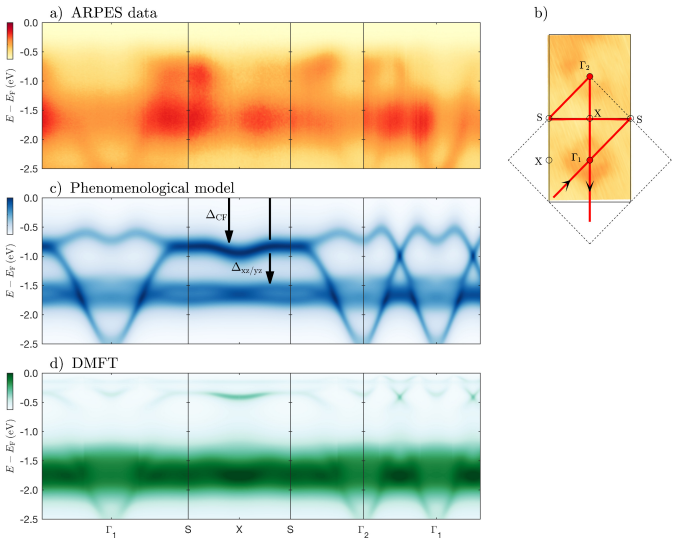

FIG. 12.1 – Band structure of Ca_2RuO_4: (a) ARPES spectra recorded along high symmetry directions with 65 eV circularly polarised light. (b) Constant energy map at binding energy $E - E_F = -2.7$ eV. (c) DFT-derived spectra for Ca_2RuO_4, upon inclusion of a Mott gap $\Delta_{xz/yz} = 1.55$ eV acting on, d_{yz}/d_{xz} bands and an enhanced crystal field $\Delta_{CF} = 0.6$ eV, shifting spectral weight of the d_{xy} bands. (d) DMFT calculation of the spectral function, with Coulomb interaction $U = 2.3$ eV and a Hund's coupling $J = 0.4$ eV.

12.2 Superconducting fluctuations in the Hall effect in a NbN thin film

The transition from a superconductor to a normal conductor above the critical temperature T_c can be caused by a lack of phase coherence, leading to phase fluctuations, or by a destruction of Cooper pairs, leading to (Gaussian) amplitude fluctuations. The nature of the fluctuation is, for example, still debated in the copper-oxide materials (cuprates). The discovery of a pseudogap in NbN has made it an interesting system to compare with the cuprate superconductors [9].

In a recent theoretical paper the Hall effect response of superconducting fluctuations above T_c was calculated for the amplitude fluctuation regime [10]. This theory has already been tested successfully on thin films of TaN [11], which is similar to NbN. However, no pseudogap has been observed in TaN so far. The constraints of the theory are that the electrons must behave three-dimensionally while superconductivity is essentially two-dimensional. This is the case for our film, where the electronic mean free path $\ell = 0.2$ nm is much smaller than the film thickness $d = 11.9$ nm while the coherence length $\xi = 4.3$ nm is comparable.

We have performed Hall effect and resistivity measurements on a thin film of NbN with a critical temperature $T_c = 14.96$ K. The most striking feature of the Hall signal is a sign change from positive in the low-field, fluctuation dominated, region to negative in the high-field, quasiparticle dominated, region. This effect appears in a very small temperature range (≈ 0.5 K) above T_c, and has previously been overlooked [12, 13]. By subtracting the quasiparticle response from the Hall signal, which is linear in the magnetic field strength, we can obtain the pure fluctuation contribution. The same procedure can be applied to the resistivity which then leads to the conductivity tensor of the superconducting fluctuations containing $\Delta\sigma_{xx}$ and $\Delta\sigma_{xy}$. For low temperatures $\Delta\sigma_{xy}$ is linear in field strength and thus the quantity $\nu_H = \Delta\sigma_{xy}/B$ becomes a constant ($\nu_{H,0}$) for $B \to 0$. The quantities $-\Delta\sigma_{xy}$ and $\Delta\sigma_{xx}$ are shown in Fig. 12.2, plotted against $\epsilon = \ln(T/T_c) \approx (T - T_c)/T_c$. The theoretical prediction for the fluctuations in the conductivity is

$$\Delta\sigma_{xx} = \frac{e^2}{16\hbar d}\frac{1}{\epsilon}, \tag{12.1}$$

as calculated by Aslamazov and Larkin [14]. The prediction for the Hall conductivity is a rather complicated expression, but simplifies heavily for the low-field limit, where it becomes

$$\frac{\Delta\sigma_{xy}}{B} = \frac{|e|D\kappa}{3}\frac{e^2}{16\hbar d}\frac{1}{\epsilon^2}. \tag{12.2}$$

Here D is the electron diffusion constant and κ is defined

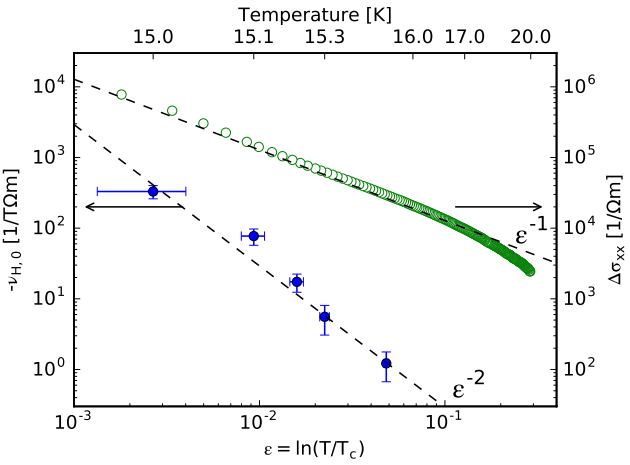

FIG. 12.2 – The low-field value $\nu_{H,0} = \Delta\sigma_{xy}/B$ for $(B \to 0)$ (left axis) and the paraconductivity $\Delta\sigma_{xx}$ (right axis) as a function of ϵ. Dashed lines are the predicted dependencies from Gaussian fluctuation theory without any adjustable parameters. Horizontal error bars correspond to an uncertainty in T_c of 20 mK.

as $-\mathrm{d}\ln(T_c)/\mathrm{d}\mu$, where μ is the chemical potential. The dependence on ϵ and thus temperature is much stronger for $\Delta\sigma_{xy}$ than for $\Delta\sigma_{xx}$. The dashed lines in Fig. 12.2 correspond to these two predictions. As can clearly be seen, the data follow the predicted behaviour perfectly, showing that the superconducting fluctuations in NbN are amplitude fluctuations.

Furthermore, from the value of ν_H, the ghost critical field can be extracted, which we define as the value of the magnetic field, for which ν_H deviates from the linear low-field behaviour. We find that the ghost critical field scales linearly with ϵ. These results are published in Phys. Rev. B [15].

[9] M. Mondal *et al.*, Phys. Rev. Lett. **106**, 047001 (2011).

[10] K. Michaeli *et al.*, Phys. Rev. B **86**, 014515 (2012).

[11] N. Breznay *et al.*, Phys. Rev. B **86**, 014514 (2012).

[12] S. Chockalingam *et al.*, Phys. Rev. B **77**, 214503 (2008).

[13] M. Chand *et al.*, Phys. Rev. B **80**, 134514 (2009).

[14] L. G. Aslamazov and A. Varlamov, Sov. Phys. Solid State **10**, 875 (1968).

[15] D. Destraz *et al.*, Phys. Rev. B **95**, 224501 (2017).

12.3 Damped spin-excitations in a doped cuprate superconductor with orbital hybridization

Considerable research is being undertaken in the quest to reach consensus on the mechanism of high-temperature superconductivity and the associated pseudogap phase in cuprates. The energy scales governing the physical properties of these layered materials therefore remain of great interest. It is known that these materials are characterized by a strong super-exchange interaction $J_1 = 4t^2/U$ where t is the nearest-neighbor hopping integral and U is the Coulomb interaction. To first order, this energy scale sets the band-width of the spin-excitation spectrum. Resonant inelastic x-ray scattering (RIXS) experiments have demonstrated that this band-width stays roughly unchanged across the entire phase diagram [15, 16] of hole doped cuprates. It has also been demonstrated that the cuprates belong to a regime (of t and U) where the second order exchange-interaction $J_2 = 4t^4/U^3$ contributes to a spin-excitation dispersion along the antiferromagnetic zone boundary (AFZB) [17]. Moreover, it is known from band structure calculations and experiments that the next nearest-neighbor (diagonal) hopping integral t' constitutes a non-negligible fraction of t [18]. Empirically [19], the superconducting transition scales with the ratio t'/t whereas Hubbard type models predict the opposite trend [20, 21]. As a resolution, a two-orbital model – in which hybridization of d_{z^2} and $d_{x^2-y^2}$ states suppresses T_c and enhances t' – has been put forward [22].

Here, we address the question as to how t' influences the spin-excitation spectrum at, and in vicinity to, the antiferromagnetic zone boundary. We have therefore studied – using the RIXS technique – slightly underdoped compounds of $La_{2-x}Sr_xCuO_4$ (LSCO) with $x = 0.12$ and 0.145. RIXS spectra (see Fig. 12.3 (a)-(b)) were acquired along high symmetry directions and the resultant pole position of the magnetic excitations were extracted and are presented in Fig. 12.3 (c)-(e). The extracted spin-excitation dispersion of LSCO $x = 0.12$ and 0.145 is to be compared with the magnon dispersion of the parent compound La_2CuO_4 [17, 23]. Along the anti-nodal $(\frac{1}{2}, 0)$-direction comparable dispersions are found. This is consistent with the weak doping dependence reported on LSCO [16] and the $YBa_2Cu_3O_{7-\delta}$ (YBCO) system , [15]. For the nodal $(\frac{1}{4}, \frac{1}{4})$-direction, the dispersion of the doped compound is, however, strongly softened compared to La_2CuO_4 (as also reported for LSCO $x = 0.23$ [24]).

The spin-excitation dispersion of doped LSCO is analyzed using an effective Heisenberg Hamiltonian derived from a $t - t' - t'' - U$ Hubbard model [25]. Within this model the zone boundary dispersion can be quantified by $E_{ZB} = \omega(\frac{1}{2}, 0) - \omega(\frac{1}{4}, \frac{1}{4})$ [26]:

$$\frac{E_{ZB}}{12ZJ_2} \approx 1 + \frac{1}{12}\left[112 - \left(\frac{U}{t}\right)^2\right]\left(\frac{t'}{t}\right)^2. \qquad (12.3)$$

A key prediction is thus that E_{ZB} scales as $(t'/t)^2$ with a pre-factor that depends on $(U/t)^2$.

This effective Heisenberg model is in principle not applicable to doped and hence antiferromagnetically disordered cuprates. However, in the absence of analytical

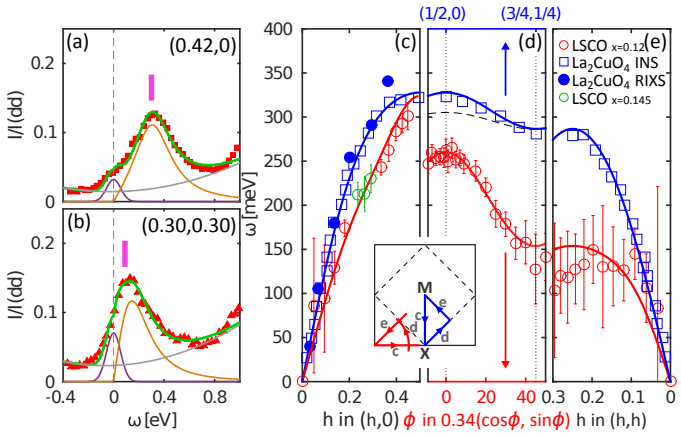

FIG. 12.3 – RIXS spectra for anti-nodal (a) and nodal (b) directions with the indicated in-plane momentum. The fit (solid green curve) is composed of three components: elastic line (purple), spin-excitation (orange) modeled by an anti-symmetric Lorentzian function and a quadratic background (grey). Vertical bars indicate the obtained poles of the Lorentzian function. (c)-(e) dispersion of the magnetic excitations in La_2CuO_4 (blue squares) and $La_{2-x}Sr_xCuO_4$ with $x = 0.12$ (red circles) observed by neutron scattering and RIXS (Ref. [17] and Ref. [23]), and RIXS (this work), respectively. Green circles in (c) are extracted from $La_{2-x}Sr_xCuO_4$ with $x = 0.145$ data. Within the antiferromagnetic zone scheme (indicated by the dashed line in the insert), red and blue cuts c and e are the equivalent anti-nodal and nodal directions. Solid lines in (c)-(e) are fits using a Heisenberg model. In (d) the thin dashed line is the correspective azimuthal scan, for La_2CuO_4, extracted from the above mentioned model.

models, the Heisenberg model serves as a useful effective parametrization tool to describe the damped spin-excitations. Within a single-band tight-binding model, angle resolved photoemission spectroscopy (ARPES) experiments have found that t' decreases slightly with increasing doping [18, 27]. The stronger zone boundary dispersion can thus not be attributed to an increase of t'. Furthermore it is not possible to obtain a good fit to the data using the small value of t' reported in Ref. [18].

This failure combined with the observation of a reduced level splitting between the d_{z^2} and $d_{x^2-y^2}$ states motivates a two-band model. It has been demonstrated that d_{z^2} states contribute to effectively increase the t' hopping parameter [22]. Furthermore, with hybridization of d_{z^2} and $d_{x^2-y^2}$ states, a renormalized Coulomb interaction U is expected. Thus keeping $Z = 1.219$ as in La_2CuO_4 [25] and $t'' = -t'/2$, a satisfactory description (solid line in Fig. 12.3(c)-(d)) of the spin-excitation dispersion is obtained for $t'/t = -0.38$ and $U/t = 6.5$. Notice that a similar ratio of t'/t has previously been inferred from the rounded Fermi surface topology of $Tl_2Ba_2CuO_{6+x}$ [28, 29], a material for which the d_{z^2} states are expected to be much less important [30]. It could thus suggest that $t'/t \approx -0.4$ is common to single layer cuprates but masked in LSCO due to the repulsion between the $d_{x^2-y^2}$ and d_{z^2} bands that pushes the van Hove singularity close to the Fermi level and effectively reshapes the Fermi surface topology [22]. The realistic values of U and Z, suggest that – for LSCO – the two-orbital character of this system is an important ingredient to accurately describe the spin-excitation spectrum.

To conclude, we argue that hybridization between d_{z^2} and $d_{x^2-y^2}$, which is especially strong in LSCO, leads to an enhanced t' and a renormalization of the Coulomb interaction U. Both these effects – consistent with the observations – lead to a stronger zone boundary dispersion within the $t - t' - t'' - U$ Hubbard model.

[15] M. L. Tacon *et al.*, Nat. Phys. **7**, 725 (2011).

[16] M. P. M. Dean *et al.*, Nat. Mater. **12**, 1019 (2013).

[17] N. S. Headings *et al.*, Phys. Rev. Lett. **105**, 247001 (2010).

[18] T. Yoshida *et al.*, Phys. Rev. B **74**, 224510 (2006).

[19] E. Pavarini *et al.*, Phys. Rev. Lett. **87**, 047003 (2001).

[20] S. R. White and D. J. Scalapino, Phys. Rev. B **60**, R753 (1999).

[21] T. Maier *et al.*, Phys. Rev. Lett. 85, **1524** (2000).

[22] H. Sakakibara *et al.*, Phys. Rev. Lett. **105**, 057003 (2010).

[23] L. Braicovich *et al.*, Phys. Rev. Lett. **104**, 077002 (2010).

[24] C. Monney *et al.*, Phys. Rev. B **93**, 075103 (2016).

[25] J.-Y. P. Delannoy *et al.*, Phys. Rev. B **79**, 235130 (2009).

[26] O. Ivashko *et al.*, accepted in Phys. Rev. B, arXiv:1702.02782 (2017).

[27] J. Chang *et al.*, Phys. Rev. B **78**, 205103 (2008).

[28] M. Plate *et al.*, Phys. Rev. Lett. **95**, 077001 (2005).

[29] D. C. Peets *et al.*, New Journal of Physics **9**, 28 (2007).

[30] H. Sakakibara *et al.*, Phys. Rev. B **85**, 064501 (2012).

13 Phase Transitions and Superconducting Photon Detectors

A. Gazizulina, S. Huangfu, A. Schilling, S. Siegrist, Q. Wang and X. Zhang

in collaboration with: University of Bern (K. Krämer), Deutsches Zentrum für Luft- und Raumfahrt (Prof. Alexei Semenov), Paul-Scherrer Institut (Dr. Marisa Medarde), Paul-Scherrer Institut (Prof. Kazimierz Conder), McMaster University (Dr Hanna Dabkowska), Max Planck Institute for Chemical Physics and Solids, Dresden (Prof. C. Felser), Universidad del Pais Vasco (Prof. Evgeny Sherman), Academy of Sciences of Uzbekistan (Prof. Abdulla Rakhimov), Leibniz-Institut für Festkörper- und Werkstoffforschung (IFW) (Dr. Vladimir Kataev), Helmholtz Research Centre Dresden-Rossendorf (Dr. Tobias Förster), Radboud University Nijmegen (Dr. Laurens Peters), Universitetet i Stavanger (Prof. Diana Quintero Castro), Helmholtz Zentrum für Materialien und Energie HZB (Dr. Illya Glavatskyy), Laboratoire National des Champs Magnetiques Intenses (lmcmi) (Dr. Albin De Muer), Deutsches Zentrum für Luft- und Raumfahrt (Dr. Heinz-Wilhelm Hübers), Karlsruhe Institut für Technologie (Dr. Konstantin Ilín)

13.1 Superconducting nanowire single photon detectors (SNSPD)

13.1.1 Detection mechanisms

All of the currently proposed detection mechanisms for SNSPDs are based on a photon induced non-equilibrium area, namely a hotspot, playing an important role in most SNSPDs. The different detection models predict different hotspot sizes depending on the superconducting material, but they are unable to explain all the experimental results so far. By measuring the inelastic interaction time, electron diffusion constant, and quasiparticle lifetime, we defined the hotspot size more precisely [1]. With this definition, we can explain all the current phenomena in SNSPDs, for instance, the temperature, current and wavelength dependences of the detection efficiency. The definition of the hotspot size has also been experimentally confirmed by a two-photon delay experiment [2].

WSi has become the most fascinating material for SNSPDs, which holds the record of detection efficiency (up to $\approx$ 93%) [3]. The underlying mechanism responsible for the good performance of this promising material, however, is still unknown. We successfully deposited ultrathin amorphous WSi films with critical temperatures T_c comparable to and even higher than those used by other groups, as it is shown in Fig. 13.1. In order to figure out the mechanism of the high detection efficiency for WSi-based SNSPDs, we measured the superconducting material parameters through magneto-transport experiments [1]. We found that the superconducting coherence length in this amorphous material is larger than that in crystalline or granular NbN materials. Therefore, detectors based on this material are more robust to electrical and geometrical constrictions. As a result, the experimental critical current is closer to the local depairing current, and the detection efficiency becomes very high. The most striking characteristics of WSi are the long electron-phonon interaction time and intrinsic quasiparticles lifetime, as shown in Fig 13.2.

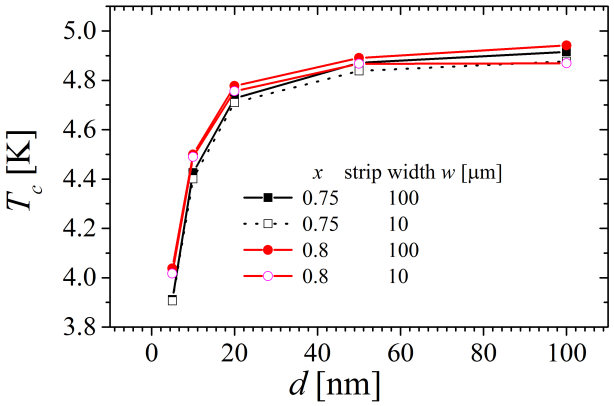

FIG. 13.1 – Critical temperatures of WSi films as a function of the film thickness.

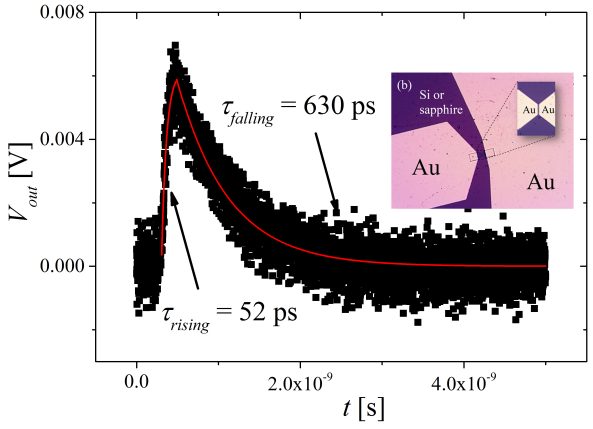

FIG. 13.2 – Measurement of the quasiparticle lifetime in amorphous WSi. Inset: the device used for the measurement [1].

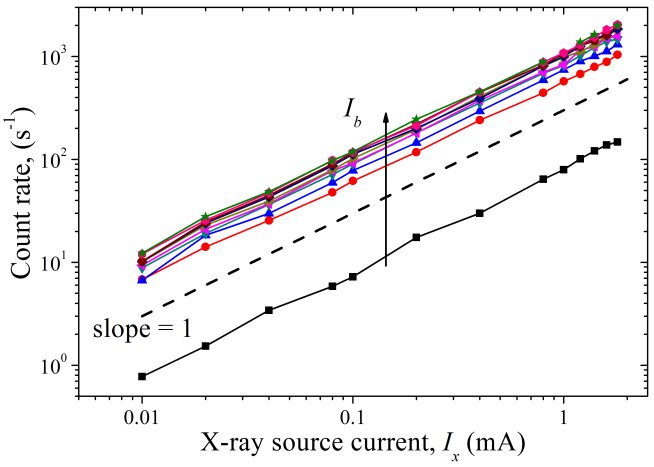

FIG. 13.3 – Measured count rates vs the X-ray source current I_x (with an acceleration voltage V_A = 30 kV) at bias current I_b ranging from 10 μA to 100 μA, with an increment of 10 μA. The dashed line indicates a slope of 1.

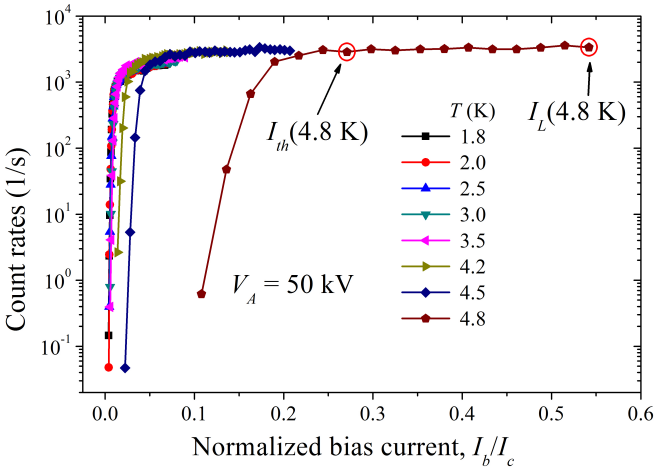

FIG. 13.4 – Count rates as functions of the reduced bias current (normalized to the critical current at each temperature) with an acceleration voltage of 49.9 kV.

The relatively long electron-phonon interaction time suppresses the probability of electron thermalization through the phonon channel, which makes the photon energy conversion efficiency higher in WSi than in other materials. Moreover, a large intrinsic quasiparticle lifetime results in a larger hotspot in WSi. In summary, our models and experimental data successfully explain the remarkable detection efficiency of WSi as compared to NbN.

[1] Zhang X., Engel A., Wang Q., Schilling A., Semenov A., Sidorova M., Hübers H.-W., Charaev I., Ilin K., and Siegel M.,
Rev. B, 94:174509, 2016.

[2] Marsili F., Stevens M. J., Kozorezov A., Verma V. B., Lambert C., Stern J. A., Horansky R. D., Dyer S., Duff S., Pappas D. P., Lita A. E., Shaw M. D., Mirin R. P., and Nam S. W.,
Phys Rev. B, 93:094518, 2016.

[3] Marsili F., Verma V. B., Stern J. A., Harrington S., Lita A. E., Gerrits T., Vayshenker I., Baek B., Shaw M. D., Mirin R. P., and Nam S. W.,
Nature Photonics, 7:210, 2013.

13.1.2 X-ray sensitive superconducting photon detectors

One of our most interesting results in our research on single X-ray photon detectors (X-SNSPD) comes from the amorphous nature of the WSi films [4]. The amorphous structure makes this type of detectors more robust against radiation damage and therefore makes them suitable for detecting high-energy particles. Moreover, due to their modest requirements on substrate quality and deposition conditions, very large and complicated WSi X-SNSPDs can be produced relatively easily on different substrates.

Our WSi X-SNSPDs show no degradation of their superconducting properties after the device fabrication, which is very different from the commonly used NbN based devices. In Fig. 13.3, we illustrate the single X-ray photon resolving ability of a WSi X-SNSPD. The linear slope of the curves indicates that our detector works in the single-photon regime at all bias currents. The detection performance of our detector is shown in Fig. 13.4. A saturated detection efficiency is observed at all temperatures, which ensures a high signal-to-noise ratio. Unlike optical SNSPDs, which need to be operated at ultralow temperature ($T/T_c << 1$) our WSi detector is able to sense X-ray photons up to the critical temperature. Due to the amorphous nature and relatively large magnetic penetration depth, the bias current is very stable within the nanowire, and thermal fluctuations can therefore be ignored. As a consequence, the dark counts in our X-SNSPD are negligible. All these properties, saturated quantum detection efficiency, negligible dark counts and ultrafast response, make our X-SNSPDs competitive to the best ultrafast X-ray photon detectors on the market.

[4] Zhang X., Wang Q., and Schilling A.,
AIP Advances, 6:115104, 2016.

13.2 Insulator-to-metal transition in $CsAuCl_3$ and $CsAuBr_3$

In a series of experiments, we studied the physical properties of $CsAuCl_3$ and $CsAuBr_3$. It is known that $CsAuCl_3$ undergoes an insulator-to-metal transition under the application of external pressure, which is accompanied by a tetragonal-to-cubic phase transition at $p \approx 12.5$ GPa at $T = 300$ K [5]. Corresponding Raman investigations strongly indicate a transition from mixed valent (MV) Au(I)Au(III) to formally single valent (SV) Au(II)Au(II) in the metallic state

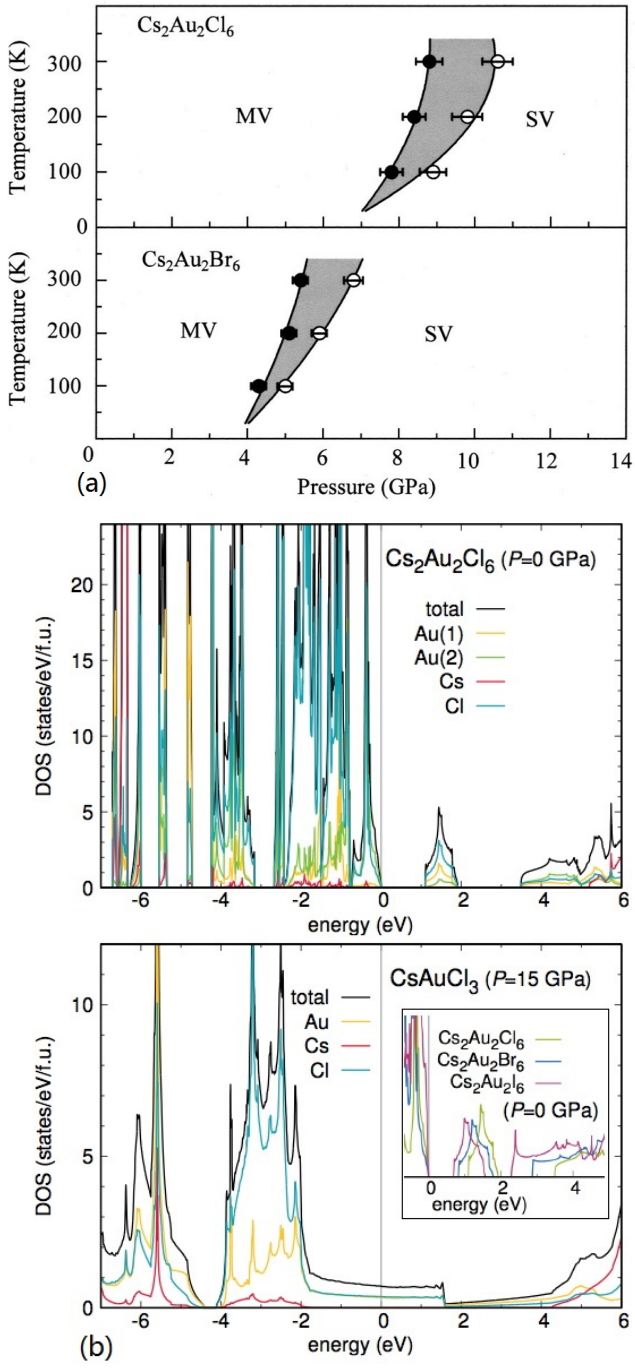

FIG. 13.5 – (a) Mixed valent (MV) to single valent (SV) transition of Au in $CsAuX_3$ with X = Cl and Br (taken from Ref. [6]); (b) Electron density of states (EDOS) of $CsAuCl_3$ for ambient and high pressure. The inset displays the EDOS at ambient pressure for the respective Cl, Br and I variants.

with delocalized charge carriers (see Fig. 13.5(a)) [6]. This situation is very similar to $Ba_{1-x}K_xBiO_3$ [7], in which the substitution of Ba by K not only changes the crystal structure from monoclinic to cubic but also lifts the mixed-valent character of Bi(III)Bi(V) of the insulator $BaBiO_3$, leading to

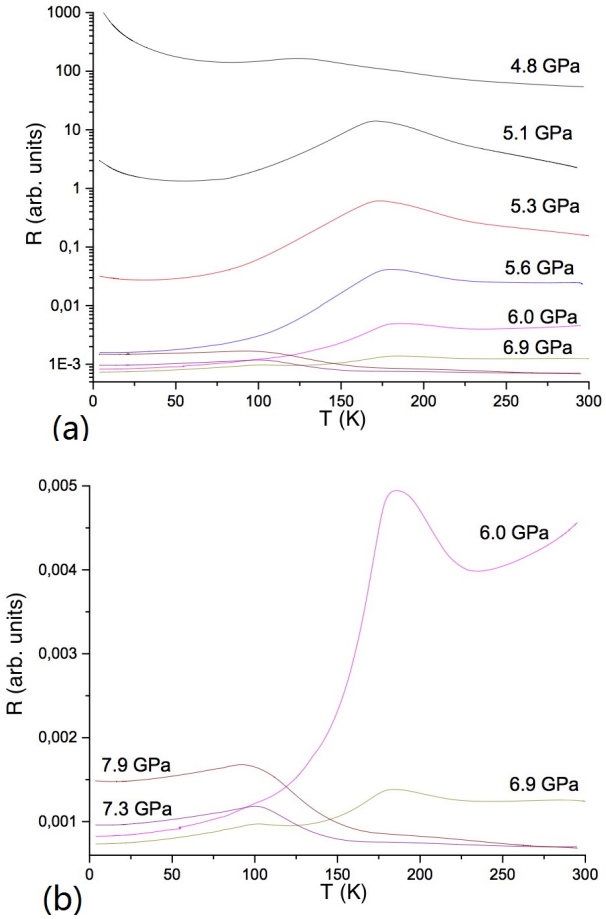

FIG. 13.6 – Evolution of the resistivity of a single crystal of $CsAuBr_3$ under external pressure

a quasi single valent Bi(IV)Bi(IV) state, which is metallic and even superconducting below $T_c \approx 30$ K for $x \approx 0.37$ [7].

In a first step, we wished to obtain more precise information on the electronic structure of these compounds (in collaboration with Prof. R. Thomale, Univ. Würzburg, Germany). Corresponding electronic structure calculations using the full-potential local-orbital minimum-basis scheme confirmed that the high-pressure phase of $CsAuCl_3$ shows a finite density of states at the Fermi level, in contrast to the situation at ambient pressure (see Fig. 13.5(b)). Moreover, at $p = 15$ GPa, the Au(I)-Au(III) character is lost, with a nominal Au(II) valency, but without stabilization of a magnetic moment. The energy gap at ambient pressure is gradually reduced when Cl is replaced by Br or I (see inset of Fig. 13.5(b)).

We have grown single crystals of $CsAuCl_3$ and $CsAuBr_3$ according to the recipe published in Ref. [8]. Inspired by the diagram shown in Fig. 13.5(a), we have measured the resistivity of $CsAuBr_3$ at external pressures up to 7.9 GPa (see Fig. 13.6, in collaboration with Dr. S. Medvedev and Prof. C. Felser, Max Planck Institute for Chemical Physics and Solids, Dresden, Germany). At 4.8 GPa, $CsAuBr_3$ is

semiconducting with some anomaly at ∼130 K. The resistivity decreases several orders of magnitude upon increasing the pressure up to 6-7 GPa (see Fig. 13.6(a)). At pressures above 6 GPa (Fig. 13.6(b)), the evolution of the resistivity is peculiar, with a slight gradual increase at low temperature, with some resemblance to the behaviour of $CsAuI_3$ [9]. There must be various phase transitions (or crossovers) involved, whose origin remains to be investigated.

[5] Matsushita N., Ahsbahs H., Hafner S. S., and Kojima N., Rev. High Pressure Sci. Technol., 7:329, 1998.

[6] Liu X. J., Moritomo Y., Nakamura A., and Kojima N., J. Chem. Phys., 110:9174, 1999.

[7] Cava R. J., Batlogg B., Krajewski J. J., Farrow R., Rupp L. W., Short K., Peck W. F., and Kometani T., Nature, 332:814, 1998.

[8] Riggs S. C., Shapiro M. C., Corredor F., Geballe T. H., Fisher I. R., MAcCandless G. T., and Chan J. Y., J. Crystal Growth, 355:13, 2012.

[9] Kojima N., Fukuhara F., Kitagawa H., Takahashi H., and Mori N., Synthetic Metals, 86:2175, 1997.

13.3 Investigations on the quantum magnets $Sr_3Cr_2O_8$ and $Ba_3Cr_2O_8$

$Sr_3Cr_2O_8$ and $Ba_3Cr_2O_8$ are two insulating dimerized spin systems with the spin 1/2 magnetic ions Cr^{5+}. These ions are located in hexagonal bilayers with a strong antiferromagnetic interaction that leads to a singlet ground state and triplet states separated from the singlet state by an energy gap Δ. This gap closes as soon as the external magnetic field reaches a critical value H_c which is given by the Zeeman splitting of the triplet states. We have previously shown that the intradimer interaction constant J_0 as well as H_c strongly depend on stoichiometry if Ba is successively replaced by Sr ($Ba_{3-x}Sr_xCr_2O_8$), thereby introducing disorder and an expansion of the unit cell [10–12].

[10] Grundmann H., Schilling A., Medarde M., and Sheptyakov D., Physical Review B, 90:075101, 2014.

[11] Grundmann H., Schilling A., Marjerrison C.A., Dabkowska H.A., and Gaulin B.D., Mat. Res. Bull., 48:3108, 2013.

[12] Grundmann H., Gazizulina A., Schilling A., von Rohr F., Forster T., and Peters L., New J. Phys., 18:033001, 2016.

13.3.1 Magnetization measurements on single crystals

Single crystals of $Ba_{3-x}Sr_xCr_2O_8$ were successfully grown for x = 2.8 and 2.9 at the Helmholtz Zentrum Berlin (HZB) by using a high-temperature optical floating-zone furnace (in collaboration with Prof. Bella Lake). In Fig.13.7, we show the magnetic susceptibilities for magnetic fields applied parallel and perpendicular to the c-axes, respectively [13]. The magnetic behaviour is typical for dimerized spin systems, and is in agreement with our previous measurements on polycrystalline samples [11]. However, the data show a certain directional dependence, particularly for x = 2.8, which suggests a weakly anisotropic tensor of the gyromagnetic g factor, as it has been also reported for the pure $Br_3Cr_2O_8$ (x = 0) [14].

[13] Gazizulina A., Quintero-Castro D., and Schilling A., in preparation.

[14] Kofu M., Ueda H., Nojiri H., Oshima Y., Zenmoto T., Rule K. C., Gerischer S., Lake B., Batista C. D., Ueda Y., and Lee S.-H., Physical Review Letters, 102:177204, 2009.

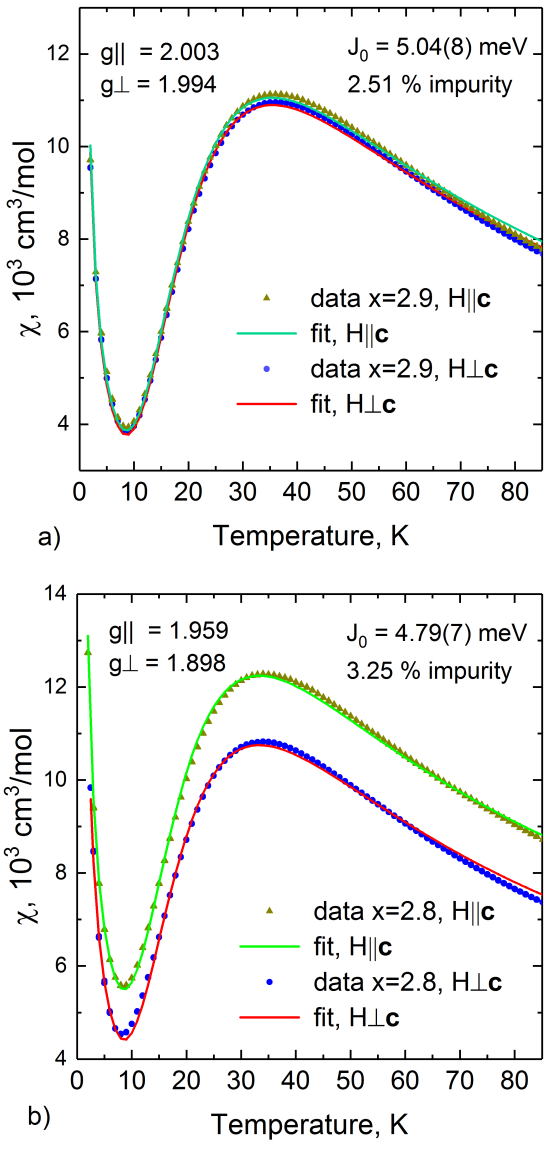

FIG. 13.7 – Magnetic susceptibilities for single crystals of *a*) $Ba_{0.1}Sr_{2.9}Cr_2O_8$ and *b*) $Ba_{0.2}Sr_{2.8}Cr_2O_8$ with magnetic fields parallel and perpendicular to c, respectively.

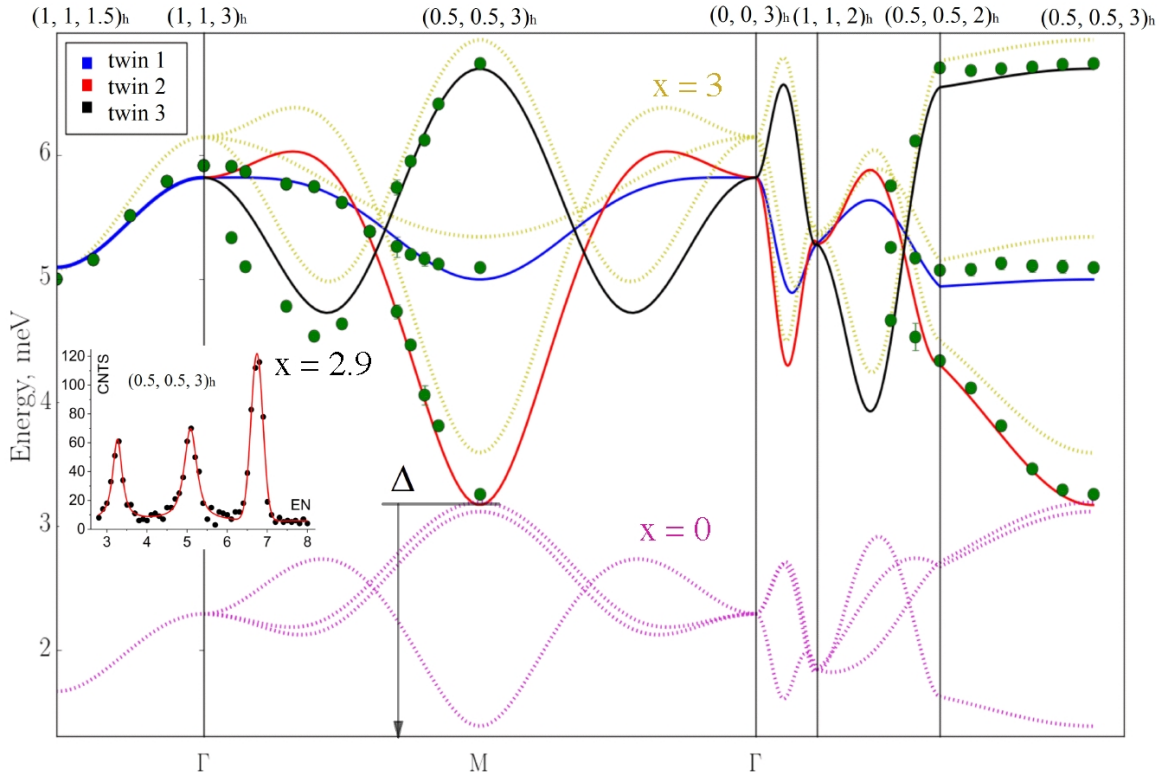

FIG. 13.8 – Measured room-temperature dispersion relation for $Ba_{0.1}Sr_{2.9}Cr_2O_8$ from our inelastic neutron scattering experiments [15]. The solid lines correspond to a random-phase approximation model for three different Jahn-Teller induced crystal domains, rotated 60° with respect to each other. The calculated relations for $Sr_3Cr_2O_8$ (x = 3) and $Ba_3Cr_2O_8$ (x = 0) are shown for comparison.

13.4 Magnetic dispersion relation in $Ba_{0.1}Sr_{2.9}Cr_2O_8$

To complement our investigations on $Ba_{3-x}Sr_xCr_2O_8$, we have performed a series of inelastic neutron scattering measurements (at HZB Berlin, Germany), to directly measure the magnetic coupling constants and the spin gap Δ [15]. In Fig.13.8, we show our corresponding data that we obtained on a $Ba_{0.1}Sr_{2.9}Cr_2O_8$ single crystal, and we fitted them with a random-phase approximation model similar to that described in Ref. [16] for $Sr_3Cr_2O_8$. To achieve this, we had to respect the fact that due to a Jahn-Teller distortion (see our last annual report), three different crystal twin domains, rotated by 60° with respect to each other, have to be taken into account, resulting in three dispersion modes that merge in the center of the Brioullin zone (i.e., in the Γ point). The result for the intradimer interaction constant J_0 is consistent with our previously published results [17–19]. The spin gap Δ (i.e., the minimum in the dispersion relation) is at Δ = 3.23 meV (see Fig. 13.8) resulting in a critical field $\mu_0 H_c = \Delta/g\mu_B \approx 28.8$ T (using $g = 2$), which compares favourably with our published value $\mu_0 H_c \approx 28.6(1)$ T from our high-field magnetization measurements [19]. The corresponding value for pure $Sr_3Cr_2O_8$ is $\mu_0 H_c \approx 30.4$ T [16,18].

[15] Gazizulina A., Quintero-Castro D., and Schilling A. in preparation.

[16] Quintero-Castro D. L., Lake B., Wheeler E. M., Islam A.T.M.N., Guidi T., Rule K. C., Izaola Z., Russina M., Kiefer K., Skourski Y., and Herrmannsdorfer T., Physical Review B, 81:014415, 2010.

[17] Grundmann H., Schilling A., Medarde M., and Sheptyakov D., Physical Review B, 90:075101, 2014.

[18] Grundmann H., Schilling A., Marjerrison C.A., Dabkowska H.A., and Gaulin B.D.m Mat. Res. Bull., 48:3108, 2013.

[19] Grundmann H., Gazizulina A., Schilling A., von Rohr F., Forster T., and Peters L.m New J. Phys., 18:033001, 2016.

14 Surface Physics

M. Hengsberger, L. Castiglioni, H.Y. Cun, L. H. de Lima, A. Hemmi, D. Leuenberger, E. Miniussi, C. Monney, Z. Novotny, C. Bernard, P. Kliuiev, A. Kostanyan, A. Schuler, R. Stania, K. Waltar, W.-D. Zabka, M. Hotz, M. Meier, H. Nussbaumer, B. Salzmann, K. von Arx, P. Dona, T. Kälin, T. Greber, and J. Osterwalder

Our laboratory is equipped for the investigation of surface and interface phenomena at the atomic level, for the preparation and characterization of clean single-crystalline surfaces, metal and molecular monolayer films, as well as sp^2-bonded single layers on surfaces. In addition, we are part of a user consortium of the soft x-ray beamline *PEARL (PhotoEmission and Atomic Resolution Laboratory)* at the Swiss Light Source. Our group has built and commissioned a compact and mobile angle-resolved photoemission (ARPES) instrument, while a second ARPES spectrometer is currently being set up together with a high-harmonic gas jet source for producing short VUV light pulses.

The research carried out during the report period can be grouped into four topics:

- 2D materials
  Monolayer hexagonal boron nitride (*h*-BN) and graphene are grown by chemical vapor deposition (CVD) on metal surfaces. We used *h*-BN on a thin film of Rh(111) in a sessile drop electrochemical cell that allowed to change the wetting angle with an electrochemical potential (cover story in Nature, June 30). The related knowledge on the electrochemical behavior is used to optimize methods for delaminating single layer *h*-BN from their metal substrate. This project is currently pursued within the European Flagship Graphene.

- Adsorbed molecular catalysts and photosensitizers
  Within the University Research Priority Program *Light to Chemical Energy Conversion* (LightChEC) we develop and study model catalyst surfaces for solar water splitting. In Section 14.1 we present results on the adsorption of Co-pyrphyrin on $Cu_2O(111)$ where the band and molecular orbital alignment appears to be particularly optimal for the charge separation process needed for photolysis of water.

- Ultrafast processes at surfaces
  This year we report on a reconstruction scheme for the recovery of the phase of molecular orbitals, in this case pentacene from angle scanned VUV photoelectron diffraction data (see Section 14.2). The nodal structure of the wave function may be reconstructed. This will serve as a tool for time resolved experiments, where the symmetry of molecular orbitals and their evolution will be studied.

- Spin shuttles
  Monolayers of endohedral Fullerenes (*spin shuttles*) like $Dy_3N@C_{80}$ order their carbon cages on surfaces. On metals they furthermore display a tendency to orient their endohedral units. Within a collaboration with the ENS Paris, the Paul Scherrer Institut and the IFW Dresden we succeeded to trace back this orientation effect to anisotropic polarization of the carbon cage that must be induced by the ionic endohedral units (see Section 14.3).

We like to highlight the award of an SNF professorship to Dr. Claude Monney, who currently has an Ambizione fellowship on "Time- and angle-resolved photoemission spectroscopy on correlated materials" in our lab.

In the following, three highlights of last year's research are presented in more detail.

14.1 Atomically resolved charge density profile in a photocatalytic p-n heterojunction

In collaboration with: Stephan Schnidrig, Benjamin Probst and Roger Alberto, Chemistry Department, Universität Zürich.

Within the University Research Priority Program *Light to Chemical Energy Conversion (LightChEC)* the group investigates model systems formed by molecular catalysts for photoinduced water splitting which are immobilized on single-crystalline oxide surfaces. The focus was set on Co-pyrphyrin, which is a porphyrin-like organometallic macrocycle that has shown a high activity for light-induced hydrogen evolution in homogeneous systems [1]. In a previous study we have characterized the adsorption behavior of pyrphyrin on Au(111) and the in-situ metalation by Co evaporation [2].

Cu_2O is a p-type semiconductor with a band gap of 2.2 eV that is well suited for solar light harvesting in a photocathode. The downward band bending in the $Cu_2O(111)$ surface directs photoexcited electrons towards the surface where they can be made available for

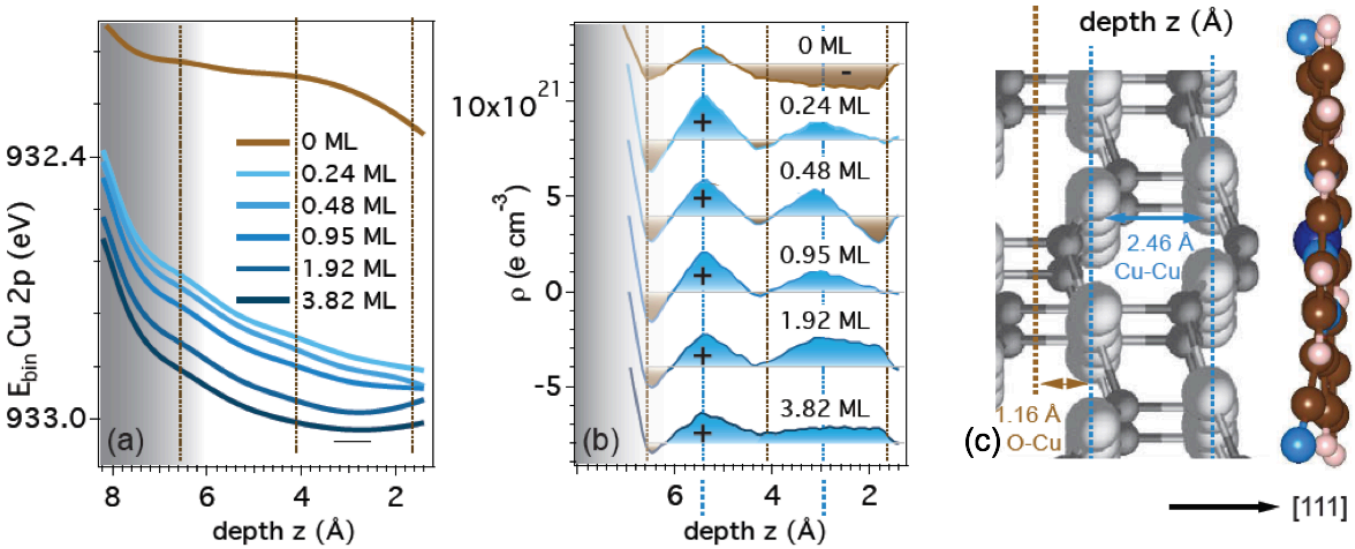

FIG. 14.1 – (a) Band bending profiles in clean and Co-pyrphyrin covered $Cu_2O(111)$ surfaces from polar-angle dependent Cu 2p core-level binding energies. The depth z represents a mean probing depth associated with a particular polar angle according to a cosine law. The different traces represent different Co–pyrphyrin coverages in units of monolayers (ML); (b) charge density profile obtained from applying Poisson's equation to the data in (a); and (c) cross sectional ball-and-stick model of the junction showing a Co-pyrphyrin molecule on the $Cu_2O(111)$ surface.

the reduction of protons via a catalyst. Measurements of the binding energies of substrate core levels by XPS can provide information on how the presence of the catalyst molecules affects the band bending.

Measurements at different photoelectron emission angles probe different depth ranges within the surface. Fig. 14.1a shows the depth dependence of the Cu 2p binding energies as a function of mean probing depth. The overall downward band bending towards the surface is readily seen, and it is conserved upon the adsorption of Co-pyrphyrin layers of various thicknesses. The observed downward offset for the molecule covered surfaces indicates an enhanced overall band bending, as these measurements show only the topmost nanometer while the band bending extends much further into the bulk of the oxide. One notices further that the curvature of the band-bending profiles close to the surface changes sign with increasing layer thickness. Moreover, slight oscillations in curvature can be observed for all curves.

Shifts in the core-level binding energies follow directly the local changes in the electrostatic potential at the position of the respective atoms. Poisson's equation relates the second derivative of the potential energy profile $V(z)$ to the local charge density profile $\rho(z)$. Corresponding curves are shown in Fig. 14.1b. Here, the oscillations are much more prominent. The maxima (positive charge) appear consistently at a distance that corresponds to the Cu-Cu layer distance (Fig. 14.1c), suggesting that the method can reveal the charge density variations with atomic resolution. On the clean $Cu_2O(111)$ surface the presence of oxygen vacancies leads to an effective negative charge on the surface Cu atoms, while the presence of adsorbed Co-pyrphyrin molecules changes this sign. This observation can be explained by a polarization of the molecular layer in response to the electric field at the oxide surface.

[1] E. Joliat, *et al.*, Dalton Trans. **45**, 1737 (2016).

[2] G. Mette *et al.*, Nanoscale **8**, 7958 (2016).

14.2 Reconstruction of molecular wavefunctions from photoemission data

In collaboration with: Tatiana Latychevskaja (Physik-Institut, UZH), Achim Schöll (University of Würzburg, Germany); NCCR MUST.

The efficiency of molecular optoelectronic devices critically depends on charge transfer mechanisms at metal-organic interfaces. The optimization of charge transfer across interfaces thus requires rigorous time-resolved spatial visualization of these processes. A few years ago, it was shown that information about the wave functions of well-ordered organic large planar molecules on single crystalline metal substrates is encoded in angle-resolved photoelectron spectroscopy (ARPES) data [3–5]. More explicitly, the angular distribution of the photocurrent depends amongst others on the shape and phase of the initial state wavefunction.

In the case of negligible final state scattering, the final state of the photoelectron can well be approximated by a plane wave, whose momentum component parallel to the

surface plane $\vec{k}_{||}$ is preserved in the emission process:

$$\|\vec{k}_{||}\| = \sqrt{\frac{2m^\star}{\hbar^2}\left(h\nu - E_i - \phi\right)}\,\sin\theta,$$

where $m^\star$ denotes the effective mass of the final state, $h\nu$ the photon energy, E_i the binding energy of the initial state, ϕ the workfunction of the surface, and θ the emission angle.

Within the plane wave approximation for the photoelectron final state $\psi_f(\vec{k}) \propto \exp(\imath\vec{k}\vec{r})$, the recorded ARPES intensity distribution is related to the squared modulus of the Fourier transform of the initial state wave function $\psi_i(\vec{k})$ (the energy variables are dropped for the sake of readability) [3]:

$$\begin{aligned} I(\vec{k}_f) &\propto \sum_i \sum_{\vec{k}_{i||},\vec{G}_{||}} & \left|\left\langle \psi_f(\vec{k}_{f||}, r) \left| \vec{A}\cdot\vec{p} \right| \psi_i(\vec{k}_{i||}, r)\right\rangle\right|^2 \quad \delta\left(\vec{k}_{f||} - \vec{k}_{i||} - \vec{G}_{||}\right) \\ &\propto \sum_i \sum_{\vec{k}_{i||},\vec{G}_{||}} & \left(\vec{A}\cdot\vec{k}_f\right)^2 \left| \underbrace{\int e^{\imath\vec{k}_{f||}\vec{r}_{||}}\, \psi_i(\vec{k}_{i||}, \vec{r}_{||})\, \delta\left(\vec{k}_{f||} - \vec{k}_{i||} - \vec{G}_{||}\right) d^2 r_{||}}_{} \right|^2 \\ &= \sum_i & \left(\vec{A}\cdot\vec{k}_f\right)^2 \qquad \left|\mathcal{F}\left\{\psi_i(\vec{r}_{||})\right\}\right|^2. \end{aligned}$$

$\vec{A}$ denotes the vector potential of the light and $\vec{G}_{||}$ a reciprocal lattice vector of the surface. The selection of the initial state i is made by choosing the corresponding peak in the energy spectrum. The angular intensity distribution of the peak intensity $I(\vec{k}_f, E_i)$ with $E_i = h\nu - E_{\text{kin}} - \phi$ thus represents the Fourier transform of $\psi_i(\vec{r}_{||})$ modulated by a slowly varying envelope function $\vec{A}\cdot\vec{k}_f$.

The initial state wavefunction $\psi_i(\vec{r}_{||})$ can be computed by inverse Fourier transform of the ARPES data, provided that the phase distribution in the detector plane is known. The phase distribution missing in the experiment may be inferred from the parity of the wave function [3], dichroism measurements [4] or iteratively, by employing knowledge about the shape of the wave function [5].

We suggest that the phase problem in ARPES based reconstruction of molecular wave functions can be solved in a more robust manner by exploiting the analogy to the phase problem in coherent diffraction imaging (CDI) [6]: provided that the far field optical intensity distribution is measured at the oversampling condition, both the amplitude and the phase of the object can be reconstructed purely from the experimentally available modulus of its Fourier transform using state-of-the-art phase retrieval algorithms, currently available in CDI [7–9]. The oversampling condition means that the ARPES image in the Fourier domain is sampled fine enough such that the ob-

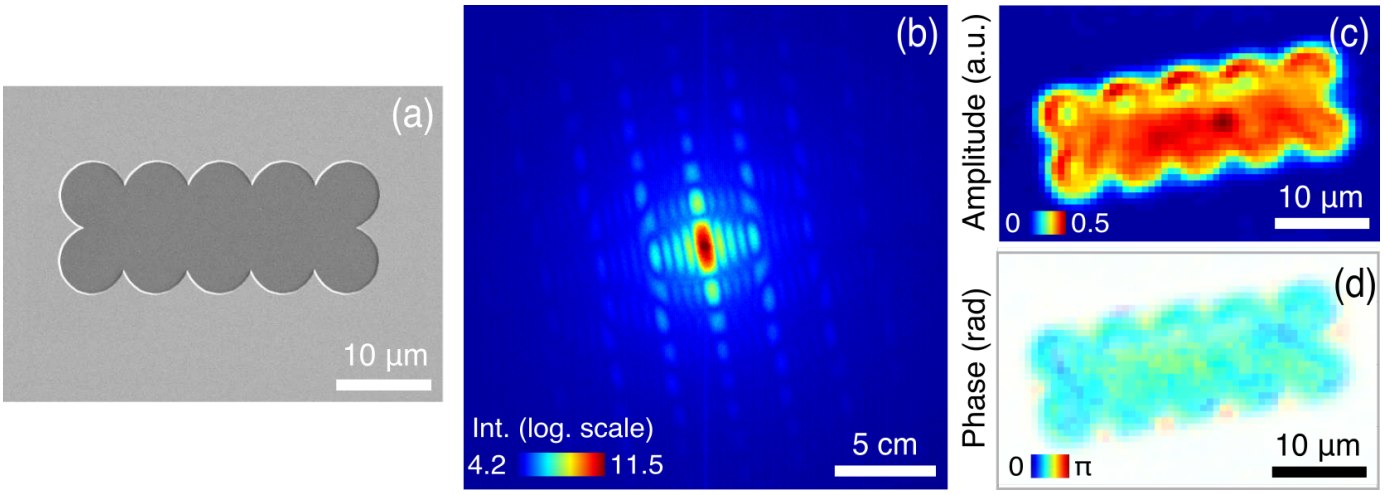

FIG. 14.2 – Results of the CDI experiment (from Ref. [10]). (a) Electron microscope picture of the pentacene orbital mimicked lithographically in Cr/SiO_2. (b) Diffraction pattern recorded in transmission using 532 nm laser light in normal incidence. (c) and (d) Reconstructed amplitude (c) and phase (d).

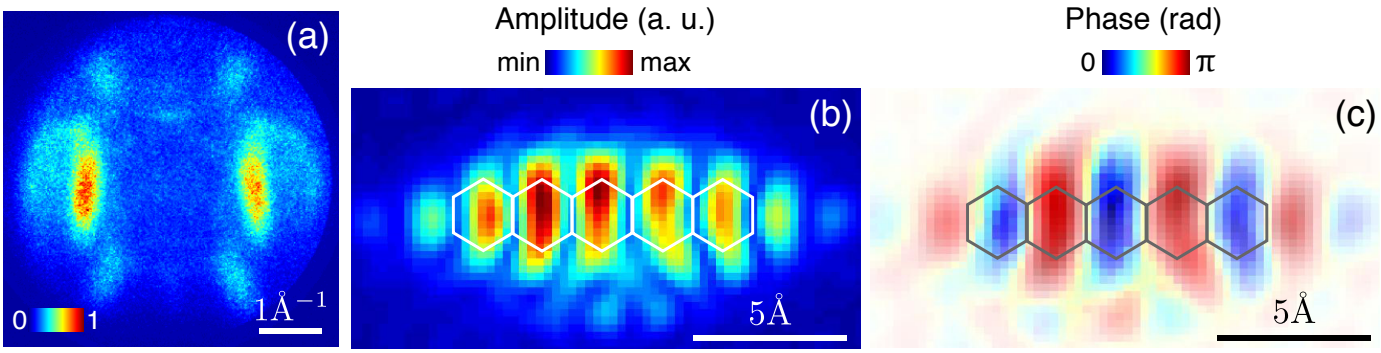

FIG. 14.3 – Reconstruction of the pentacene LUMO (from Ref. [10]). (a) Angular photoemission intensity distribution recorded using a so-called momentum microscope [11] from a sub-monolayer of pentacene on Ag(110) at a photon energy of 50 eV. (b) and (c) Reconstructed amplitude (b) and phase (c) of the LUMO. The color brightness in (c) is weighted with the corresponding amplitude values for illustration purposes.

ject distribution in real space is surrounded by a zero-padded region and the ratio between the total number of pixels in the image and the number of pixels belonging to the object exceeds two [10].

In order to demonstrate the analogy between CDI and ARPES based reconstructions, we perform an optical analogue experiment on micrometer-sized structures together with T. Latychevskaja from the group of H.-W. Fink. From the far-field diffraction patterns recorded using a 532 nm laser and a CCD camera, the amplitude and phase distributions could be reconstructed [10]. Obviously, the phase is uniform for this lithographic mimic. The ratio of the size and the laser wavelength corresponds to the ratio of the molecular orbital to the de Broglie wavelength of the photoelectrons used for the imaging of the pentacene LUMO. The results are shown in Fig. 14.2.

By applying the same algorithm to a set of ARPES data taken by the group of A. Schöll (University of Würzburg) at the Elettra Sychrotron in Trieste from an ordered sub-monolayer of pentacene molecules on Ag(110), both the amplitude and phase of the lowest unoccupied molecular orbital (LUMO) could be reproduced (see Fig. 14.3).

It has to be emphasized that no assumption on the shape or symmetry of the molecule is required as input for our algorithm. The oversampling condition is fulfilled in the present case by the length of the molecules and the resolution (pixel size) of the recorded ARPES data [10].

[3] P. Puschnig *et al.*, Science **326**, 702 (2009).

[4] M. Wiessner *et al.*, Nat. Comm. **5**, 4156 (2014).

[5] D. Lueftner *et al.*, PNAS **111**, 605 (2014).

[6] J. Miao *et al.*, Nature **400**, 342 (1999).

[7] J. Fienup, Opt. Lett. **3**, 27 (1978).

[8] S. Marchesini *et al.*, Phys. Rev. B **68**, 140101 (2003).

[9] R. Harder *et al.*, New J. Phys. **12**, 035019 (2010).

[10] P. Kliuiev, T. Latychevskaia, J. Osterwalder, M. Hengsberger, and L. Castiglioni, New J. Phys. **18**, 093041 (2016).

[11] C. Schneider *et al.*, J. Elec. Spectr. Rel. Phen. **185**, 330 (2012).

14.3 Understanding the orientation of endohedral clusters in C_{80} on surfaces

In collaboration with: Ari P. Seitsonen, Département de Chimie, École Normale Supérieure, Paris, France, Matthias K. Muntwiler, Swiss Light Source, Paul Scherrer Institut, Villigen, Switzerland, and Alexey A. Popov, Nanoscale Chemistry Leibniz Institute for Solid State and Materials Research, IFW Dresden, Germany.

Endohedral Fullerenes like $TbSc_2N@C_{80}$ (Fig. 14.4a) contain isolated physical entities that are in the present case $TbSc_2N$ clusters. The carbon cage separates the endohedral from the exohedral world. This is an ideal scenario if for example magnetization shall be protected from unwanted chemical interaction. The interaction of the endohedral unit across the carbon cage is weak but finite. This is shown by the fact that different endohedral molecules like $Tb_2ScN@C_{80}$ and $TbSc_2N@C_{80}$ may be separated by high pressure liquid chromatography [12], by the observation of orientation of the endohedral units on surfaces [13], and by their magnetic ordering [14]. Although the orientation of the molecules on surfaces may be measured, and an interaction across the cage may be conjectured, [13, 14] an understanding of this effect is lacking. In combining density functional theory and electrostatics, and with comparison to experimental high-resolution x-ray photoelectron spectra we succeeded to calculate, identify and measure the interaction between the carbon cage and the ionic endohedral units. Electrostatics and concomitant polarization is im-

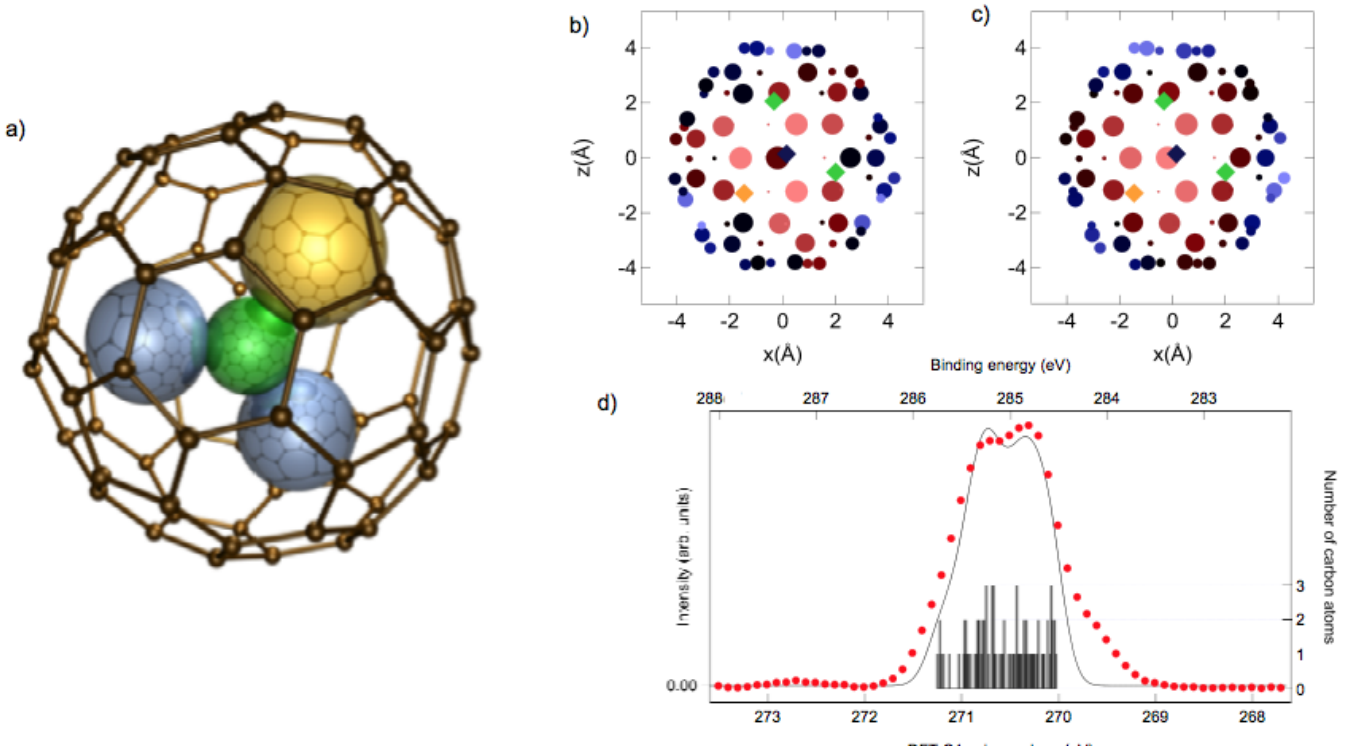

FIG. 14.4 – (a) Model of an endohedral Fullerene such as $TbSc_2N@C_{80}$. 80 carbon atoms form the cage into which fit a terbium (yellow) two scandium (light blue) and a central nitrogen atom (green). (b) C1s Density Functional Theory DFT eigenvalues (red-blue) of the 80 C atoms in $YSc_2@C_{80}$. The size of the circles represents the y-coordinate. The diamonds indicate the endohedral atoms. (c) Coulomb potential (red-blue) on the 80 C atom-sites as imposed by the endohedral ions. Note the similarity to (b). (d) Comparison of high resolution x-ray photoelectron spectroscopy (XPS) data of a submonolayer $TbSc_2N@C_{80}$ on *h*-BN/Ni(111) with the DFT C1s eigenvalues. The eigenvalue-spectrum (black) is convoluted and shifted to the experiment (red dots) from [15].

portant because the endohedral unit is very ionic: C_{80} is stable, if six electrons are transferred to the carbon shell. They completely fill the 8-fold degenerate highest occupied molecular orbital and stabilize it accordingly. For the case of trimetal nitride Fullerenes three trivalent rare earth atoms contribute nine electrons, where three of them fill the nitrogen 2p shell and the rest stabilizes the carbon cage.

The density functional theory (DFT) calculations of the C1s eigenvalues are shown for $YSc_2N@C_{80}$ in Fig. 14.4 b). Yttrium is isovalent to terbium and has a similar size, though may be much better handled with DFT than the open shell $4f^8$ Tb^{3+}. Theory indicates a C1s eigenvalue spectrum that is linear in the electrostatic potential, which is imposed by the ionic species inside the carbon cage. For $TbSc_2N@C_{80}$ we observe with x-ray photoelectron spectroscopy a splitting of the C1s core level that quantitatively agrees with the splitting in the calculated DFT spectrum. This is the key fact for the understanding of chemical interaction across the Fullerene cage. These findings may be important as well for the understanding of ionic interactions across graphene or other single layer two dimensional materials.

[12] A.A. Popov, S.F. Yang, and L. Dunsch, Chem. Rev. **113**, 5989 (2013).

[13] M. Treier *et al.* Phys. Rev. B **80**, 081403(R) (2009).

[14] R. Westerström *et al.* Phys. Rev. Lett, **114**, 087201 (2015).

[15] R. Stania, PhD thesis University of Zürich 2016.

15 Physics of Biological Systems

Conrad Escher, Hans-Werner Fink, Tatiana Latychevskaia, Jean-Nicolas Longchamp (until February 2017), Marianna Lorenzo, Flavio Wicki (until July 2016)

in collaboration with: Dr. Roger Morin, CNRS Marseille (France), Prof. Peter Hommelhoff, University of Erlangen (Germany), Prof. Klaus Kern and Dr. Stephan Rauschenbach, Max Planck Institute, Stuttgart (Germany), Prof. Christian Schönenberger, University of Basel (Switzerland).

15.1 Overview of Current Projects

The structural investigation of individual biological objects by employing coherent low-energy electrons is at the center of our research. It involves in-line holography with low-energy electrons as well as coherent diffraction imaging and is assisted by micro-structuring techniques using a focussed gallium ion beam device for miniaturized electron optics and sample preparation. Major challenging experimental developments are ongoing to improve the interference resolution, establish methods for creating free standing thin films of graphene transparent for low-energy electrons as well as appropriate techniques to present a single protein to the coherent electron wave front. Next to these experimental issues, a second, equally important aspect for achieving high resolution structural information is the numerical reconstruction of the electron holograms respectively iterative phase retrieval in coherent diffraction. This is achieved by employing newly developed numerical algorithms to solve the integrals governing these coherent optics problems. In this way, it has become possible to image individual proteins for the first time in the history of structural biology. During the past year, strategies for helping to bring this novel tool for single protein structural biology into routine operation to the benefit of medical and pharmaceutical research and development have been developed.

15.2 Novel applications of coherent point source beams

While holography and coherent diffraction applied to biological systems are the most prominent applications pursued by us, in the frame of the PhD thesis of Flavio Wicki, some quite different and novel applications of electron point sources have been developed. A miniaturized electron column exhibiting electrostatic lenses in the micrometer regime has been realized following the notion that the intrinsic lens aberrations of cylindrical symmetric electron lenses scale with their dimensions. This approach has led to a tiny electron microscope column with excellent beam shaping performance due to aberrations reduced by about a factor of thousand using this downscaling principle.

A further novel application is the in-situ combination of low-energy electron holography with Scanning Tunneling Microscopy (STM) technology in order to add a novel contrast mechanism to Low Energy Electron Point Source (LEEPS) microscopy. Holograms of clusters and their reconstruction were thus combined with image information arising from scanning the electron point source in close proximity to the free-standing graphene support to measure the absorption as well as the electron transmission through the very same individual clusters present on free-standing graphene.

This novel mode of operation leads to very low kinetic energies, below 30 eV, of the emitted electrons which has led to another previously unknown application of a coherent electron point source, namely a direct mapping of electronic structure details of free-standing graphene. Under those angles where the k-vector component of the incoming electron parallel to graphene matches unoccupied states in graphene, high absorption is observed. This translates in a direct mapping of the unoccupied bands of graphene revealed by a hexagonal structure in the transmission image observed on a distant detector. Owing to the high numerical aperture of the detection system, the hexagons reflecting the unoccupied bands grow accordingly by decreasing the primary kinetic energy of the electrons from 30 down to 18 eV. The measurement principle and the observed pattern are illustrated in Fig. 15.1.

15.3 Imaging the potential distribution of individual charged impurities on graphene by low-energy electron holography

While imaging individual atoms can routinely be achieved in high resolution transmission electron microscopy, visualizing the potential distribution of individually charged adsorbates leading to a phase shift of the probing electron wave is still a challenging task. Low-energy electrons (30 - 250 eV) are sensitive to localized potential gradients. We employed low-energy electron holography to acquire in-line holograms of individual charged impurities on free-standing graphene. By applying an iterative phase retrieval reconstruction routine, we recover the potential distribution of the localized charged impurities present on free-standing graphene.

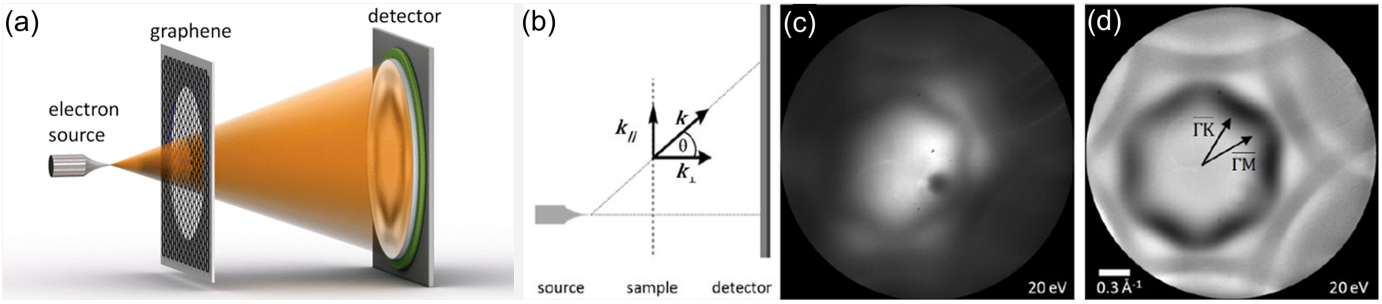

FIG. 15.1 – (a) Schematic of the experimental setup. The in-plane k-vector of the electrons impinging onto graphene under a certain angle is illustrated in (b). The in-plane momentum dependency of the transmission through free-standing graphene thus allows probing the unoccupied bands by observing the electron transmission pattern at a distant detector. In (c) raw data of such a transmission pattern for 20 eV electrons are shown while in (d) the same data are displayed after background subtraction and transformed into coordinates of the k-vector parallel to graphene. The arrows indicate the direction of the high symmetry points K and M in the Brillouin zone, determined from the first order diffraction disks observed at higher electron energies.

The experimental setup is depicted in Fig. 15.2. Electrons are field emitted from a sharp tungsten tip and the electron wave passes through the sample while part of the wave is scattered by the object. Interference between the scattered and non-scattered wave leads to a hologram recorded at a distant detector. The sample is free-standing graphene with some residual adsorbates after sample preparation. Since transparent free-standing graphene provides an overall equipotential plane, a neutral adsorbate present on graphene results in an ordinary hologram, as illustrated in Fig. 15.2(b). However, a charged impurity locally creates a high electric field deflecting the passing electrons. The presence of a positively charged impurity thus leads to a distinctive signature in the hologram, a bright spot, as illustrated in Fig. 15.2(c).

In the case of imaging a charged object with an electron wave, the distribution of the electron wave is altered by the object. A charged impurity deflects even those electrons which are passing the localized charge at some distance. Therefore, a clean separation between the reference wave (not affected by the object) and the object wave (affected by the object) is not possible any more. Consequently, the lack of a well-defined reference wave precludes an ordinary hologram reconstruction. A sensible hologram reconstruction becomes thus more involved. The problem of object reconstruction from the recorded interference pattern is similar to the phase retrieval problem in coherent diffraction imaging (CDI), where only the intensity of the scattered wave is detected but no reference wave is present. In CDI, typically, an iterative procedure is applied to retrieve the missing phase distribution in the detector plane and consequently to reconstruct the object distribution. We therefore apply such an iterative procedure to reconstruct holograms of charged impurities. It starts with an initial random phase distribution in the detector plane. In this way, it could finally be

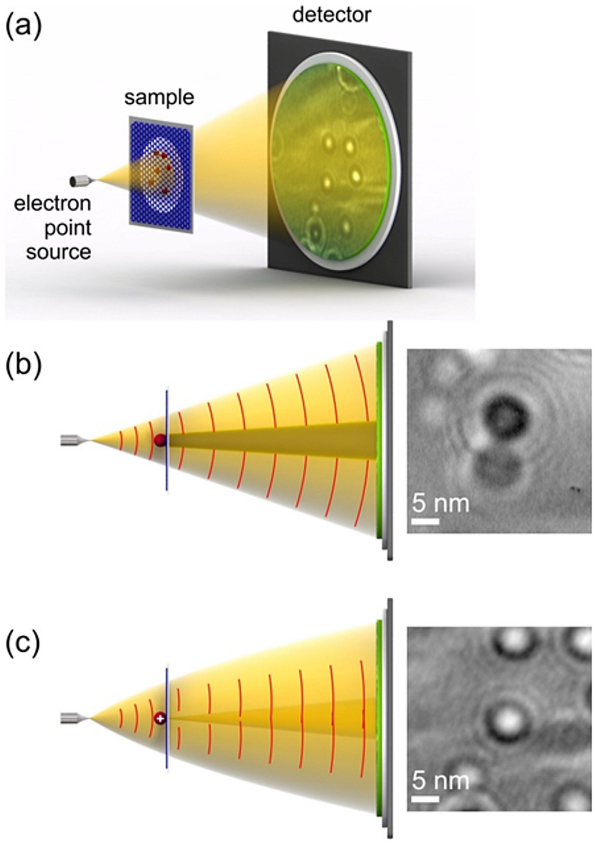

FIG. 15.2 – Experimental arrangement. (a) Low-energy electron holographic microscope. The distance from the source to the sample is in the range of tens of nanometers and the distance from the source to the detector is 47 mm. (b) Imaging of a neutral adsorbate whereby part of the beam is absorbed resulting in an overall dark interference pattern. (c) Imaging of a positively charged adsorbate. The trajectories of electrons are deflected inward by the presence of a positive charge resulting in a bright spot on the detector.

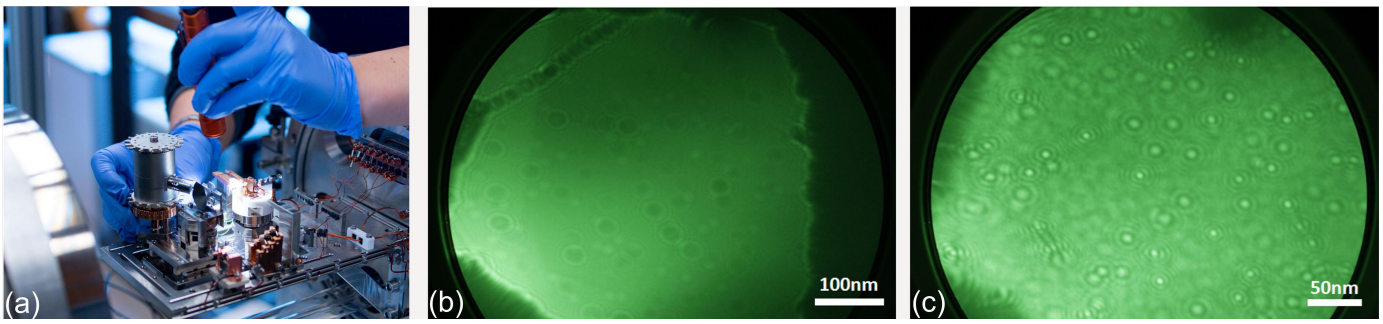

FIG. 15.3 – (a) View into the new LEEPS microscope featuring a rotatable metal evaporator with up to four different metal sources. (b) Clean graphene imaged with 145 eV electrons. (c) Image taken with 100 eV electrons after Cesium deposition onto graphene.

demonstrated that projected potentials of individual adsorbates can be obtained from their low-energy electron holograms by iterative phase retrieval reconstruction.

15.4 Metal nucleation on free-standing graphene

A modified LEEPS microscope has been employed to study in situ metal nucleation on free-standing graphene in the frame of the PhD thesis of Marianna Lorenzo. Up to four different metal sources allow the in-situ deposition of alkali metals under UHV conditions. Alkali atoms were chosen because of an expected significant charge transfer from the atoms to the free-standing graphene support. The transfer of the s-electron to graphene should lead to a strong dipole which should be detectable with low-energy electrons. The experimental setup is shown in Fig. 15.3(a), together with an image of the clean, 15.3(b), as well as a Cesium covered graphene window, 15.3(c). It seems that the transfer of the s-electron causes a remaining positive charge attracting the low-energy electrons leading to bright spots as signatures for charged objects. Detailed studies with different alkali atoms, namely Potassium and Lithium, have also been carried out as well as control experiments with Palladium atoms leading to compact cluster formation.

Figure 15.4 shows a region of a graphene sample where a transition between a single layer and a double layer is displayed which allows studying intercalation effects with alkali atoms. It turns out that Cesium is highly mobile on graphene at room temperature as apparent from observing the situation in-situ during the evaporation process. Upon stopping the evaporation, an equilibrium with constant overall coverage is eventually established. Apparently, as evident from the bottom part of Fig. 15.4, the density of Cesium atoms intercalated in between the double layer appears to be significantly higher than that on the single graphene layer. This translates into an enhanced free energy of binding of intercalated Cesium which is the subject of ongoing studies.

15.5 Imaging proteins at the truly single molecule level

Imaging a single protein has been a long-standing aspiration for advancing structural biology along with various fields in natural science. In particular, revealing the distinct conformations of an individual protein is of utmost

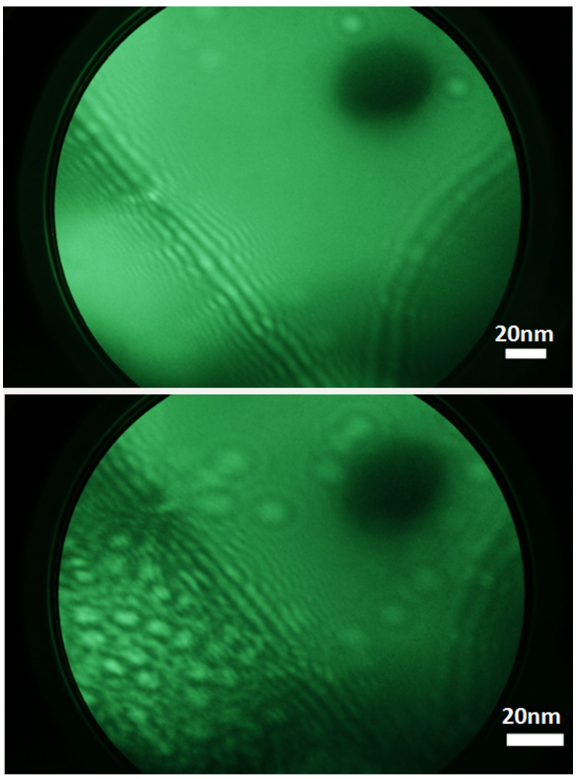

FIG. 15.4 – Top: Graphene sample exhibiting a transition from single to double layer graphene imaged with 66 eV electrons. Bottom: Same region, again imaged with 66 eV electrons, after evaporation of Cesium. After an appropriate waiting time, the system assumes an equilibrium state which is apparently characterized by an enhanced density of intercalated Cesium atoms compared to the density observed for the single layer.

importance. We have shown that imaging individual proteins and protein complexes has become possible by low-energy electron holography. Samples of individual proteins and protein complexes on ultraclean freestanding graphene were prepared by soft-landing electrospray ion beam deposition, carried out by our colleagues from the Max Planck Institute in Stuttgart. Their technology allows for chemical- and conformational-specific selection and gentle deposition. Low-energy electrons do not induce radiation damage, which enables acquiring sub-nanometer resolution images of individual proteins (cytochrome C and bovine serum albumin) as well as of protein complexes (hemoglobin), which are not the result of an averaging process. It was thus the first time that an individual protein has ever been observed at a meaningful spatial resolution.

15.5.1 Current state of the art and perspectives

In Fig. 15.5, two micrographs of individual Bovine Serum Albumin (BSA) are presented and confronted to electron density maps simulated at a resolution of 8 Å with the software package Chimera, originally developed for the analysis of Cryo-EM images. We find a considerable conformance between the simulated density maps and the micrographs and the resolution estimate made from the holographic record is in good agreement with the simulation. To demonstrate that even proteins as large as BSA are sufficiently transparent for low-energy electrons to deliver three-dimensional structural information from a single hologram, the contrast in these micrographs has been enhanced.

Especially in the low-energy electron image presented in the right column, variations of the inner contrast can easily be recognized. To understand the origin of the darker region in the center of the protein image and to associate it with structural features, one may take a look at the protein from a direction parallel to the plane of graphene. The red arrows in the middle row of Fig. 15.5 indicate the direction of observation corresponding to the side views presented in the third row of this image. With the help of these side view representations of the density maps, in which graphene is indicated by a solid blue line, it is possible to address how the proteins are actually adsorbed on the graphene substrate. Of particular interest is the side view presented in the right column as it shows that in this specific orientation, BSA is of strongly varying thickness with a maximum towards the center. The darker region observed

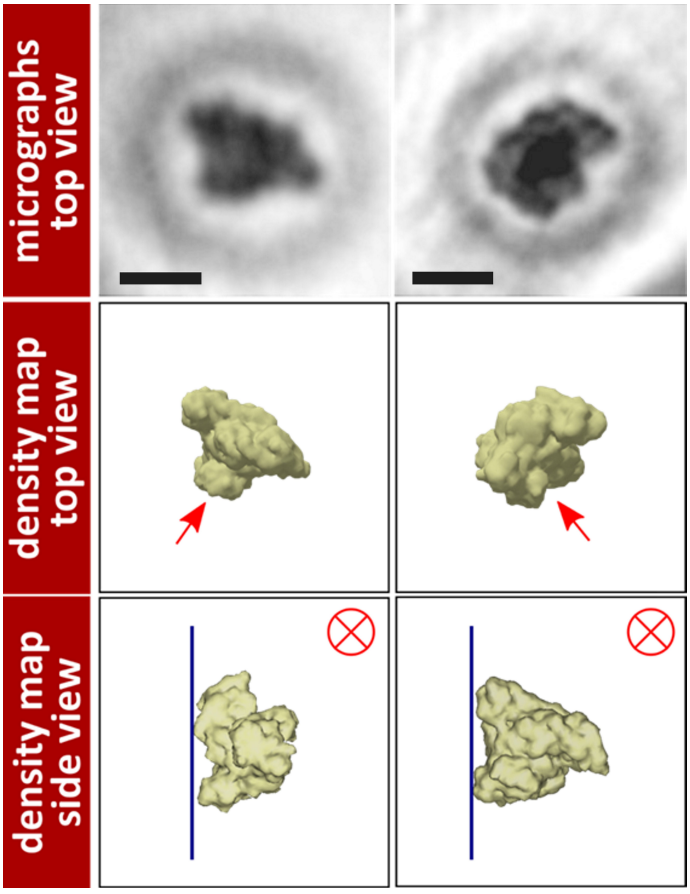

FIG. 15.5 –
Comparison of low-energy electron micrographs of BSA with simulated electron density maps. Top: Low-energy electron micrographs of BSA. The scale bars correspond to 5 nm. Middle: Electron density maps simulated at a resolution of 8 Å and rotated to match the orientation of the proteins presented in the top row. Bottom: Side view of the density map along the directions of observation indicated by the arrows shown in the middle row.

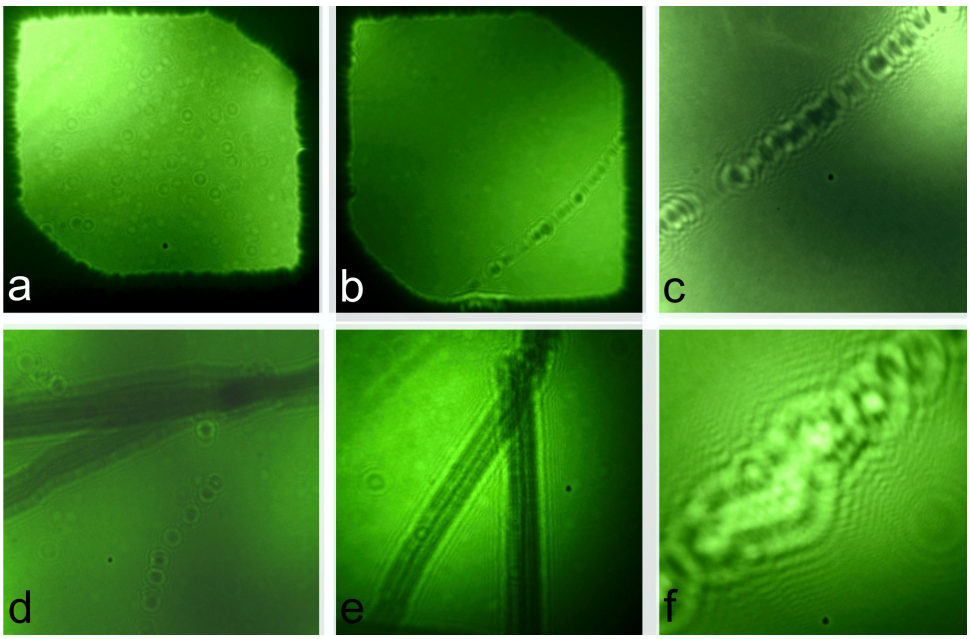

FIG. 15.6 – Low-energy, typically around 100 eV here, transmission images of free-standing graphene. (a) Perfect 500 nm by 500 nm graphene window representative for about 60% of all 400 windows inspected. An apparent grain boundary with some adsorbates is shown in (b) and with higher magnification in (c). Ribbons are shown in (d) and (e) and occasionally holes in otherwise perfect graphene are also apparent (f).

in the micrograph evidently corresponds to a higher absorption due to an increased protein thickness in this area. This observation and analysis demonstrate that already with a resolution of 8 Å, information on the three-dimensional structure of the protein can be gained. In-prospect of an improved resolution of the order of 1-2 Å, it also illustrates the future ability to gain a complete three-dimensional structure from a single low-energy electron hologram of proteins at least as large as 60 kDa.

In this context, it should be noted that the protein data taken so far have been obtained with a LEEPS microscope equipped with the feature of linking up a UHV suitcase for transporting samples to and from Stuttgart where the protein deposition took place. Since its original design was optimized for coherent diffraction imaging for which residual vibrations are not relevant, it was not optimized for best possible vibration damping. It appears that our newest generation LEEPS microscope is already capable to deliver interference resolution in the 3 Å regime at least. Further improvement is to be expected from modifications of the electron point source leading to an increased emission angle.

15.5.2 Properties of free-standing graphene

It seems that graphene, at least until no other two-dimensional structure with high electron transmission properties becomes known, constitutes an optimal support for deposing proteins onto it for subsequent imaging with low-energy electrons. It can be considered as equivalent to the cover slip in light optical microscopy. And, just like for a cover slip in light optical microscopy, one wishes to render it as featureless as possible in order to image just the object that it is supposed to hold fixed in space. So far, we have been using commercially available graphene placed over micro-structured square windows with a typical side length of 500 nm in a SiN membrane. Next to single layer graphene, these commercial samples also feature double and triple layers as well as defects and grain boundaries. While it is not too difficult identifying appropriate windows covered with just a single layer, it seems desirable to maximize the number of perfect graphene windows for imaging proteins deposited onto them. It turns out that our colleagues in the mesoscopic physics group, led by Christian Schönenberger in Basel, are capable of growing superior high quality graphene on copper substrates. Samples from Basel were provided to us and some transmission images are shown in Fig. 15.6.

15.5.3 Perspectives for the first compact single protein structural biology tool

Up to now, protein imaging has been done ex-situ. Holographic imaging and hologram reconstructions were carried out in Zurich while protein deposition has been performed at the May-Planck Institute in Stuttgart. Given the interest of the live science community to eventually arriving at a routine single protein imaging tool, also exemplified by the significant efforts associated with the worldwide XFEL projects, it seems appropriate to work towards a single structural biology tool featuring protein deposition and imaging in-situ. During the past year, extensive interaction with colleagues in the field of protein mass spectrometry as well as with companies active in the field have been undertaken. The goal is to help bringing this novel tool for single protein structural biology into routine operation to the benefit of medical and pharmaceutical research and development. One possible

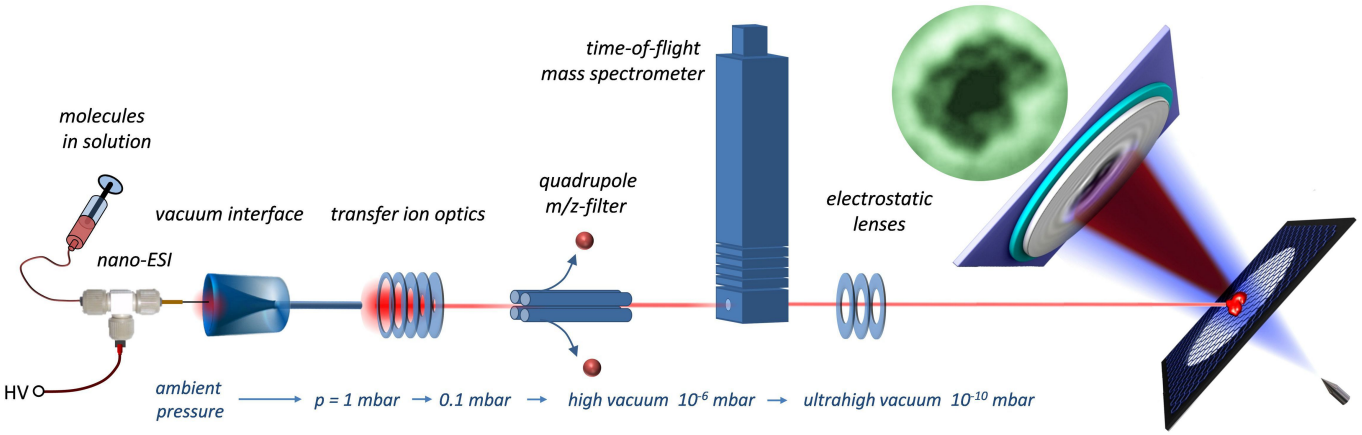

FIG. 15.7 – Schematic, showing the elements of an envisioned future compact single protein structural biology tool. From left to right: Protein ion source and beam shaping part for selecting a specific mass to charge ratio of a selected protein. Time of flight mass-spectrometer to verify the desired protein state. Coupling of the protein beam into the imaging chamber featuring soft landing and holographic imaging of single proteins.

route is to engage companies active in the field of protein mass spectrometry, also to the benefit of the University of Zurich that holds a patent for the combination of low-energy electron holography with protein mass spectrometry. A schematic showing how such a future system might look like, is depicted in Fig. 15.7. If the proteins, as hinted in the schematic here, might even be observable right during the process of landing on the graphene support, still remains to be explored in some more detail.

15.5.4 References

More details about properties and applications of coherent low-energy electron sources can be found here:

- Holography and coherent diffraction with low-energy electrons: A route towards structural biology at the single molecule level, by Tatiana Latychevskaia, Jean-Nicolas Longchamp, Conrad Escher, Hans-Werner Fink, Ultramicroscopy, Volume 159, Part 2, December 2015, Pages 395-402.

The imaging of single proteins using low energy electron holography is described in:

- Imaging proteins at the single molecule level, by Jean-Nicolas Longchamp, Stephan Rauschenbach, Sabine Abb, Conrad Escher, Tatiana Latychevskaia, Klaus Kern, Hans-Werner Fink, PNAS, February 14, 2017, vol. 114 no. 7.

16 Disordered and Biological Soft Matter

M. Ackermann, C. M. Aegerter, F. Atzeni, P. Dagenais (since September 2015), D. Dreher, D. Eder, A. Keller, F. Lanfranconi, A. Mallavalli, A. Pataki (Master student), S. Puri, R. Rüttimann (Master student), L. Schertel (since April 2015), J. Schneider, L. Selvaggi and S. Urdy

in collaboration with: Institute of Molecular Life Sciences (K. Basler, T. Aegerter-Wilmsen, L. Pelkmans, D. Brunner), ETH Zürich (P. Koumoutsakos), MPI für Planzenforschung Köln (R.S. Smith), University of Fribourg (A. Jazwinska), University of Bern (C. Kulemeier, S. Robinson), Biozentrum Basel (M. Affolter), University of Konstanz (G. Aubry, G. Maret), MPI für Selbstorganisation Göttingen (C.C. Maass), Deutsches Luft- und Raumfahrtzentrum (M. Sperl), University of Twente (A. Mosk), Université Joseph Fourier Grenoble (S. Skipetrov), Université Paris Denis Diderot (F. Graner), Technion Haifa (E. Akkermans).

The group of disordered and biological soft-matter investigates the behaviour of disordered materials outside of thermal equilibrium, where instabilities arise that lead to emergent structures. Specifically, three overarching themes are currently studied: The first is focussing on light transport in disordered, multiple-scattering media. This is carried out in connection to Anderson localization, which appears in the case of extreme disorder and which we have studied in detail. In addition, other fundamental properties of multiple-scattering transport are studied, such as the influence of the breaking of path-reciprocity in Faraday-active materials. On the more applied side, the understanding of multiple scattering processes is used to create novel microscopy techniques that are capable of compensating the turbidity using wave-front shaping. Such novel imaging techniques are also developed for use in the second class of problems where the regulation of biological development via mechanical forces is investigated. This is studied in the growth of the Drosophila wing and its folds as well as in the regeneration of fins of the zebrafish. Besides studying the direct growth regulation, the control of developmental processes by mechanical forces is also investigated in the context of shaping three dimensional structures as a driver of morphogenesis. The process of dorsal closure in Drosophila embryos is used for this study. As a complement to these biological systems physical model systems far outside of equilibrium, such as granular gases and foams are investigated. These are studied in diamagnetic levitation in order to obtain information on long time dynamics, which is otherwise masked by the effects of gravity. This allows to understand overall properties of instabilities in disordered non-equilibrium systems.

In the last year, we have made progress in several of these areas, which are discussed in detail below. These subjects concern multiple-scatting Faraday-active materials, imaging in turbid media, as well as the development of molecular force sensors to study the force distributions in tissues, such as the Drosophila wing imaginal disc.

16.1 Multiple Scattering in Faraday-active Materials

Wave propagation in multiple scattering media shows various coherent phenomena connected to the localization of the wave transport, first described by Anderson almost 60 years ago [1]. One aspect, known as weak localization is manifest in the enhancement of multiple scattered light in the direct back direction, known as coherent backscattering [2–4]. These coherent effects are closely connected to the concept of reciprocity on multiply scattering paths, leading to constructive interference. Manipulating the path-reciprocity in such media is a powerful tool to study these phenomena in experiments [5]. In optical experiments, this can be achieved by using Faraday active materials as scattering media and carrying out the experiments in high magnetic fields. It is then possible to destroy the coherence even in strongly scattering samples with a mean free path ℓ^* in the μm range, see Fig. 16.1, provided the Faraday rotation of the sample is strong enough. For this purpose, high magnetic fields of 18 T and low temperatures (T < 10 K) are necessary. These experiments were carried out in TiO_2 samples containing Faraday active CeF_3. In addition to the coherent backscattering cone (CBC) shown in Fig. 16.1, these effects can also be studied in a transmission geometry by investigating the speckle correlation functions [6], where a combination of these two different experiments allows for a quantitative determination of the Verdet constant in the multiple scattering regime. In the extreme case of high magnetic fields and low temperaturess, shown in Fig. 16.2, we have been able to observe the onset of saturation of Faraday rotation in our multiple scattering experiments [6].

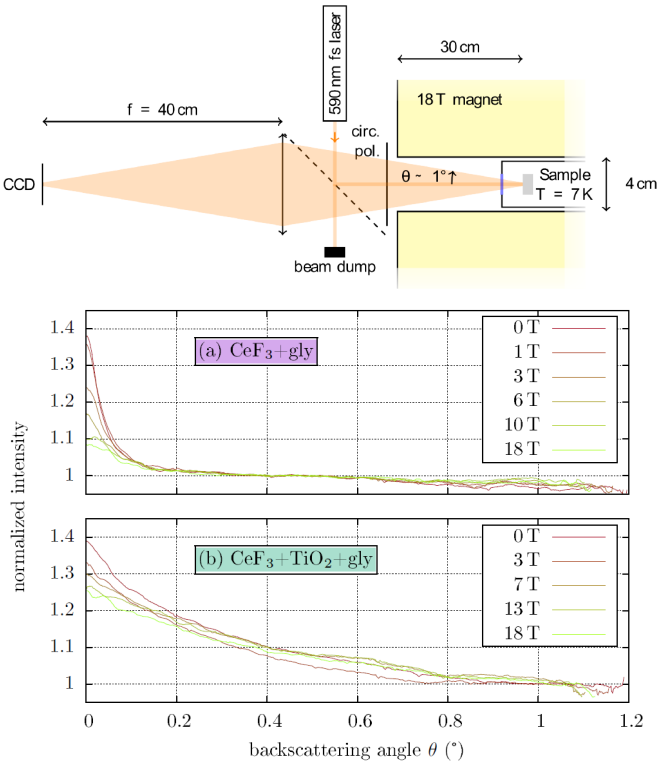

FIG. 16.1 – Top: Schematic CBC setup: A laser beam ($\lambda \approx 590$ nm) illuminates via a 50:50 beamsplitter a powder sample which is placed in a flow cryostat. The cryostat is located in a vertical bore 18 T magnet. A circular polarizer blocks single backscattered light. The reflected multiple scattered light is collected in k-space on a CCD via a lens (f = 40 cm) for scattering angles of up to $\theta \simeq 1°$. Bottom: CBC results for different magnetic fields between 0 and 18 T for a sample consisting of (a) 26 vol% CeF_3 powder mixed with glycerol and (b) 26 vol% CeF_3 powder mixed with 2 vol% TiO_2 powder and glycerol. Experiments were carried out at T = 7 K. Cones in (a) are normalized to a baseline between 0.4° and 0.5°. Cones in (b) are normalized to a baseline between 1.0° and 1.1°.

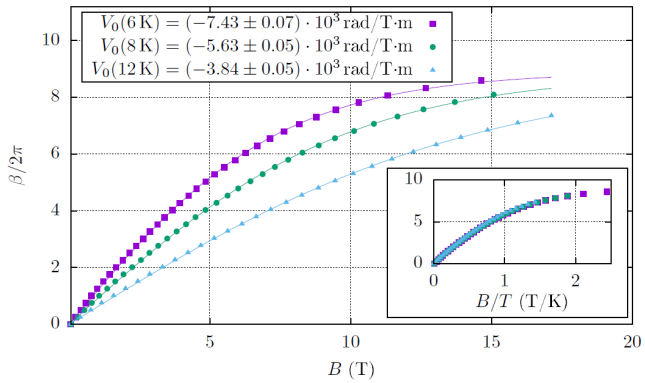

FIG. 16.2 – Faraday rotation angle β of a bulk crystal slab shaped sample (L = 1 mm) as a function of magnetic field at 6, 8 and 12 K. A 532 nm CW-laser was used for illumination. The data were fitted with $V_0 L \frac{T}{\alpha} \tanh(\frac{\alpha B}{T})$ to obtain the B = 0 bulk Verdet constant V_0 and the saturation parameter α (solid lines). For all three temperatures, $\alpha = (0.81 \pm 0.01)$ K/T. The inset shows that all the data collapse on a single curve when plotted as a function of B/T. The Verdet constant is proportional to the derivative of the curve and shows a saturation for high B/T ratios.

16.2 Single-Plane Illumination Microscopy (SPIM) Using Spatial Light Modulation

In the past, we have used the principle of wave-front shaping in order to image structures behind turbid layers [7–9] as well as to control the illumination of a sample behind turbid layers [10]. The control of the light passed through turbid objects can also be used in modern forms of microscopy, where a light sheet is used to image single planes of a three dimensional sample with less photo-toxicity and higher speed than e.g. standard confocal microscopes [11, 12]. One problem with such single-plane illumination microscopes (SPIM) is that the quality of the light sheet often deteriorates quickly in deeper layers of a sample, such that only comparatively thin or transparent samples can be studied. We have now used dynamic wave-front shaping to create high quality light sheets even behind turbid layers that can be used to build a SPIM that works for situations with a turbid layer obscuring the sample of interest. The schematic setup using a technical phantom sample as a proof of principle is shown in Fig. 16.3. The illumination is from the front and is scrambled by a layer of tape attached to a glass slide. The sample consists of fluorescent beads in a glass capillary.

Using feedback from the detection objective 1, looking directly at the illumination light behind the sample, we form a light sheet in this illumination using a genetic algorithm changing the phase mask on a spatial light modulator (SLM) in the illumination path. We then obtain a narrow light sheet extending more than

[1] P.W. Anderson, Phys. Rev. **109**, 5 (1958).

[2] Meint P. Van Albada and Ad Lagendijk, Phys. Rev. Lett. **55** 2692 (1985).

[3] Pierre-Etienne Wolf and Georg Maret, Phys. Rev. Lett. **55** 2696 (1985).

[4] S. Fiebig, C. M. Aegerter, W. Bührer, M. Störzer, E. Akkermans, G. Montambaux, and G. Maret, EPL (Europhysics Letters) **81** 64004 (2008).

[5] F. A. Erbacher, R. Lenke, and G. Maret, EPL (Europhysics Letters) **21** 551 (1993).

[6] L. Schertel, G. J. Aubry, C. M. Aegerter, and G. Maret, Europ. J. Phys. E to be published (2017).

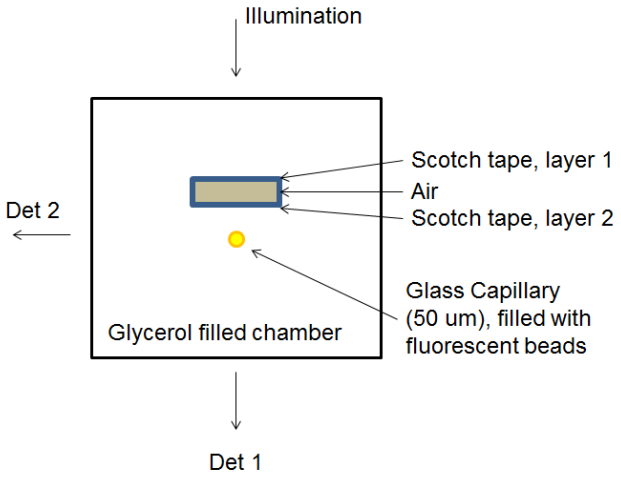

FIG. 16.3 – Schematic setup of a single-plane illumination microscopes (SPIM) behind turbid layers. The illuminating light is observed with detecting objective 1, where we can also observe the fluorescence of the particles imaged. The light sheet is observed using detection objective 2, at right angles to the illumination.

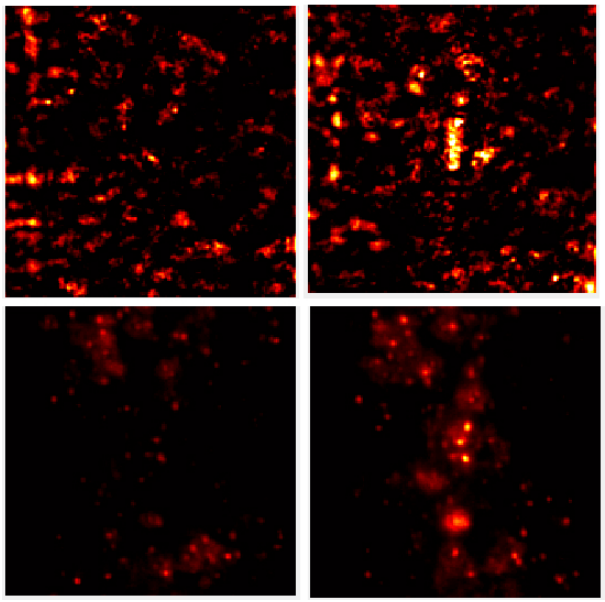

FIG. 16.4 – Creation of a dynamic light sheet behind a turbid layer. Top: transmission speckle pattern observed by detection objective 1, before (left) and after (right) application of a phase mask onto the spatial light modulator (SLM). The optimisation algorithm targets a line in the field of view for increased contrast, which corresponds to the light sheet used for illumination below (see Fig. 16.5). Bottom: fluorescence signal observed by detection objective 1 before (left) and after (right) application of the optimisation phase mask onto the SLM. The fluorescent particles within the light sheet are enhanced after application of the phase mask.

10 µm in the transverse direction. This is shown in the top panels of Fig. 16.4, where the direct illuminating light before and after application of the phase mask is shown. The corresponding fluorescent signal is shown in the bottom panels of Fig. 16.4, which clearly shows that fluorescent particles are more strongly illuminated by the light sheet.

This fluorescent signal can also be observed using detection objective 2 at right angles to the illumination, thus marking the entire depth of the sample in the field of view. This is shown in Fig.16.5, again before and after application of the phase mask to the spatial light modulator. As can be clearly seen, the creation of a light sheet in this situation leads to a drastically increased quality of the obtained image in a situation where a normal light sheet microscope would not be able to image, due to the multiple scattering of the turbid layer in front of the region of interest [13].

In conclusion, we have shown that wave-front shaping is capable of creating light-sheet imaging behind turbid layers at high resolution.

[7] I. M. Vellekoop and C. M. Aegerter, Opt. Lett. **35**, 1245 (2010).

[8] G. Ghielmetti and C. M. Aegerter, Opt. Express **20**, 3744 (2012).

[9] G. Ghielmetti and C .M. Aegerter, Opt. Express **22**, 1981 (2014). Science 305, 1007 (2004).

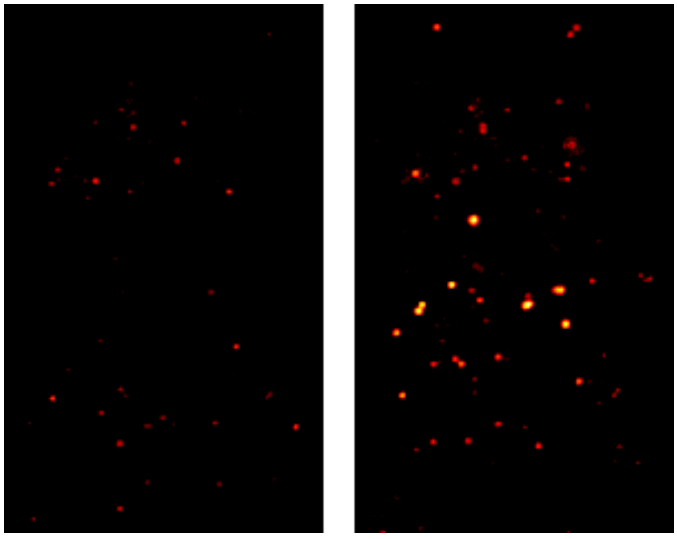

FIG. 16.5 – Fluorescent particles imaged with a light sheet behind a turbid layer using detection objective 2. The left panel shows the situation before application of the optimisation phase mask, whereas the right panel shows the situation after application of the phase mask. The fluorescent particles within the full depth of the light sheet are illuminated more strongly and allow for a depth resolved determination of the fluorescent structure.

[10] A. Malavalli, M. Ackermann, C. M. Aegerter, Opt. Express (2016).

[11] J. Huisken, J. Swoger, F. D. Bene, J. Wittbrodt, and E. H. K. Stelzer, Science 305, 1007 (2004).

[12] U. Krzic, S. Gunther, T.E. Saunders, S. J. Streichan, L. Hufnagel, Nat. Methods **9**, 730 (2012).

[13] J. Schneider and C. M. Aegerter to be published (2017).

16.3 FRET-Based Molecular Force Sensors in Drosophila Tissues

In the past, we have investigated the influence of mechanical forces on growth regulation and development in the wing imaginal disc of Drosophila, both theoretically [14,15] and experimentally [16,17]. In order to study the influence of tissue wide forces more directly on a cellular level, we have recently been active in the creation of molecular force sensors based on Forster resonance energy transfer (FRET) between two different fluorophores (in our case enhanced cyan and yellow fluorescent proteins, ECFP and EYFP, respectively) connected using an elastic linker and incorporated into a tension carrying structure of cell-cell contacts (E-Cadherin) [18]. The principle is illustrated in Fig. 16.6 A. As a control for the proper working of the construct as a force sensor, we have also introduced the same construct outside of the tension carrying structures of the cell-cell contacts, see Fig. 16.6 B.

When introducing the genetically altered construct of the adherens junction molecule into tissues of the Drosophila wing imaginal disc, we could observe resonance transfer by way of studying the change in intensity of the two different fluorophores, see Fig. 16.6 C, showing a difference between the sensor and control constructs. However, the efficiency in the control construct was lower than the sensor construct, which is contrary to the expectation that in the absence of a tension on the contact, the FRET efficiency should be higher due to the closer proximity of the fluorophores. The results in Fig. 16.6 C and D are an ensemble average over the whole tissue, whereas cell-cell junctions can show widely varying tensile forces acting on them, even in different parts of the cell. This is illustrated in Fig. 16.7 A for differently deformed cells. In order to account for such effects, we have studied the FRET efficiency for different segments of a cell boundary as well as for differently sized cells, see Fig. 16.7 A. As in the previous case, we have not found a significant difference between different types of cell junctions or between the sensor and control constructs.

To study this finding in more detail, in particular whether this is due to the absence of forces in the wing disc tissue, we have performed several determinations of the FRET efficiency in wing disc tissues with a direct change in the mechanical tension across the tissue. These were both biochemical and mechanical, increasing and decreasing the tension. The results of these experiments

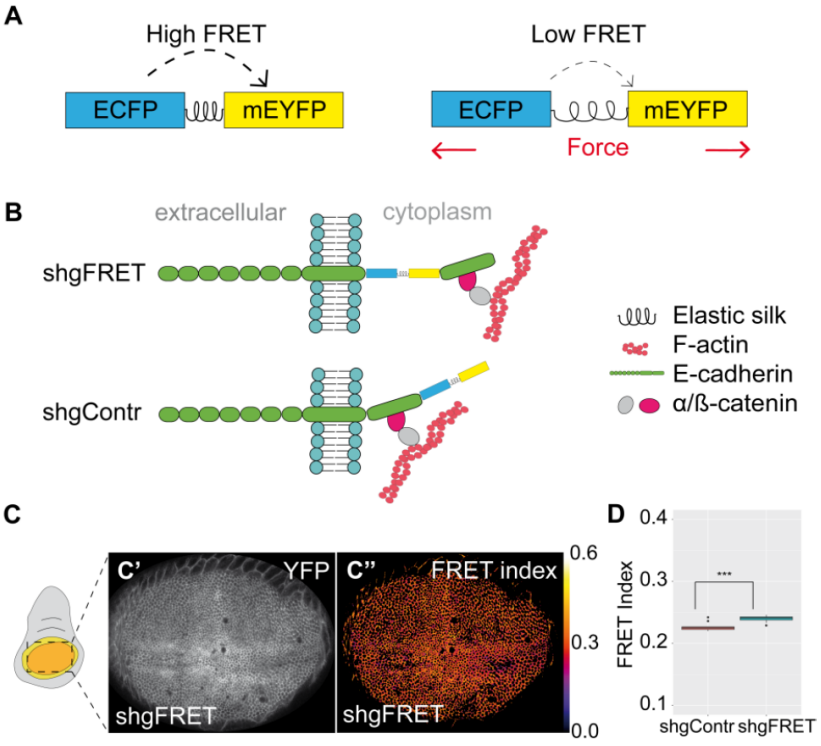

FIG. 16.6 – (A) The tension sensor consists of ECFP and mEYFP connected by an elastic linker (GPGGA)8. The FRET efficiency is high in a relaxed state but should decrease if external forces extend the sensor module.
(B) The sensor module was either integrated into the cytoplasmic domain of E-Cadherin adjacent to the transmembrane domain (shgFRET) to measure forces along the protein. The sensor module was also attached at the C-terminus of E-Cadherin (shgContr) lying outside of the force transducing domain to serve as a zero-force control.
(C) YFP expression (C') and corresponding FRET index (C'') of shgFRET shows that FRET was detectable in the wing pouch.
(D) FRET index in the wing pouch of shgContr (0.227, n=10) was significantly lower than for shgFRET (0.240, n=10).

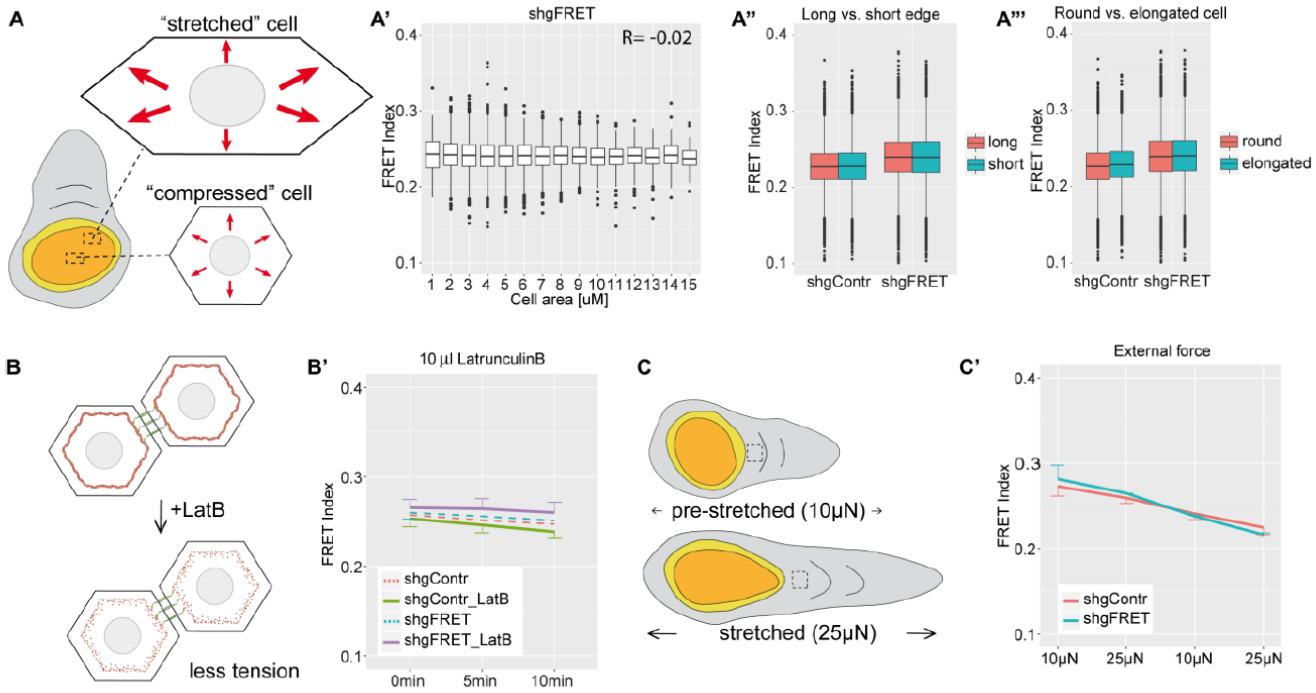

FIG. 16.7 – (A) Schematic drawing illustrates that cells in the center of the pouch are small, round and supposed to be mechanically compressed, whereas marginal cells are larger, elongated and mechanically stretched. In the marginal cells, the short edges are exposed to more mechanical stress than the long edges. These assumptions lead to following comparisons:
(A') The FRET index did not correlate with cell area in the wing pouch (here shown for shgFRET).
(A'') The FRET index did not differ between long and short edges for shgContr (0.228 vs. 0,227) and shgFRET (0.240 vs. 0.240).
(A''') The FRET index did not differ between round and elongated cells for shgContr (0.229 vs. 0.226) and shgFRET (0.240 vs. 0.240). (Data for $A', A''andA'''$ were pooled from 14 wing discs.)
(B) LatrunculinB treatment reduces cortical tension.
(B') FRET index decreased for shgContr (6%, n=18) and shgFRET(2%, n=18) upon treatment within 10 minutes. But also without treatment (dashed lines) the FRET index decreased over time for shgContr (4%, n=9) and shgFRET (3%, n=9).
(C) Using a stretching device, a pre-stretched (applied force of 10µN) and a stretched (25 µN) wind disc were compared. The dashed rectangle indicates the analyzed area.
(C') When cyclically altered between the two states of stretching every 5 minutes, a strong decay over time was observed for shgContr (18%, n=2) and shgFRET (23%, n=2), but no impact of the force change.

are visible in Fig. 16.7 B and C, indicating that both the sensor and the control construct show the same response to an applied force and that this response is also independent of the sign of the applied force. This indicates that either the sensor construct does not fulfill its function or the obtained FRET response is too small to be observed by the crude method of determining intensity ratios of the fluorophores, which is inherently sensitive to large systematic errors based in intensity fluctuations, photodetector efficiency etc.

In order to study the influence of systematic errors of the ratiometric FRET determination, we have also studied the efficiency of fluorescence transfer directly by measuring the fluorescent lifetime changes in the sensor and control constructs respectively. This has been done using a pulsed laser excitation and a time correlated photon counting module on a confocal microscope. In the presence of FRET, the lifetime of the donor fluorophore decreases, independent of any intensity-based imaging artifacts. The results are shown in Fig. 16.8 A, where the fluorescent lifetime of the donor (CFP) is shown for both constructs as well as in the absence of an acceptor fluorophore.

As can be seen by the decrease of the lifetime of the constructs relative to the pure donor fluorophore, FRET is taking place at small efficiency, however the comparison between the sensor and control constructs shows that this is irrespective of the mechanical tension carried by the construct. This implies that the construct does not

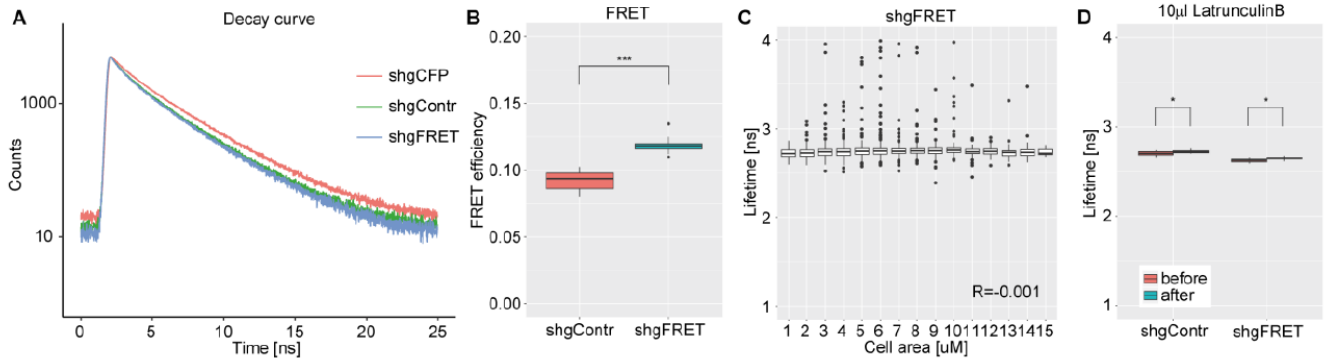

FIG. 16.8 – (A) Fluorescence decay curves of shgContr and shgFRET were almost overlapping, and both revealed lower lifetimes than shgCFP (n=5).
(B) Calculated FRET efficiency was significantly lower for shgContr (0.09, n=15) than for shgFRET (0.12, n=14).
(C) Lifetimes of single cells in the wing pouch did not correlate with cell size (here for shgFRET, n=8 wing discs).
(D) Lowering tensions by LatrunculinB treatment similarly increased lifetimes of shgContr and shgFRET for 1% (n=9).

work as a tension sensor, but rather the FRET signal is quenched either by angular conformations within the crowded cell environment or by intermolecular FRET of neighbouring molecules.

These findings are in contrast to earlier studies of a similar construct used in cell migration in the Drosophila oocyte, which has found differences in mechanical tension in different migrating situations [19]. To test for this, we have used the molecular force sensor in the same tissue of migrating cells, as well as in dorsal closure in the embryo, where large cellular forces are at work. In neither case could we find that the control construct gives different results from the sensor construct. We have also used the same construct as [19] and could not replicate their findings.

Thus, we conclude that in the crowded environment of a cell and a tissue, the FRET based molecular force sensor cannot be used as a measure of mechanical tension.

[14] T. Aegerter-Wilmsen, C.M. Aegerter, E. Hafen, and K. Basler,
Mechanisms of Development **124**, 318 (2007).

[15] T. Aegerter-Wilmsen, M.B. Heimlicher, A.C. Smith, P. Barbier de Reuille, R.S. Smith, C.M. Aegerter, and K. Basler,
Development **139** 3221 (2012).

[16] T. Schluck, U. Nienhaus, T. Aegerter-Wilmsen, and C.M. Aegerter,
PLoS One **8**, e76171 (2013).

[17] U. Nienhaus, T. Aegerter-Wilmsen, and C.M. Aegerter,
Mechanisms of Development **126**, 942 (2009).

[18] C. Grashoff, B.D. Hoffman, M.D. Brenner, R. Zhou, M. Parsons, M.T. Yang, M.A. McLean, S.G. Sligar, C.S. Chen, T. Ha, and M.A. Schwartz,
Nature **466**, 263 (2010).

[19] D. Cai, S.-C. Chen, M. Prasad, L. He, X. Wang, V. Choesmel-Cadamuro, J.K. Sawyer, G. Danuser, and D.J. Montell, Cell **157**, 1146 (2014).

[20] D. Eder, K. Basler, and C.M. Aegerter,
Sci. Reports to be published (2017).

17 Mechanical Workshop

C. Albrecht, B. Lussi, R. Maier, M. Schaffner, and S. Scherr
Apprentices: G. Knüsel, B. Markwalder, and P. Weyeneth

Infrastructure
In the past year the student workshop was rearranged, the modifications included dismantling of the soldering room and the relocation of small drilling machines and workbenches. In future, soldering work can be carried out in the locksmithery. A new wall crane (Fig. 17.1) was installed which will be used to handle heavy workpieces. Furthermore, in order to create more space in the main workshop the big lathe will be moved to the student workshop. Finally, the outdated scale in the material storage room was replaced to ensure precise weight measurement of the materials for customers.

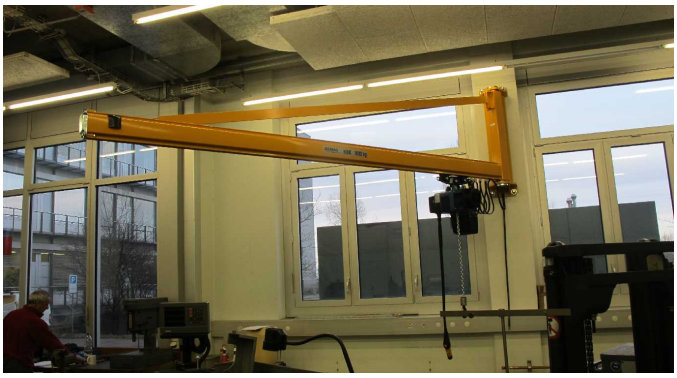

FIG. 17.1 – Installation of the wall crane in the student workshop.

To promote the exchange with many of our customers from various institutes of UZH, ETH Zurich, universities of applied sciences, as well as the customers of the material storage, our annual aperitif was organized in autumn.

Personnel
In Autumn 2016 we already signed the apprenticeship agreement with Noah Regensburger who will start the four-year apprenticeship as a polytechnic EFZ in August in our workshop. Marcel Schaffner celebrated his 15th anniversary in our team. Congratulations again! Our two apprentices in their final year are presently in the examination period. Brandon Markwalder has already completed the practical exam (Fig 17.2) while Pascal Weyeneth will start soon. We wish both all the best and good luck!

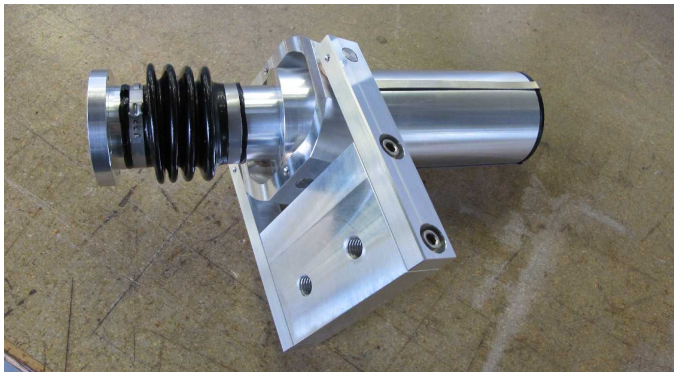

FIG. 17.2 – Mirror actuator for CTA.

Teaching
As every year, our annual workshop courses for bachelor students, which took place in August/September 2016 and January/February 2017 were received with great enthusiasm (Fig. 17.3). In Autumn 2016 ETHZ apprentices trained their welding skills in our workshop. Finally, we held a workshop course for PhD students in physics with a focus on learning the basics of mechanical manufacturing as well as technical drawing.

FIG. 17.3 – Students in the workshop course are being instructed by Reto Maier.

Projects

Last year, our workshop was busy producing very complex parts for the large projects CTA (Sec. 6) and CMS (Sec. 10). Besides that we were involved in various internal and external projects. In the following some projects are listed to which we significantly contributed:

- CTA Cherenkov Telescope Array (Sec. 6)
  In the previous year the prototype camera was put together and shipped to DESY Zeuthen in Berlin. This year the mechanical components for two additional cameras have been manufactured.

- CMS Barrel Pixel detector upgrade (Sec. 10)
  Many milling- and turned parts including the large cover hood were produced for the supply tube of the CMS pixel detector.

- Surface Physics (Sec. 14)
  During roughly one month the group studied the excitation of molecular vibrations with the help of THz pulses at the Free-Electron Laser FLASH at DESY in Hamburg. The experiments were performed by means of photoelectron diffraction using WAL-küre, a mobile electron spectrometer. The necessary modifications, in particular the holder of a special parabolic mirror for focusing the THz radiation onto the sample, were made in the workshop. In addition we completed another production series made from the not easily machinable material molybdenum.

- IPHO2016, International Physics Olympiad
  The workshop team was responsible for preparing the exam halls and the installation and dismanteling of the exam desks for the 400 students in the training halls of the ASVZ (Fig.17.5).

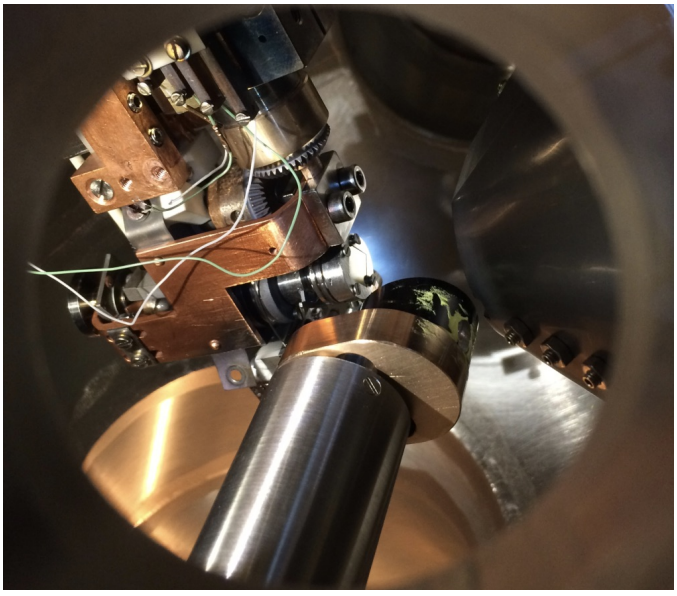

FIG. 17.4 – Fixation for a parabolic mirror.

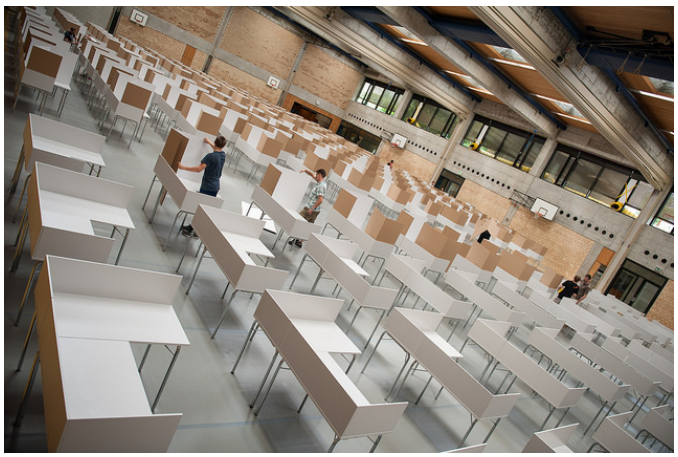

FIG. 17.5 – Preparing the examination hall for the physics olympiad.

- Astroparticle Physics (Sec. 4)
  We designed and constructed a screening cell for the GATOR facility (a low-background germanium spectrometer) at the Gran Sasso underground laboratory (Fig.17.6). Currently this demanding project is being completed. The parts will be assembled in the next weeks at the Gran Sasso laboratory.

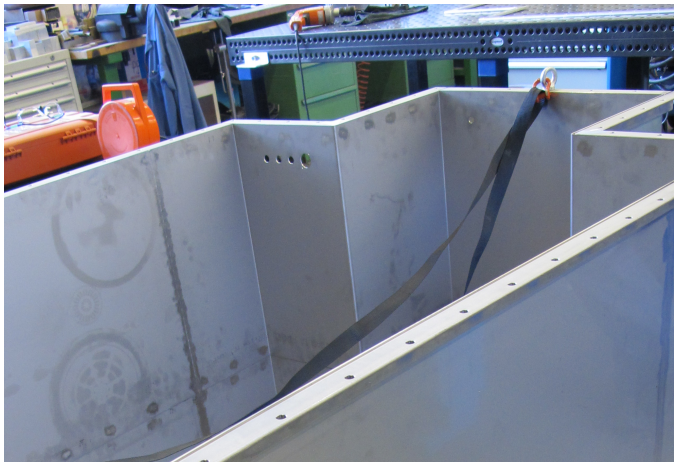

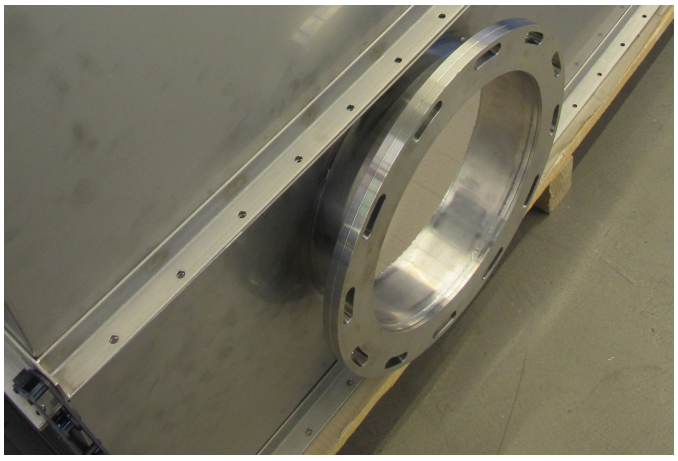

FIG. 17.6 – Screening cell for the GATOR facility.

- Disordered and Biological Soft Matter (Sec. 16)
  An integrated swimming channel (Fig. 17.7) was developed and built for the determination of three-dimensional speed profiles of the water around a swimming zebra fish. It includes two recirculation basins and an adjustable mirror support for the laser camera. Additionally, a robust metal rack was designed to accommodate the laser together with the electronics and the cooling system.

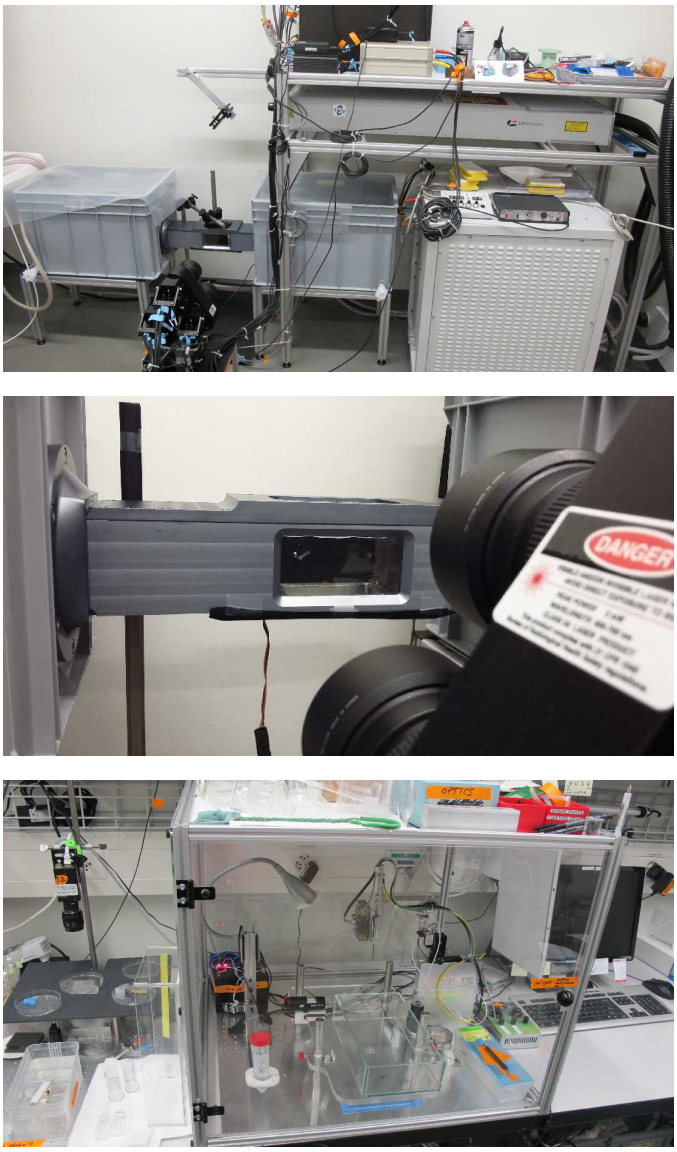

FIG. 17.7 – Top: Full setup, in the centre the fish channel with the laser camera is visible. Middle: Laser camera system. Bottom: Protective housing.

  Specially manufactured spring-steel was used to fix the electronic sensors that are used to determine the mechanical properties of the fins of the zebra fish. Furthermore, a new protective housing (Fig. 17.7 bottom) for the integrated setup of the measurement, which was also developed and built in the workshop, was constructed. This is needed to avoid turbulences from the ambient air during the measurement.

- Phase transitions, materials and applications (Sec. 13)
  As in previous years, several sample holders to be used inside a cryostat were produced.

- Demonstration experiments for the lectures
  In order to guarantee excellent demonstration experiments for the student lectures we designed and produced some new devices and revised and maintained several older parts, an example is shown in Fig. 17.8.

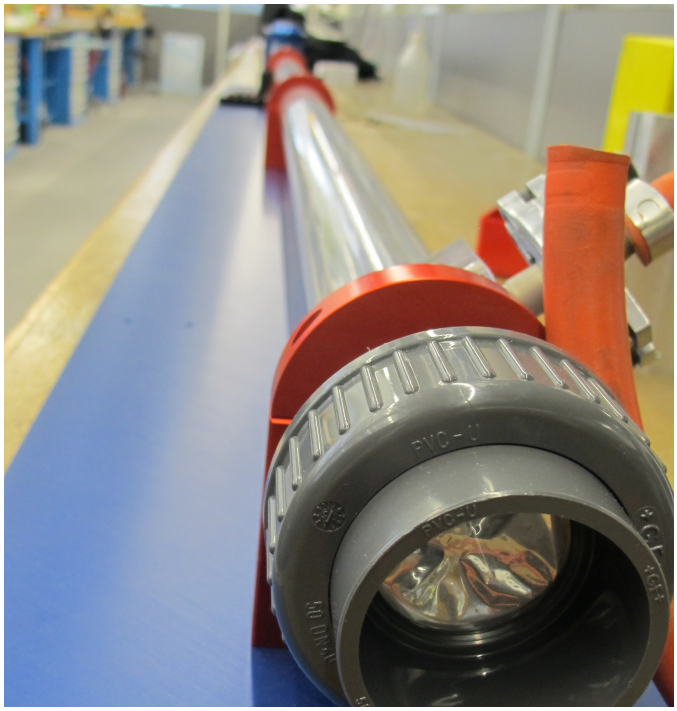

FIG. 17.8 – Vacuum cannon.

- External orders
  Thanks to our highly motivated and competent workshop team many orders were placed from external institutions, universities and private companies (Fig. 17.9). This shows that our workshop is well known for its competence and high quality work even outside of our institute.

FIG. 17.9 – A selection of parts produced for external institutions, universities and private companies.

18 Electronics Workshop

D. Florin, S. Karrer, A. Vollhardt, and D. Wolf

In parallel to ongoing maintenance work for existing laboratory equipment and constant support for the experimental setups of the scientists the electronics workshop contributed to various projects of the research groups.

For the group of Prof. Baudis, prototype amplifier modules with dual outputs (gains of 1 and 20) for each channel have been developed (Fig. 18.1) to be used in the XENONnT project (Sec. 4). Several versions have been developed to match the signal input levels of the existing DAQ system while aiming for low input amplifier noise. A compact design allows for integration of 16 low-noise channels into a standard NIM-module by mounting the required voltage regulators on a dedicated backplane which not only acts as a mechanical mount but also as thermal radiator.

We also contributed to the final commissioning of the CMS pixel detector upgrade (Fig. 18.2) for the groups of Profs. Kilminster and Canelli (Sec. 10). Printed circuit boards for the pixel supply tube were designed in our workshop and their production in industry was supervised. The required cabling for those boards was manufactured in house followed by the assembly of the pixel detector in the mechanics workshop. A LabView graphic user interface was developed to visualize the temperatures that are recorded with these circuit boards.

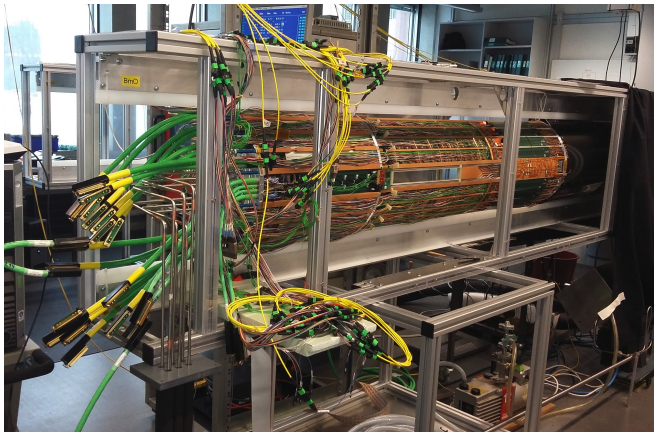

FIG. 18.2 – CMS Pixel detector during final assembly.

When operating experimental setups in remote locations with little human intervention, close monitoring of the current state is crucial. However, for some situations a response within a short time frame is still required. To allow for fast automated reporting, independent of the state of internet access, a Raspberry Pi single board computer was interfaced to a GSM-modem to enable both messaging and voice calls to predefined piquet telefone numbers (Fig. 18.3). Voice messages can be synthesized in real-time or pre-recorded sound files are played once the call receiver has picked up the phone. The device will be used in the CONNIE experiment (Sec. 5).

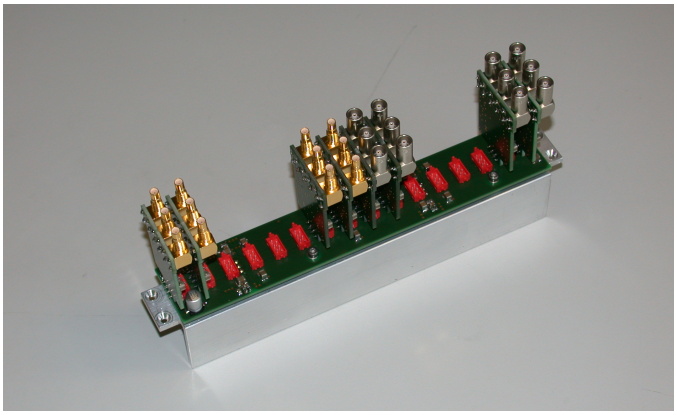

FIG. 18.1 – Prototype of a 16-channel amplifier unit for the Xe-nT detector.

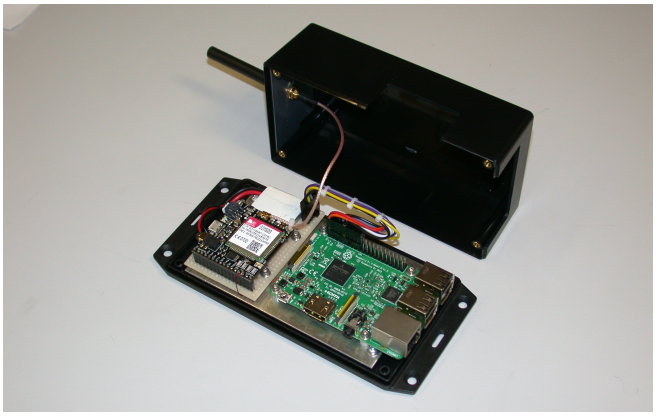

FIG. 18.3 – GSM-alarm unit.

A quad channel bias voltage supply to operate Geiger-mode APDs (Fig. 18.5) has been developed for the group of Prof. Straumann. The channels are individually adjustable between 2 and 80 Volts with a resolution of 1.3 mV while maintaining an excellent temperature stability of less than 5 ppm/K. The power supply unit can be operated locally via the touch screen display or remotely via a USB interface.

Other activities for the CTA project of Prof. Straumann included the development of a new power supply for the photon detector plane of the FlashCam project (Sec. 6). Measurements during integration of the first prototype indicated an excess of noise which was found to originate from the switched mode power supply. A new version with vastly reduced electromagnetic emissions has been successfully tested and is being included in the next version of the photon detector plane electronics. Two power supply cabinets were completed and are undergoing long-term testing. One cabinet will provide the supply for one camera. The integrated FlashCam safety firmware was upgraded and documented for discussion with the CTA consortium. The active mirror control (AMC) actuators are further contributions to the CTA project. They serve to fine adjust the mirror facets of the Large Size Telescopes (LST). Together with collaborators of the Institute for Cosmic Ray Research (ICRR) in Japan it was determined that the actuator sensor package stops working properly below -15° C. Upgrades to the design and changes in the controller firmware mitigated this problem. The modifications will be integrated in a future mass production for the CTA project. Further changes in the actuator electronics will allow for in-field upgrades of the firmware without physically accessing the unit (wireless bootloader) and monitoring of the internal humidity to check for leaking seals.

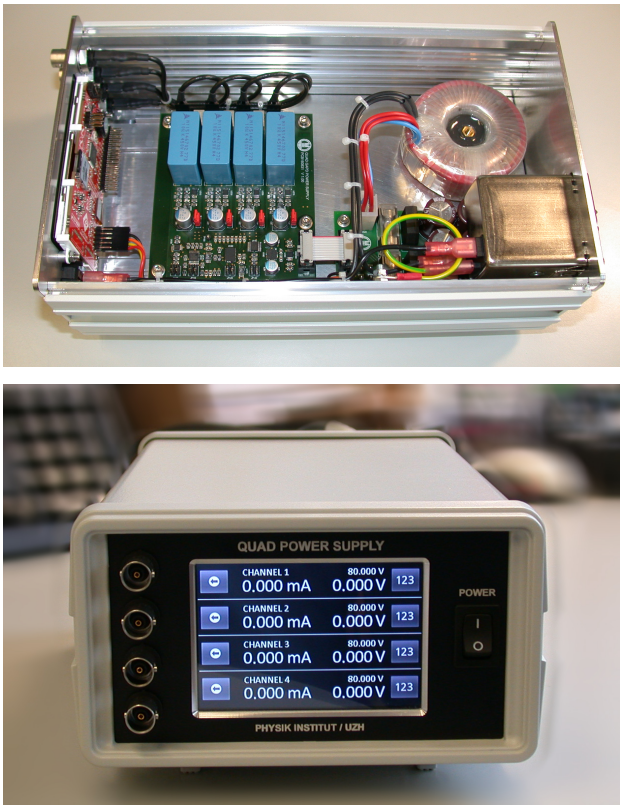

FIG. 18.5 – Internal (top) and front (bottom) view of the Geiger-APD bias power supply.

For the International Physics Olympiad (IPHO) 2016 250 experimental setups were built and tested. The electronics for two experimental problems was included in one electronics box design (Fig 18.6) to keep the manufacturing cost low and allow for a fast commissioning of the box.

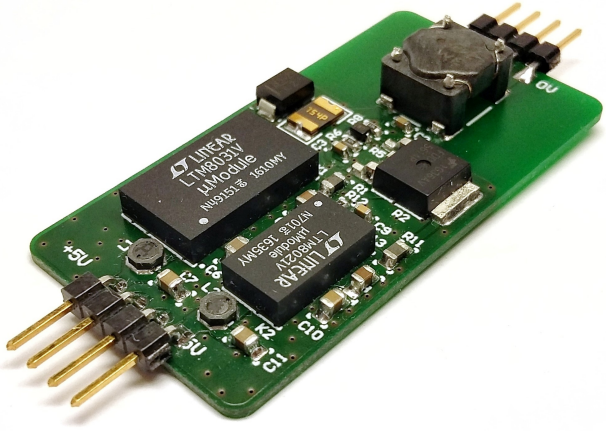

FIG. 18.4 – Switched mode power supply, optimized for low EM-emissions.

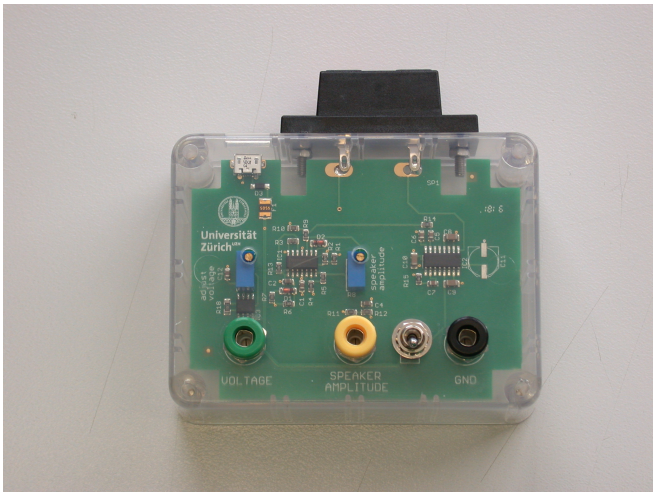

FIG. 18.6 – Electronic box for the two IPHO 2016 experimental problems.

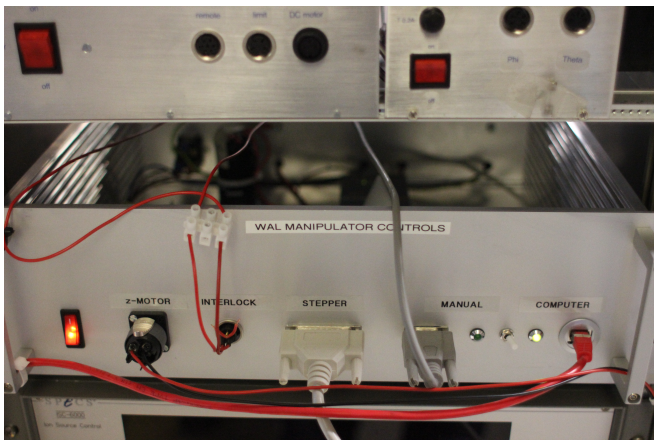

FIG. 18.7 – Ethernet-based controller for a 5-DOF UHV manipulator

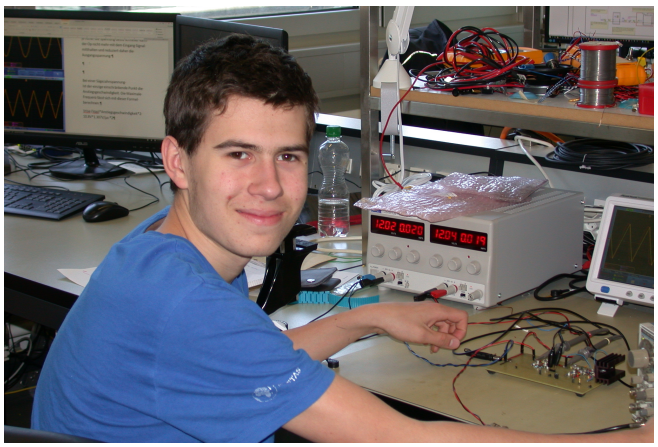

FIG. 18.8 – Simon Karrer - apprentice in the electronics workshop since August 2016.

A 5-DOF manipulator inside an ultra-high vacuum setup was designed and commissioned (Fig. 18.7) for the group of Prof. Osterwalder (Sec. 14). Previously, the five stepper motors were individually connected with separate USB interfaces to a host computer for remote control. The upgrade was performed to significantly simplify the cabling via daisy-chaining the motors over a common control bus which is then connected to the host computer via Ethernet. This setup allows for long-range cabling. Furthermore a manual remote controller was added to the setup to allow for individual local steering of any of the five motors.

Since August 2016, the electronics workshop educates an apprentice (Simon Karrer, Fig. 18.8), who has started his 4-year higher education as electronic technician (Elektroniker EFZ). Three days a week he is being trained in the electronics workshop where he joins ongoing work for the research groups where possible in addition to his general training. The remaining two days per week he follows external courses in general education, languages and science. It is planned to have a second apprentice starting in August 2018.

19 International Physics Olympiad 2016

Summary from L. Philippoz

The International Physics Olympiad (IPhO) is an annual competition for high-school students, which takes place every year in a different country. Each delegation can send a team of up to five students which will then compete individually in theoretical as well as in experimental problems. Teams from Switzerland participate since 1995. In July 2016, the 47th IPhO was jointly organized by the UZH, with the dedicated support of the Physics Department, the ASSO (Association of the Swiss Scientific Olympiads), and the Office of Education of the Principality of Liechtenstein. Many members of the organization committee also came from the SwissPhO, the association in charge of organizing the national selection in Switzerland. In total, 84 countries took part in the competition, with 398 students (unfortunately only 25 of them being female), 161 leaders and 84 observers.

19.1 Competition

The competition always follows the same scheme: After the opening ceremony, with the introduction of all the delegations and the official opening of the competition, the experimental problems are presented to the leaders. In the following discussion session, the leaders may still propose changes to the problems before they are translated into the languages of the participating countries. The five-hour experimental exam then takes place the following day. The procedure for the theoretical exam is similar. The exams are then corrected and marked independently by the official markers (from our department for the IPhO 2016) and the team leaders. Afterwards the leaders discuss the grades with the markers in the moderation session to establish the final ranking announced during the closing ceremony. While the organizers are free to present one to two tasks for the experimental exam, four problems are prepared for the theoretical exam, one of which is chosen as backup.

19.2 Role of the Physics Department

19.2.1 Preparation of the problems

Besides all the logistical aspects of the event, the core of the success of the IPhO relies on the quality of the exam questions. The first meetings to gather ideas about possible topics already started back in mid 2014, within a small group. The combined experience from SwissPhO members, knowing the requirements for IPhO problems, and researchers from the Physics Department, able to give insights into modern research topics, allowed to prepare attractive theoretical and experimental problems. For the latter, more than 200 setups were produced with the help of the mechanical and electronics workshops.

19.2.2 Marking and moderation

The fundamental task of marking the problems of all the participants could only be achieved thanks to the strong engagement of the members of the Physics Department at all levels: professors, post-docs and PhD students were all part of the marking team. A total of 89 markers managed to finish the marking within the limited time - including night shifts - and successfully negotiated the results with the leaders the next day. The feedback from the leaders was very positive, their vast majority had never experienced such a smooth moderation session.

19.3 Conclusion

In the end, IPhO 2016 was a big success. It is difficult to compare various editions due to the specificities of each organizing country, but the general feeling and consensus was that the 2016 edition counts amongst the best ones. Of course, we all had to deal with unexpected issues which are unavoidable in an event of that scale, but they could all be solved. The involvement of everyone, but especially of all the members of the Physics Department at all levels - academic staff, administrative staff and workshops - was the fundament for this overall success, so as a conclusion: Thank you again!

FIG. 19.1 – Closing ceremony with the gold medal winners.

20 Publications

20.1 Elementary particles and their interactions

20.1.1 Theory of Elementary particles

Articles

- The forward-backward asymmetry for massive bottom quarks at the Z peak at next-to-next-to-leading order QCD
Bernreuther, Werner and Chen, Long and Dekkers, Oliver and Gehrmann, Thomas and Heisler, Dennis,
JHEP **01** (2017) 053.

- NNLO QCD corrections for Drell-Yan p_T^Z and ϕ^* observables at the LHC
Gehrmann-De Ridder, A. and Gehrmann, T. and Glover, E. W. N. and Huss, A. and Morgan, T. A.,
JHEP **11** (2016) 094.

- NNLO QCD corrections to Higgs boson production at large transverse momentum
Chen, X. and Cruz-Martinez, J. and Gehrmann, T. and Glover, E. W. N. and Jaquier, M., JHEP **10** (2016) 066.

- Precise QCD predictions for the production of dijet final states in deep inelastic scattering
Currie, James and Gehrmann, Thomas and Niehues, Jan, Phys. Rev. Lett. **117** (2016) no4 042001.

- CP-even scalar boson production via gluon fusion at the LHC
Anastasiou, Charalampos and Duhr, Claude and Dulat, Falko and Furlan, Elisabetta and Gehrmann, Thomas and Herzog, Franz and Lazopoulos, Achilleas and Mistlberger, Bernhard, JHEP **09** (2016) 037.

- The NNLO QCD corrections to Z boson production at large transverse momentum
Gehrmann-De Ridder, Aude and Gehrmann, T. and Glover, E. W. N. and Huss, A. and Morgan, T. A.,
JHEP **07** (2016) 133.

- High precision determination of the gluon fusion Higgs boson cross-section at the LHC
Anastasiou, Charalampos and Duhr, Claude and Dulat, Falko and Furlan, Elisabetta and Gehrmann, Thomas and Herzog, Franz and Lazopoulos, Achilleas and Mistlberger, Bernhard, JHEP **05** (2016) 058.

- Precise QCD predictions for the production of a Z boson in association with a hadronic jet
Gehrmann-De Ridder, A. and Gehrmann, T. and Glover, E. W. N. and Huss, A. and Morgan, T. A.,
Rev. Lett. **117** (2016) no2 022001

- Full top quark mass dependence in Higgs boson pair production at NLO
Borowka, S. and Greiner, N. and Heinrich, G. and Jones, S. P. and Kerner, M. and Schlenk, J. and Zirke, T.,
JHEP **10** (2016) 107.

- Higgs Boson Pair Production in Gluon Fusion at Next-to-Leading Order with Full Top-Quark Mass Dependence
Borowka, S. and Greiner, N. and Heinrich, G. and Jones, S. P. and Kerner, M. and Schlenk, J. and Schubert, U. and Zirke, T., Phys. Rev. Lett. **117** (2016) no1 012001.

- Full mass dependence in Higgs boson production in association with jets at the LHC and FCC
Greiner, Nicolas and Höche, Stefan and Luisoni, Gionata and Schönherr, Marek and Winter, Jan-Christopher,
JHEP **01** (2017) 091.

- Reweighting QCD matrix-element and parton-shower calculations
Bothmann, Enrico and Schönherr, Marek and Schumann, Steffen, Eur. Phys. J. C **76** (2016) no11 590.

- On the computation of finite bottom-quark mass effects in Higgs boson production
Mueller, Romain and Öztürk, Deniz Gizem, JHEP **08** (2016) 055.

- Modeling BSM effects on the Higgs transverse-momentum spectrum in an EFT approach
Grazzini, Massimiliano and Ilnicka, Agnieszka and Spira, Michael and Wiesemann, Marius, JHEP **03** (2017) 115.

- W^+W^- production at the LHC: fiducial cross sections and distributions in NNLO QCD
Grazzini, Massimiliano and Kallweit, Stefan and Pozzorini, Stefano and Rathlev, Dirk and Wiesemann, Marius, JHEP **08** (2016) 140.

- $W^\pm Z$ production at hadron colliders in NNLO QCD
Grazzini, Massimiliano and Kallweit, Stefan and Rathlev, Dirk and Wiesemann, Marius, Phys. Lett. B **761** (2016) 179-183.

- Heavy-quark mass effects in Higgs plus jets production
Frederix, Rikkert and Frixione, Stefano and Vryonidou, Eleni and Wiesemann, Marius, JHEP **08** (2016) 006.

- Differential Higgs Boson Pair Production at Next-to-Next-to-Leading Order in QCD
de Florian, Daniel and Grazzini, Massimiliano and Hanga, Catalin and Kallweit, Stefan and Lindert, Jonas M. and Maierhöfer, Philipp and Mazzitelli, Javier and Rathlev, Dirk, JHEP **09** (2016) 151.

- Two-loop corrections to the triple Higgs boson production cross section
de Florian, Daniel and Mazzitelli, Javier, JHEP **02** (2017) 107.

- Double-real corrections at $\mathcal{O}(\alpha\alpha_s)$ to single gauge boson production
Bonciani, Roberto and Buccioni, Federico and Mondini, Roberto and Vicini, Alessandro, Eur. Phys. J. C **77** (2017) no2 187.

- Prompt photon production and photon-hadron jet correlations with POWHEG
Jezo, Tomas and Klasen, Michael and König, Florian, JHEP **11** (2016) 033.

- NLO QCD predictions for off-shell $t\bar{t}$ and $t\bar{t}H$ production and decay at a linear collider
Chokoufé Nejad, Bijan and Kilian, Wolfgang and Lindert, Jonas M. and Pozzorini, Stefano and Reuter, Jürgen and Weiss, Christian, JHEP **12** (2016) 075.

- Four-loop QCD β-function with different fermion representations of the gauge group
Zoller, M. F., JHEP **10** (2016) 118.

- Next-to-leading order QCD predictions for top-quark pair production with up to three jets
Höche, Stefan and Maierhöfer, Philipp and Moretti, Niccolo and Pozzorini, Stefano and Siegert, Frank, Eur. Phys. J. C **77** (2017) no3 145.

- An NLO+PS generator for $t\bar{t}$ and Wt production and decay including non-resonant and interference effects
Jezo, Tomas and Lindert, Jonas M. and Nason, Paolo and Oleari, Carlo and Pozzorini, Stefano, Eur. Phys. J. C **76** (2016) no12 691.

- Leading QCD-induced four-loop contributions to the β-function of the Higgs self-coupling in the SM and vacuum stability
Chetyrkin, K. G. and Zoller, M. F., JHEP **06** (2016) 165.

- On the renormalization of operator products: the scalar gluonic case
Zoller, Max F., JHEP **04** (2016) 165.

- NLO QCD+EW predictions for V + jets including off-shell vector-boson decays and multijet merging
Kallweit, Stefan and Lindert, Jonas M. and Maierhöfer, Philipp and Pozzorini, Stefano and Schönherr, Marek, JHEP **04** (2016) 021.

- Fully differential NLO predictions for the rare muon decay
Pruna, G. M. and Signer, A. and Ulrich, Y., Phys. Lett. B **765** (2017) 280-284.

- Regularization-scheme dependence of QCD amplitudes in the massive case
Gnendiger, Christoph and Signer, Adrian and Visconti, Andrea, JHEP **10** (2016) 034.

- $(g-2)\mu$, lepton flavor violation, and Z decays with leptoquarks: Correlations and future prospects
Coluccio Leskow, Estefania and D'Ambrosio, Giancarlo and Crivellin, Andreas and Müller, Dario, Phys. Rev. D **95** (2017) no5 055018.

- Lepton Flavor Non-Universality in B decays from Dynamical Yukawas
  Crivellin, Andreas and Fuentes-Martin, Javier and Greljo, Admir and Isidori, Gino, Phys. Lett. B **766** (2017) 77-85.

- Likelihood Analysis of Supersymmetric SU(5) GUTs
  Bagnaschi, E. *et al.*, Eur. Phys. J. C **77** (2017) no2 104.

- Measuring the breaking of lepton flavor universality in $B \to K^* \ell^+ \ell^-$
  Serra, Nicola and Silva Coutinho, Rafael and van Dyk, Danny, Phys. Rev. D **95** (2017) no 3 035029.

- Confronting lepton flavor universality violation in B decays with high-p_T tau lepton searches at LHC
  Faroughy, Darius A. and Greljo, Admir and Kamenik, Jernej F., Phys. Lett. **B764** (2017) 126-134.

- Anomalous Triple Gauge Couplings in the Effective Field Theory Approach at the LHC
  Falkowski, Adam and Gonzalez-Alonso, Martin and Greljo, Admir and Marzocca, David and Son, Minho, JHEP **02** (2017) 115.

- QCD Factorization Theorem for $B \to \pi\pi\ell\nu$ Decays at Large Dipion Masses
  Böer, Philipp and Feldmann, Thorsten and van Dyk, Danny, JHEP **02** (2017) 133.

- Massive vectors and loop observables: the $g-2$ case
  Biggio, Carla and Bordone, Marzia and Di Luzio, Luca and Ridolfi, Giovanni, JHEP **10** (2016) 002.

- On the Standard Model predictions for R_K and R_{K^*}
  Bordone, Marzia and Isidori, Gino and Pattori, Andrea, Eur. Phys. J. **C76** (2016) no8, 440.

- Toward a coherent solution of diphoton and flavor anomalies
  Buttazzo, Dario and Greljo, Admir and Isidori, Gino and Marzocca, David, JHEP **08** (2016) 035.

Articles in press

- Semi-leptonic B-physics anomalies: a general EFT analysis within $U(2)^n$ flavor symmetry
  Bordone, Marzia and Isidori, Gino and Trifinopoulos, Sokratis, arXiv:1702.07238.

- Likelihood Analysis of the Minimal AMSB Model
  Bagnaschi, E. *et al.*, arXiv:1612.05210.

Oral Presentations

- M. Bordone: On precise predictions for LFU ratios in B physics
  Implications of LHCb measurements and future prospects, CERN, 12.10.2016.

- M. Bordone: On the theory prediction of R_K and $R_K^\star$
  9th International Workshop on the CKM Unitarity Triangle, Mumbai, 29.11.2016.

- S. Borowka: Higgs Pair Production in gluon fusion at NLO with full top mass dependence
  Seminario de fisica teorica, UNAL Bogota, Colombia, 03.08.2016.

- S. Borowka: Higgs Pair Production in gluon fusion at NLO with full top mass dependence
  28th Rencontres de Blois, Blois, France, 01.06.2016.

- S. Borowka: Numerical evaluation of multi-loop integrals and Higgs boson pair production
  Dirk Kreimer research seminar, HU Berlin, Berlin, Germany, 04.07.2016.

- D. Buttazzo: Singlet-like Higgs production
  FCC workshop, CERN, 18.1.2017.

- D. Buttazzo: Towards a coherent picture of flavour and diphoton anomalies
  Heavy Flavour workshop, Islay, 28.4.2016.

- D. Buttazzo: Higgs mass and unified gauge coupling in the NMSSM with vector-like matter
  GGI Firenze, 19.5.2016.

- D. Buttazzo: Search for two-body resonances
  pp@LHC workshop, Pisa, 16.5.2016.

- D. Buttazzo: Toward a coherent picture of diphoton and flavour anomalies
  LNF Frascati, 28.4.2016.

- L. Cieri: Resummation, Universality and the Hard-Functions
  Calcoli analitici e Fisica di precisione. Università degli Studi e INFN Milano, Italy, 15.2.2017.

- L. Cieri: Diphoton production at the LHC
  HP2.6. ICAS-UNSAM, Buenos Aires, Argentina, 9.9.2016.

- L. Cieri: Diphoton production at the LHC
  New Frontiers in Theoretical Physics - XXXV Convegno Nazionale di Fisica Teorica and GGI 10th anniversary, Galileo Galilei Institute, Florence, Italy, 19.5.2016.

- T. Gehrmann: Advances in QCD Predictions
  opening talk, 24th International Workshop on Deep Inelastic Scattering and Related Topics (DIS 2016), DESY, Hamburg, Germany, 11.4.2016.

- T. Gehrmann: Transverse Momentum Distributions and Jet Cross Sections
  Workshop on Effective Field Theories for Collider Physics, Eltville, Germany, 14.9.2016.

- T. Gehrmann: Transverse Momentum Distributions and Jet Cross Sections
  Workshop on Future Challenges for Precision QCD, Durham, 26.10.2016.

- T. Gehrmann: Higgs Production Through Gluon Fusion
  Workshop HiggsCouplings, SLAC, Stanford, USA, 9.11.2016.

- T. Gehrmann: Standard Model Theory for the LHC
  12th Vienna Central European Seminar: Physics at LHC Run 2, Vienna, Austria, 1.12.2016.

- T. Gehrmann: Precision Physics with Jet Observables
  Theory Seminar, TÃijbingen University, Germany, 16.3.2017.

- M. Grazzini: Vector boson pair production at NNLO
  2nd Higgstools Meeting, Granada, Spain, 14.4.2016.

- M. Grazzini: SM Higgs signal and background cross sections for the LHC Run 2
  ATLAS H→ZZ Meeting, Munich, Germany, 29.4.2016.

- M. Grazzini: Standard Model Higgs Physics
  WE Heraeus Seminar, Bad Honnef, Germany, 17.10.2016.

- M. Grazzini: Vector boson pair production at NNLO
  Seminar at Annecy, France, 26.01.2017.

- N. Greiner: Higgs plus jets in gluon fusion at the LHC
  Seminar at the Florida State University, Tallahassee, Florida, 6.5.2016.

- N. Greiner: NLO/MC tools
  Pheno 2016, University of Pittsburgh, USA 9.-11.5.2016.

- N. Greiner: SM/BSM physics with GoSam
  Monte Carlo Tools for Physics Beyond the Standard Model Beijing, China, 20.7-24.7.2016.

- A. Greljo: Anomalous Higgs and Triple Gauge Couplings in the Effective Field Theory Approach
  ICHEP 2016, Chicago, USA, 05.08.2016.

- A. Greljo: Implications of new physics in B decays for high-p_T searches at LHC
  Mainz Institute for Theoretical Physics, Germany, 06.09.2016.

- A. Greljo: Implications of Lepton Flavor Non-Universality in B decays
  CERN BSM forum, CERN, 08.12.2016.

- A. Greljo: Flavour Anomalies vs. High-p_T Physics
  La Thuile 2017, Italy, 10.03.2017.

- A. Greljo: Hints in semi-tauonic B meson decays: The physics case for high-p_T LHC
  Mini-workshop on $D^\star \to \tau\nu$ and related topics, Nagoya University, Japan, 28.03.2017.

- A. Ilnicka: Effective Field Theory in quest to parametrise Higgs properties: the transverse momentum spectrum case
  Discrete 2016, Uni. Warsaw, Poland 30.11.2016.

- A. Ilnicka: Effective Field Theory for Higgs properties parametrisation: the transverse momentum spectrum case
  Recontred de Moriond QCD, La Thuile, Italy, 26.03.2017.

- A. Ilnicka: Modeling BSM effects on the Higgs p_T spectrum in a EFT approach
  PhD seminar, Zürich, Switzerland, 25.11.2016.

- G. Isidori: Flavor Physics beyond the Standard Model
  Latin-American Conference on High-Energy Physics, Havana, Cuba, 19.07.2016.

- G. Isidori: Kaon Physics: the Next Step
  Kaon 2016 Conference, Birmingham, UK, 17.09.2016.

- G. Isidori: Flavor Physics beyond the Standard Model
  AJB 70 Symposium, TU Munich, Germany, 28.10.2016.

- G. Isidori: Higgs Pseudo Observables
  Workshop Higgs Couplings, SLAC, Stanford, USA, 10.11.2016.

- T. Ježo: Theory talk I: SM modeling
  3rd CMS Single-Top Workshop, IPHC, Strasbourg, France, 2.6.2016.

- T. Ježo: An NLO+PS generator for top pair production and decay including non-resonant and interference effects
  Large Hadron Collider Physics (LHCP 2016), Lund University, Sweden, 14.6.2016.

- T. Ježo: nCTEQ15 nuclear parton distributions with uncertainties
  Large Hadron Collider Physics (LHCP 2016), Lund University, Sweden, 14.6.2016.

- T. Ježo: Latest Developments in POWHEG
  LHC top working group meeting, CERN, Geneva, Switzerland, 21.11.2016.

- A. Karlberg: VBF Higgs production in the structure function approach and beyond
  Future challenges for precision QCD, University of Durham, United Kingdom, 25.10.2016.

- A. Karlberg: VBF Higgs production at NNLO ... and beyond
  Tübingen Particle Theory Seminar, University of Tübingen, Germany, 17.11.2016.

- J. Lindert: Resonance aware NLO+PS in POWHEG for top-pair and single-top physics
  QCD@LHC, Zurich, Switzerland, 23.08.2016.

- J. Lindert: Differential Higgs Boson Pair Production at Next-to-Next-to-Leading Order in QCD
  QCD@LHC, Zurich, Switzerland, 25.08.2016.

- J. Lindert: NLO+PS predictions for top-pair and Wt production and decay
  High Precision for Hard Processes (HP2), Buenos Aires, Argentina, 08.09.2016.

- J. Lindert: NLO QCD+EW for Dark Matter Backgrounds
  LHC Dark Matter WG, CERN, 20.09.2016.

- J. Lindert: EWK corrections to non-VBF processes
  Future of VBF measurements, Durham, UK, 21.09.2016.

- J. Lindert: Pseudo Observables in EW Higgs production
  Future of VBF measurements, Durham, UK, 22.09.2016.
- J. Lindert: Differential Higgs Boson Pair Production at Next-to-Next-to-Leading Order in QCD
  DESY Theory workshop, DESY, Hamburg, Germany, 28.09.2016.
- J. Lindert: NLO+PS predictions for top-pair and Wt production and decay
  DESY Theory workshop, DESY, Hamburg, Germany, 29.09.2016.
- N. A. Lo Presti: Two-loop five-point integrals in massless QCD
  Loops and Legs Conference, Leipzig, Germany, 24.-29.4.2016.
- D. Marzocca: Template cross sections and pseudo-observable for Higgs physics
  SM@LHC, Pittsburgh, USA, 3-6.05.2016.
- D. Marzocca: A composite model for flavor and diphoton anomalies
  Holography, conformal field theories, and lattice, Edinburgh, UK, 27-30.06.2016.
- D. Marzocca: Violation of Lepton Flavor Universality in B decays
  BSM faces LHC Run-2 realities workshop, DESY, Germany, 12.09.2016.
- D. Marzocca: EFT constraints from precision measurements and prospects
  Rencontres du Vietnam, Quy Nhon, Vietnam, 28.09.2016.
- D. Marzocca: Pseudo-observables in Higgs physics
  HEFT, Copenhagen, Denmark, 28.10.2016.
- J. Mazzitelli: Double-Higgs production
  Sinergia Meeting, Zurich, Switzerland, 21.12.2016.
- A. Pattori: On the Standard Model predictions for R_K and $R_K^\star$
  BEACH2016 workshop, George Mason University, USA, 16.06.2016.
- A. Pattori: Lepton Flavor Violation in Composite Higgs Models
  CLFV2016, Charlottesville, VA, USA, 20.06.2016.
- A. Pattori: About the explanation of R_D through left-handed currents
  seminar at LAPTh, Annecy, France, 01.12.2016.
- S. Pozzorini: Precision for V+jets and Dibosons
  KITP Workshop LHC Run II and the Precision Frontier, University of California Santa Barbara, USA, 23.4.2016.
- S. Pozzorini: Theory tools for precision SM and Higgs Physics
  Strategy Workshop on High-Energy Particle Physics in Switzerland, Aegerisee,Switzerland, 7.6.2016.
- S. Pozzorini: Electroweak Theory and Higgs Mechanism
  Lecture at 2016 CTEQ & MCnet School, DESY Hamburg, Germany, 6.7.2016.
- S. Pozzorini: Theory precision for ttH signals and backgrounds
  QCD@LHC 2016, Zurich, Switzerland, 22.8.2016.
- S. Pozzorini: Electroweak corrections and off-shell effects in tt production and decay
  9th International Workshop on Top Quark Physics (TOP 2016), Olomouc, Czech Republic, 19.9.2016.
- S. Pozzorini: Theory simulations for multi-particle processes and applications to Top Physics
  Seminar at CP3-Origins, Odense, 23.1.2017.
- S. Pozzorini: NLO+PS Simulations for Top Physics with OpenLoops
  Seminar at Freiburg University, Germany, 18.1.2107.
- H. Sargsyan: Transverse-momentum resummation for top-quark pair production at hadron colliders
  QCD@LHC, Zürich, Switzerland, 23.08.2016.

- H. Sargsyan: Transverse-momentum resummation for top-quark pair production at hadron colliders
  HP2.6, Buenos Aires, Argentina, 08.09.2016.

- H. Sargsyan: Transverse-momentum resummation for top-quark pair production at hadron colliders
  Seminar at Freiburg University, Freiburg, Germany, 18.10.2016.

- H. Sargsyan: Transverse-momentum resummation for top-quark pair production at hadron colliders
  PhD seminar, Zürich, Switzerland, 25.11.2016.

- H. Sargsyan: Transverse-momentum resummation for top-quark pair production at hadron colliders
  SMP-J workshop, CERN, Geneva, Switzerland, 23.08.2016.

- M. Schönherr: Electroweak corrections for the LHC
  Seminar at Milano-Bicocca University, Milano, Italy, 14.04.2016.

- M. Schönherr: Electroweak corrections for the LHC
  Seminar at Göttingen University, Göttingen, Germany, 03.06.2016.

- M. Schönherr: Status of electroweak corrections in Sherpa+OpenLoops
  MW-Meeting, CERN, 08.06.2016.

- M. Schönherr: NLO electroweak corrections in V+jets
  LHCP 2016, Lund, Sweden, 16.06.2016.

- M. Schönherr: Reweighting QCD matrix element and parton shower calculations
  Parton showers and resummation, Paris, France, 04.07.2016.

- M. Schönherr: Monte Carlo event generation: Introduction I, II, III & Tutorial
  4th African School of Fundamental Physics and its Applications, Kigali, Rwanda, 03.-04.08.2016.

- M. Schönherr: Electroweak corrections to V+jets production
  LoopFest XV, Buffalo, USA, 16.08.2016.

- M. Schönherr: Sherpa: overview and recent developments
  QCD@LHC, Zürich, Switzerland, 23.08.2016.

- M. Schönherr: Sherpa-2.2.1: overview, developments and usage
  CMS Sherpa Tutorial, CERN, 29.08.2016.

- M. Schönherr: Electroweak corrections for LHC physics
  Seminar at Michigan State University, East Lansing, USA, 01.11.2016.

- M. Schönherr: Monte-Carlo simulation and uncertainties
  Higgs Couplings, SLAC, Stanford, USA, 09.11.2016.

- M. Schönherr: Sherpa: scaling on HPCs
  ATLAS Software & Computing Week, CERN, 16.03.2017.

- M. Wiesemann: MATRIX: A fully-differential NNLO(+NNLL) process library
  Loops&Legs 2016, Leipzig, Germany, 28.04.2016.

- M. Wiesemann: Transverse-momentum resummation of colorless final states at the NNLL+NNLO
  28th Rencontres de Blois, Blois, France, 01.06.2016.

- M. Wiesemann: Theory/MC status of Higgs production in association with bottom quarks
  CMS Higgs PAG - H2tau subgroup meeting, CERN, Switzerland, 06.07.2016.

- M. Wiesemann: bbH: status and future plans
  Preparatory Meeting of the LHC Higgs Cross Section Working Group, CERN, Switzerland, 08.07.2016.

- M. Wiesemann: MATRIX: A fully-differential NNLO(+NNLL) process library
  LoopFest XV, Buffalo, USA, 16.08.2016.

- M. Wiesemann: MATRIX: A fully-differential NNLO(+NNLL) process library
  QCD@LHC 2016, Zürich, Switzerland, 25.08.2016.

- M. Wiesemann: MATRIX: A fully-differential NNLO(+NNLL) process library
  High Precision for Hard Processes 6, Buenos Aires, Argentina, 09.09.2016.

- M. Wiesemann: bbH: report and future plans
  12th Workshop of the LHC Higgs Cross Section Working Group, CERN, Switzerland, 13.10.2016.

- M. Wiesemann: Higher-order corrections to differential WW production
  LHC EWK WG multiboson discussion, CERN, Switzerland, 13.02.2017.

- M. Wiesemann: MATRIX: A fully-differential NNLO(+NNLL) process library
  CMS Generator Meeting, CERN, Switzerland, 06.03.2017.

- M. Wiesemann: Vector-boson pair production at NNLO(+NNLL)
  LHCTheory ERC meeting, Louvain-La-Neuve, Belgium, 23.03.2017.

- D. van Dyk: Exclusive $b \to c\ell\bar{\nu}$ decays: SM predictions and uncertainties
  Prospects and challenges for semitauonic decays at LHCb, CERN, 28.04.2016.

- D. van Dyk: $B \to \pi\pi\ell\nu$ – Accessing theory estimates in various phase space corners
  MIAPP Workshop Flavour Physics with High-Luminosity Experiments München, Germany, 04.11.2016.

- D. van Dyk: QCD sum rules predictions for exclusive $b \to c$ transitions
  9th International Workshop on the CKM Unitarity Triangle (CKM2016), Mumbai, India, 29.11.2016.

- D. van Dyk: Semileptonic b decays: Preparing theory predictions for the era of high-luminosity experiments
  DPG Spring Conference, Münster, Germany, 30.03.2017.

- M.F. Zoller: Four-loop beta functions in the Standard Model: Leading contributions and their impact on vacuum stability
  Particle physics seminar, DESY Zeuthen, Germany, 09.06.2016.

- M.F. Zoller: Vacuum stability in the Standard Model: Towards a four-loop precision analysis
  HP2.6, Buenos Aires, Argentina, 06.09.2016.

- M.F. Zoller: Four-loop renormalization group functions in the Standard Model and beyond
  Workshop: Precision versus Energy, Present and Future Colliders KIT, Germany, 10.11.2016.

20.1.2 Astrophysics and General Relativity

Articles

- Gravitational wave polarization modes in f(R) theories
  R. Kausar, L. Philippoz and Ph. Jetzer, Phys. Rev. D**93**, (2016) 124071.

- Sub-femto-g free-fall for space-based gravitational wave observatories: LISA Pathfinder results
  M. Armano *et al.*, (The LISA Pahtfinder collaboration), Phys. Rev. Lett. **116**, (2016) 231101.

- The Triangulum galaxy seen by Planck
  F. De Paolis, V.G. Gurzadyan, A.A. Nucita, L. Chemin, A. Qadir, A.L. Kashin, H.G. Khachatryan, S. Sargsyan, G. Yegorian, G. Ingrosso, Ph. Jetzer, D. Vetrugno, Astron. and Astrophys. **593**, (2016) A57.

- Constraints on LISA Pathfinder's self-gravity: design requirements, estimates and testing procedures
  M. Armano *et al.*, (The LISA Pahtfinder collaboration) Class. Quantum Grav. **33**, 235015 (2016).

- LISA Pathfinder: first results
  Ph. Jetzer, SPG Mitteilungen, **50**, (2016) 60-62.

- Self-gravitating stellar collapse: explicit geodesics and path integration
  J. Balakrishna , R. Bondarescu and C. Corbett Moran, Front. Astron. Space Sci. **3** (2016) 29.

- Quantifying substructures in Hubble Frontier Field clusters: comparison with ΛCDM simulations
I. Mohammed, P. Saha, L. L. R. Williams, J. Liesenborgs, Jori, K. Sebesta, Monthly Notices of the Royal Astronomical Society, **459** (2016) 1698–1709.

- Strong gravitational lensing and the stellar IMF of early-type galaxies
D. Leier, I. Ferreras, P. Saha, S. Charlot, G. Bruzual, F. La Barbera, Monthly Notices of the Royal Astronomical Society, **459**, (2016) 3677–3692.

- Testing light-traces-mass in Hubble Frontier Fields Cluster MACS-J0416.1-2403
K. Sebesta, L. L. R. Williams, I. Mohammed, P. Saha, J. Liesenborgs, Monthly Notices of the Royal Astronomical Society, **461**, (2016) 2126–2134.

Oral Presentations

- Philippe Jetzer: Fundamental physics with space clocks in highly elliptic orbits
General Relativity GR21 Meeting, New York, 12 July 2016.

- Rafael Küng: Lensing galaxies in the CFHT legacy survey
Swiss Cosmology Days, Basel, 7 February 2017.

- Maria Haney: Joint update on eccentric waveform development in the CBC group
March 2017 LSC-Virgo Collaboration Meeting, Pasadena, 13 March 2017.

- Andreas Schärer: PPN Parameters in Scalar-Tensor Theories
Seminar at Institute of Physics Tartu, Estonia, 21 March 2017.

- Lionel Philippoz: Detecting Additional Polarization Modes with LISA
Rencontres de Moriond, La Thuile, 28 March 2017.

- Yannick Bötzel: On solving post-Newtonian accurate Kepler Equation
Rencontres de Moriond, La Thuile, 30 March 2017.

Outreach

- Lionel Philippoz: Ondes gravitationnelles : Le retour d'Einstein
Société Valaisanne de Physique, Sion, 23 September 2016.

- Philippe Jetzer: Gravitationswellen: Ein neues Fenster zur Erforschung des Universums (von LISA Pathfinder zu LISA)
Emeritenstamm ETH, Winterthur, 26 September 2016.

- Philippe Jetzer: Onde Gravitazionali
TechDay, Liceo di Bellinzona, 11 November 2016.

- Philippe Jetzer: Gravitationswellen: Ein neues Fenster zur Erforschung des Universums
Physikalische Gesellschaft Zürich, Zürich, 26 November 2016.

20.1.3 GERDA

Articles

- Background-free Search for Neutrinoless Double Beta Decay with GERDA Phase II
M.Agostini *et al.* (GERDA Collaboration), NATURE Vol. **544** No. 7648, pp.47-52 (2017).

- Limits on uranium and thorium bulk content in GERDA Phase I detectors
M.Agostini *et al.* (GERDA Collaboration), Astropart.Phys. **91** (2017) 15-21.

- Limit on the Radiative Neutrinoless Double Electron Capture of 36-Ar from GERDA Phase I
M. Agostini *et al.* (GERDA Collaboration), Europ. Phys. J. C, 76(12), 1-6 (2016).

- Flux Modulations seen by the Muon Veto of the GERDA Experiment
M. Agostini *et al.* (GERDA Collaboration), Astropart. Phys. **84** (2016) 29-35.

Oral Presentations

- R. Hiller: Prospects for keV-DM searches with the GERDA experiment
DPG meeting, Munster, Germany, March 29, 2017.

- R. Mingazheva: Current status and plans of the Gerda experiment
SPS Meeting, Lugano, August 26, 2016.

- R. Mingazheva: Search for neutrinoless double beta decay with the Gerda experiment
From the Vacuum to the Universe, Kitzbuhel, Austria, June 28, 2016.

20.1.4 XENON/DARWIN

Articles

- Search for Electronic Recoil Event Rate Modulation with 4 Years of XENON100 Data
E. Aprile *et al.* (XENON Collaboration), Phys. Rev. Lett. **118** (2017) no.10, 101101.

- Search for Two-Neutrino Double Electron Capture of 124-Xe with XENON100
E. Aprile *et al.* (XENON Collaboration), Phys. Rev. C **95** (2017) no.2, 024605.

- Results from a Calibration of XENON100 Using a Source of Dissolved Radon-220
E. Aprile *et al.* (XENON Collaboration), Phys. Rev. D **95** (2016) 072008.

- XENON100 Dark Matter Results from a Combination of 477 Live Days
E. Aprile *et al.* (XENON Collaboration), Phys. Rev. D **94** (2016) no.12, 122001.

- Qualification Tests of the R11410-21 Photomultiplier Tubes for the XENON1T Detector
P. Barrow, L. Baudis, D. Cichon, M. Danisch, D. Franco, F. Kaether, A. Kish, M. Lindner, T. Marrodan Undagoitia, D. Mayani, L. Rauch, Y. Wei, J. Wulf, JINST **12** (2017) no.01, P01024

- DARWIN: towards the ultimate dark matter detector
E. Aalbers *et al.* (DARWIN Collaboration), JCAP 1611 (2016) no.11, 017.

- A low-mass dark matter search using ionization signals in XENON100
E. Aprile *et al.* (XENON Collaboration), Phys. Rev. D**94** (2016) no.9, 092001.

Oral Presentations

- L. Baudis: Illuminating the dark side: direct searches for cold dark matter in the Milky Way
Physics Colloquium, University of Geneva, Geneva, March 20, 2017.

- L. Baudis: Prospects for direct dark matter detection and neutrinoless double beta decay experiments
La Thuile 2017, La Thuile, Italy, March 7, 2017.

- L. Baudis: Illuminating the dark side: direct searches for cold dark matter with XENON and DARWIN
Physics Seminar, Physics Department, Stanford, Palo Alto, USA, February 21, 2017.

- L. Baudis: Illuminating the dark side: direct searches for cold dark matter with XENON and DARWIN
Physics Seminar, Physics Department, UCLA, USA, February 15, 2017.

- L. Baudis: Dark matter detection in the Milky Way
Physics Colloquium, KIT, Karlsruhe, January 27, 2017.

- L. Baudis: Dark matter detection - an overview
Zurich Phenomenology Workshop (ZPW) 2017, Zurich, January 10, 2017.

- L. Baudis: Dark matter detection in the Milky Way
  Physics Colloquium, PSI, November 17, 2016.

- Y. Wei: Photodetectors for the XENON1T Dark Matter Experimentt
  2016 IEEE NSS/MIC, Strasbourg, France, October 30 2016.

- L. Baudis: Illuminating the dark side: the XENON experiment and the nature of dark matter
  Seminar, Physics Department, Milano Bicocca University, Milano, October 11, 2016.

- A. Kish: DARWIN: Towards the Ultimate Dark Matter Detector
  TeV Particle Astrophysics (TeVPA-2016), CERN, Switzerland, September 16, 2016.

- L. Baudis: The state-of-the art in the search for dark matter
  SPS Meeting, Lugano, August 25, 2016.

- Y. Wei: The XENON1T Dark Matter Experiment
  SPS Meeting, Lugano, August 25, 2016.

- J. Wulf: Characterization of VUV Silicon-Photomultipliers for xenon based dark matter detectors
  SPS Meeting, Lugano, August 24, 2016.

- M. Galloway: Design and characterisation of the Xurich II dual-phase xenon time projection chamber
  SPS Meeting, Lugano, August 24, 2016.

- M. Galloway: Dark Matter Search at the Multi-Ton Scale with XENONnT
  Identification of Dark Matter, Sheffield, England, July 20, 2016.

- J. Wulf: Direct Dark Matter Detection with XENON1T
  Direct Dark Matter Detection with XENON1T, Quy Nhon, Vietnam, July 13, 2016.

- L. Baudis: Illuminating the dark side: liquid xenon and the nature of dark matter
  Julius Wess Award Ceremony KCETA, Karlsruhe, July 8, 2016.

- M. Galloway: Direct Dark Matter Detection with XENON1T
  From the Vacuum to the Universe, Kitzbuhel, Austria, June 28, 2016.

- L. Baudis: Noble liquid dark matter experiments
  Dark Matter 2016: from the smallest to the largest scales Santander, June 29, 2016.

- A. Kish: XENON: Dual-phase TPCs for Dark Matter Detection
  Excellence Cluster Universe 'Detectors and Instrumentation' Workshop, MPE Munich, Germany, 31 May 2016.

Outreach

- L. Baudis: Exploring the vast dark universe
  TEDxCERN talk, CERN, Geneva, November 5, 2016.

- L. Baudis: Supersymmetrie und das Universum
  Volkshochschule Zurich, Zurich, September 19, 2016.

- L. Baudis: Dark matter
  zurich.minds Deep Dive, Zurich Uniturm, Zurich, April 6, 2016.

20.1.5 DAMIC and CONNIE

Articles

- First Direct-Detection Constraints on eV-Scale Hidden-Photon Dark Matter with DAMIC at SNOLAB
  DAMIC Collaboration, A. Aguilar-Aravelo *et al.*, Phys. Rev. Lett. **118**, 141803 (2017).

- Search for low-mass WIMPs in a 0.6 kg day exposure of the DAMIC experiment at SNOLAB
  DAMIC Collaboration, A. Aguilar-Aravelo *et al.*, Phys. Rev. D **94**, no. 8, 082006 (2016).
- Status of the DAMIC Direct Dark Matter Search Experiment
  DAMIC Collaboration, A. Aguilar-Aravelo *et al.*, arXiv:1510.00044 [physics.ins-det].
- The CONNIE experiment
  CONNIE Collaboration, A. Aguilar-Aravelo *et al.*, J. Phys. Conf. Ser. **761**, no. 1, 012057 (2016).
- Results of the engineering run of the Coherent Neutrino Nucleus Interaction Experiment (CONNIE)
  CONNIE Collaboration, A. Aguilar-Aravelo *et al.*, JINST **11**, no. 07, P07024 (2016).

Oral presentations

- B. Kilminster: Coherent neutrino nucleus interaction experiment in CCDs
  Applied Antineutrino physics 2016, Dec. 2016, Liverpool, U.K.
- J. Liao: The status of the DAMIC experiment at Snolab
  Identification of Dark Matter 2016, July 18 - 22 2016, Sheffield, U.K.

20.1.6 SHiP

Oral presentations

- Elena Graverini: SHiP: a new facility with dedicated detectors to search for new long-lived neutral particles and study the τ neutrino properties
  Seminar, Université Libre de Bruxelles, Bruxelles, Belgium, February 26, 2016.
- Elena Graverini: SHiP: a new facility with a dedicated detector to search for new long-lived neutral particles and study the τ neutrino properties
  8th Rencontres de Blois on Particle Physics and Cosmology, Blois (FR), May 29 – June 3, 2016.
- Elena Graverini: Heavy neutrino searches from MeV to TeV
  International Workshop on Neutrino Factories, Super Beams and Beta Beams , Quy Nhon, Vietnam, August 21 – 27, 2016.
- Christopher Betancourt: The SHiP Experiment at CERN
  Strasbourg, France, November 3, 2016.
- Christopher Betancourt: SiPM readout for the SHiP timing detector
  14th Topical Seminar on Innovative Particle and Radiation Detectors (2016), Siena, Italy, October 3, 2016, proceedings published in JINST **12** no. 02, C02058 (2017).
- Christopher Betancourt: Development of the SHiP Timing Detector Based on Scintillating Bars Readout by SiPMs, 12th Trento Workshop on Advanced Silicon Radiation Detectors, Trento, Italy, February 22, 2017.

20.1.7 H1

The 2015 H1 Collaboration has 141 members including K. Müller, P. Robmann, U. Straumann and P. Truöl.
Articles

- Measurement of Jet Production Cross Sections in Deep-inelastic ep Scattering at HERA
  H1 Collaboration, V. Andreev *et al.*, Eur. Phys. J. C **77** (2017) no.4, 215.
- Search for QCD Instanton-Induced Processes at HERA in the High-Q^2 Domain
  H1 Collaboration, V. Andreev *et al.*, Eur. Phys. J. C**76** (2016) 7, 1.

20.1.8 CMS

Articles

- The Triple GEM Detector Control System for CMS forward muon spectrometer upgrade
  CMS Muon Collaboration, W. Ahmed *et al.*, JINST **12**, no. 02, P02003 (2017).

- Search for dark matter and unparticles in events with a Z boson and missing transverse momentum in proton-proton collisions at $\sqrt{s} = 13$ TeV
  CMS Collaboration, A. M. Sirunjan *et al.*, JHEP **1703**, 061 (2017).

- Search for massive resonances decaying into WW, WZ or ZZ bosons in proton-proton collisions at $\sqrt{s} = 13$ TeV
  CMS Collaboration, A. M. Sirunjan *et al.*, JHEP **1703**, 162 (2017).

- Search for electroweak production of a vector-like quark decaying to a top quark and a Higgs boson using boosted topologies in fully hadronic final states
  CMS Collaboration, A. M. Sirunjan *et al.*, JHEP **1704**, 136 (2017).

- Search for heavy neutrinos or third-generation leptoquarks in final states with two hadronically decaying τ leptons and two jets in proton-proton collisions at $\sqrt{s} = 13$ TeV
  CMS Collaboration, A. M. Khachatryan *et al.*, JHEP **1703**, 077 (2017).

- Search for CP violation in $t\bar{t}$ production and decay in proton-proton collisions at $\sqrt{s} = 8$ TeV
  CMS Collaboration, A. M. Khachatryan *et al.*, JHEP **1703**, 101 (2017).

- Search for supersymmetry in events with photons and missing transverse energy in pp collisions at 13 TeV
  CMS Collaboration, A. M. Khachatryan *et al.*, Phys. Lett. B **769**, 391 (2017).

- Search for heavy resonances decaying to tau lepton pairs in proton-proton collisions at $\sqrt{s} = 13$ TeV
  CMS Collaboration, A. M. Khachatryan *et al.*, JHEP **1702**, 048 (2017).

- Measurement of the $t\bar{t}$ production cross section using events in the eμ final state in pp collisions at $\sqrt{s} = 13$ TeV
  CMS Collaboration, A. M. Khachatryan *et al.*, Eur. Phys. J. C **77**, 172 (2017).

- Measurements of differential production cross sections for a Z boson in association with jets in pp collisions at $\sqrt{s} = 8$ TeV
  CMS Collaboration, A. M. Khachatryan *et al.*, JHEP **1704**, 022 (2017).

- Charged-particle nuclear modification factors in PbPb and pPb collisions at $\sqrt{s_{\mathrm{NN}}} = 5.02$ TeV
  CMS Collaboration, A. M. Khachatryan *et al.*, JHEP **1704**, 039 (2017).

- Relative modification of prompt psi(2S) and J/psi yields from pp to PbPb collisions at $\sqrt{s_{\mathrm{NN}}} = 5.02$ TeV
  CMS Collaboration, A. M. Sirunjan *et al.*, Phys. Rev. Lett. **118**, 162301 (2017).

- Searches for invisible decays of the Higgs boson in pp collisions at $\sqrt{s} = 7$, 8, and 13 TeV
  CMS Collaboration, A. M. Khachatryan *et al.*, JHEP **1702**, 135 (2017).

- Search for heavy resonances decaying into a vector boson and a Higgs boson in final states with charged leptons, neutrinos, and b quarks
  CMS Collaboration, A. M. Khachatryan *et al.*, Phys. Lett. B **768**, 137 (2017).

- Search for R-parity violating supersymmetry with displaced vertices in proton-proton collisions at $\sqrt{s} = 8$ TeV
  CMS Collaboration, A. M. Khachatryan *et al.*, Phys. Rev. D **95**, 012009 (2017).

- Search for electroweak production of charginos in final states with two leptons in pp collisions at $\sqrt{s} = 8$ TeV
  CMS Collaboration, A. M. Khachatryan *et al.*, JHEP **1704**, 018 (2017).

- Search for top quark decays via Higgs-boson-mediated flavor-changing neutral currents in pp collisions at $\sqrt{s} = 8$ TeV
  CMS Collaboration, A. M. Khachatryan *et al.*, JHEP **1702**, 079 (2017).

- Measurements of differential cross sections for associated production of a W boson and jets in proton-proton collisions at $\sqrt{s} = 8$ TeV
  CMS Collaboration, A. M. Khachatryan *et al.*, Phys. Rev. D **95**, 052002 (2017).

- Search for anomalous Wtb couplings and flavour-changing neutral currents in t-channel single top quark production in pp collisions at $\sqrt{s} = 7$ and 8 TeV
  CMS Collaboration, A. M. Khachatryan *et al.*, JHEP **1702**, 028 (2017).

- Search for high-mass Zγ resonances in $e^+e^-\gamma$ and $\mu^+\mu^-\gamma$ final states in proton-proton collisions at $\sqrt{s} = 8$ and 13 TeV
  CMS Collaboration, A. M. Khachatryan *et al.*, JHEP **1701**, 076 (2017).

- Suppression and azimuthal anisotropy of prompt and nonprompt J/ψ production in PbPb collisions at $\sqrt{s_{NN}} = 2.76$ TeV
  CMS Collaboration, A. M. Khachatryan *et al.*, Eur. Phys. J. C **77**, no. 4, 252 (2017).

- Observation of charge-dependent azimuthal correlations in pPb collisions and its implication for the search for the chiral magnetic effect
  CMS Collaboration, A. M. Khachatryan *et al.*, Phys. Rev. Lett. **118**, 122301 (2017).

- Search for supersymmetry in events with one lepton and multiple jets in proton-proton collisions at $\sqrt{s} = 13$ TeV
  CMS Collaboration, A. M. Khachatryan *et al.*, Phys. Rev. D **95**, no. 1, 012011 (2017).

- Inclusive search for supersymmetry using razor variables in pp collisions at $\sqrt{s} = 13$ TeV
  CMS Collaboration, A. M. Khachatryan *et al.*, Phys. Rev. D **95**, no. 1, 012003 (2017).

- Measurement of the WZ production cross section in pp collisions at $\sqrt{s} = 7$ and 8 TeV and search for anomalous triple gauge couplings at $\sqrt{s} = 8$ TeV
  CMS Collaboration, A. M. Khachatryan *et al.*, Eur. Phys. J. C **77**, no. 4, 236 (2017).

- Search for narrow resonances in dilepton mass spectra in proton-proton collisions at $\sqrt{s} = 13$ TeV and combination with 8 TeV data
  CMS Collaboration, A. M. Khachatryan *et al.*, Phys. Lett. B **768**, 57 (2017).

- Measurement and QCD analysis of double-differential inclusive jet cross sections in pp collisions at $\sqrt{s} = 8$ TeV and cross section ratios to 2.76 and 7 TeV
  CMS Collaboration, A. M. Khachatryan *et al.*, JHEP **1703**, 156 (2017).

- Search for high-mass diphoton resonances in proton-proton collisions at 13 TeV and combination with 8 TeV search
  CMS Collaboration, A. M. Khachatryan *et al.*, Phys. Lett. B **767**, 147 (2017).

- The CMS trigger system
  CMS Collaboration, A. M. Khachatryan *et al.*, JINST **12**, no. 01, P01020 (2017).

- Measurement of the production cross section of a W boson in association with two b jets in pp collisions at $\sqrt{s} = 8$ TeV
  CMS Collaboration, A. M. Khachatryan *et al.*, Eur. Phys. J. C **77**, no. 2, 92 (2017).

- Measurement of the WZ production cross section in pp collisions at $\sqrt{(s)} = 13$ TeV
  CMS Collaboration, A. M. Khachatryan *et al.*, Phys. Lett. B **766**, 268 (2017).

- Jet energy scale and resolution in the CMS experiment in pp collisions at 8 TeV
  CMS Collaboration, A. M. Khachatryan *et al.*, JINST **12**, no. 02, P02014 (2017).

- Observation of the decay $B^+ \to \psi(2S)\phi(1020)K^+$ in pp collisions at $\sqrt{s} = 8$ TeV
  CMS Collaboration, A. M. Khachatryan *et al.*, Phys. Lett. B **764**, 66 (2017).

- Evidence for collectivity in pp collisions at the LHC
  CMS Collaboration, A. M. Khachatryan *et al.*, Phys. Lett. B **765**, 193 (2017).

- Measurement of the transverse momentum spectra of weak vector bosons produced in proton-proton collisions at $\sqrt{s} = 8$ TeV
  CMS Collaboration, A. M. Khachatryan *et al.*, JHEP **1702**, 096 (2017).

- Measurement of the transverse momentum spectrum of the Higgs boson produced in pp collisions at $\sqrt{s} = 8$ TeV using $H \to WW$ decays
CMS Collaboration, A. M. Khachatryan *et al.*, JHEP **1703**, 032 (2017).

- Search for Dark Matter and Supersymmetry with a Compressed Mass Spectrum in the Vector Boson Fusion Topology in Proton-Proton Collisions at $\sqrt{s} = 8$ TeV
CMS Collaboration, A. M. Khachatryan *et al.*, Phys. Rev. Lett. **118**, no. 2, 021802 (2017).

- Search for top squark pair production in compressed-mass-spectrum scenarios in proton-proton collisions at $\sqrt{s} = 8$ TeV using the α_T variable
CMS Collaboration, A. M. Khachatryan *et al.*, Phys. Lett. B **767**, 403 (2017).

- Multiplicity and rapidity dependence of strange hadron production in pp, pPb, and PbPb collisions at the LHC
CMS Collaboration, A. M. Khachatryan *et al.*, Phys. Lett. B **768**, 103 (2017).

- Measurements of the $\mathrm{t\bar{t}}$ production cross section in lepton+jets final states in pp collisions at 8 TeV and ratio of 8 to 7 TeV cross sections
CMS Collaboration, A. M. Khachatryan *et al.*, Eur. Phys. J. C **77**, no. 1, 15 (2017).

- Search for supersymmetry in electroweak production with photons and large missing transverse energy in pp collisions at $\sqrt{s} = 8$ TeV
CMS Collaboration, A. M. Khachatryan *et al.*, Phys. Lett. B **759**, 479 (2016).

- Search for heavy resonances decaying to two Higgs bosons in final states containing four b quarks
CMS Collaboration, A. M. Khachatryan *et al.*, Eur. Phys. J. C **76**, no. 7, 371 (2016).

- Measurement of the $\mathrm{Z}\gamma \to \nu\bar{\nu}\gamma$ production cross section in pp collisions at $\sqrt{s} = 8$ TeV and limits on anomalous $\mathrm{ZZ}\gamma$ and $\mathrm{Z}\gamma\gamma$ trilinear gauge boson couplings
CMS Collaboration, A. M. Khachatryan *et al.*, Phys. Lett. B **760**, 448 (2016).

- Search for supersymmetry in the multijet and missing transverse momentum final state in pp collisions at 13 TeV
CMS Collaboration, A. M. Khachatryan *et al.*, Phys. Lett. B **758**, 152 (2016).

- Measurement of dijet azimuthal decorrelation in pp collisions at $\sqrt{s} = 8\,\mathrm{TeV}$
CMS Collaboration, A. M. Khachatryan *et al.*, Eur. Phys. J. C **76**, no. 10, 536 (2016).

- Search for R-parity violating decays of a top squark in proton-proton collisions at $\sqrt{s} = 8$ TeV
CMS Collaboration, A. M. Khachatryan *et al.*, Phys. Lett. B **760**, 178 (2016).

- Combined search for anomalous pseudoscalar HVV couplings in VH(H $\to b\bar{b}$) production and H $\to$ VV decay
CMS Collaboration, A. M. Khachatryan *et al.*, Phys. Lett. B **759**, 672 (2016).

- Search for direct pair production of scalar top quarks in the single- and dilepton channels in proton-proton collisions at $\sqrt{s} = 8$ TeV
CMS Collaboration, A. M. Khachatryan *et al.*, JHEP **1607**, 027 (2016)
Erratum: [JHEP **1609**, 056 (2016).]

- Search for supersymmetry in pp collisions at $\sqrt{s} = 8$ TeV in final states with boosted W bosons and b jets using razor variables
CMS Collaboration, A. M. Khachatryan *et al.*, Phys. Rev. D **93**, no. 9, 092009 (2016).

- Azimuthal decorrelation of jets widely separated in rapidity in pp collisions at $\sqrt{s} = 7$ TeV
CMS Collaboration, A. M. Khachatryan *et al.*, JHEP **1608**, 139 (2016).

- Search for massive WH resonances decaying into the $\ell\nu\mathrm{b\bar{b}}$ final state at $\sqrt{s} = 8$ TeV
CMS Collaboration, A. M. Khachatryan *et al.*, Eur. Phys. J. C **76**, no. 5, 237 (2016).

- Forward-backward asymmetry of DrellÐYan lepton pairs in pp collisions at $\sqrt{s} = 8$ TeV
CMS Collaboration, A. M. Khachatryan *et al.*, Eur. Phys. J. C **76**, no. 6, 325 (2016).

- Measurement of inclusive jet production and nuclear modifications in pPb collisions at $\sqrt{s_{\mathrm{NN}}} = 5.02$ TeV
  CMS Collaboration, V. Khachatryan *et al.*, Eur. Phys. J. C **76**, no. 7, 372 (2016).

Invited talks

- Florencia Canelli: Highlights from ICHEP
  Swiss Physical Society, 23-25 August 2016, Lugano, Switzerland

- Florencia Canelli: Results on Higgs Physics at the LHC
  CHEP, 3-10 August 2016, Chicago, U.S.

Oral presentations

- Florencia Canelli: The top quark and its searches
  ETH and UZH Physics Colloquium 14 December 2016, Zurich, Switzerland.

- Florencia Canelli: The phase I pixel detector upgrade
  Universidad de San Martin HEP seminar 4 May 2016, Buenos Aires, Argentina.

- Silvio Donato: Run 1 Higgs legacy combination
  LHCP 2016, 13-16 June 2016, Lund, Sweden.

- Silvio Donato: Higgs Physics at CMS
  DISCRETE, 28 November - 3 December 2016, Warsaw, Poland

- Deborah Pinna : Dark Matter Searches at CMS and Future Plans
  Dark Side of the Universe conference, Bergen, 25 - 29 July 2016, Bergen, Norway.

- Claudia Seitz: SUSY search in the single lepton final state
  Helmholtz 2016, Physics at the Tera Scale, 21 - 23 November 2016 Hamburg, Germany.

- Giorgia Rauco: Jet performance in Run 2 of the LHC
  BOOST2016, Zurich, 18-22 July 2016, Zurich, Switzerland.

- Giorgia Rauco: Quark-gluon separation at the LHC
  Parton Radiation and Fragmentation from LHC to FCC-ee, CERN, 21- 22 November 2016, Meyrin, Switzerland.

- Giorgia Rauco: Distinguish quark and gluon jets at the CMS experiment
  Zurich PhD Seminar, 24 - 25 November 2016, Zurich, Switzerland.

- Giorgia Rauco: Quark vs Gluon discrimination Jet Substructure
  Planning for the future event 30 November - 1 December 2016, Batavia (IL), US.

- Giorgia Rauco: Search for single produced B′ decaying to bH in the full-hadronic channel
  Beyond Two Generations Winter Workshop, CERN, 3- 4-December 2016, Meyrin, Switzerland.

- Giorgia Rauco : Distinguish quark and gluon jets at the CMS experiment
  Posters@LHCC, CERN, 22 February 2017, Meyrin, Switzerland.

- Daniel Salerno : Studies of Higgs bosons decaying to fermions with CMS
  LHC SKI 2016, Obergurgl University Center, Austriam 10 -15 April 2016 Tirol, Austria.

- Daniel Salerno : Study of Higgs Production in Fermionic Decay Channels at CMS
  SUSY 2016, The University of Melbourne, Australia , 4 - 8 July 2016, Melbourne, Australia.

- Camilla Galloni : Tau identification in boosted topologies in CMS
  BOOST, 18- 22 July 2016, Zurich, Switzerland.

- Camilla Galloni : Search for signatures with top, bottom, tau and exotics
  pp@LHC Workshop 16 - 18 May 2016, Pisa, Italy.

- Annapaola de Cosa : Searches for Dark Matter at the LHC
  Seminar, University of Zurich, 4 April 2016, Zurich, Switzerland.

- Annapaola de Cosa : Searching for Dark Matter at colliders
  Universitá degli Studi di Napoli, FedericoII - seminar, 2 May 2016, Napoli, Italy.

- Annapaola de Cosa : DM + tt
  Dark Matter Brainstorming, London, 6 May 2016, London, U.K.

- Annapaola de Cosa: Searching for DM at CMS
  International conference on High Energy Physics: Theory to Experiment IHEP-T2E, Malaysia, 27 February - 1 March 2017, Kuala Lampur, Malaysia.

- Annapaola de Cosa : Looking for DM with the CMS experiment
  Queen Mary University of London - seminar, 3 March 2017, London, U.K.

- Andreas Hinzmann : Search for new physics in bosonic final states at the LHC
  LHCP 2016, 13- 16 June 2016, Lund, Sweden.

- Lea Caminada : The Phase 1 Upgrade of the CMS Pixel Detector
  Imperial College London, UK - Seminar, 18 May 2016, London, U.K.

- Lea Caminada : Swiss participation in LHC experiments
  RECFA visit, Switzerland, 1 April 2016, Zurich, Switzerland.

- Ben Kilminster : New physics beyond the Higgs boson
  Universidad Nacional de San Martin particle seminar, 4 May 2016, Buenos Aires, Argentina.

20.1.9 LHCb

Articles

- Measurement of the $B^{\pm}$ production asymmetry and the CP asymmetry in $B^{\pm} \to J/\psi K^{\pm}$ decays
  LHCb-Collaboration, R. Aaij *et al.*, Phys. Rev. D **95** (2017) no.5, 052005.

- Observation of $B_c^+ \to D^0 K^+$ decays
  LHCb-Collaboration, R. Aaij *et al.*, Phys. Rev. Lett. **118** (2017) no.11, 111803.

- Observation of $B_c^+ \to J/\psi D^{(*)} K^{(*)}$ decays
  LHCb-Collaboration, R. Aaij *et al.*, Phys. Rev. D **95** (2017) no.3, 032005.

- Measurement of the phase difference between short- and long-distance amplitudes in the $B^+ \to K^+ \mu^+ \mu^-$ decay
  LHCb-Collaboration, R. Aaij *et al.*, Eur. Phys. J. C **77** (2017) 161.

- Measurement of the ratio of branching fractions and difference in CP asymmetries of the decays $B^+ \to J/\psi \pi^+$ and $B^+ \to J/\psi K^+$
  LHCb-Collaboration, R. Aaij *et al.*, JHEP **1703** (2017) 036.

- Measurement of the b-quark production cross-section in 7 and 13 TeV pp collisions
  LHCb-Collaboration, R. Aaij *et al.*, Phys. Rev. Lett. **118** (2017) no.5, 052002.

- Observation of the decay $\Xi_b^- \to p K^- K^-$
  LHCb-Collaboration, R. Aaij *et al.*, Phys. Rev. Lett. **118** (2017) no.7, 071801.

- Search for decays of neutral beauty mesons into four muons
  LHCb-Collaboration, R. Aaij *et al.*, JHEP **1703** (2017) 001.

- Measurements of charm mixing and CP violation using $D^0 \to K^{\pm} \pi^{\mp}$ decays
  LHCb-Collaboration, R. Aaij *et al.*, Phys. Rev. D **95** (2017) no.5, 052004.

- Measurement of the CKM angle γ from a combination of LHCb results
LHCb-Collaboration, R. Aaij *et al.*, JHEP **1612** (2016) 087.

- Measurement of CP asymmetry in $D^0 \to K^-K^+$ decays
LHCb-Collaboration, R. Aaij *et al.*, Phys. Lett. B **767** (2017) 177.

- Measuring the Breaking of Lepton Flavour Universality in $B \to K^\star \ell^+ \ell$
N. Serra, R. Silva Coutinho, D. van Dyk, Phys.Rev. D **95** (2017) no.3, 035029.

- Observation of the annihilation decay mode $B^0 \to K^+K^-$
LHCb-Collaboration, R. Aaij *et al.*, Phys. Rev. Lett. **118** (2017) no.8, 081801.

- Measurement of forward $t\bar{t}$, $W + b\bar{b}$ and $W + c\bar{c}$ production in pp collisions at $\sqrt{s} = 8$ TeV
LHCb-Collaboration, R. Aaij *et al.*, Phys. Lett. B **767** (2017) 110.

- Observation of the decay $B_s^0 \to \phi\pi^+\pi^-$ and evidence for $B^0 \to \phi\pi^+\pi^-$
LHCb-Collaboration, R. Aaij *et al.*, Phys. Rev. D **95** (2017) no.1, 012006.

- Search for the CP-violating strong decays $\eta \to \pi^+\pi^-$ and $\eta'(958) \to \pi^+\pi^-$
LHCb-Collaboration, R. Aaij *et al.*, Phys. Lett. B **764** (2017) 233.

- Observation of $B^+ \to J/\psi 3\pi^+ 2\pi^-$ and $B^+ \to \psi(2S)\pi^+\pi^+\pi^-$ decays
LHCb-Collaboration, R. Aaij *et al.*, Eur. Phys. J. C **77** (2017) no.2, 72.

- Measurement of matter-antimatter differences in beauty baryon decays
LHCb-Collaboration, R. Aaij *et al.*, Nature Phys. (2017).

- Differential branching fraction and angular moments analysis of the decay $B^0 \to K^+\pi^-\mu^+\mu^-$ in the $K^*_{0,2}(1430)^0$ region
LHCb-Collaboration, R. Aaij *et al.*, JHEP **1612** (2016) 065.

- Search for Higgs-like bosons decaying into long-lived exotic particles
LHCb-Collaboration, R. Aaij *et al.*, Eur. Phys. J. C **76** (2016) no.12, 664.

- First experimental study of photon polarization in radiative B_s^0 decays
LHCb-Collaboration, R. Aaij *et al.*, Phys. Rev. Lett. **118** (2017) no.2, 021801 Addendum: [Phys. Rev. Lett. **118** (2017) no.10, 109901].

- Measurement of CP violation in $B^0 \to D^+D^-$ decays
LHCb-Collaboration, R. Aaij *et al.*, Phys. Rev. Lett. **117** (2016) no.26, 261801.

- First study of the CP -violating phase and decay-width difference in $B_s^0 \to \psi(2S)\phi$ decays
LHCb-Collaboration, R. Aaij *et al.*, Phys. Lett. B **762** (2016) 253.

- Measurement of forward $W \to e\nu$ production in pp collisions at $\sqrt{s} = 8$ TeV
LHCb-Collaboration, R. Aaij *et al.*, JHEP **1610** (2016) 030.

- Search for the suppressed decays $B^+ \to K^+K^+\pi^-$ and $B^+ \to \pi^+\pi^+K^-$
LHCb-Collaboration, R. Aaij *et al.*, Phys. Lett. B **765** (2017) 307.

- Amplitude analysis of $B^- \to D^+\pi^-\pi^-$ decays
LHCb-Collaboration, R. Aaij *et al.*, Phys. Rev. D **94** (2016) no.7, 072001.

- Search for Structure in the $B_s^0\pi^\pm$ Invariant Mass Spectrum
LHCb-Collaboration, R. Aaij *et al.*, Phys. Rev. Lett. **117** (2016) no.15, 152003 Addendum: [Phys. Rev. Lett. **118** (2017) no.10, 109904].

- Measurement of the ratio of branching fractions $\mathcal{B}(B_c^+ \to J/\psi K^+)/\mathcal{B}(B_c^+ \to J/\psi\pi^+)$
LHCb-Collaboration, R. Aaij *et al.*, JHEP **1609** (2016) 153.

- Measurement of the forward Z boson production cross-section in pp collisions at $\sqrt{s} = 13$ TeV
LHCb-Collaboration, R. Aaij *et al.*, JHEP **1609** (2016) 136.

- Measurement of the $B_s^0 \to J/\psi\eta$ lifetime
  LHCb-Collaboration, R. Aaij *et al.*, Phys. Lett. B **762** (2016) 484.

- Study of B_c^+ decays to the $K^+K^-\pi^+$ final state and evidence for the decay $B_c^+ \to \chi_{c0}\pi^+$
  LHCb-Collaboration, R. Aaij *et al.*, Phys. Rev. D **94** (2016) no.9, 091102.

- Amplitude analysis of $B^+ \to J/\psi\phi K^+$ decays
  LHCb-Collaboration, R. Aaij *et al.*, Phys. Rev. D **95** (2017) no.1, 012002.

- Observation of $J/\psi\phi$ structures consistent with exotic states from amplitude analysis of $B^+ \to J/\psi\phi K^+$ decays
  LHCb-Collaboration, R. Aaij *et al.*, Phys. Rev. Lett. **118** (2017) no.2, 022003.

- Evidence for exotic hadron contributions to $\Lambda_b^0 \to J/\psi p\pi^-$ decays
  LHCb-Collaboration, R. Aaij *et al.*, Phys. Rev. Lett. **117** (2016) no.8, 082003 Addendum: [Phys. Rev. Lett. **117** (2016) no.10, 109902].

- Measurements of the S-wave fraction in $B^0 \to K^+\pi^-\mu^+\mu^-$ decays and the $B^0 \to K^*(892)^0\mu^+\mu^-$ differential branching fraction
  LHCb-Collaboration, R. Aaij *et al.*, JHEP **1611** (2016) 047.

- Measurement of the CP asymmetry in $B_s^0 - \overline{B}_s^0$ mixing
  LHCb-Collaboration, R. Aaij *et al.*, Phys. Rev. Lett. **117** (2016) no.6, 061803.

- Measurement of the CKM angle γ using $B^0 \to DK^{*0}$ with $D \to K_S^0\pi^+\pi^-$ decays
  LHCb-Collaboration, R. Aaij *et al.*, JHEP **1608** (2016) 137.

- Measurement of forward W and Z boson production in association with jets in proton-proton collisions at $\sqrt{s} = 8$ TeV
  LHCb-Collaboration, R. Aaij *et al.*, JHEP **1605** (2016) 131.

- Model-independent evidence for $J/\psi p$ contributions to $\Lambda_b^0 \to J/\psi pK^-$ decays
  LHCb-Collaboration, R. Aaij *et al.*, Phys. Rev. Lett. **117** (2016) no.8, 082002.

- Measurement of the properties of the Ξ_b^{*0} baryon
  LHCb-Collaboration, R. Aaij *et al.*, JHEP **1605** (2016) 161.

- A precise measurement of the B^0 meson oscillation frequency
  LHCb-Collaboration, R. Aaij *et al.*, Eur. Phys. J. C **76** (2016) no.7, 412.

- Model-independent measurement of the CKM angle γ using $B^0 \to DK^{*0}$ decays with $D \to K_S^0\pi^+\pi^-$ and $K_S^0K^+K^-$
  LHCb-Collaboration, R. Aaij *et al.*, JHEP **1606** (2016) 131.

- Measurement of the mass and lifetime of the Ω_b^- baryon
  LHCb-Collaboration, R. Aaij *et al.*, Phys. Rev. D **93** (2016) no.9, 092007.

- Measurement of CP observables in $B^\pm \to DK^\pm$ and $B^\pm \to D\pi^\pm$ with two- and four-body D decays
  LHCb-Collaboration, R. Aaij *et al.*, Phys. Lett. B **760** (2016) 117.

- Search for B_c^+ decays to the $p\bar{p}\pi^+$ final state
  LHCb-Collaboration, R. Aaij *et al.*, Phys. Lett. B **759** (2016) 313.

- Observation of $\Lambda_b^0 \to \psi(2S)pK^-$ and $\Lambda_b^0 \to J/\psi\pi^+\pi^-pK^-$ decays and a measurement of the Λ_b^0 baryon mass
  LHCb-Collaboration, R. Aaij *et al.*, JHEP **1605** (2016) 132.

- Search for violations of Lorentz invariance and CPT symmetry in $B_{(s)}^0$ mixing
  LHCb-Collaboration, R. Aaij *et al.*, Phys. Rev. Lett. **116** (2016) no.24, 241601.

- Observation of the $\Lambda_b^0 \to \Lambda\phi$ decay
  LHCb-Collaboration, R. Aaij *et al.*, Phys. Lett. B **759** (2016) 282.

- Observation of $B_s^0 \to \bar{D}^0K_S^0$ and evidence for $B_s^0 \to \bar{D}^{*0}K_S^0$ decays
  LHCb-Collaboration, R. Aaij *et al.*, Phys. Rev. Lett. **116** (2016) no.16, 161802.

- Observations of $\Lambda_b^0 \to \Lambda K^+\pi^-$ and $\Lambda_b^0 \to \Lambda K^+K^-$ decays and searches for other Λ_b^0 and Ξ_b^0 decays to $\Lambda h^+h'^-$ final states
  LHCb-Collaboration, R. Aaij *et al.*, JHEP **1605** (2016) 081.

- Measurement of the $B_s^0 \to D_s^{(*)+}D_s^{(*)-}$ branching fractions
  LHCb-Collaboration, R. Aaij *et al.*, Phys. Rev. D **93** (2016) no.9, 092008.

- A new algorithm for identifying the flavour of B_s^0 mesons at LHCb
  LHCb-Collaboration, R. Aaij *et al.*, JINST **11** (2016) no.05, P05010.

- First observation of $D^0 - \bar{D}^0$ oscillations in $D^0 \to K^+\pi^-\pi^+\pi^-$ decays and measurement of the associated coherence parameters
  LHCb-Collaboration, R. Aaij *et al.*, Phys. Rev. Lett. **116** (2016) no.24, 241801.

- Constraints on the unitarity triangle angle γ from Dalitz plot analysis of $B^0 \to DK^+\pi^-$ decays
  LHCb-Collaboration, R. Aaij *et al.*, Phys. Rev. D **93** (2016) no.11, 112018 Erratum: [Phys. Rev. D **94** (2016) no.7, 079902].

- Measurement of the difference of time-integrated CP asymmetries in $D^0 \to K^-K^+$ and $D^0 \to \pi^-\pi^+$ decays
  LHCb-Collaboration, R. Aaij *et al.*, Phys. Rev. Lett. **116** (2016) no.19, 191601.

- Study of $\psi(2S)$ production and cold nuclear matter effects in pPb collisions at $\sqrt{s_{NN}} = 5$ TeV
  LHCb-Collaboration, R. Aaij *et al.*, JHEP **1603** (2016) 133.

- Observation of the $B_s^0 \to J/\psi\phi\phi$ decay
  LHCb-Collaboration, R. Aaij *et al.*, JHEP **1603** (2016) 040.

- Study of $D_{sJ}^{(*)+}$ mesons decaying to $D^+ K_S^0$ and $D^{*0} K^+$ final states
  LHCb-Collaboration, R. Aaij *et al.*, JHEP **1602** (2016) 133.

- Angular analysis of the $B^0 \to K^{*0}\mu^+\mu^-$ decay using 3 fb^{-1} of integrated luminosity
  LHCb-Collaboration, R. Aaij *et al.*, JHEP **1602** (2016) 104.

- First observation of the rare $B^+ \to D^+K^+\pi^-$ decay
  LHCb-Collaboration, R. Aaij *et al.*, Phys. Rev. D **93** (2016) no.5, 051101 Erratum: [Phys. Rev. D **93** (2016) no.11, 119902].

- Measurements of long-range near-side angular correlations in $\sqrt{s_{NN}} = 5$TeV proton-lead collisions in the forward region
  LHCb-Collaboration, R. Aaij *et al.*, Phys. Lett. B **762** (2016) 473.

- Measurement of forward W and Z boson production in pp collisions at $\sqrt{s} = 8$ TeV
  LHCb-Collaboration, R. Aaij *et al.*, JHEP **1601** (2016) 155.

- First observation of the decay $D^0 \to K^-\pi^+\mu^+\mu^-$ in the ρ^0-ω region of the dimuon mass spectrum
  LHCb-Collaboration, R. Aaij *et al.*, Phys. Lett. B **757** (2016) 558.

- Production of associated Y and open charm hadrons in pp collisions at $\sqrt{s} = 7$ and 8 TeV via double parton scattering
  LHCb-Collaboration, R. Aaij *et al.*, JHEP **1607** (2016) 052.

Invited lectures

- Olaf Steinkamp: The Eyes of the Particle Physicist
  Inaugural lecture, Zurich, March 20, 2017.

Oral presentations

- Patrick Haworth Owen: Heavy flavour physics at LHCb
  Aspen winter conference: From the LHC to dark matter and beyond, March 20 – 25, 2017.

- Rafael Silva Coutinho: Experimental results from b-hadron decays to three-body final states
  Mini-workshop: multi-particle final states in B decays, Siegen, Germany, February 21, 2017.

- Barbara Storaci: How operational works convert into physics: novels concepts from LHCb
  University of Liverpool, Liverpool, UK, January 13, 2017.

- Andrea Mauri: Heavy flavour highlights from LHCb
  XXIII Epiphany conference, Krakov, Poland, January 9 – 12, 2017.

- Elena Graverini: Semi-tauonic physics at LHCb
  Miami Conference on Elementary Particles, Astrophysics and Cosmology, Miami, Florida, USA, December 14 – 20, 2016, proceedings to be published in JPCS.

- Katharina Müller: Heavy Flavour and Quarkonia Production at LHCb
  Kruger2016 - Workshop on Discovery Physics at the LHC, Mpumulanga, South Africa, December 4 – 9, 2016, proceedings to be published in JPCS (https://cds.cern.ch/record/2252717).

- Olaf Steinkamp: CP violation in b and c-hadron decays at LHCb
  Kruger2016 - Workshop on Discovery Physics at the LHC, Mpumulanga, South Africa, December 4 – 9, 2016, proceedings to be published in JPCS (https://cds.cern.ch/record/2256913).

- Rafael Silva Coutinho: Heavy flavour spectroscopy at LHCb (including exotic states)
  Kruger2016 – Workshop on Discovery Physics at the LHC, Mpumulanga, South Africa, December 4 – 9, 2016.

- Patrick Haworth Owen: Experimental mini-review on SL decays
  9th International Workshop on the CKM Unitarity Triangle, Mumbai, India, November 28 – December 2, 2016.

- Marcin Chrząszcz: Hunting for New Physics November 24, 2016
  H. Niewodniczanski institute of nuclear physics, Krakow, Poland, November 24, 2016.

- Marcin Chrząszcz: New Physics signatures in Rare Decays from LHCb
  Adelaide university, Adelaide, Australia, October 25, 2016.

- Barbara Storaci: Tracking, calibration and alignment, and data processing in the LHCb upgrade
  VERTEX 2016, La Biodola, Italy, September 25 – 30, 2016.

- Marcin Chrząszcz: Quark flavour anomalies of the SM
  12th Quark Confinement and the Hadron Spectrum, Thessaloniki, Greece, August 29 – September 2, 2016.

- Patrick Haworth Owen: Rare B decays in the HL-LHC era
  Heavy Flavour physics at HL-LHC, Meyrin, Switzerland, August 31, 2016.

- Rafael Silva Coutinho: Charm, bottom and top production in the forward region
  QCD@LHC International Conference, Zurich, Switzerland, August 22 – 26, 2016.

- Katharina Müller: Impact of LHC measurements on parton density functions
  QCD@LHC International Conference, Zurich, Switzerland, August 22 – 26, 2016.

- Marcin Chrząszcz: Search for massive neutrinos at LHCb and discovery potential of the FCC
  International Workshop on Neutrino Factories, Super Beams and Beta Beams , Quy Nhon, Vietnam, August 21 – 27, 2016.

- Federica Lionetto: Test of lepton flavour universality at LHCb
  International Workshop on Neutrino Factories, Super Beams and Beta Beams , Quy Nhon, Vietnam, August 21 – 27, 2016.

- Marcin Chrząszcz: Anomalies in electroweak penguins at LHCb
  Meson-Nucleon Physics and the Structure of the Nucleon, Kyoto, Japan, July 25 – 30, 2016.

- Espen Eie Bowen: Rare semileptonic b-hadron decays at LHCb
  The 24th International Conference on Supersymmetry and Unification of Fundamental Interactions, Melbourne, Australia, July 3 – 8, 2016.

- Rafael Silva Coutinho: Rare decays at LHCb
  BEACH 2016: XIIth International Conference on Beauty, Charm, and Hyperons in Hadronic Interactions, Fairfax, Virginia, United States Of America, June 12 – 18, 2016.

- Katharina Müller: Impact of LHC measurements on parton density functions
  4th Conference on Large Hadron Collider Physics 2016 (LHCP 2016), Lund, Sweden, June 13 – 18, 2016.

- Rafael Silva Coutinho: Experimental review of three-body hadronic B-meson decays
  14th Conference on Flavor Physics and CP Violation, Pasadena, California, USA, June 6 – 9, 2016.

- Marcin Chrzaszc: Overview of LHCb results
  Collider Physics. 2nd Symposium of the Division for Physics of Fundamental Interactions of the Polish Physical Society , Katowice, Poland, May 13 – 15, 2016.

- Marcin Chrzaszc: Overview of recent experimental results in flavour physics
  Standard Model at LHC 2016, Pittsburgh, United States Of America, May 3 – 6, 2016.

- Christopher Betancourt: Radiation Damage in Silicon Detectors
  Zurich seminar, Zurich, April 25, 2016.

- Rafael Silva Coutinho: Additional measurements [ideas] of LF(U,v) tests at LHCb using Run-I and II data
  Rare B decays: theory and Experiment workshop, Barcelona, Spain, April 18 – 20, 2016.

- Katharina Müller: QCD at colliders
  24th International Workshop on Deep Inelastic Scattering and related subjects, Hamburg, Germany, April 11 – 15, 2016, Proceedings published PoS DIS **2016** (2016) 004.

- Barbara Storaci: LHCb measurements at 13 TeV with online data analysis exploiting new trigger and real time alignment and calibration
  LHC Ski 2016, Obergurgl, Austria, April 10 – 15, 2016.

20.2 Condensed matter

20.2.1 Condensed matter theory group

Articles

- Hallmarks of Hund's coupling in the Mott insulator Ca_2RuO_4
  D. Sutter, C.G. Fatuzzo, S. Moser, M. Kim, R. Fittipaldi, A. Vecchione, V. Granata, Y. Sassa, F. Cossalter, G. Gatti, M. Grioni, H.M. Ronnow, N.C. Plumb, C.E. Matt, M. Shi, M. Hoesch, T.K. Kim, T.R. Chang, H.T. Jeng, C. Jozwiak, A. Bostwick, E. Rotenberg, A. Georges, T. Neupert, J. Chang, Nature Comm. (2017).

- Suppression of magnetic excitations near the surface of the topological Kondo insulator SmB_6
  P. K. Biswas, M. Legner, G. Balakrishnan, M. Ciomaga Hatnean, M. R. Lees, D. McK. Paul, E. Pomjakushina, T. Prokscha, A. Suter, T. Neupert, and Z. Salman, Phys. Rev. B **95**, 020410(R) (2016).

- Topological Nonsymmorphic Metals from Band Inversion
  L. Muechler, A. Alexandradinata, T. Neupert, R. Car, Phys. Rev. X **6**, 041069 (2016).

- Robust spin-polarized midgap states at step edges of topological crystalline insulators
  P. Sessi, D. Di Sante, A. Szczerbakow, F. Glott, S. Wilfert, H. Schmidt, T. Bathon, P. Dziawa, M. Greiter, T. Neupert, G. Sangiovanni, T. Story, R. Thomale, M. Bode, Science **354**, 1269-1273 (2016).

- Density wave instabilities and surface state evolution in interacting Weyl semimetals
  M. Laubach, C. Platt, R. Thomale, T. Neupert, S. Rachel, Phys. Rev. B **94**, 241102(R) (2016).

- No-Go Theorem for Boson Condensation in Topologically Ordered Quantum Liquids
  T. Neupert, H. He, C. von Keyserlingk, G. Sierra, A. Bernevig, New Journal of Physics **18**, 123009 (2016).

Invited conference talks and colloquia

- Titus Neupert: Shiba lattices as novel platforms for topological superconductivity
  March Meeting of the American Physical Society, March 13 – 17, 2017, New Orleans, USA.
- Titus Neupert: Exotic fermions in topological metals
  Workshop on geometry in correlated quantum systems, August 22 – 25, 2017, Banff, Canada.
- Titus Neupert: Edge states of three-dimensional topological insulators
  Freie Universitaet Berlin, January 23, 2017, Berlin, Germany.
- Titus Neupert: Edge states of three-dimensional topological insulators
  University of Cologne, December 7, 2016, Cologne, Germany.
- Ashley Cook: Design Principles of Shift Current Photovoltaics
  University of Alberta, January 26, 2017, Alberta, Canada.

Invited lectures

- Titus Neupert: A cosmos of emergent particles in crystalline solids
  Inaugural lecture, University of Zurich, February 20, 2017, Zurich.
- Titus Neupert: Axiomatic topological quantum field theory
  School on Entanglement in Strongly Correlated Systems, February 6 – 17, 2017, Benasque, Spain.
- Titus Neupert: Interacting topological phases of matter
  3rd International Fall School Tocotronics2016, October 3 – 7, 2016, Wuerzburg, Germany.
- Titus Neupert: Floquet topological insulators
  Topological Matter School, August 22 – 26, 2016, Donostia-San Sebastian, Spain.

Posters and oral presentations

- Ashley Cook: Design Principles of Shift Current Photovoltaics
  3rd International Fall School Tocotronics2016, October 3 – 7, 2016, Wuerzburg, Germany (poster).
- Frank Schindler: Higher-order topological insulators
  MaNEP Workshop on Topological Quantum Phenomena, November 21 – 22, 2016, Zurich, Switzerland (poster).
- Seulgi Ok: Magnetic Weyl and Dirac Kondo semimetal phases in heterostructures
  MaNEP Workshop on Topological Quantum Phenomena, November 21 – 22, 2016, Zurich, Switzerland (poster).
- Frank Schindler: Higher-order topological insulators
  34th Jerusalem Winter School, December 27 – January 5, 2017, Jerusalem, Israel (poster).
- Ashley Cook: Design Principles of Shift Current Photovoltaics
  Topological Metamaterials conference, Aspen Center for Physics, January 2 – 8 2017, Aspen, CO, USA (poster).
- Frank Schindler: Higher-order topological insulators
  Workshop Entanglement in Strongly Correlated Systems, February 5 – 18, 2017, Benasque, Spain.
- Ashley Cook: Design Principles of Shift Current Photovoltaics
  Quantum Dynamics: From Models to Materials, Aspen Center for Physics, January 15 – 21 2017, Aspen, CO, USA (poster).
- Ashley Cook: Topological gapped edge states in fractional quantum Hall-superconductor heterostructures
  March Meeting of the American Physical Society, March 13 – 17, 2017, New Orleans, USA.
- Seulgi Ok: Magnetic Weyl and Dirac Kondo semimetal phases in heterostructures
  March Meeting of the American Physical Society, March 13 – 17, 2017, New Orleans, USA.
- Frank Schindler: Higher-order topological insulators
  March Meeting of the American Physical Society, March 13 – 17, 2017, New Orleans, USA.

20.2.2 Superconductivity and Magnetism

Articles

- Magnetic field controlled charge density wave coupling in underdoped $YBa_2Cu_3O_{6+x}$
  J. Chang, E. Blackburn, O. Ivashko, A. T. Holmes, N. B. Christensen, M. Hücker, Ruixing Liang, D. A. Bonn, W. N. Hardy, U. Rütt, M. v. Zimmermann, E. M. Forgan and S. M. Hayden, Nature Communications **7** 11494 (2016)

- Hallmarks of Hund's coupling in the Mott insulator Ca_2RuO_4
  D. Sutter, C.G. Fatuzzo, S. Moser, M. Kim, R. Fittipaldi, A. Vecchione, V. Granata, Y. Sassa, F. Cossalter, G. Gatti, M. Grioni, H.M. Ronnow, N.C. Plumb, C.E. Matt, M. Shi, M. Hoesch, T.K. Kim, T.R. Chang, H.T. Jeng, C. Jozwiak, A. Bostwick, E. Rotenberg, A. Georges, T. Neupert, J. Chang, arXiv:1610.02854 (Accepted in Nature Communications 2017)

- Damped spin-excitations in a doped cuprate superconductor with orbital hybridization
  O. Ivashko, N. E. Shaik, X. Lu, C. G. Fatuzzo, M. Dantz, P. G. Freeman, D. E. McNally, D. Destraz, N. B. Christensen, T. Kurosawa, N. Momono, M. Oda, C. Monney, H. M. Rønnow, T. Schmitt, J. Chang, arXiv:1702.02782

Conference contributions

- Christian Matt: $NaFe_{0.56}Cu_{0.44}As$: A pnictide insulating phase induced by on-site Coulomb interaction
  March Meeting American Physical Society, 13. – 17. March 2017, New Orleans, Louisiana, USA.

- Johan Chang: Diffraction in Pulsed-Magnetic Fields: Problem solver for Superconductors
  Satellite meeting to the European XFEL Users meeting, 24 January 2017, Hamburg, Germany .

- Denys Sutter: Twofold insulating energy scales in the Mott-insulator Ca_2RuO_4
  SPS Jahrestagung, 25. August 2016, Lugano, Switzerland.

- Johan Chang: Magnetic-field control of high-temperature superconductivity and charge order
  MaNEP meeting, 6. – 9. July 2016, Les Diableret, Switzerland .

- Johan Chang: Magnetic-field control of high-temperature superconductivity and charge order
  Spectroscopies in Novel Superconductors (SNS2016), 19. – 24. June 2016, Stuttgart.

- Johan Chang: Magnetic-field control of high-temperature superconductivity and charge order
  International workshop (SCHTC16), 23. –27. May 2016, Dresden.

- Johan Chang: Magnetic-field control of high-temperature superconductivity and charge order
  Probing Superconductivity at the Nanoscale, 15. – 18. April 2016, Saas Fee, Switzerland.

20.2.3 Phase transitions and superconducting photon detectors

Articles

- Tuning the critical magnetic field of the triplon Bose-Einstein condensation in $Ba_{3-x}Sr_xCr_2O_8$
  H. Grundmann, A. Gazizulina, F. von Rohr, L. Peters, T. Förster and, A. Schilling, New. J. Phys. **18** (2016) 033001.

- Cobalt complexes of tetradentate, bipyridine-based macrocycles: their structures, properties and photocatalytic proton reduction
  E. Joliat, S. Schnidrig, B. Probst, C. Bachmann, B. Spingler, K.K. Baldridge, F. von Rohr, A. Schilling and R. Alberto, Dalton Trans. **45** (2016) 1737.

- Field-induced transition of the magnetic ground state from A-type antiferromagnetic to ferromagnetic order in $CsCo_2Se_2$
  F. von Rohr, A. Krzton-Maziopa, V.Yu. Pomjakushin, H. Grundmann, Z. Guguchia, W. Schnick, and A. Schilling, J. Phys.: Condensed Matter. **28** (2016) 276001.

- Characteristics of superconducting tungsten silicide W_xSi_{1-x} for single photon detection
  X. Zhang, A. Engel, Q. Wang, A. Schilling, A. Semenov, M. Sidorova, H.-W. Hübers, I. Charaev, K. Ilin, and M. Siegel,
  Phys. Rev. B **94** (2016) 174509.

- Superconducting single X-ray photon detector based on $W_{0.8}Si_{0.2}$
  X. Zhang, Q. Wang, and A. Schilling, AIP Advances **6** (2016) 115104.

Conference contributions

- Q. Wang: Position dependent detection efficiency in NbN SSPDs
  Workshop of Nanowire Superconducting Single Photon Detectors, 28.November – 1. December 2016, Leiden (NL).

- X. Zhang: Superconducting nanowire single X-ray photon detectors based on WSi (Poster)
  Workshop of Nanowire Superconducting Single Photon Detectors, 28. November – 1.December 2016, Leiden (NL).

- A. Gazizulina: Magnetic excitations in the spin-dimer system $Ba_{0.1}Sr_{2.9}Cr_2O_8$
  Helmholtz Zentrum HZB User Meeting, 7. – 10. December 2016, Berlin, Germany.

- X. Zhang: Hotspot dynamics in WSi materials
  Workshop of Nanowire Superconducting Single Photon Detectors, 28. November – 1. December 2016, Leiden (NL).

- Q.Wang: Local response of a superconducting nanowire single-photon detector (Poster)
  Single Photons Single Spins (SPSS) Meeting, 12. – 13. September 2016, Oxford University, UK.

- X. Zhang: Hotspot dynamics of Superconducting Nanowire Single Photon Detectors
  Applied Superconductivity Conference, 4. – 9. September 2016, Denver CO (U.S.A.).

- A. Gazizulina: Study of the Magnetic Excitations in the Dimer Compound $Ba_{3-x}Sr_xCr_2O_8$
  SPS Annual meeting, 23. – 25. August 2016, Lugano, Switzerland.

- A. Gazizulina: Study of the Magnetic Excitations in the Dimer Compound $Ba_{3-x}Sr_xCr_2O_8$ (Poster)
  Workshop MaNEP, 6. – 8. July 2016, Les Diablerets, Switzerland.

20.2.4 Surface Physics

Articles

- Circular Dichroism in Cu Resonant Auger Electron Diffraction
  F. Matsui, N. Maejima, Hirosuke Matsui, H. Nishikawa, H. Daimon, T. Matsushita, M, Muntwiler, R. Stania, T. Greber, Z. Phys. Chemie, 230, 519 (2016)

- Self-assembly of nanoscale lateral segregation profiles
  R. Stania, W. Heckel, I. Kalichava, C. Bernard, T. C. Kerscher, H. Y. Cun, P. R. Willmott, B. Schönfeld, J. Osterwalder, S. Müller, and T. Greber, Phys. Rev. B 93, 161402 (2016)

- Sputtering-induced reemergence of the topological surface state in Bi2Se3
  R. Queiroz, G. Landolt, S. Muff, B. Slomski, T. Schmitt, V. N. Strocov, J. Mi, B. Brummerstedt Iversen, P. Hofmann, J. Osterwalder, A. P. Schnyder, and J. H. Dil, Phys. Rev. B 93, 165409 (2016)

- Switching stiction and adhesion of a liquid on a solid
  S. F. L. Mertens, A. Hemmi, S. Muff. O. Gröning, S. De Feyter, J. Osterwalder and T. Greber, Nature 534, 676 (2016)

- Access to phases of coherent phonon excitations by femtosecond ultraviolet photoelectron diffraction
  M. Greif, L. Kasmi, L. Castiglioni, M. Lucchini, L. Gallmann, U. Keller, J. Osterwalder, and M. Hengsberger, Phys. Rev. B 94, 054309 (2016)

- Application of iterative phase-retrieval algorithms to ARPES orbital tomography
  P. Kliuiev, T. Latychevskaia, J. Osterwalder, M. Hengsberger and L. Castiglioni, New J. Phys. 18, 093041 (2016)

- Triangular Monometallic Cyanide Cluster Entrapped in Carbon Cage with Geometry-Dependent Molecular Magnetism
  F. Liu, C-L. Gao, Q. Deng, X. Zhu, A. Kostanyan, R. Westerström, S. Wang, Y-Z. Tan, J. Tao, S-Y. Xie, A. Popov, T. Greber, and SF. Yang, J. Am. Chem. Soc. 138, 14764 (2016)

- Delayed electron emission in strong-field driven tunnelling from a metallic nanotip in the multi-electron regime
H. Yanagisawa, S. Schnepp, C. Hafner, M. Hengsberger, D. E. Kim, M. F. Kling, A. Landsman, L. Gallmann, J. Osterwalder, Sci. Rep. 6, 35877 (2016)

- Laser-induced asymmetric faceting and growth of a nano-protrusion on a tungsten tip
H. Yanagisawa, V. Zadin, K. Kunze, C. Hafner, A. Aabloo, D. E. Kim, M. F. Kling, F. Djurabekova, J. Osterwalder, and W. Wuensch, APL Photonics 1, 091305 (2016)

- Some Like It Flat: Decoupled h-BN MonolayerSubstrates for Aligned Graphene Growth
S. Roth, T. Greber and J. Osterwalder, ACS Nano 10, 11187 (2016)

- Subsurface Oxygen in Oxide-Derived Copper Electrocatalysts for Carbon Dioxide Reduction
A. Eilert, F. Cavalca, F. S. Roberts , J. Osterwalder, C. Liu, M. Favaro, E. J. Crumlin, H. Ogasawara, D. Friebel, L. G. M. Pettersson, and A. Nilsson, J. Phys. Chem. Lett. 8, 285 (2016)

- Mononuclear Clusterfullerene Single-Molecule Magnet Containing Strained Fused-Pentagons Stabilized by a Nearly Linear Metal Cyanide Cluster
F. Liu, S. Wang, C-.L Gao, Q. Deng, X. Zhu, A. Kostanyan, R. Westerström, F. Jin, S-Y. Xie, A. A. Popov, T. Greber and S. Yang, Angew. Chem. Int. Ed. 56, 1830 (2017)

- Surface science at the PEARL beamline of the Swiss Light Source
M. Muntwiler, J. Zhang, R. Stania, F. Matsui, P. Oberta, U. Flechsig, L. Patthey, C.Quitmann, T. Glatzel, R. Widmer, E. Meyer, T. A. Jung, P. Aebi, R. Fasel and T. Greber, J. Synchrotron Rad. 24, 354 (2017)

- Sensitivity of photoelectron diffraction to conformational changes of adsorbed molecules: Tetra-tert-butyl-azobenzene/Au(111)
A. Schuler, M. Greif, A. P. Seitsonen, G. Mette, L. Castiglioni, J. Osterwalder and M. Hengsberger,
Struct. Dyn. 4, 015101 (2017)

- Reading and writing single-atom magnets
F.D. Natterer, K. Yang, W. Paul, P. Willke, T. Choi, T. Greber, A.J. Heinrich and C.P. Lutz, Nature 354, 226 (2017)

Contributed conference presentations

- L. Castiglioni: Accessing the photoemission phase by attosecond interferometry (Poster)
PLESI 16 Focus Workshop, Max Planck Institute for the Physics of Complex Systems, Dresden, Germany, 26.04.2016.

- P. Kliuiev: Phase retrieval problem in molecular wave function imaging (Poster)
PLESI 16 Focus Workshop, Max Planck Institute for the Physics of Complex Systems, Dresden, Germany, 26.04.2016.

- W.-D. Zabka: Wet-chemical deposition of Re-photosensitizers on alumina/NiAl(110)
11th MOLCH discussion, Bern, Switzerland, 13.06.2016.

- P. Kliuiev: Phase problem in photoemission-based imaging of molecular wave functions (Poster)
Local 3D atomic and electronic structure imaging of functionally active sites, Satellite workshop of VUVX 2017, Zurich, Switzerland, 01.07.2016.

- C. Monney: Transient band gap enhancement in the excitonic insulator phase of Ta2NiSe5 upon photoexcitation
39th International conference on Vacuum Ultraviolet and X-ray Physics (VUVX), Zurich, Switzerland, 03.07.2016.

- W.-D. Zabka: Electron spectroscopy on thin oxide films: Crystalline alumina of variablethickness on NiAl(110) (Poster)
39th International conference on Vacuum Ultraviolet and X-ray Physics (VUVX), Zurich, Switzerland, 04.07.2016.

- L. Castiglioni: Final state effects in attosecond photoemission from solids (Poster)
39th International conference on Vacuum Ultraviolet and X-ray Physics (VUVX), Zurich, Switzerland, 04.07.2016.

- K. Waltar: Investigations on the adsorption geometry of CO adsorbed on Pt(111) (Poster)
39th International conference on Vacuum Ultraviolet and X-ray Physics (VUVX), Zurich, Switzerland, 04.07.2016.

- A. Kostanyan: Investigation of magnetic properties of R1M2N@C80 (R = Dy, Tb, Ho; M = Sc, Lu) endohedral metallofullerenes by means of X-ray magnetic circular dichroism (XMCD) and SQUID magnetometry (Poster)
39th International conference on Vacuum Ultraviolet and X-ray Physics (VUVX), Zurich, Switzerland, 04.07.2016.

- A. Schuler: Sensitivity of photoelectron diffraction to conformational changes of adsorbed molecules: Tetra-tert-butyl-azobenzene/Au(111) (Poster)
  39th International conference on Vacuum Ultraviolet and X-ray Physics (VUVX), Zurich, Switzerland, 04.07.2016.

- D. Leuenberger: Ultrafast dehybridisation between f- and d-states in a Heavy-Fermion System
  39th International conference on Vacuum Ultraviolet and X-ray Physics (VUVX), Zurich, Switzerland, 04.07.2016.

- P. Kliuiev: Reconstruction of molecular wave functions from angle-resolved photoemission data
  39th International conference on Vacuum Ultraviolet and X-ray Physics (VUVX), Zurich, Switzerland, 05.07.2016.

- M. Hengsberger: Study of structural dynamics by means of time- and angle-resolved photoelectron spectroscopy and diffraction
  39th International conference on Vacuum Ultraviolet and X-ray Physics (VUVX), Zurich, Switzerland, 06.07.2016.

- A. Kostanyan: Switching the molecular conformation of endohedral single-molecule magnets using magnetic torque
  SPS meeting, Lugano, Switzerland, 23.08.2016.

- C. Bernard: Single-Domain Transfer and Stacking of sp^2-Layers on a 4inch-Scale
  SPS meeting, Lugano, Switzerland, 24.08.2016.

- J. Osterwalder: Adsorption studies of molecular catalysts and photosesitizers on metal oxide surfaces
  Symposium and Summer School: Solar Light to Chemical Energy Conversion, Les Diablerets, Switzerland, 29.08.2016.

- D. Leuenberger: Band Bending Effects and Atomically Resolved Charge Transfer in a Photocatalytic Heterojunction (Poster)
  Symposium and Summer School: Solar Light to Chemical Energy Conversion, Les Diablerets, Switzerland, 30.08.2016.

- W.-D. Zabka: Electron Dynamics in Re-photosensitizers on thin Alumina Films (Poster)
  Symposium and Summer School: Solar Light to Chemical Energy Conversion, Les Diablerets, Switzerland, 31.08.2016.

- P. Kliuiev: Reconstruction of molecular wave functions from angle-resolved photoemission data (Poster)
  International Science@FELs Conference, Trieste, Italy, 05.09.2016.

- H.Y. Cun: Nanotents - 2nm void-formation and self-healing in 2D monolayers on metals
  TNT Conference Fribourg, Switzerland, 08.09.2016.

- C. Monney: Transient band gap enhancement in the excitonic insulator phase of Ta2NiSe5 upon photoexcitation
  2nd Workshop on Ultrafast Dynamics in Strongly correlated Systems, PSI, Villigen, Switzerland, 10.10.2016.

- H.Y. Cun: Nanotents and 2nm void-formation in 2D materials
  SICC9 Conference Singapore, Singapore, 14.12.2016.

- W.-D. Zabka: Ultrathin Alumina on NiAl(110): Functionalization with Self-Assembled Monolayers
  33rd SAOG Meeting, Fribourg, Switzerland, 27.01.2017.

- A. Hemmi: Shedding light on large molecule assisted wet transfer of single orientation single layer CVD boron nitride
  Workshop on synthetic methods across the flagship, Tenerife, Spain, 07.02.2017.

- T. Greber: 4f Single Molecule Magnets
  32nd High Tc Workshop on Novel Materials and Superconductivity , Obertraun, Austria, 17.02.2017.

- T. Greber: Interaction across a single layer of carbon (Poster)
  3S - Symposium on Surface Science 2017, St. Moritz, Switzerland, 07.03.2017.

- L. Castiglioni: Direct reconstruction of molecular wave functions by ARPES orbital tomography
  3S - Symposium on Surface Science 2017, St. Moritz, Switzerland, 09.03.2017.

- A. Kostanyan: Changing the Molecular Conformation of Endohedral Rare Earth Single-Molecule Magnets with Magnetic Torque
  DPG Tagung, Dresden, Germany, 21.03.2017.

Invited lectures

- C. Monney: Probing the out-of-off-equilibrium dynamics of an exciton condensate
  Probing Superconductivity at the Nanoscale, COST meeting Saas-Fee, Switzerland, 03.04.2016.
- J. Osterwalder: Photoelectron diffraction and holography; Hard x-ray photoelectron spectroscopy and ambient pressure XPS
  3 hours lecture, School on Synchrotron and Free Electron Laser Based Methods: Multidisciplinary Applications and Perspectives, ICTP Trieste, Italy, 12.04.2016.
- T. Greber: One layer of Boron Nitride on Rhodium: From Nanomesh to Nanotents
  IBS Center for Multidimensional Carbon Materials (CMCM), Ulsan, South Korea, 13.04.2016.
- T. Greber: The electronic structure of single layer h-BN and graphene on transition metals: From Nanomesh to quantum dots
  Center for Artificial Low Dimensional Electronic Systems Institute for Basic Science (POSTECH Campus), CALDES Seminar, Pohang, South Korea, 15.04.2016.
- C. Monney: Looking for a realization of the excitonic insulator phase in low-dimensional crystals
  Photon Science Seminar, PSI, Villigen, Switzerland, 15.04.2016.
- T. Greber: Bottom-up nanoscience: From nano-tents to endohedral Fullerenes
  1st workshop on Quantum Nanosciences at EWHA University, Seoul, South Korea, 19.04.2016.
- T. Greber: Accessing the magnetic content of endohedral Fullerenes
  Korean physical society (KPS) Meeting, Daejong, South Korea, 21.04.2016.

- J. Osterwalder: Final state scattering in electronic structure imaging by ARPES
  Workshop on Prospects and Limitations of Electronic structure imaging by ARPES, MPI Physik komplexer Systeme, Dresden, Germany, 25.04.2016.
- T. Greber: From Nanomesh in the vacuum to smart membranes in liquids
  HKUST Seminar, Hong Kong, China, 25.04.2016.
- T. Greber: 4f single molecule magnets in Fullerenes
  Jeffrey Long Group Seminar, U Berkeley, U.S.A., 03.06.2016.
- T. Greber: Magnets inside C_{80}
  Seminar U. Lincoln, Nebraska, U.S.A., 08.06.2016
- J. Osterwalder: Ultrafast electron dynamics and scattering
  Conference on 'The future of x-ray and Electron Spectroscopy", Uppsala, Sweden, 15.06.2016.
- T. Greber: Looking inside magnetic Endofullerenes with x-rays
  Seminar LBNL, Berkeley, U.S.A., 15.06.2016.
- T. Greber: From Double-deckers to Spin-shuttles: 4f Single Molecule magnets
  Seminar U Stanford, Stanford, U.S.A., 23.06.2016
- T. Greber: Single layer boron nitride: From Nanomesh in the vacuum to smart membranes in liquids
  Ames Lab NASA, Moffett Field, U.S.A., 25.06.2016.
- R. Stania:: Conformational changes in TbSc2N@C80 on h-BN/Ni(111)
  POSTECH, Pohang, South Korea., 02.08.2016.
- C. Monney: How fast can we close the gap, and how fast does it recover?
  TNT Conference, Fribourg, Switzerland, 08.09.2016.
- T. Greber: Single layer boron nitride: From Nanomesh to smart membranes in liquids
  TNT Conference, Fribourg, Switzerland, 08.09.2016.

- T. Greber: Building blocks for molecular spintronics: Endohedral rare earth single molecule magnets?
  Workshop on experimental Physics, EWHA University, Seoul, South Korea, 31.10.2016.
- T. Greber: Hexagonales Bornitrid: Eine dünnst mögliche zweidimensionale Membran
  Kolloquium GDCh, Hanover, 10.11.2016.
- Z. Novotny: Model catalytic oxide systems: From clusters to single atoms
  CEITEC Nano user meeting, Brno, Czech Republic, 01.12.2017.
- L. Castiglioni: Attosecond delays in valence band photoemission from metals
  International Workshop on Atomic Physics, Max Planck Institute for the Physics of Complex Systems, Dresden, Germany, 01.12.2016.
- T. Greber: Changing molecular conformation with magnetic torque
  SSNS Conference, Furano, Japan, 14.01.2017.
- C. Monney: RIXS as a tool to measure short-range magnetic order
  Spectroscopy of Novel Materials, Group Workshop, Saas-Grund, Switzerland, 15.01.2017.
- C. Monney: Time-resolved photoemission of ordered phases in low dimnsional materials
  21st Hiroshima international symposium on synchrotron radiation, Hiroshima, Japan, 03.03.2017.

20.2.5 Biological systems

Articles

- Imaging proteins at the single molecule level
  J.-N. Longchamp, S. Rauschenbach, S. Abb, C. Escher, T. Latychevskaia, K. Kern and H.-W. Fink,
  PNAS 114(7), 1474 - 1479 (2017).
- Application of iterative phase-retrieval algorithms to ARPES orbital tomography
  P. Kliuiev, T. Latychevskaia, J. Osterwalder, M. Hengsberger and L. Castiglioni,
  New Journal of Physics 18, 093041 (2016).
- Direct observation of individual charges and their dynamics on graphene by low-energy electron holography
  T. Latychevskaia, F. Wicki, J.-N. Longchamp, C. Escher and H.-W. Fink, Nano Letters 16 (9), 5469 - 5474 (2016).
- Resolution enhancement by extrapolation of coherent diffraction images: a quantitative study about the limits and a numerical study of non-binary and phase objects
  T. Latychevskaia, Y. Chushkin and H.-W. Fink, Journal of Microscopy 264 (1), 3 - 13 (2016).
- Mapping unoccupied electronic states of freestanding graphene by angle-resolved low-energy electron transmission
  F. Wicki, J.-N. Longchamp, T. Latychevskaia, C. Escher, H.-W. Fink, Phys. Rev. B **94** (7), 075424 (2016).
- Creating Airy beams employing a transmissive spatial light modulator
  T. Latychevskaia, D. Schachtler and H.-W. Fink, Applied Optics 55 (22), 6095 - 6101 (2016).
- Inverted Gabor holography principle for tailoring arbitrary shaped three-dimensional beams
  T. Latychevskaia and H.-W. Fink, Scientific Reports 6, 26312 (2016).

Patents

- Method and apparatus for imaging single molecules
  Inventors: Jean-Nicolas Longchamp, Conrad Escher, Hans-Werner Fink
  PCT application number: PCT/EP2016/065222, June 29th, 2016.

Invited talks

- Jean-Nicolas Longchamp: Imaging Single Proteins
  Seminar for Professorship Position, EPFL, Lausanne, Switzerland February 2nd, 2017.

- Jean-Nicolas Longchamp: Imaging Single Proteins
  Free-Space Quantum Electron Optics, Half Moon Bay, USA, October 14-15, 2016.

- Jean-Nicolas Longchamp: Imaging Single Proteins
  ACS National Meeting, Symposium on Advances in Biological Imaging, Philadelphia, USA, August 21-25, 2016.

- Jean-Nicolas Longchamp: Imaging Single Proteins
  Seminar in Structural Biology, SGC Oxford, United Kingdom, June 1st, 2016.

- Jean-Nicolas Longchamp: Imaging Single Proteins
  Seminar in Physics, EPFL, Lausanne, Switzerland, May 12, 2016.

- Jean-Nicolas Longchamp: Imaging Single Proteins
  Seminar in Structural Biology, University of Pavia, Pavia, Italy, April 15, 2016.

- Tatiana Latychevskaia: Coherent imaging with low-energy electrons (30 - 250 eV): Imaging charged impurities and three-dimensional topography of graphene
  Electron Holography Workshop organized by the Japanese government at the Hitachi facility, Tokyo, Japan, February 2017.

- Hans-Werner Fink: Holography with Low-Energy Electrons: A Tool for Single Molecule Structural Biology
  Molecular Nanosystems, Congressi Stefano Franscini, Monte Verità, Ascona, March 5-10, 2017.

Poster Presentations

- Marianna Lorenzo: Investigation of alkali metal adsorption on freestanding graphene
  European Graphene Forum 2016, Paris, France, June 01-03, 2016.

- Marianna Lorenzo: Low -energy electron point source microscopy
  Graphene 2016 Conference, Genova, Italy, April 19-22, 2016.

- Flavio Wicki: Visualization of unoccupied states in the electronic structure of freestanding graphene by means of LEEPS microscopy
  Graphene 2016 Conference, Genova, Italy, April 19-22, 2016.

20.2.6 Disordered and Biological Soft Matter

Articles

- Can Anderson localization of light be reached with white paint?
  T. Sperling, L. Schertel, M. Ackermann, G. Aubry, C.M. Aegerter, and G. Maret, New Journal of Physics, **18** 013039 (2016).

- SnapShot: Mechanical forces in Development I
  L. Pasakarnis, D.Dreher, and D. Brunner, Cell **165** 754 (2016).

- SnapShot: Mechanical forces in Development II
  D.Dreher, L. Pasakarnis, and D. Brunner, Cell **165** 1028 (2016).

- Looking Beyond the Genes: The Interplay Between Signaling Pathways and Mechanics in the Shaping and Diversification of Epithelial Tissues.
  S. Urdy, N. Goudemand, and S. Pantalacci, Current Topics in Developmental Biology **119** 227 (2016).

- Structured illumination behind turbid media.
  A. Malavalli, M. Ackermann, and C.M. Aegerter, Opt. Exp. **24** 23018 (2016).

- Mechanical forces in organ growth
  D. Eder, C.M. Aegerter, and K. Basler, Mech. Dev. **144** 53 (2017).

Articles in press

- Faraday-Effect in multiply scattered light
  L. Schertel, M. Ackermann, G. Aubry, C.M. Aegerter, and G. Maret, Europ. Phys J. E (2017).

Conference reports

- P. Dagenais: Determining forces from hydrodynamic flows
  Fluid Mechanics and Collective Behavior: "From Cells to Organisms", Monte Verità, Ascona, Switzerland, April 2 - 7, 2016.

- F. Atzeni: Modelling active contractions in a multicellular embryonic tissue
  Summer School on Biomechanics of Soft Tissue: "Multiscale Modeling, Simulation and Application", Graz University of Technology, July 4-8th, 2016.

- S. Puri: Determining the mechanical properties of zebrafish caudal fins
  Sinergia retreat, Olten, Switzerland, September 1, 2016.

- P. Dagenais: Determining forces from hydrodynamic flows
  Sinergia retreat, Olten, Switzerland, September 1, 2016.

- S. Urdy: Phenoid3D: a high-throughput image-processing tool to quantify organoid phenotypes in 3D in vitro culture using spinning disk confocal microscopy
  EMBL conference: "Organoids: Modelling Organ Development and Disease in 3D Culture", Heidelberg, Germany, October 12 - 15, 2016.

- J. Schneider: Dynamic light sheet generation in turbis tssue
  Biomedical Optics and Photonics Network Meeting, USZ, Zurich, Switzerland, November 28, 2016 (Poster).

- A. Malavalli: Structured illumination behind turbid media
  Biomedical Optics and Photonics Network Meeting, USZ, Zurich, Switzerland, November 28, 2016 (Poster).

- F. Atzeni: Mechanochemical modelling as an eplorative tool to study Drosophila dorsal closur
  Biology for Physics: "Is there new physics in living matter?", Barcelona Biomedical Research Park (PRBB), January 15-18th, 2017 (Poster).

- F. Atzeni: Mechanochemical modelling as an explorative tool to study Drosophila dorsal closure
  IMLS Retreat 2017, Emmetten, January 18-20th, 2017.

- D. Dreher: SPIM of whole Drosophila embryos
  IMLS Retreat 2017, Emmetten, January 18-20th, 2017 (Poster).

Invited lectures

- C.M. Aegerter: Scaling and dimensional analysis in Biology
  Course in Plant and Animal development, ENS, Lyon, 25. May 2016.

- C.M. Aegerter: Mechanical forces in Development
  Developmental Biology seminar, ENS, Lyon, 25. May 2016.

- C.M. Aegerter: Quattro Staggioni, Frühling und Sommer
  Theater am Rigiblick, Zurich, 17. June 2016.

- C.M. Aegerter: Biological Physics and Physical Biology
  Biophysics Minisymposium, UZH, Zurich, 23. June 2016.

- C.M. Aegerter: Quattro Staggioni, Herbst und Winter
  Theater am Rigiblick, Zurich, 24. June 2016.

- C.M. Aegerter: Force Measurement and Mechanical Properties in the Wing Disc
  KITP Programme "From Genes to Growth and Form", Santa Barbara, USA, 16. August 2016.

- J. Schneider: Fluorescence imaging in biological tissue
  PostDoc Day, Schloss Au, Switzerland, 20. October 2016.

- C.M. Aegerter: Physikalische Weihnachtsvorlesung
  Kinderuniversität Winterthur, Winterthur, Switzerland, 14. December 2016.

- C.M. Aegerter: Molecular force sensors in Drosophila tissues
  Soft matter seminar, University of Konstanz, Konstanz, Germany, 13. January 2017.

- C.M. Aegerter: Firlefax der Wettermacher
  Gemeindezentrum Wipkingen, Zürich, Switzerland, 4. March 2017.

- S. Urdy: From molluscan shell growth to epithelial morphogenesis: the influence of D'Arcy Thompson
  Workshop: "The biological challenges in morphogenesis", Mathematical Biosciences Institute, Ohio, USA, 20. February 2017.

20.3 PhD, Master and Bachelor Theses

20.3.1 PhD Theses

- Heavy-Quark Pair Production at Hadron Collider: Transverse-Momentum Resummation, NNLO Corrections and Azimuthal Asymmetries
  Hayk Sargsyan, PhD thesis, March 2017.

- Tracking and Particle Identification at LHCb and Strange Hadron Production in Events with Z Boson
  Marco Tresch, PhD thesis, February 2017.

- Searching for Dark Matter with XENON100, Research and Development for XENON1T, and Modulating Radioactive Decay Rates
  Peter Barrow, PhD thesis, February 2017.

- Upstream Tracking and the Decay $B^0 \to K^+\pi^-\mu^+\mu^-$ at the LHCb Experiment
  Espen Eie Bowen, PhD thesis, January 2017

- Search for Dark Matter in Association with Top Quarks with the CMS Detector
  Deborah Pinna, PhD thesis, January 2017.

- Photomultiplier Tubes for the XENON1T Dark Matter Experiment and Studies on the XENON100 Electromagnetic Background
  Daniel Mayani Paras, PhD thesis, December 2016.

- Topics in non-perturbative quantum field theory
  Peter Lowdon, PhD thesis, November 2016.

- Mechanical forces in growth regulations - challenging force measurements and force manipulations in the Drosophila wing imaginal disc
  Dominik Eder, PhD Thesis, Universität Zürich, 2016

- Scintillating Fiber Detector for the Mu3e Experiment
  Roman Gredig, PhD thesis, October 2016.

- Precise Predictions for Top-quark Pair Production in Association with Multiple Jets
  Niccolò Moretti, PhD thesis, October 2016.

- Regularization-scheme dependence of QCD amplitudes
  Andrea Visconti, PhD thesis, September 2016.

- Nanotemplates and Conformations of Tri-Metal Endofullerenes on Surfaces
  Roland Stania, PhD thesis, September 2016.

- Four Novel Electron Point Source Applications
  Flavio Wicki, PhD thesis, September 2016.

- Low Mass WIMP Detection with CCDs
  Junhui Liao, PhD thesis, September 2016.

- Top-Bottom Interference for Higgs Production in Gluon Fusion at NLO in QCD
  Gizem Oeztürk, PhD thesis, June 2016.

- Inelastic WIMP-Nucleus Interactions in XENON100 and Cables and Connectors for XENON1T
  Gaudenz Kessler, PhD thesis, June 2016.

20.3.2 Master theses

- Probing Lepton Flavor Universality with $K \to \pi\nu\bar{\nu}$ decays
  Joachim Monnard, Master thesis ETH, March 2017.

- Hydrodynamic analysis of swimming zebrafish in the context of fin regeneration
  Ronny Rüttimann, Master thesis, December 2016.

- Bifold insulating energy scales in the Mott-insulator Ca_2RuO_4
  Denys Sutter, Master thesis, October 2016.

- $U(2)$ flavor symmetry and a general EFT approach to B-decay anomalies
  Sokratis Trifinopoulos, Master thesis ETH, September 2016.

- Automated computation of the muon decay at NLO
  Yannick Ulrich, Master thesis, July 2016.

- Characterization of silicon photomultiplier arrays in liquid xenon and development of dedicated read-out electronics
  Sandro D'Amato, Master thesis, July 2016.

- Measurement of Open Charm and Double Open Charm Production Cross Sections and Ratios in pp Collisions at $\sqrt{s} =$ 2.76 TeV with the LHCb Experiment
  Enzio Crivelli, Master thesis, June 2016.

- Alloying CdTe with Se, a possible route to improve CdTe solar cells
  Annina Spescha, Master thesis, June 2016.

- Electronic and Spatial Structures of Self-Assembled Diamondoid Monolayers
  Markus Baumgartner, Master thesis, June 2016.

- Development of an experimental setup for fluorescence lifetime imaging microscopy using time-corraleted single photon counting technique
  Anna Pataki, Master thesis, May 2016.

20.3.3 Bachelor theses

- Maxwell-Demon experiment for a cyclic 8-box system
  Nicolas Kunz, Bachelor thesis, March 2017.

- Estimation of the Energy Gap of the Spin-1/2 Dimer Compound $Ba_{(3-x)}Sr_{(x)}Cr_2O_8$ from Heat Capacity Measurements
  Michele Masseroni, Bachelor thesis, March 2017.

- Blind Deconvolution of Fluorescence Microscopy Images
  Nicholas LeBow, Bachelor thesis, March 2017.

- Doping Graphene on SiO_2 using X-rays
  Björn Salzmann, Bachelor thesis, February 2017.

- Characterization of the NaI(Tl) detectors for radioactive decay rate modulation search experiment
  Magnus Gienal, Bachelor thesis, February 2017.

- Preparation and Characterization of (Co)Pyr/TiO_2(110) for a Synchrotron Beamtime
  Karin von Arx, Bachelor thesis, December 2016.

- Testing of the Readout Chain and Data Acquisition of the CMS Pixel Upgrade Detector System
  Benno Neuenschwander, Bachelor thesis, December 2016.

- Electronic Level-Alignment and Band-Bending Effects in a Cobalt-Pyrphyrin/Cu_2O(111) Heterojunction for a Photocatalytic Water Reduction Cathode
  Oliver Shah, Bachelor thesis, September 2016.

- Herstellung möglichst perfekter Kupferfilme für Graphen-Wachstum und Untersuchung des Einflusses von Annealing auf deren Oberflächenstruktur
  Laura Stucki, Bachelor thesis, September 2016.

- Aufbau eines Raman-Spektrometers zur Charakterisierung von Graphen
  Hubert Nussbaumer, Bachelor thesis, August 2016.

- Feasibility studies of $B \to K^\star \tau\tau$ decay
  Alexander Dätwyler, Bachelor thesis, July 2016.

- Orbital Selective Mott Physics in Ca_2RuO_4 - An angle resolved photo emission study
  Fabio Cossalter, Bachelor thesis, July 2016.

- Aufbau eines Demonstrationsexperiments zum Photoeffekt
  Till Stöckli, Bachelor thesis, July 2016.

- Construction and Characterization of a Doubochinski Pendulum
  Tranquillo Janisch, Bachelor thesis, July 2016.